University of Barcelona

Faculty of Earth Sciences

Doctoral Program in Earth Sciences

Experimental and numerical study of chemo-hydro-mechanical effects of CO_2 injection on permeable limestone

Dissertation presented by

Atefeh Vafaie

Director	Director	Tutor
Dr. Jordi Cama	Dr. Josep M. Soler	Dr. M. Àngels Canals Sabaté
IDAEA-CSIC	IDAEA-CSIC	University of Barcelona

Barcelona, May 2023

This Ph.D. study has received funding from the European Joint Programme on Radioactive Waste Management, EJP-EURAD of the European Union's Horizon 2020 Research and Innovation Programme 2014-2018 under agreement No. 847593, specifically from the WP MAGIC, and also from the Catalan Government through project 2017SGR1733.

Dedicated to

The reason for my smiles

ایمان

&

The li'l Pirouz (پیروز)

The symbol of light in the darkest of times.
May we all become the meaning of his name in the end.

Abstract

Carbon capture and storage (CCS) in saline aquifers is a proven technology aimed at reducing atmospheric CO_2 emissions and mitigating the climate change crisis. CO_2 injection acidifies the formation water inducing mineral dissolution and alterations in the pore structure and hydromechanical properties of the rock, particularly in carbonate reservoirs with large contents of fast-reacting minerals. Improving the current understanding of the form, extent, and governing mechanisms of such interactions is central to optimizing and securing the implementation of CCS and serves as the primary goal of this study. To achieve this goal, this study combines (i) percolation experiments with CO_2-saturated water and HCl solutions on cm-scale cores of highly permeable Pont du Gard Limestone and (ii) 3D Darcy-scale reactive transport simulations of the performed experiments. Effluent chemistry analyses, X-ray Micro Computed Tomography (XMCT) imaging, and measurements of the hydromechanical properties of intact and altered specimens are employed to quantify acid-induced changes in the two acid-rock systems. Further, a digital rock approach is developed to construct heterogeneous permeability maps of the intact specimens from CT images that feed as inputs into 3D Darcy-scale reactive transport models.

Experimental results show that the acid type and pore space heterogeneity have primary control on dissolution patterns formed in limestone specimens and the resulting alterations in their hydromechanical properties. Under the flow conditions of these experiments, the complete dissociation of HCl as a strong acid leads to rapid limestone dissolution and the formation of compact dissolution patterns that only affect the hydromechanical properties at the core inlet. In contrast, partial dissociation of H_2CO_3 as a weak acid extends the dissolution reaction along the core and induces wormhole formation that markedly enhances the rock permeability. Altered cores render significant attenuation in both mechanical rock properties and ultrasonic velocities. Chemically-driven alterations in rock stiffness are reproduced using a Differential Effective Medium (DEM) homogenization approach.

Numerical simulations using the 3D Darcy-scale reactive transport model satisfactorily reproduce the experimentally measured changes in effluent chemistry, porosity, permeability, and the observed dissolution features in CT images of reacted limestone samples. Simulation results indicate that the pore space heterogeneity controls calcite dissolution from the very beginning of acidic fluid injections while the acid type becomes progressively important as the reaction front further penetrates into the rock. The compact dissolution pattern formed in the HCl-limestone system can be numerically captured using the classical Kozeny-Carman porosity-permeability relationship with a power-law exponent of 3 applied to the grid blocks of the numerical domain. In the case of CO_2 injection, however, formation of wormhole by continuous acid renewal exerts strong feedback between the fluid flow and the dissolution reaction. This dissolution pattern can only be reproduced using an exponent as large as 15 that increases to ≈ 27 for the bulk behavior of the core containing a wormhole. This demonstrates that acid-induced permeability evolution in carbonate rocks is highly scale-dependent.

The percolation experiments performed using CO_2-saturated water represent a severe scenario of CO_2-brine-rock interactions in carbonate reservoirs that needs to be considered in predictions and monitoring of CO_2 storage. This study highlights (1) the importance of small-

scale heterogeneities in controlling flow properties and localization of flow and chemical reactions in limestones and (2) the need for developing rigorous upscaling approaches to account for them in field-scale simulations.

Resum

La captura i emmagatzematge de carboni (CCS) en aqüífers salins és una tecnologia provada per reduir les emissions de CO_2 a l'atmosfera i mitigar la crisi del canvi climàtic. El CO_2 injectat acidifica l'aigua soterrània, tot induint la dissolució dels minerals rocosos i l'alteració de l'estructura porosa de la roca. Com a conseqüència, les propietats hidro-mecàniques de la roca varien, especialment en dipòsits de minerals carbonats les velocitats de dissolució dels quals són ràpides. Així doncs, per optimitzar una implementació segura del CCS, cal entendre bé la forma, l'abast i els mecanismes que governen aquestes interaccions. Per aconseguir aquest objectiu, s'han realitzat (i) experiments de percolació [aigua saturada de CO_2 i solucions de HCl que circulen a través de mostres centimètriques de roca calcària i permeable del Pont du Gard (França)] i (ii) simulacions 3D de transport reactiu d'aquests experiments a escala Darcy. Els canvis originats en les mostres rocoses s'han detectat mesurant les concentracions dels efluents i fent imatges de tomografia de raigs X (XMTC) i mesurant les propietats hidro-mecàniques de les mostres abans i després dels experiments. A més a més, a partir de les imatges de TC s'ha desenvolupat un tractament digital per construir mapes de distribució de permeabilitat en les mostres intactes. Les dades d'aquets mapes s'han utilitzat en els models 3D de transport reactiu.

Els resultats experimentals mostren que el tipus d'àcid i l'heterogeneïtat de l'espai porós controlen els patrons de dissolució i l'alteració de les propietats hidro-mecàniques. En les condicions de flux d'aquests experiments, la dissociació completa de l'HCl (àcid fort) produeix reaccions ràpides amb els minerals de la roca i la formació d'un patró de dissolució compacte que només afecta les propietats hidro-mecàniques de l'entrada de la mostra. En canvi, la dissociació parcial de H_2CO_3 (àcid feble) estén les reaccions químiques al llarg de la mostra causant la formació d'un forat de cuc que incrementa notablement la permeabilitat de la roca. Les mostres alterades atenuen significativament les propietats mecàniques de les roques i les velocitats ultrasòniques. Aquestes alteracions químiques que afecten la rigidesa de la roca s'han reproduït mitjançant un eficaç esquema diferencial del mitjà eficaç diferencial (DEM).

Les simulacions numèriques en 3D reprodueixen satisfactòriament l'evolució de la química de l'efluent i de la porositat i permeabilitat de la roca calcària, així com els patrons de dissolució. Les simulacions mostren que l'heterogeneïtat de l'espai de porus controla les reaccions químiques durant les injeccions dels fluids àcids i que el tipus d'àcid esdevé important en l'evolució del front de reacció. Utilitzant la relació clàssica de porositat-permeabilitat de Kozeny-Carman amb un exponent de 3 aplicat als blocs de quadrícula del domini numèric es pot reproduir el patró de dissolució compacte produït en el sistema HCl-calcària. Tanmateix, en el cas de la injecció de CO_2, els forats de cuc formats per la renovació contínua d'àcid al llarg de la mostra comporten una forta retroalimentació entre el flux de fluid i les reaccions que només es pot reproduir usant exponents tan grans com 15 i que augmenta fins a ≈ 27. D'aquesta manera es demostra que el canvi de permeabilitat induït per l'àcid a les roques carbonatades depèn en gran mesura de l'escala.

Els experiments de percolació amb aigua saturada de CO_2 representen un escenari sever d'interacció "CO_2-salmorra-roca" en dipòsits rocosos formats per minerals carbonats que cal tenir en compte en les prediccions i/o en el monitoratge de l'emmagatzematge de CO_2. Aquest estudi destaca que les heterogeneïtats a petita escala controlen les propietats del flux i la localització del flux i de les reaccions químiques a les roques calcàries. Indica, per tant, la necessitat de desenvolupar estratègies dirigides a l'augment d'escala que contemplin aquestes heterogeneïtats en les simulacions numèriques a escala de camp.

List of publications

Journal articles

Vafaie, A., Cama, J., Soler, J.M., Kivi, I.R., Vilarrasa, V., 2023. Chemo-hydro-mechanical effects of CO_2 injection on reservoir and seal rocks: A review on laboratory experiments. Renewable and Sustainable Energy Reviews, 178, 113270.

Vafaie, A., Cama, J., Soler, J.M., Grgic, D., Vilarrasa, V., 2023. Chemo-hydro-mechanical effects of CO_2 injection into permeable limestone. Under review in the International Journal of Coal Geology.

Vafaie, A., Soler, J.M., Cama, J., Kivi, I.R., Vilarrasa, V., 2023. A MATLAB approach to developing digital rock models of heterogeneous limestones for reactive transport modeling. Submitted to Geologica Acta.

Vafaie, A., Soler, J.M., Cama, J., Vilarrasa, V., 2023. Understanding the effect of small-scale heterogeneities on reactive transport in carbonate rocks. Will be submitted to Advances in Water Resources.

Conference presentations

Vafaie, A., Cama, J., M Soler, J., Morlot, C., Vilarrasa, V., 2023. Changes in chemo-hydro-mechanical properties of limestone in contact with CO_2-rich water. Proceedings WR-17 & AIG-14 Sendai, Japan, August 18-22.

Vafaie, A., 2022. Effect of CO_2-rich water injection on hydromechanical properties of a grain-supported limestone sample: laboratory experiment and numerical modeling. Subsurface Hydrology Group Seminar Series (Seminario Grupo Hidrología Subterránea), Polytechnic University of Catalonia (Universitat Politècnica de Catalunya · Barcelona Tech), July 23.

Vafaie, A., Cama, J., M Soler, J., 2022. 3D reactive transport modeling of laboratory-scale CO_2 injection in limestone leading to wormhole formation. Poster presentation at Interpore2022 conference, Khalifa University, Abu Dhabi, United Arab Emirates,May 30-June 3 .

Vafaie, A., Cama, J., M Soler, J., 2022. Effect of CO_2-rich water injection on the hydromechanical properties of Pont Du Gard limestone. Oral presentation in the EGU General Assembly, Vienna, Austria, May 23–27.

Vafaie, A., Cama, J., M Soler, J., 2021. Percolation experiments to study the impact of acidic solutions on porous limestones in the context of CO_2 storage. Oral presentation at Interpore Spanish Chapter, Valencia, Spain, October 26.

Vafaie, A., Cama, J., M Soler, J., 2021. Laboratory assessment of the coupled chemo-hydro-mechanical (CHM) response of limestone to supercritical CO_2 injection. Oral presentation at 5th summer school on Flow and Transport in Porous and Fractured Media, IESC Cargese, France, July 30.

Vafaie, A., Cama, J., M Soler, J., 2021. Laboratory measurements of the hydraulic-geochemical-mechanical properties of limestone during injection of CO_2-rich water under CO_2 supercritical conditions. Oral presentation at Goldschmidt, Paris, France, July 6.

Vafaie, A., Cama, J., M Soler, J., 2021. Evolution of mechanical and hydraulic properties in a calcareous rock induced by CO_2 injection. Oral presentation at II Conference of Young SEM Researchers, Spain.

Vafaie, A., Cama, J., M Soler, J., 2021. Study of the evolution of mechanical and hydraulic properties of sedimentary rocks induced by CO_2 injection at lab-scale. Poster presentation at King Abdullah University of Science and Technology's (KAUST) Research Conference: Enabling CO_2 Geological Storage within a Low-Carbon Economy, February 22-24.

Vafaie, A., Cama, J., M Soler, J., 2020. An experimental investigation of the chemo-hydro-mechanical effects of CO2 injection into sedimentary rocks. Poster presentation at Young Researcher's Week (YRW), IDAEA-CSIC, Barcelona, Spain.

Acknowledgments

First and foremost, I would like to express my gratitude to my supervisors, Dr. Jordi Cama and Dr. Josep M Soler for their availability and their help to identify flaws and strengths in my work. This work was only possible with their advice and support and I am profusely grateful for the opportunities they have given me.

I give my profound thanks to my unofficial supervisor Dr. Victor Vilarrasa for providing me with guidance, encouragement, and infinite support throughout my Ph.D. program.

I would also like to thank my UB tutor Dr. M. Àngels Canals Sabaté for her help during the past three years.

A special thanks to my examination committee Dr. Maarten Saaltink, Dr. Enrique Gomez Rivas, and Dr. Fidel Grandia for their insightful feedback and their contribution to making this work possible.

I must thank Jordi Bellés not only for his help in the lab but also for all the good moments and laughs we have shared.

I must also thank Dr. Juan Hidalgo for his great assistance in software-related parts of my work.

A special thanks to Dr. Dragan Grgic, Dr. Jérôme Sterpenich, Christophe Morlot, and Laurent Schoumacker at the University of Lorraine for helping me in conducting mechanical tests and X-ray Micro Computed Tomography.

To my beloved husband Iman. Thank you for all devotions you have made during these years. You know better that you are not only my best friend and supporter, but also my best adviser in scientific works.

To my family, Maman, Baba, and my two little chicks; Afsaneh and Mansoureh. Living abroad without you all by my side was not easy, but thanks to your love and support I could go through it. Love you all. I hope I have made you proud.

Last but not least, I want to thank all my friends in IDAEA for their positive influence on my life.

تا چه بازی رخ نماید بیدقی خواهیم راند...

Table of Contents

Abstract I
Resum III
List of publications IV
Acknowledgments VI
Introduction 1
1.1. Motivation and background 1
1.2. Objectives 2
1.3. Thesis outline 3
Scientific background 5
2.1. CO_2-brine-rock interactions 5
2.2. Chemically-induced alterations of rocks 8
2.3. Experimental approaches 9
2.3.1. Batch experiments 13
2.3.2. Flow-through experiments 13
2.3.3. Natural analogue samples 14
2.4. CHM effects of CO_2 on reservoir rocks 14
2.4.1. Changes in hydraulic properties 14
2.4.1.1. Role of mineralogy and flow conditions 14
2.4.1.2. Wormhole formation and rock heterogeneity 18
2.4.1.3. Geochemical controls on multiphase flow 20
2.4.2. Geochemical effects on mechanical behavior 22
2.4.2.1. Elastic-Poroelastic properties 23
2.4.2.2. Failure behavior 24
2.4.2.3. Time-dependent behavior 26
2.5. CHM effects of CO_2 on shales 28
2.5.1. Changes in hydraulic properties: concerns about caprock sealing capacity 28
2.5.2. Geochemical effects on mechanical behavior: effect on caprock integrity 29
2.6. Geochemical processes for CO_2 injection into fractured rocks 31
2.6.1. Evolution of reaction and flow trajectories 31
2.6.2. Localized deformation and fracture propagation 33
2.7. Recent advances and the path forward 34
2.7.1 Fundamental understanding of the CHM processes of CO_2 injection 34
2.7.2. Upscaling in time and space 40
Methodology 42

3.1. Experimental Methodology 42
3.1.1. Samples and experimental plan 42
3.1.2. Percolation experiments: apparatus and procedure 43
3.1.3. Evaluation of microstructural and transport properties 44
3.1.3.1. Porosity and pore size distribution 44
3.1.3.2. Pore-scale imaging 45
3.1.3.3. Permeability measurement 45
3.1.3.4. Quantification of calcite dissolution 46
3.1.4. Evaluation of mechanical properties 46
3.1.4.1. Uniaxial compression test 46
3.1.4.2. Ultrasonic wave propagation 47
3.2. Digital rock models 47
3.2.1. Description of the approach 48
3.2.1.1. Image acquisition 48
3.2.1.2. Domain discretization 50
3.2.1.3. Porosity map reconstruction 51
3.2.2. Application to Pont du Gard Limestone 54
3.2.2.1. Porosity distribution of the samples 54
3.2.2.2. Code Performance 58
3.3. Reactive transport modeling 58
3.3.1. Description of the reactive transport code 59
3.3.2. Model setup 60
3.3.3. Rock and solution compositions 62
3.3.4. Constructing the initial permeability map 62
3.3.5. Porosity-permeability-surface area relationship 64
Results 66
4.1. Experimental results 66
4.1.1. Acid-induced dissolution 66
4.1.2. Transport properties and pore structure evolution 67
4.1.2.1. Change in porosity and dissolution patterns 67
4.1.2.2. Variation in permeability 70
4.1.2.3. Variation in pore size distribution 71
4.1.3. Stiffness and strength weakening 72
4.2. Reactive transport simulation results 75
4.2.1. CO_2-saturated water injection: wormhole formation 75
4.2.2. HCl solution injection: compact dissolution 80
Discussion 84

5.1. Limitations of the Darcy-scale numerical model 84
5.2 Factors controlling limestone alteration and dissolution patterns 85
5.3 Porosity-permeability relationship 86
5.4 Pore structure controls on the mechanical behavior 87
5.5. Implications for field injections 89
Conclusions and recommendations 91
6.1. Conclusions 91
6.2. Recommendations 92
References 95
Appendix I 116
Complementary information on earlier experimental studies 116
Appendix II 131
Experimental setups 131
High-pressure flow-through setup 131
Atmospheric-pressure flow-through setup 131
Classical permeability measurement setup 132
Uniaxial loading setup 133
Ultrasonic velocity measurement setup 134
Appendix III 135
A MATLAB code for digital reconstruction of rock porosity and permeability 135
Porosity and permeability calculation 135
Plotting 2D images 141
Plotting 3D images 143
Appendix VI 151
Functional form of geometric factors P and Q 151

List of Tables

Table 1. Summary of common laboratory techniques used to evaluate the alterations in rock properties upon interaction with CO_2. The references point to some examples of using the techniques in the context of CO_2-water-rock interaction. 11
Table 2. Experimental conditions and experimental techniques. 43
Table 3. Data of numerical discretization and flow properties of different zones used in 3D numerical simulations. 62
Table 4. Reaction parameters, calcite volume fraction in cores and chemical composition and pH of input solutions. 63
Table 5. Porosity and permeability calculated using the intact and altered cores. ϕ_{bulk}: porosity calculated by weight measurement. 69
Table 6. Static and dynamic elastic moduli values measured for intact and altered cores. 74
Table A1. Summary of experimental conditions and measured parameters before and after exposure to CO_2. Reported studies are sorted chronologically for each rock type 116
Table A2. List of laboratory studies conducted on different reservoir and seal rocks with varying carbonate content and initial hydraulic properties under different flow (i.e., Batch (B), or Flowthrough (F-T)) and experimental conditions (i.e., pressure, temperature, and duration) together with resultant hydraulic properties of altered rocks 124
Table A3. List of laboratory studies on different reservoir or seal rocks and their acoustic and mechanical properties before and after exposure to CO_2 128

List of Figures

Figure 1. Schematic of a geological CO_2 storage site with zones formed around the injection well (a) and potential reactions in these zones (b). A_1 to A_4 represent zones formed in the reservoir rock. A_1, or the near-wellbore zone, is fully occupied by dry supercritical CO_2. A_3 is a two-phase flow zone and is surrounded by zones A_2 and A_4 comprising water-bearing CO_2 and CO_2-bearing brine, respectively. A_5 is the far-field or uninvaded zone. The caprock is divided into 3 zones: two-phase CO_2-brine zones (dry CO_2 in C_1 and wet CO_2 in C_2) and a CO_2-rich brine zone (C_3). 7
Figure 2. Schematic experimental setups used to expose rock samples to CO_2: (a) static (no flow) batch and (b) flow-through experiments. In the flow-through setup, $\sigma 1$ and $\sigma 3$ represent axial and radial (confining) stresses, respectively, and V_1 and V_2 are three-sided valves allowing free-phase CO_2 or CO_2-rich water to be injected. 12
Figure 3. Porosity changes in carbonate rocks during CO_2 injection: (a) cross-plot of porosity for treated Ekofisk and Tor Chalks subjected to supercritical CO_2 injection versus intact porosities (modified from Alam et al., 2014) and (b) porosity variations in a limestone specimen with injected pore volumes of CO_2-rich water (modified from Vialle and Vanorio, 2011). 16
Figure 4. Variation in porosity in sandstones with different mineral contents reacted with CO_2-rich water under no-flow (Akono et al., 2020; Nover et al., 2013; Farquhar et al., 2015; Fuchs et al., 2019; Shi et al., 2019; Li et al., 2020; Tariq et al., 2018; Fischer et al., 213; Harbert et al.,2020) (a) and open-flow conditions (Luquot et al., 2016; Rimmelé et al., 2010; Tarokh et al., 2020; Zhou et al., 2016; Yu et al., 2019; Kim and Makhnenko, 2021; Canal et al., 2013; Foroutan et al., 2021a; Lamy-Chappuis et al., 2016) (b). The duration of the experiments, if reported, is also illustrated. 17
Figure 5. Decrease in porosity and permeability for quartz-rich Fontainebleau sandstone specimens after injection of gaseous CO_2 (modified after Vanorio et al., 2011). 18
Figure 6. Neutron radiographs of different dissolution patterns caused by reactive fluids in limestone: (a) uniform dissolution, (b) compact dissolution, (c) conical wormhole, (d) ramified wormhole, and (e) dominant wormhole formation (adapted from Fredd and Fogler, 1998). Ranges of Damkohler *(Da)* and Peclect *(Pe)* numbers are taken from Menke, 2016. 19
Figure 7. Permeability changes as a function of porosity in an Estaillades Limestone specimen flooded with a CO_2-rich brine/distilled water sequence for 115 days (modified from Vialle et al., 2014)..... 20
Figure 8. Relative permeability curves at intermediate water saturations and pore size distribution for limestone samples from the Ketton (a and b, respectively) and Estaillades Formations (c and d, respectively) before and after treatment with CO_2 (adapted from Niu and Krevor, 2020). 22
Figure 9. Deviatoric versus mean effective stress *q-p´* plots of failure properties of intact and CO_2-injected specimens from the (a) Ekofisk Chalk and (b) Tor Chalk. Circles, triangles, and solid lines indicate pore collapse onset (i.e., the point at which stress-strain curves deviate from linear elastic behavior), shear strength (i.e., the point where rock failure occurs under elevated deviatoric stresses), and failure envelopes (laboratory data fitting). Characteristics of intact and altered rocks are discriminated by blue and red colors, respectively (adapted from Alam et al., 2014). 25
Figure 10. Deformation and failure characteristics of Entrada Sandstones (a and b) and Summerville Siltstone (c and d) (modified from Espinoza et al., 2018). (a) X-ray CT section of the altered specimen with an evident single plane shear failure. The magnified CT image shows enhanced porosity (black area) by cement dissolution (red arrows); (b) stress-strain curves show brittle failure for both intact and altered Entrada Sandstone; (c) X-ray CT image illustrating initial heterogeneities (red arrows) which likely affect strain localization and failure pattern in the altered sample; and (d) stress-strain curves depicting brittle failure for intact Summerville Siltstone and ductile slightly strain-softening for altered ones. 26
Figure 11. Overview of the geochemical effects of CO_2 injection on hydromechanical properties of the reservoir and sealing rocks and the associated key issues, including reservoir injectivity, deformation and integrity, caprock integrity and sealing capacity and induced seismicity. Note that zones A_1 to A_5 in the reservoir and C_1 to C_3 in the caprock are defined in the same way as in Fig. 1. 36

Figure 12. Box-and-whisker plots for changes in porosity (a), permeability (b), Young´s modulus (c), and Poisson´s ratio (d). The CO_2 exposure types, batch, flow-through, or natural, are highlighted in different colors. The dividing lines in the boxes indicate the median values, and the bottom and top edges illustrate the first and third quartiles, respectively. The whiskers extend to the most extreme data points not statistically considered outliers. The permeability enhancement of 125 folds measured by Noiriel et al. (200%) for Lérouville limestone is not illustrated in the figure for the sake of more clear observation of other experimental data. Data listed in Table A3 (Appendix I) used to plot this figure. 38
Figure 13. Schematics of the two setups used to run the (a) supercritical CO_2 and (b) atmospheric HCl percolation experiments. 44
Figure 14. (a) A 2D grayscale cross-section image of the Pont Du Gard limestone, (b) flow diagram of adjusting segmentation threshold using the ImageJ software, and (c) extracted 2D binary images. 50
Figure 15. (a) Photograph of a sample of Pont Du Gard Limestone used in this study, (b) illustration of the horizontal segments (HS) along the core length, (c) 2D binary cross-section (CS) images in one segment, and (d) a magnified pixel-based illustration of a pore in a cross-section. 51
Figure 16. (a) Illustration of a discretized 2D binary image in X and Y directions and (b) the corresponding (0,1) matrix representation of the image with the size of Pixel_No × Pixel_No. 52
Figure 17. Workflow of the algorithm proposed to reconstruct 3D maps of porosity and associated parameters. 53
Figure 18. (a) An 8-bit gray-level image from the XMCT data of sample P_3 (Pont Du Gard Limestone), (b) the corresponding binary image, and (c) the segmentation procedure based on the Otsu method. 55
Figure 19. Distribution of initial and adjusted XMCT porosity along sample P_3 (Pont Du Gard Limestone). 56
Figure 20. 2D illustrations of: (a) a raw binary cross-section image, (b) a reconstructed grid-based porosity map with a size of 20 × 20 and (c) a reconstructed grid-based porosity map with a size of 40 × 40. Similar plots (d, e, and f) provided for the cross-section after adjusting the XMCT porosity to effective porosity from mercury porosimetry. 57
Figure 21. Heterogeneous distribution of porosity over the examined core: (a) histogram showing the grid-based distribution of total porosity obtained from image processing and (b) 3D porosity map reconstructed over sample P_3 (Pont Du Gard Limestone). 58
Figure 22. Overview of the workflow and data used. The grayscale images illustrate center vertical XMCT scans of a specimen before and after flooding with acidic solutions. To the left of the XMCT data before injection are the resulting initial porosity and permeability maps from image processing and a power-law porosity-permeability relationship, respectively. To the left of the XMCT data after injection are dissolution patterns inferred directly from image processing or indirectly from continuum-scale reactive transport modeling, respectively (illustrating an example for the specimen flooded with CO_2-rich water). Configuration of the best predictive model is achieved through comparison between model predictions and measurements of the effluent chemistry evolution. 59
Figure 23. 3D conceptual model, numerical discretization and boundary conditions of flow domain used in the reactive transport simulations. 61
Figure 24. Permeability for sample P_3 (Pont Du Gard Limestone): (a) histogram and (b) 3D map of the grid-based distribution of permeability. 64
Figure 25. Possible range of changes in the reactive surface area and permeability of each numerical grid block as a result of chemically-induced changes in porosity 65
Figure 26. Variation in water chemistry as a function of time: $[Ca]_{output}$ for (a) CO_2-saturated water experiments and (b) HCl solution experiments and (c) output pH in the HCl experiments. 68
Figure 27. Average XMCT porosity profiles along the cores before and after the experiments: (a) and (b) = CO_2-saturated water; (c) and (d) = HCl solution. Increments in porosity ($\Delta\phi$) due to calcite dissolution are shown by gray dashed lines. In (b), the inset shows lower porosity values after the core inlet (between 1 cm and 4.5 cm). 70

Figure 28. Porosity changes and dissolution patterns deduced from XMCT images. 2D porosity maps for a central slice along the P_5 and P_3 cores before (a and c) and after (b and d) injection of HCl and CO_2-saturated solutions. A two-color filter is used in images (a) to (d) to distinguish between calcite grains (red areas) and pore space (blue areas). 3D reconstruction of dissolution-induced porosity changes in P_3 (e), resolving the structure of the formed wormhole. 71
Figure 29. (a) Cumulative and (b) incremental distributions of the pore throat size in intact (P_1) and HCl-altered specimens (P_4 and P_5). 72
Figure 30. Variation in the sonic velocity as a function of porosity in the studied limestone under study (large symbols) upon exposure to acid solutions. Higher porosity-lower velocity data for each specimen consistently refer to the post-injection state. Colored symbols represent the velocity-porosity data for intact carbonate rocks reported in earlier experimental studies (El Husseiny and Vanorio, 2015; Eberli et al., 2003; Vanorio et al., 2008)..... 73
Figure 31. Stress-strain response of (a) intact P_1 and altered (b) P_2-CO_2-*14*, (c) P_4^{**}-*HCl-14*, and (d) P_5-*HCl-28* cores under uniaxial compression. Axial stress is shown as a function of axial (black solid line), lateral (red solid line), and volumetric (gray dashed line) strains..... 75
Figure 32. Simulated spatial development of porosity at the core inlet after CO_2-saturated water injection for 96 h using porosity-permeability relationship (Eq. 14) with n ranging between 3 and 15 (a-f)..... 76
Figure 33. 2D XMCT cross-section images perpendicular to the flow direction (Z) along the P_3 core before (upper row) and after (lower row) 28 days of reaction with CO_2-saturated water. In the lower sequence, the dark area is new porosity caused by calcite dissolution. The numbers indicate the position of the images along the Z axis separated at a constant distance of 0.88 mm (1: inlet, 6: outlet). Section AA´ along the core was used to plot the simulations displayed in Fig. 35. 76
Figure 34. Experimental and simulated variation in the output fluid chemistry over time in the P_3 experiment with n = 3, 4, 8, 10, 15, and 20 (Eq. 14): (a) Ca concentration and (b) solution pH. Line colors are gradually lightened with the decrease in the n value..... 77
Figure 35. Experimental (a-c) and simulated (d-o) distribution of porosity in a vertical cross-section along the flow direction in sample P_3 (section AA' shown in Fig. 33): (a) before CO_2 injection and (b,c) after CO_2 injection for 14 days and 28 days inferred from XMCT images; (d-o) simulations after reaction with CO_2-saturated water for 14 days and 28 days using n = 3, 4, 8, 10, 12, and 15 (Eq. 14). 79
Figure 36. Change in bulk core permeability as a function of average porosity estimated from numerical simulations (black circles). The fitted core-scale power-law correlation (solid line) measures an exponent of 27.6..... 80
Figure 37. Experimental (solid symbols) and calculated with n = 3, 4, 8, 12, and 15 (lines) variation in the outflow chemistry in the P_5 experiment: (a) experimental output Ca concentration and (b) experimental output pH. Note that the scale of the Ca concentration is one order of magnitude smaller than that in Fig. 34 for CO_2-saturated water injection. All simulations coincide because changes were not observed in the effluent chemistry by varying the n exponent (Eq. 14). 81
Figure 38. 2D XMCT images perpendicular to the flow direction (Z) along the P_5 core before (upper row) and after (lower row) reaction with HCl solution. The large dark area in the first slice shows dissolution-induced porosity enhancement concentrated at the inlet (compact dissolution). The numbers indicate the position of the images along the Z axis separated by a constant distance of 1.56 mm (1: inlet, 6: outlet). Section AA´ along the core was used to plot results in Fig. 39..... 82
Figure 39. Distribution of measured (a,b) and simulated (c-h) porosity in a vertical cross-section along the P_5 core (section AA' shown in Fig. 38): (a) before and (b) after HCl injection inferred from XMCT images; (c,d) simulations of the core-HCl interaction after17 and 28 days using n = 3 and (e-h) simulations of core-HCl interaction after 17 days using n = 4, 8, 10, 12 and 15 (Eq. 14)..... 83
Figure 40. Grain-supported structure of the intact Pont du Gard Limestone: (a) a representative XMCT slice and (b) the histogram of grayscale values of the XMCT image. Vertical dashed lines indicate grayscale values of macropores and calcite grains. 88

Figure 41. Evolution of (a) the effective bulk K* and (b) shear G* moduli measured in the laboratory for Pont du Gard specimen (cross symbols) and estimated using the DEM model (lines colored according to the aspect ratio of the inclusions).....89
Figure A1. Photograph of the high-pressure flow-through setup used to inject CO_2-saturated water in the limestone cores under supercritical CO_2 conditions……131
Figure A2. Photograph of the atmospheric flow-through setup used to inject HCl solution in the limestone cores under atmospheric pressure……131
Figure A3. Schematic of the permeability measurement setup……132
Figure A4. Photograph of the uniaxial loading setup……...133
Figure A5. Photographs of: (a) a centimeter-scale core with attached pulser and receiver and (b) the EPOCH650 ultrasonic flaw detector used to measure compressional and shear wave velocities…..…134

Chapter 1

Introduction

1.1. Motivation and background

Carbon Capture and Storage (CCS) in deep geological formations is a reliable strategy to mitigate climate change (Bachu and Adams, 2003; Celia, 2017; Ringrose and Meckel, 2019). CCS involves capturing CO_2 from industrial processes or from the atmosphere to be injected into suitable deep formations (e.g., saline aquifers, depleted oil and gas reservoirs, coal beds and salt domes). Most mitigation pathways consistent with the Paris climate goal of limiting global warming to well below 2 ºC rely on large-scale deployment of CCS. The annual storage rates are expected to increase around the globe and reach up to 10 Gt and 25 Gt per year in 2050 and 2100, respectively, indicating cumulative storage of 800-3000 Gt CO_2 in the current century (Bui et al., 2018).

Among all suitable repositories, saline aquifers have received notable attention for storage of large amounts of CO_2 owing to their large capacity and wide availability around the world. At geological storage sites, the injected CO_2 into these reservoirs (at depth larger than 800 m) reaches supercritical conditions (pressure > 7.3 MPa and temperature > 31.1 °C), leading to a liquid-like density that makes the storage volumetrically efficient. Yet, supercritical CO_2 density is lower than that of resident brine, challenging the storage as buoyancy tends to drive CO_2 upward back to the surface. Low-permeability caprocks are therefore essential to permanently maintain CO_2 deep underground. Another challenge that CCS at the gigatonne scale may encounter is the interference between multiple CO_2 injection wells targeting the same formation, giving rise to basin-wide pressurization of several megapascals (Zhou et al., 2009). This overpressure may impose constraints on the maximum allowable injection rates and storage capacities and raise concerns about CO_2 and brine leakage through the overlying caprock(s) and induced earthquakes (Birkholzer et al., 2009; Rutqvist, 2012). These phenomena could negatively impact the environment and harm the public perception of CCS, which may jeopardize its widespread implementation. Consequently, the hydrogeological response of the subsurface to CO_2 injection becomes a matter of paramount importance when assessing potential geological storage sites and the long-term fate of the stored CO_2.

CO_2 injection into saline aquifers triggers a series of thermo-chemo-hydro-mechanical processes (THMC). These processes play a key role in CO_2 transport and storage deep underground. Among them, chemical reactions at the fluid-rock interface are of fundamental importance (Metz et al., 2005; Gaus, 2010). When injected into the aquifer, CO_2 dissolves in the resident brine forming carbonic acid, which causes mineral dissolution. These chemical interactions are particularly important in carbonate rocks because (1) they contain significant amounts of highly reactive calcite, (2) they are widespread and constitute several candidate reservoirs for underground CO_2 storage (Gray, 2015). Carbonate dissolution may induce modifications in the pore structure and hydromechanical properties of the rock with effects on reservoir injectivity, mechanical integrity, and storage capacity. For instance, insights gained from CO_2-EOR operation in the SACROC field, USA, showed significant mineral dissolution that resulted in 50% injectivity enhancement (Kane et al., 1979). A thorough understanding of the mechanisms, magnitude, and distribution of carbonate dissolution in the CO_2-brine-carbonate rock system is therefore essential for predicting the long-term fate of CO_2 underground.

Characterization of acid-carbonate rock interactions has a long history in the scientific community and the industry. In particular, extensive studies have been carried out in the context of stimulating hydrocarbon reservoirs using hydrochloric acid (HCl). The interests have recently shifted toward understanding the geochemical interactions of CO_2 and rock. The utilized methodologies span a wide range but can be broadly categorized into laboratory experiments on centimeter-scale specimens, in-situ experiments on meter-scale rock masses in underground rock laboratories, monitoring field-scale fluid injections and numerical simulations at varying scales. Centimeter-scale laboratory experiments under controlled conditions and high-resolution monitoring found a basis for a fundamental understanding of acid-rock interactions. Yet, common analytical approaches may not be sufficient to fully address the underlying physico-chemical mechanisms owing to their tightly-coupled and complex nature. Numerical simulations of the conducted experiments provide a powerful tool to shed lights on these processes.

1.2. Objectives

This thesis aims to improve our understanding of the effects of geochemical reactions during CO_2-water-rock interactions on hydromechanical properties of limestone. To this end, the following tasks have been carried out:

- Comprehensive review of the current knowledge on chemo-hydro-mechanical (CHM) effects of CO_2 injection into sedimentary rocks gained from laboratory experiments
- Flow-through experiments with CO_2-saturated water and HCl solutions on a highly permeable limestone
- 3D Darcy-scale reactive transport modeling of the experiments employing accurate digital rock models

Using this approach, the following specific goals have been accomplished:

- Assessment of the extent of chemical reactions of the permeable Pont du Gard Limestone (representative reservoir rock for CCS) with CO_2-saturated water and HCl solutions
- Measurement of chemically-driven changes in hydraulic and mechanical properties of the limestone
- Adoption of an effective elastic medium theory to reproduce chemically-induced alterations in the mechanical stiffness of the limestone
- Development of a computationally-efficient method to construct digital rock models from X-ray micro-computed tomography
- 3D Darcy-scale reactive transport modeling to address the effects of small-scale pore space heterogeneities on coupled flow and reaction process in carbonate rocks
- Development of a numerically-calibrated porosity-permeability relationship as a critical factor in coupling flow and chemical fields
- Evaluation of the key factors controlling acid-induced dissolution processes in heterogeneous carbonate rocks
- Interpretation of differences between the two acid-rock systems (HCl and CO_2-rich water), to unravel if insights gained from acid-stimulation operations in the petroleum industry are correlated with CCS

1.3. Thesis outline

The thesis is composed of 6 chapters including introduction (Chapter 1) and conclusions (Chapter 6).

Chapter 2 provides a comprehensive review of the current knowledge of chemical, hydraulic, and mechanical processes involved in geological carbon storage that has been acquired from laboratory experiments using both intact and fractured rock samples. The experimental approaches employed to assess the coupled CHM processes in rocks induced by injected CO_2 are first described. Then, geochemical controls on the transport, flow, and mechanical properties of reservoir rocks, caprocks, and fractured rocks are discussed. The chapter is concluded with recent advances in the understanding of coupled CHM processes and their implications for field CO_2 storage practices. Emphasis is given on knowledge gaps that deserve further investigation. This Ph.D. research attempts to addressing part of these challenges.

Chapter 3 presents the methodology used in this study, including experimental and numerical approaches. The experimental methodology consists of conducting percolation experiments by injecting acidic fluids (CO_2-saturated water and HCl solution) into heterogeneous grain-supported samples from the Pont du Gard Limestone for 14 and 28 days. Combination of effluent chemistry analysis with pore-scale imaging, and measurements of pore size distribution, porosity and permeability before and after injection are performed to characterize the evolution of the pore structure and hydraulic properties of the rock. Changes in the elastic and strength properties are assessed by conducting ultrasonic velocity measurements and uniaxial compression tests on intact and acid-altered specimens. The numerical methodology includes (1) developing a simple but computationally efficient and accurate MATLAB-based method to construct 3D distributions of porosity and permeability in the limestone samples,

and (2) directly integrating the digital rock models into a 3D continuum-scale reactive transport model in the CrunchFlow code.

Chapter 4 presents the experimental and modeling results. A detailed analysis of experimental observations enables us to characterize the magnitude of the reactions induced by the two different acids and their impacts on the hydromechanical properties of the limestone. It is shown that an accurate reproduction of the key experimental features is possible through proper model parameterization.

Chapter 5 brings together insights gained from the utilized approaches to improve our current understanding of the chemically-driven effects of CO_2 and HCl injection on limestone. The following topics are discussed: (1) coupled flow and reaction processes governing acid-rock interactions, (2) effects of the acid type and pore space heterogeneity on dissolution processes, (3) porosity-permeability relationships in altered limestones, (4) the capability of an effective medium model to capture the time-evolving elastic behavior of the limestone, and (5) possible implications of this study for acidizing operations and geological carbon storage.

Chapter 6 presents the conclusions of this thesis and proposes some perspectives for future research.

Note that based on the Thesis chapters one article entitled “Chemo-hydro-mechanical effects of CO_2 injection on reservoir and seal rocks: A review on laboratory experiments” has been published as Vafaie et al. (2023) in Renewable and Sustainable Energy Reviews 178, 113270, a manuscript entitled “Chemo-hydro-mechanical effects of CO_2 injection into permeable limestone” has been submitted for publication in the International Journal of Coal Geology and the manuscripts entitled “A MATLAB approach to developing digital rock models of heterogeneous limestones for reactive transport modeling” and “Understanding the effect of small-scale heterogeneities on reactive transport in carbonate rocks” will be submitted for publication in Geologica Acta and Geochimica et Cosmochimica Acta journals, respectively.

Chapter 2

Scientific background

This chapter presents some scientific concepts and laboratory observations on CO_2 interactions with rock through a comprehensive review of the literature (recently published as a review paper in the journal of Renewable and Sustainable Energy Reviews, Vafaie et al., 2023). The review mainly focuses on processes related to interactions of dry CO_2 and aqueous solutions containing dissolved CO_2, i.e., aqueous-phase dominated reactions, with rocks as they have been investigated in more detail so far. Although mineral reactivity with the counterpart water-bearing CO_2 phase, i.e., non-aqueous dominated system, is also important for CO_2 transport and storage underground and the literature on relevant processes has become rich (Loring et al., 2011; Schaef et al., 2011; Pearce et al., 2016), it is not covered here. Furthermore, the potential impacts of CO_2 impurities, such as SO_2, NO_X, H_2S, NH_3, and O_2, on interactions with rocks have been assessed in several experimental studies (Thaysen et al., 2017; Pearce et al., 2018; Dawson et al., 2015; Turner et al., 2022), but are not reviewed here.

This review targets studies on sedimentary rocks, including seventy-six studies on the intact reservoir and shaly caprock specimens and sixteen on fractured rocks, conducted mainly since 2005. Of the former group, 30 studies used carbonate rocks (mainly chalks and limestones), 41 sandstones, and 13 shales. It complements some recent reviews on experimental studies dealing with chemo-mechanical aspects of CO_2 injection into rocks (Vilarrasa et al., 2019a; Akono et al., 2019; Bhuiyan et al., 2020). A detailed information is provided on geochemical controls on mechanical, transport and multi-phase flow properties, which received relatively little attention in earlier studies.

2.1. CO_2-brine-rock interactions

Large volumes of stored supercritical CO_2 disturb the existing equilibrium between formation brine and reservoir/caprocks (Fig. 1), triggering several chemical, mechanical, thermal, and transport processes (e.g., mineral dissolution and precipitation, porosity and permeability variations, injection-induced overpressure and thermal and poroelastic stresses) over different spatial and temporal scales (Gaus, 2010; Kampman et al., 2013; Pawar et al., 2019). These coupled processes give rise to uncertainties concerning the reservoir pressurization response (Nguyen et al., 2016; Zhang et al., 2019) and the sealing capacity and integrity of caprocks

(Noiriel et al., 2007; Gherardi et al., 2007; Liteanu et al., 2012; Hangx et al., 2015; Niu and Krevor, 2020).

The type and extent of chemical interactions vary across different zones around the wellbore, divided by fluid phase saturations, i.e., volumetric proportions of CO_2 and aqueous phases (or brine) in pores, and the concentration of dissolved CO_2 and water molecules in the two phases (Bemer et al., 2010; Kim and Santamarina, 2014; Rathnaweera et al., 2015; Rohmer et al., 2016) (Fig. 1a). A_1 is the nearest-wellbore zone, where the rock pore network is fully occupied by dry supercritical CO_2. A_2 represents a zone of water-bearing supercritical CO_2 (wet CO_2). A_3 illustrates the transition zone where the two fluid phases coexist at varying proportions, and A_4 is the zone of CO_2-rich brine surrounding the CO_2 plume. The zones A_2 and A_4 are driven by the mutual solubilities of CO_2 and water, which are pressure and temperature dependent (Spycher et al., 2003). On the one hand, the CO_2 phase in zones A_2 and A_3 may host variable amounts of dissolved water, i.e., hardly exceeding 1 mol% at temperatures < 60 °C, but reaching 2 to 3 mol% at an elevated temperature of 100 °C and pressures > 10 MPa (Greenwood and Barnes, 1966). On the other hand, CO_2 dissolves into the aqueous phase in zones A_3 and A_4, where CO_2 solubility has a strong pressure dependence and generally ranges between 2 and 3 mol% at pressures > 10 MPa and temperatures < 60 °C (Spycher et al., 2003; Kaszuba et al., 2013). Finally, A_5 is the uninvaded zone, which is furthest from the injection well. Unlike zone A_5, which remains unaffected by CO_2, the other zones that are in direct contact with CO_2 may experience different physicochemical phenomena explained below.

Continuous injection of dry supercritical CO_2 with low chemical reactivity sweeps out and dries the rock from the resident brine in the near-wellbore zone, which may result in salt precipitation and possible changes in the hydraulic properties of zone A_1 (Fig. 1) (Gaus, 2010; Kim and Santamarina, 2014; Andre et al., 2017). In contrast to dry CO_2, multiple lines of evidence from laboratory experiments suggest the reactive nature of wet CO_2 towards the surface of some minerals, in particular those comprising divalent metal cations (Miller et al., 2013). Separated water from wet CO_2 may form a thin, reactive water film on the surface of silicate minerals that promotes a series of mineral transformation reactions, including silicate carbonation (Kwak et al., 2011; Loring et al., 2011). These reactions are of paramount importance to the mineral trapping of CO_2 in basaltic and ultramafic rocks owing to their high mineral carbonation potential (Oelkers et al., 2008; Rosenbauer et al., 2012; Assayag et al., 2009; Zhang et al., 2020).

Dissolution of CO_2 into water (zones A_3 and A_4) forms carbonic acid (H_2CO_3), which dissociates into protons (H^+), bicarbonate (HCO_3^-) and carbonate (CO_3^{2-}) ions as follows (Gaus, 2010)

$$CO_2(g) + H_2O \leftrightarrow H_2CO_3(aq) \quad (1)$$

$$H_2CO_3(aq) \leftrightarrow H^+(aq) + HCO_3^-(aq) \quad (2)$$

$$HCO_3^-(aq) \leftrightarrow H^+(aq) + CO_3^{2-}(aq) \quad (3)$$

These H^+-producing reactions lead to a pH drop in the resident brine from approximately 7.0 to an acidic range of 3.5-5.0 (Gaus, 2010; Kaszuba et al., 2013). The acidic fluid induces chemical reactions with the reservoir and caprock, mainly mineral dissolution and precipitation, with potential pivotal impacts on their hydraulic and mechanical properties (Kim and Santamarina, 2014; Rohmer et al., 2016; Zhang et al., 2020). These irreversible interactions within the storage strata are constrained by rock mineralogy, in-situ pressure and temperature, and reservoir fluid salinity, making their assessment the main priority of the baseline geochemical evaluations of CCS sites (Gaus, 2010).

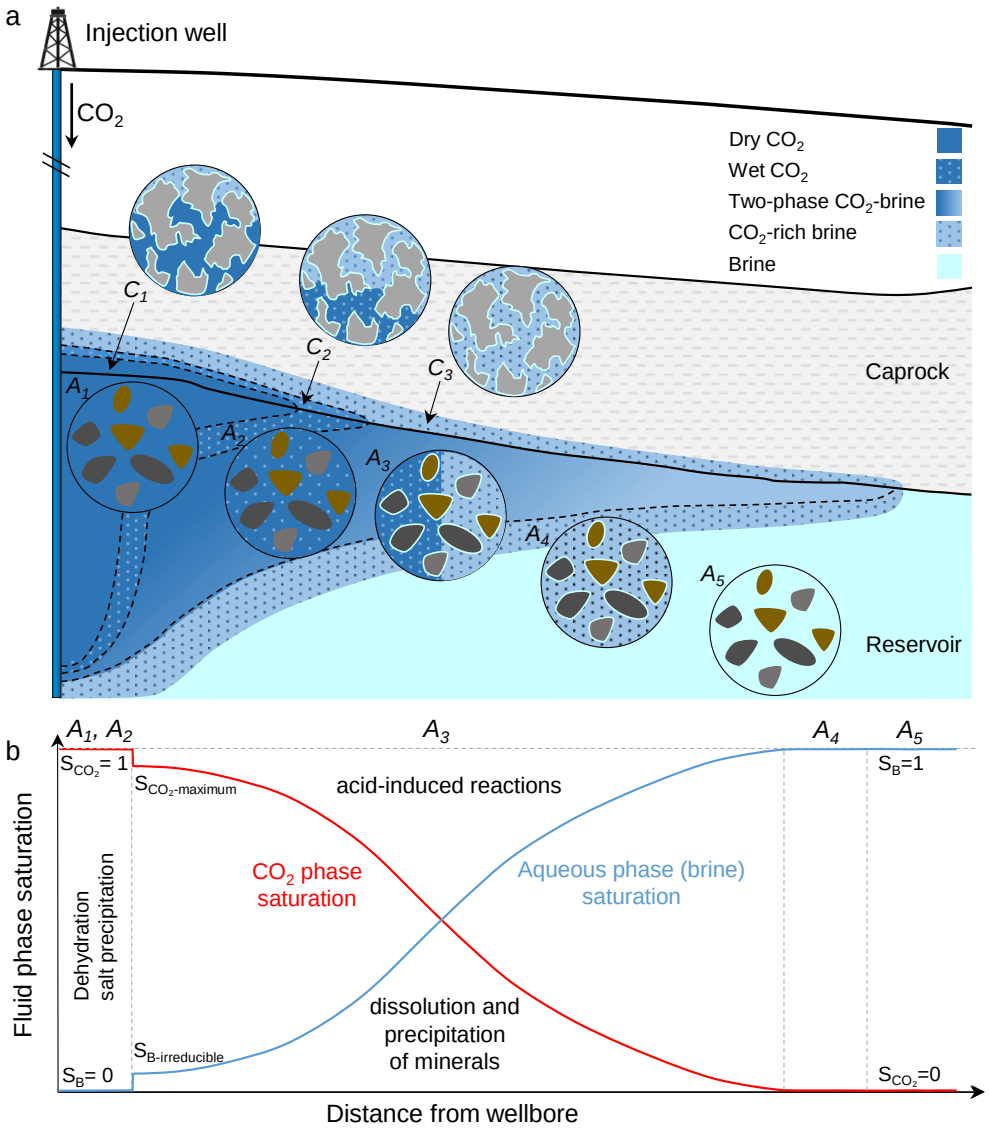

Figure 1. Schematic of a geological CO_2 storage site with zones formed around the injection well (a) and potential reactions in these zones (b). A_1 to A_4 represent zones formed in the reservoir rock. A_1, or the near-wellbore zone, is fully occupied by dry supercritical CO_2. A_3 is a two-phase flow zone and is surrounded by zones A_2 and A_4 comprising water-bearing CO_2 and CO_2-bearing brine, respectively. A_5 is the far-field or uninvaded zone. The caprock is divided into 3 zones: two-phase CO_2-brine zones (dry CO_2 in C_1 and wet CO_2 in C_2) and a CO_2-rich brine zone (C_3).

2.2. Chemically-induced alterations of rocks

CO_2 storage reservoirs in sedimentary basins are mainly chalk, limestones and dolostones (carbonate rocks), and sandstones (Oelkers et al., 2008; Rochelle et al., 2004). Thus, chemical reactions following CO_2 injection are subject to the host rock minerals, commonly carbonates (e.g., calcite and dolomite) and silicates (e.g., quartz, feldspars, and clays) (Gaus, 2010; Zhang et al., 2019). The mineral dissolution/precipitation reactions with different kinetic rates are active over distinct time scales. Calcite is the most prominent carbonate mineral in most host rocks, acting as a building block in limestones or cement in sandstones. It dissolves rapidly in acidic brines, releasing Ca^{2+} and bicarbonate (HCO_3^-) and consuming protons (Dai et al., 2019; Rosenbauer et al., 2005). The changes in ion concentrations increase the salinity and buffer the pH, resulting in less acidic conditions that favor reactions with silicates and result in precipitation of secondary minerals (e.g., dawsonite) over larger time scales (i.e., up to thousands of years), leading to permanent trapping of CO_2 (White et al., 2005; Samper et al., 2006; Johnson et al., 2001; Johnson et al., 2004; Gunter et al., 1997).

Caprocks are primarily shales, commonly known for their tight nature and low intrinsic permeability (typically, $k < 10^{-18}$ m^2) (Vafaie et al., 2015; Vafaie and Kivi, 2020; Vafaie et al., 2021; Neuzil, 2001). They possess ultrafine pore size in the micro- to the nanometer range, creating high capillary forces across the caprock. These features empower shales to function as efficient sealing barriers, preventing massive upward migration of CO_2 (Gherardi et al., 2007; Ilgen et al., 2018). Thus, CO_2 infiltration into shales that lack permeable faults or fractures occurs through sluggish molecular diffusion unless their high capillary entry pressure is exceeded (Busch et al., 2008; Makhnenko et al., 2017; Myers et al., 2018), where the non-wetting CO_2 phase expels the wetting aqueous phase out of the largest pore throats of the caprock (Hildenbrand et al., 2002; Espinoza and Santamarina, 2010). Chemical interactions between the injected CO_2 and the caprock take place at the reservoir-caprock interface, where a small fraction of CO_2 penetrates the caprock in free phase (C_1 and C_2) and, upwards, in an area that contains CO_2-rich brine (C_3) (Fig. 1a). As a result of the high capillarity of shales, the two-phase flow of CO_2 and brine occurs only in a narrow region adjacent to the reservoir rock and close to the wellbore (C_1 and C_2), where injection-induced overpressure can overcome shale capillary entry pressure. Moreover, the bulk CO_2 front spreads into the caprock at rates several orders of magnitude lower than in the reservoir, affecting the rate and extent of geochemical interactions (Luquot et al., 2016).

Fractures are ubiquitous in the subsurface and encountered at different length scales (Aguilera, 1980), resulting in strong heterogeneities in deformation, transport, and flow fields in the subsurface, which, in turn, may affect the geochemical processes of CO_2 injection (Tsang, 1991; Zimmerman et al., 1996; Hu and Rutqvist, 2022). The CO_2-induced chemical reactions may likely change the microstructure and mineral distribution in intact or fractured reservoir and sealing rocks. The resulting modifications give rise to changes in transport (pore size distribution, porosity, and permeability) (Noiriel et al., 2005; Rimmelé et al., 2010; Vanorio et al., 2011; Davila et al., 2017; Akono et al., 2020), multi-phase flow properties (capillary pressure and relative permeability curves) (Wollenweber et al., 2010; Vialle et al., 2016; Pini and Krevor, 2019; Minardi et al., 2021), and mechanical characteristics (stiffness, strength,

poroelastic response, and time-dependent behavior of the rock) (Vialle and Vanorio, 2011; Vanorio and Mavko, 2011; Miller et al., 2019). These alterations may occur at varying distances from the injection well and result in substantial rock deformation and variations in flow (Rutqvist, 2012).

Mineral dissolution is perceived to be disadvantageous when enhancing caprock porosity and permeability, known as self-enhancing (Zou et al., 2018; Hadian and Rezaee, 2019), or causing strength weakening (Al-Ameri et al., 2016; Jayasekara and Ranjth, 2021), compromising the caprock integrity and sealing capacity. Furthermore, the chemically-induced stiffness degradation and reservoir creep may speed up compaction and, consequently, surface subsidence (Jayasekara and Ranjth, 2021; Hangx et al., 2010; Espinoza et al., 2011; Nguyen et al., 2011). On the other hand, precipitation-induced improvement in caprock sealing capacity, known as self-sealing (Gherardi et al., 2007), and dissolution-induced growth of reservoir injectivity (Alam et al., 2014; El Husseiny and Vanorio, 2015; Grombacher et al., 2015; Nover et al., 2013) are considered beneficial. Therefore, assessing the subsurface perturbations brought on by coupled CHM processes at different temporal and spatial scales is essential in large-scale deployment of CCS. Direct reliance on mineralogy and pore structure renders these processes more complicated and site-specific, requiring adequate methodologies and techniques to accurately address them.

Research carried out to date on CHM processes in the context of CCS has relied on (1) laboratory experiments on centimeter-long rock specimens accompanied by accurate observations on the short-term effects (from several hours up to 2-3 years in exceptional cases), (2) characterization of analogue samples from natural CO_2 reservoirs exposed to CO_2 over geological time scales, (3) field observations, both at pilot- and commercial-scale, and (4) numerical modeling employed to better interpret laboratory and field observations (Davila et al., 2017; Gaus et al., 2005; Le Guen et al., 2007; Vilarrasa et al., 2019b). Laboratory experiments, commonly conducted at constant stress and flow conditions, are unable in essence to capture the fully coupled nature of CHM processes. They rather provide key insights into these processes individually, i.e., chemically induced changes in hydromechanical properties of the rock, on the one hand, and flow and mechanical controls on chemical reactions, on the other hand (hereinafter the term coupled CHM processes is used without referring to its exact meaning).

2.3. Experimental approaches

Many experimental studies have been carried out in the last fifteen years to assess the impacts of CO_2 injection on the hydromechanical properties of intact or fractured rocks. CO_2 injection experiments have been combined with analytical techniques to evaluate changes in microstructural, mineralogical, chemical, hydraulic, and mechanical properties of the rock before, during, and after exposure to CO_2. Table 1 summarizes these techniques and the corresponding evaluated parameters.

CO_2 injection experiments mainly differ in the flow conditions and the phase state of the injected CO_2 (Table A1, Appendix I). Batch experiments emulate static or no flow conditions

(i.e., diffusive transport conditions) to evaluate the short-term (usually for several hours and up to a few years) effects on rock exposure to CO_2 (Fig. 2a). Flow-through experiments represent open-flow conditions to assess the short-term effects of CO_2 injection on the properties of both more porous and permeable intact rocks and fractured tight rocks (Fig. 2b). The resulting residence time of the solution is longer in batch experiments than in flow-through tests, in which several hundreds of pore volumes are usually circulated.

CO_2 injection experiments on fractured rocks are mainly conducted on evaporite and carbonate samples, occasionally acting as caprocks for CO_2 storage in some geological settings (Michael et al., 2010). The high reactivity of these rocks raises concerns about chemically assisted CO_2 leakage through fractures (Ellis et al., 2011; Spokas et al., 2018). The tested specimens contain either natural (Elkhoury et al., 2013) or artificial fractures created by saw cutting (Foroutan et al., 2021b) or application of tensile stress (e.g., using the Brazilian method or chisel-type bits) (Ellis et al., 2011; Deng et al., 2015). Note that these artificial fractures may differ from shear fractures created under high normal stress due to the lack of fine-grained gouge (i.e., fracture or fault wear products upon slip).

As for the phase state of the injected CO_2 in the experiments, pure dry gaseous-phase (Adam et al., 2015; Zhou et al., 2016; Zekri et al., 2017), liquid-phase (Kim et al., 2018), supercritical-phase CO_2 (Marbler et al., 2013; Mikhaltsevitch et al., 2014; Raza et al., 2016; Huang et al., 2019; Choi et al., 2021), and dissolved CO_2 in aqueous phase commonly equilibrated with subcritical to supercritical CO_2 (Rinehart et al., 2016; Seyyedi et al., 2020; Foroutan and Ghazanfari, 2021) (hereinafter referred to as CO_2-rich water) are used. The aqueous phase in the injected solution and initial pore fluid of the rock may be deionized, fresh, brackish or saline water besides brine. The general term water is used to refer to all these compositions throughout the paper unless differently indicated. The fluid compositions for all experiments are however listed in Table A1 (Appendix I). Note also that the experimental pressures and temperatures vary largely (i.e., P = 0.1-60 MPa and T = 22-200 °C; summarized in Table A2, Appendix I) to replicate field storage conditions, considering surface temperature of 20 °C and gradients of hydrostatic pressure (10 MPa/km) and temperature (30-45 °C/km) (Bachu, 2003).

Most of the samples used in the laboratory experiments were extracted from representative reservoir and sealing formations that constitute CO_2 storage sites. The experiments have also been conducted on synthetic cores (El Husseiny and Vanorio, 2015; Falcon-Suarez et al., 2016; Yu et al., 2019) and natural analogue samples extracted from either deep CO_2 reservoirs (Hangx et al., 2015) or outcrops exposed to CO_2 leakage over geological time scales (Espinoza et al., 2018). Samples can be centimeter-size cylindrical cores, which is commonly the case in flow-through experiments, or of other shapes like cubic specimens (Fuchs et al., 2019; Shi et al., 2019), rock fragments (Hadian and Rezaee, 2019; Kaszuba et al., 2005), powder (Rezaee et al., 2017), or disk (Li et al., 2020), which are prevalent in batch experiments. The studied sedimentary rock samples are carbonates (including limestones, dolostones and chalks), sandstone, and shales with a large range of porosities (3%-42% in carbonates, 7%-29% in sandstones, and 2%-22% in shales), and permeabilities ($10^{-18} < k < 10^{-12}$ m^2 in carbonates, $10^{-17} < k < 10^{-12}$ m^2 in sandstones, and $10^{-21} < k < 10^{-19}$ m^2 in shales) (Table A2, Appendix I).

Table 1. Summary of common laboratory techniques used to evaluate the alterations in rock properties upon interaction with CO_2. The references point to some examples of using the techniques in the context of CO_2-water-rock interaction.

Measured parameters	Measurement technique	References
Chemical analysis		
Influent/effluent solution chemical composition	Inductively Coupled Plasma-Atomic Emission Spectroscopy (ICP-AES)	Garcia-Rios et al., 2015
	Inductively Coupled Plasma-Mass Spectroscopy (ICP-MS)	Sterpenich et al., 2014
	Spectrophotometry	Vialle et al., 2014
	Ion chromatography	Kaszuba et al., 2005
Influent/effluent solution pH	pH measurement	Farquhar et al., 2015
Microstructural-hydraulic analysis		
Porosity	Helium/Nitrogen porosimetry	Vanorio et al., 2011
Fracture roughness and aperture	High-resolution optical profilometer	Noiriel et al., 2007
Porosity, pore size distribution, skeletal and grain density, capillary entry pressure	Mercury Intrusion Capillary Pressure (MICP)	Niu and Krevor, 2020
Porosity and surface area	Brunauer Emmett Teller (BET)	Hadian and Rezaee, 2019
Permeability	Permeability measurement (steady-state or pulse decay methods)	Luquot et al., 2016; Busch et al., 2016
Porosity, microstructural evolution	Scanning Electron Microscopy (SEM)	Akono et al., 2020
porosity, pore size distribution, microstructural evolution, fracture aperture	X-ray Micro Computed Tomography (XMCT)	Lebedev et al., 2017
	Synchrotron X-ray Micro Computed Tomography (SXMCT)	Voltolini and Ajo-Franklin, 2019
Mineralogical analysis		
Mineral composition	Scanning Electron Microscopy (SEM)	Garcia-Rios et al., 2017
Mineral composition	X-Ray Diffraction (XRD)	Dewhurst et al., 2020
Mechanical analysis		
Friction behavior of fault gouge	Direct shear experiment	Samuelson and Spiers, 2012
Fracture toughness	Double torsion fracture mechanic test	Major et al., 2018
Scratch toughness and scratch hardness	Scratch test	Aman et al., 2018
Elastic, poroelastic, strength, and creep properties of intact rocks	Triaxial compression test	Espinoza et al., 2018
Normal stiffness of fractures		Skurtveit et al., 2020
Elastic, unconfined strength, and creep properties	Uniaxial compression test	Tarokh et al., 2020
Dynamic elastic properties	Ultrasonic velocity measurement	Vanorio et al., 2011

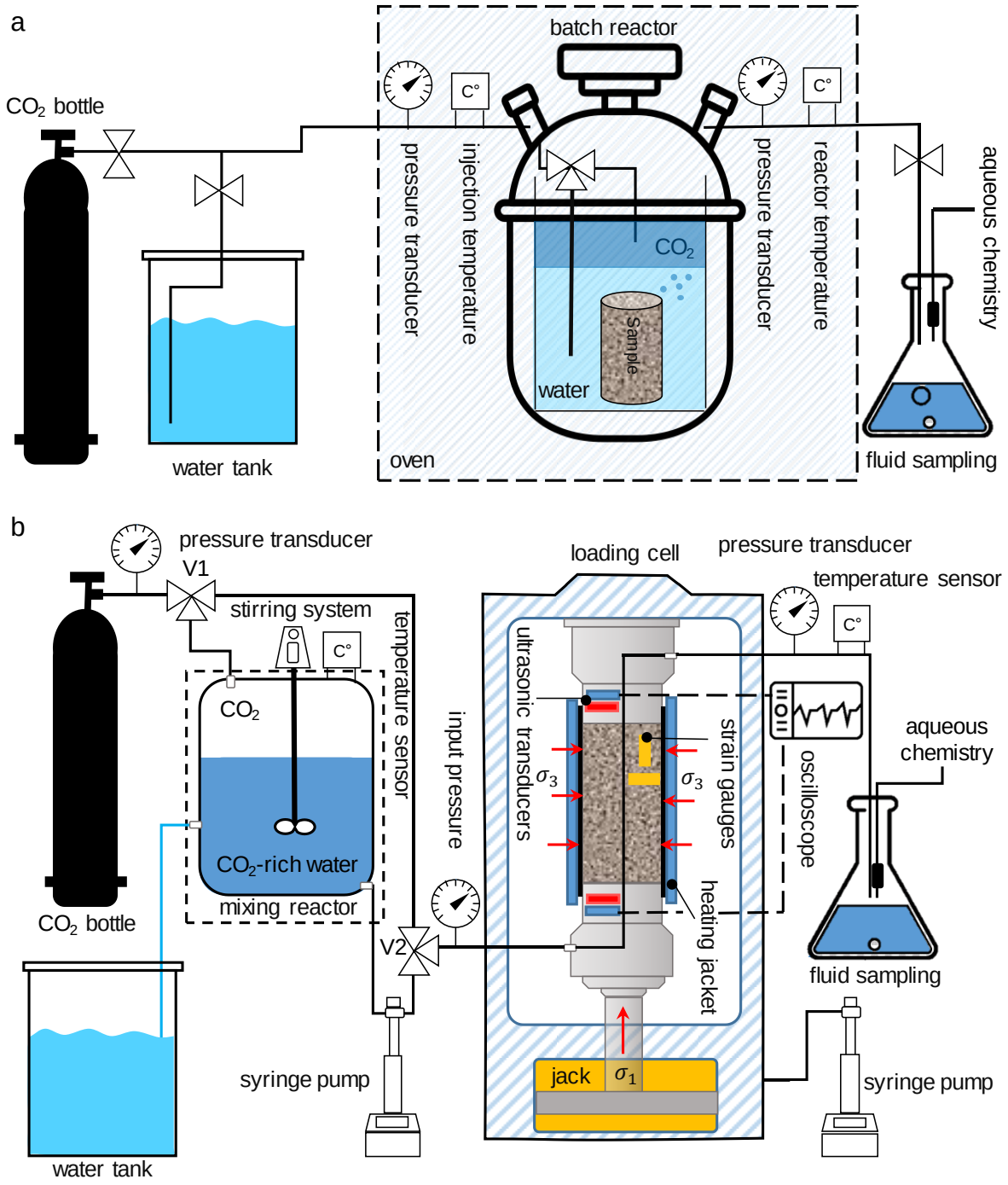

Figure 2. Schematic experimental setups used to expose rock samples to CO_2: (a) static (no flow) batch and (b) flow-through experiments. In the flow-through setup, σ_1 and σ_3 represent axial and radial (confining) stresses, respectively, and V_1 and V_2 are three-sided valves allowing free-phase CO_2 or CO_2-rich water to be injected.

2.3.1. Batch experiments

In the CCS framework, batch experiments are primarily used to characterize slow evolution of rock samples through sluggish reactions under no-flow conditions at constant temperature and pressure (e.g., Minardi et al., 2021; Rezaee et al., 2017; Lyu et al., 2016). Samples are usually immersed in CO_2-rich water by supplying supercritical CO_2 at the top and can react over a wide range of pressures and temperatures (ambient to 60 MPa and 200 °C, Table A1, Appendix I) to reproduce subsurface conditions (Nover et al., 2013; Kaszuba et al., 2005; Soong et al., 2016), where CO_2 dissolves in the pore fluid at varying degrees (Spycher et al., 2003), determining the solution pH. Aqueous CO_2 diffuses through the rock sample at a rate that inversely correlates with the pore network tortuosity (Busch et al., 2008). Long-term batch experiments (from weeks to months, even up to 2-3 years) are well suited to study alterations in clay-rich shale samples as their low intrinsic permeability renders flow-through experiments very time-consuming and cumbersome (Farquhar et al., 2015; Dewhurst et al., 2020; Bertier et al., 2006). The main limitations of batch experiments are the lack of the effects from advective transport (importantly when concerning fluid-rock interactions during and shortly after injection into the reservoir) and confining stress on chemical reactions, and restriction of sample characterization to ex-situ measurements before and after exposure to CO_2 (Table 1).

2.3.2. Flow-through experiments

Flow-through experiments (a.k.a. percolation experiments) are suitable for assessing the combined effects of advective and diffusive transport of reactive solutes on rock properties. In these experiments, CO_2 either as (1) a free phase in a gaseous, liquid, or supercritical state, (2) dissolved in water, or (3) a two-phase mixture with water, is forced to flow through permeable limestones and sandstones (Huang et al., 2019). Moreover, flow-through experiments by injecting CO_2-rich water into pre-fractured rock specimens have been usually carried out at elevated temperatures, pressures, and stresses representative of reservoir conditions. The applicability of flow-through experiments to shale samples of nano-darcy permeability is subject to discrimination between the viscous bulk flow of CO_2 and its diffusive transport through high-precision measurements together with appropriate analytical or numerical interpretations (Busch et al., 2008; Kivi et al., 2022). Furthermore, fluid permeation through the entire body of the shale specimen could be very time-consuming and has to be assured.

Rock specimens used in the flow-through experiments may be dry or saturated with water before CO_2 injection. The injected fluids are designed to reproduce fluid-rock interaction conditions at distinct zones around wellbores (Fig. 1). For instance, the injection of dry CO_2 into a water-saturated rock specimen mimics the near-wellbore zone (zone A_1 in Fig. 1a), where CO_2 displaces the resident fluid and dries out the rock (Vanorio et al., 2011; Ott et al., 2012). In such cases, the injection rate plays a significant role in replicating underground injection conditions (Luquot et al., 2018, Ott et al., 2012). It is worth mentioning that some flow-through experiments were conducted under closed downstream conditions where the fluid flow out of the specimen was impeded, and molecular diffusion is the primary CO_2 transport process through the rock in the long term (Kim et al., 2018; Grgic, 2011). This testing approach helps

overcome the limitation of neglecting stress state in conventional autoclave batch reactors although suffering from limiting reactions to low water-to-rock ratio.

2.3.3. Natural analogue samples

Some studies used samples from natural emplacements where CO_2 from mantle degassing, metamorphic processes, or organic matter breakdown was accumulated in subsurface formations and stored over geological time scales (10^4-10^6 years). Rock samples retrieved from these reservoirs provide critical insights into the long-term effects of CO_2-rock exposures after a long residence time that cannot be reproduced using laboratory timescales (Dai et al., 2005; Miocic et al., 2016). Numerous natural CO_2 accumulations are found worldwide, but experimental research on the potential long-term CO_2-rock interactions is scarce (Hangx et al., 2015; Espinoza et al., 2018).

2.4. CHM effects of CO_2 on reservoir rocks

Mineral dissolution and precipitation induced by acidified water can cause changes in pore structure, affecting the rock porosity and permeability (i.e., hydraulic properties) and, eventually, the mechanical structure and strength of the targeted reservoirs. The distribution and content of the reactive minerals constituting the rocks and flow hydrodynamics determine the extent to which rock properties may change and affect the capacity/efficiency of geological carbon storage. Most operating storage sites comprise carbonates (e.g., chalks, limestones and dolostones) and sandstones as reservoir rocks, overlain by tight, thick shales as caprocks (Tables A2 and A3, Appendix I). An exception to CO_2 injection in sedimentary rocks is storage in basalt and ultramafic rocks, e.g., the CARBFIX project (Gislason et al., 2010).

2.4.1. Changes in hydraulic properties

2.4.1.1. Role of mineralogy and flow conditions

Carbonate rocks are mainly composed of highly reactive calcite, the content of which is decisive in determining the extent of rock alterations, making carbonate rocks the focus of a large number of studies. Chemical interactions between dissolved CO_2 and carbonates involve both dissolution and precipitation reactions, whose extents are sensitive to the pH and CO_2 solubility in water which are functions of CO_2 pressure, temperature and salinity (Pokrovsky and Schott, 2003; Duan and Sun, 2003). To explore rock alterations at representative reservoir conditions, batch and flow-through experiments have been carried out under a wide range of pressure and temperature conditions (P = 0.1-60 MPa and T = 25-120 °C).

In batch experiments, i.e., a closed system, exposure of carbonates to CO_2 causes only slight alterations in the pore structures owing to the limited water-to-solid ratio. Under such conditions, the fast dissolution of calcite increases the aqueous concentration of carbonate species and consumes protons (pH buffering), leading to the stability of the solid calcite phase (equilibrium) (Rimmelé et al., 2010; Alam et al., 2014; Sterpenich et al., 2014; Grgic, 2011;

Tariq et al., 2018). An increase in porosity may occur, but barely reaches a small percentage (Rimmelé et al., 2010; Sterpenich et al., 2014; Wang et al., 2021). Correspondingly, insignificant permeability changes are expected (Bemer and Lombard, 2010; Grgic, 2011; Tariq et al., 2018; Clark and Vanorio, 2016; Kim and Makhnenko, 2021). Dissolution traits are more pronounced in samples exposed to CO_2-rich water than those treated with dry supercritical CO_2, as water is the key agent for the acid-producing reaction (Eq. 1) (Rimmelé et al., 2010). The amount of CO_2 infiltrating the rock is low under static conditions owing to the slow pace of the diffusion process, preventing pH from reaching values lower than about four (Sterpenich et al., 2014).

Assuming that the reservoir as a whole emulates a closed hydrodynamic system with some brine circulation but not renewal, results from the batch experiments would suggest negligible changes in the hydraulic properties of a carbonate reservoir (Grgic, 2011). However, this assumption may not be fulfilled locally (regions A_1 to A_4 in Fig. 1). Indeed, dissolution and/or precipitation reactions could persist over a period long enough to induce significant alterations in rock properties (Kim and Santamarina, 2014; Akono et al., 2019). Percolation experiments are supposed to simulate conditions under which continuous injection of dissolved CO_2 into carbonate rock samples results in a progressive dissolution of calcite and increase in porosity (Fig. 3). Absolute porosity enhancements of up to 5-6% (20% relative enhancement) occurred in limestone samples of the Lérouville and Savonniere Formations under open-flow conditions (Noiriel et al., 2005; Vialle et al., 2014; Lebedev et al., 2017). Moreover, calcite dissolution and pore widening may cause large enhancement in intrinsic permeability (documented by up to 3 orders) (Noiriel et al., 2005; Vialle et al., 2014; Vafaie et al., 2022) . The positive feedback between the rapid dissolution of calcite and acid renewal by fluid flow promotes chemical reactions. The higher the injection rate, the higher the extent of interactions with rock (Luquot and Gouze, 2009). However, under specific flow and reaction conditions, the unstable evolution of flow pathways in carbonates can create highly conductive channels known as wormholes (explained in Section 2.4.1.1).

In sandstones, the mineral composition of the rock cement, i.e., silicate-cemented or calcite-cemented sandstone, plays a major role in the evolution of the rock properties. Sandstones with high content of carbonates are prone to dissolution-induced porosity and permeability enhancements in a range comparable to carbonate rocks (Akono et al., 2020; Espinoza et al., 2018; Tarokh et al., 2020; Li et al., 2020; Canal et al., 2013; Foroutan et al., 2021a; Pearce et al., 2019; Lamy-Chappuis et al., 2014), particularly under open flow conditions, hindering calcite buffering effects (Lamy-Chappuis et al., 2016; Luquot et al., 2016). Likewise, in natural-analogue specimens with a marked carbonate content (14 wt% and 23-38 wt% in the Entrada Sandstone and Summerville Siltstone, respectively) exposed to CO_2 over 400k years, a porosity increase of 3-6% was observed due to the dissolution of grain-coating hematite and calcite cement.

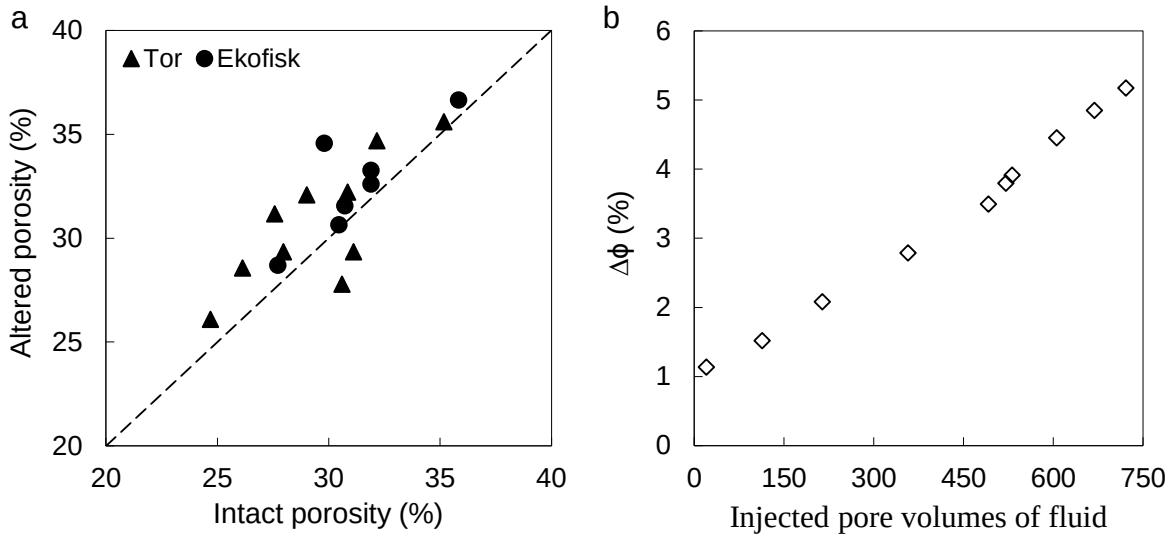

Figure 3. Porosity changes in carbonate rocks during CO_2 injection: (a) cross-plot of porosity for treated Ekofisk and Tor Chalks subjected to supercritical CO_2 injection versus intact porosities (modified from Alam et al., 2014) and (b) porosity variations in a limestone specimen with injected pore volumes of CO_2-rich water (modified from Vialle and Vanorio, 2011).

The dissolution rate of silicates (feldspars, clays, and quartz) is slower than that of calcite by up to nine orders of magnitude (White et al., 2005; Brosse et al., 2005). Hence, trivial alterations in pore structure, porosity, and permeability are conceivable for carbonate-free sandstone treated under open-flow conditions (Fig. 4b) (Espinoza et al., 2018; Kim and Makhnenko, 2021). Yet, low- or no-carbonate sandstones that contain clays and feldspars, which are more reactive than quartz, react with dissolved CO_2 over long times, implemented commonly in batch experiments (months to a few years, Fig. 4a). More complex reactions, including mineral dissolution, precipitation and transformation, may occur simultaneously or sequentially, leading to positive or negative contributions to hydraulic properties. The longer the exposure time, the greater the extent of alterations. For instance, 8% and 3-fold increases in porosity and permeability, respectively, were observed in specimens from the Hutton (Farquhar et al., 2015), Stuttgart (Fischer et al., 2013), and Mt. Simon (Fuchs et al., 2019) Formations exposed to CO_2-rich water for up to 4 months. Dissolution of clays and feldspars, widening the pore space and creating micro fractures along the bedding planes, and corrosion of quartz were responsible for the enhancement of the hydraulic properties. Conversely, the combined effects of K-feldspar dissolution, kaolinite, barite, and celestine precipitation reduced the porosity and permeability of a sandstone specimen from the Tuscaloosa Formation by 2% and 13%, respectively, after 6-month exposure to dissolved CO_2 (Soong et al., 2016).

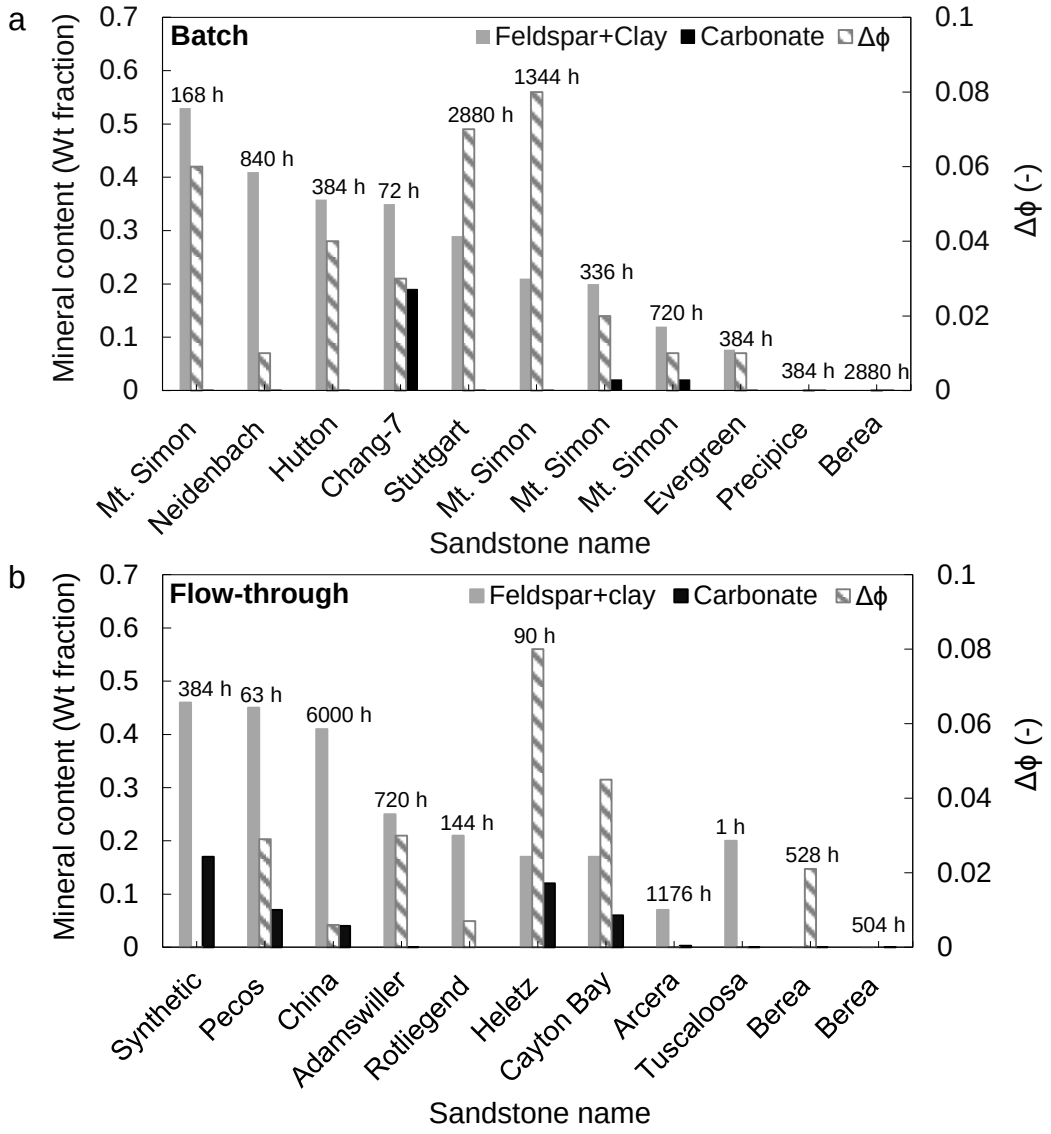

Figure 4. Variation in porosity in sandstones with different mineral contents reacted with CO_2-rich water under no-flow (Akono et al., 2020; Nover et al., 2013; Farquhar et al., 2015; Fuchs et al., 2019; Shi et al., 2019; Li et al., 2020; Tariq et al., 2018; Fischer et al., 213; Harbert et al.,2020) (a) and open-flow conditions (Luquot et al., 2016; Rimmelé et al., 2010; Tarokh et al., 2020; Zhou et al., 2016; Yu et al., 2019; Kim and Makhnenko, 2021; Canal et al., 2013; Foroutan et al., 2021a; Lamy-Chappuis et al., 2016) (b). The duration of the experiments, if reported, is also illustrated.

Mineral dissolution and precipitation processes dominate the transition zones A_3 and A_4 (Fig. 1). As the aqueous phase saturation in the region adjacent to the injection well, i.e., zone A_1, decreases toward the residual value, its mobility decreases (due merely to reduction in the relative permeability to this phase), raising a trade-off between bulk phase (water and dissolved minerals as a whole) displacement by CO_2 and water evaporation to the CO_2 phase (Vanorio et al., 2011). If the latter prevails, which is particularly the scenario in small pores due to the lower fluid velocity, the concentration of dissolved minerals progressively increases, resulting in dehydration-induced salt precipitation if exceeding the salt solubility limits (Baumann et al., 2014; Miri et al., 2016). This phenomenon is prevalent not only in the CCS context but also

during geothermal energy exploitation from depleted high-temperature gas reservoirs where CO_2 serves as a circulating fluid (Cui et al., 2016; Cui et al., 2021; Norouzi et al., 2021). Dramatic injectivity reductions due to pore clogging by salt crystals are anticipated even in the short-term for high-salinity systems (Baumann et al., 2014; Spycher and Pruess, 2010). Laboratory experiments of dry CO_2 injection into brine-saturated sandstones give credence to dehydration occurrence (Zimmerman and Bodvarsson, 1996; Ott et al., 2012; Ott et al., 2014). The lower the rock porosity, the higher the extent of changes in hydraulic properties, with up to 10% and 20% relative decreases in porosity and permeability, respectively (Fig. 5, Vanorio et al., 2011).

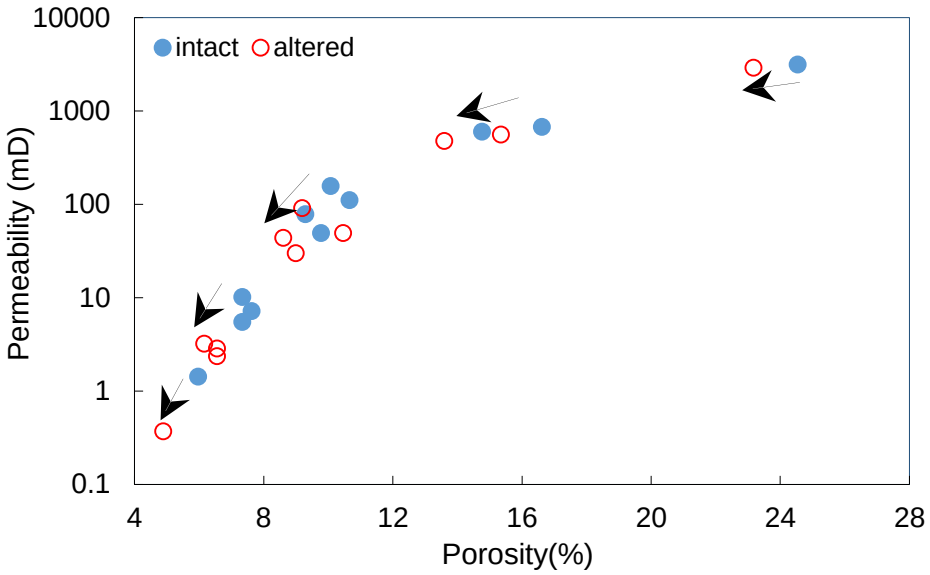

Figure 5. Decrease in porosity and permeability for quartz-rich Fontainebleau sandstone specimens after injection of gaseous CO_2 (modified after Vanorio et al., 2011).

2.4.1.2. Wormhole formation and rock heterogeneity

The feedback between dissolved CO_2 transport, rapid chemical reactions, and the highly diverse textural attributes (i.e., heterogeneity in pore size and shape, grain size and sorting, among others, encountered at different scales) in carbonate rocks leads to instabilities in the advancing reactive fronts and localized dissolution regimes (e.g., wormhole formation, Fig. 6))Vanorio et al., 2011; Vialle and Vanorio, 2011; Smith et al., 2017; Luquot and Gouze, 2009; Szymczak and Ladd, 2009; Smith et al., 2013(. Experimental and theoretical studies have demonstrated that dimensionless Péclet (*Pe*) and Damnköhler (*Da*) numbers can be used as practical criteria to determine the resulting dissolution patterns. While Péclet number measures the relative magnitude of pressure-driven advective flow to diffusive transport, Damköhler number compares the reaction rate to the advective mean fluid velocity (Szymczak and Ladd, 2009; Menke et al., 2016).

Depending on the range of *Pe* and *Da* numbers, five distinct dissolution patterns may develop in carbonate rocks: (1) Compact dissolution under high *Da* and low *Pe* conditions (diffusion-controlled system), where the reaction front advances along the flow direction, and dissolution progresses as a thin front (Fig. 6b) (Golfier et al., 2002); (2) Conical wormholes form under

similar reactive conditions but with an intermediate *Pe* number where the reaction front becomes unstable, especially in heterogeneous porous media (Fig. 6c); (3) dominant wormhole formation occurs under high *Pe* conditions (i.e., advection dominance) where dissolution concentrates along preferential flow paths (Fig. 6e). The high velocity under such conditions leads to a minimal residence time with the result that wormholes do not have a substantial width; (4) Ramified wormholes form in advection-dominated systems, in which reaction is not very rapid, resulting in longer residence times under which wormhole spreading and branching occur (Fig. 6d); (5) Uniform dissolution is typically observed when the reaction rates are slow, and the acid fluid has time to access the entire pore space in the sample (Fig. 6a) (Menke., 2016; Cohen et al., 2008). Nevertheless, the boundaries between these dissolution regimes are primary functions of pore space heterogeneity, varying largely from one carbonate rock to another and, thus, are not definite. Besides, precise determination and definition of the *Da* number are still challenging because of complexities in determining the reactive surface area as a major heterogeneity factor controlling the reaction rate.

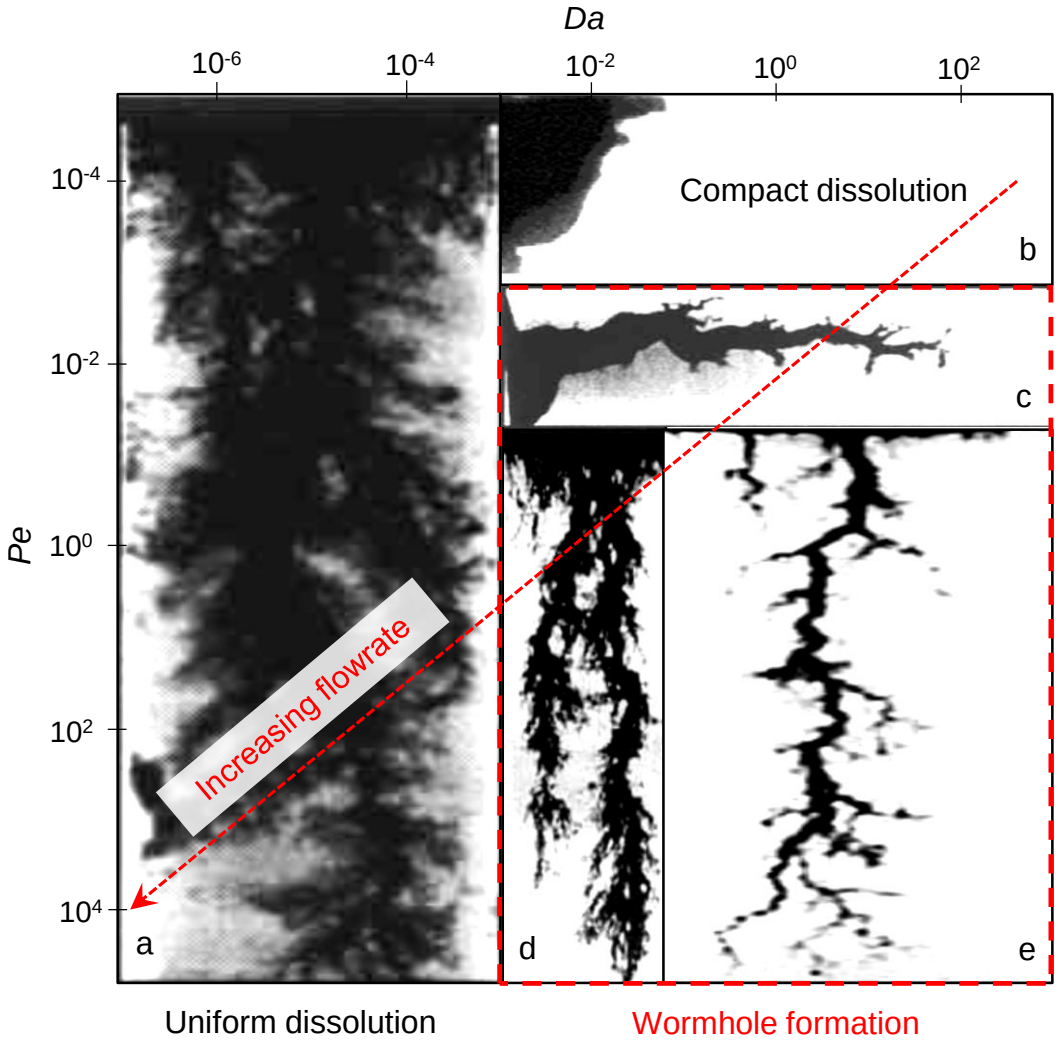

Figure 6. Neutron radiographs of different dissolution patterns caused by reactive fluids in limestone: (a) uniform dissolution, (b) compact dissolution, (c) conical wormhole, (d) ramified wormhole, and (e) dominant wormhole formation (adapted from Fredd and Fogler, 1998). Ranges of Damkohler *(Da)* and Peclect *(Pe)* numbers are taken from Menke, 2016.

The formation of wormholes is of particular importance for reservoir conductivity and its mechanical integrity as will be discussed later. Laboratory observations unravel two-stage permeability enhancements during wormhole formation (Fig. 7) (Noiriel et al., 2005; Akono et al., 2019; Vialle et al., 2014). In the initial stage, a slow to moderate increase in permeability results from dissolution-enhanced pore connectivity, removal of pore-clogging particles, the initiation of wormhole formation, and flow localization (Akono et al., 2019; Fredd and Fogler, 1998). Subsequently, permeability sharply increases as the wormhole breaks through the sample (Noiriel et al., 2005; Vialle et al., 2014). Power-law permeability-porosity relationships ($k \propto \phi^n$) with high values of n (as high as 56) are required to capture the localization of flow and reaction in wormholes (Noiriel et al., 2005; Vialle et al., 2014). Thus, the conventional choice of n = 3 in the Kozeny-Carman permeability-porosity relationship and other adapted values for porous rocks (Kozeny, 1927; Carman, 1937; Hao et al., 2019) are only valid for a finite range of pore structure evolution where the continuity of the porous medium is not questioned.

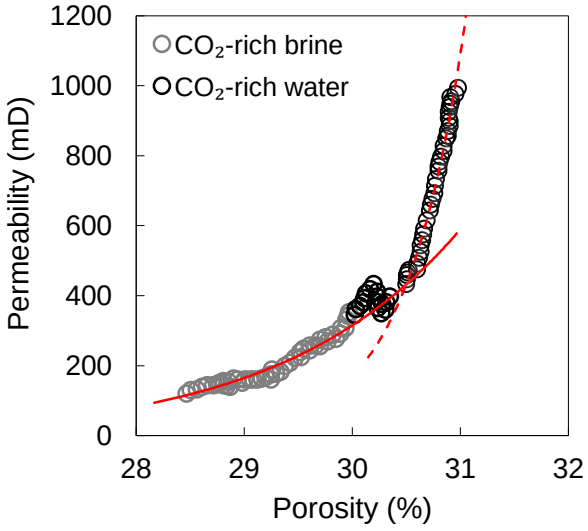

Figure 7. Permeability changes as a function of porosity in an Estaillades Limestone specimen flooded with a CO_2-rich brine/distilled water sequence for 115 days (modified from Vialle et al., 2014).

2.4.1.3. Geochemical controls on multiphase flow

Assessment of the potential impacts of chemical reactions on the two-phase flow behavior of water and CO_2 is carried out by studying relative permeability, defined as the ratio of the permeability of a given fluid in the presence of other fluids to the intrinsic rock permeability. In essence, relative permeability quantifies the extent to which CO_2 and water interfere as both migrate through rocks, affecting all critical storage processes, from residual CO_2 trapping mechanism (Juanes et al., 2006, Benson et al., 2013) to CO_2 leakage through the caprock (Kivi et al., 2022). However, relative permeability has not been adequately characterized in CO_2-altered rocks. Appraisal of two-phase flow properties in treated rocks requires a continuous pore network, a condition hardly met in carbonate rocks in the laboratory, where flooding with

CO_2 likely leads to large wormhole formation (Szymczak and Ladd, 2009; Fredd and Fogler, 1998).

Temperature-controlled acids have been proposed to overcome characterization challenges posed by wormhole formation (Egermann et al., 2006; Bemer et al., 2016; Radillal et al., 2010). These acids are water-soluble organic compounds activated above a certain temperature, resulting in uniform rock dissolution, not only at the core scale but also at the pore scales (Niu and Krevor, 2020). This treatment approach enabled Niu and Krevor (2020) to obtain the relative permeability curves of two altered specimens from the Ketton and Estaillades Limestones. The results showed increased and decreased relative permeabilities to CO_2 and water, respectively, for the Ketton Limestone specimen in response to dissolution-enhanced porosity (Fig. 8a). This selective alteration is due to the enlargement of small pores previously occupied by the wetting phase (i.e., water), but now provide pathways for the non-wetting phase (i.e., CO_2) to flow (Fig. 8b). Interestingly, the altered specimen from the Estaillades Limestone underwent a decrease in relative permeability for both water and CO_2 in spite of dissolution-induced porosity and intrinsic permeability enhancement (Fig. 8c). The reason is a rise in the volume fraction of middle-range pores while both large and small pore fractions decrease (Fig. 8d). This indicates a competition between wetting and non-wetting phases to pass through the middle-range pore network. A two-phase flow interference decreases relative permeability for both phases as increasing fractions of both CO_2 and water pass through the same-size pore cluster.

Conclusively, alterations in relative permeability curves are primarily correlated to how the pore size distribution evolves upon interaction with CO_2. However, the application of temperature-retarded acids should be further verified as they statically dissolve minerals uniformly at the pore scale that may overlook actual heterogeneous velocity fields of pore-scale CO_2 invasion, probably dissolving the larger pores (i.e., where fluid flow is focused) more easily. A combination of high-resolution in-situ imaging techniques, e.g., synchrotron XMCT imaging (Voltolini and Ajo-Franklin, 2019), and modeling approaches (Jiang and Tsuji, 2014) to capture the evolution of pore structure upon interactions with CO_2 prior to wormhole formation should enable better assessment of changes in two-phase flow properties.

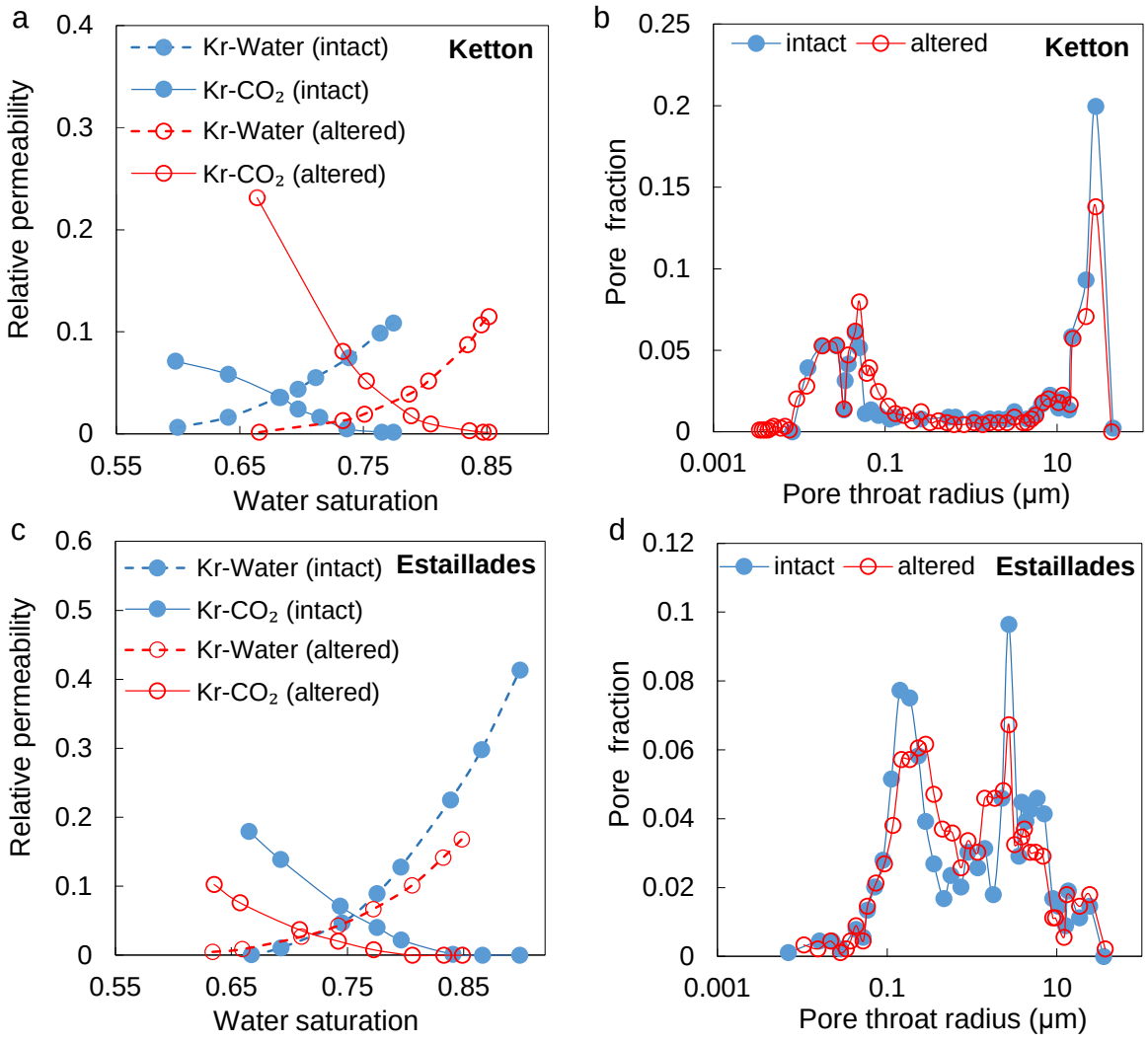

Figure 8. Relative permeability curves at intermediate water saturations and pore size distribution for limestone samples from the Ketton (a and b, respectively) and Estaillades Formations (c and d, respectively) before and after treatment with CO_2 (adapted from Niu and Krevor, 2020).

2.4.2. Geochemical effects on mechanical behavior

This section presents recent advances in understanding potential changes in rock deformation, stiffness, strength, and time-dependent behavior, i.e., compaction creep, originating from interactions with CO_2. The key concept of these studies is that the evolution of the rock microstructure, i.e., pore structure and grains as the fundamental constituents of the load-bearing framework, would potentially cause changes in the rock mechanical behavior (Eberli et al., 2003; Berryman et al., 2009). Given the short duration of laboratory experiments, the studies have mostly focused on carbonate dissolution and the subsequent effects on mechanical properties. Alterations of the mechanical properties of reservoir rocks are broadly relevant to assess the subsurface CO_2 flow and storage performance, given the tightly coupled behavior of flow, mechanical and geochemical processes (Rohmer et al., 2016; Vilarrasa et al., 2019a; Newell and Ilgen, 2019; Ilgen et al., 2019).

2.4.2.1. Elastic-Poroelastic properties

In light of the limited effects of CO_2 on the pore structure of carbonates or carbonate-rich sandstones under no-flow conditions due to the buffering effect of dissolved calcite, slight changes in elastic properties, either static or dynamic, are expected and accredited by laboratory measurements (Rimmelé et al., 2010; Shi et al., 2019; Grgic, 2011; Tariq et al., 2018). In contrast to no-flow conditions, flooding carbonate and carbonate-bearing sandstone samples with dissolved CO_2, where the injected acidic solution is continuously renewed, induces significant changes in rock porosity and, thus, in elastic constants, i.e., Young's, bulk, and shear moduli, and Poisson's ratio (Bemer and Lombard, 2010; Rathnaweera et al., 2015; Alam et al., 2014; Grgic, 2011), and in seismic behavior, i.e., compressional and shear ultrasonic velocities (Vialle and vanorio, 2011; Grombacher et al., 2015; Raza et al., 2020). Geochemical interactions, rock weakening, and ultrasonic velocity attenuation continue as long as a CO_2-rich solution is injected into the specimen (Grgic, 2011; Clark and Vanorio, 2016; Perera et al., 2016). Conversely, rock stiffening and velocity amplification is expected during the injection of dry gaseous/supercritical CO_2 into water-saturated rock samples, as salt precipitation is likely to occur (Vanorio et al., 2011). The behavior of Poisson´s ratio, however, does not show any clear trend with exposure to CO_2, not correlating with the rock type and experimental conditions, decreasing in some cases (Hangx et al., 2013) and increasing in others (Harbert et al., 2020; Perera et al., 2016).

Changes in the Biot effective stress coefficient (α) that delineates the poroelastic behavior of the rock can be evaluated as $\alpha = 1 -$ (bulk modulus of the rock)/(bulk modulus of the solid part of the rock), herein referred to as solid bulk modulus (Ahmadinejad and Kivi, 2021). Assuming an ideal porous medium, which is occasionally the case for homogeneous rocks with a low content of compressible clay minerals and an interconnected pore network, the solid bulk modulus is well correlated to the mean bulk modulus of the grains constituting the rock (Cheng, 2016). Considering this parameter as constant, a decrease in the rock bulk modulus translates into an increase in the Biot coefficient. Nevertheless, Kim and Makhnenko (2021) provided evidence for alterations in the solid bulk moduli of the Apulian and Indiana Limestone samples, as well as the bulk modulus of pure calcite crystals in contact with liquid CO_2 under no-flow conditions. These moduli decreased by up to 20% in these samples, indicating local dissolution of the calcite crystal surface. The formation of non-interconnected pores due to re-precipitation of locally dissolved calcite also gives rise to micro-scale inhomogeneities in compressibility that intensify the deformation of the solid part of the rock (equivalent to a lower solid bulk modulus). As a result, even if the bulk modulus of a rock does not change, which is plausible in a closed geochemical system (Grgic, 2011; Tariq et al., 2018; Liteanu et al., 2013), a slight decrease in the Biot coefficient can still be expected, e.g., from 0.85 to 0.81 in Apulian Limestone (Clark and Vanorio, 2016).

The observed evolution of rock stiffness and wave velocities is of critical importance to seismic monitoring of the CO_2 plume dynamics. Common geophysical monitoring approaches rely on the well-known Gassmann model (Gassmann, 1951), which benefits from the difference in physical properties (density and compressibility) of CO_2 and water to address the effect of fluid substitution on elastic wave propagation (Smith et al., 2003; Han and Batzle, 2004). However,

the Gassmann model does not account for the geochemically-induced time-dependent rock´s stiffness and seismic response. Developing alternative empirical relationships considering these interactions is a hot research topic in rock physics (Vanorio and Mavko, 2011; Miller et al., 2019).

Changes in the rock stiffness alter the reservoir propensity to expansion and compaction during and after CO_2 injection, affecting surface uplift and subsidence, respectively (Rinaldi and Rutqvist, 2013). Furthermore, rock deformation could also considerably impact CO_2 flow and the resulting geochemical processes in rock, as elaborated by Vanorio et al. (2011) through laboratory experiments. The bulk modulus of carbonate rock samples during continuous CO_2-rich water injection diminished by up to 70% under no lateral confinement, significantly higher than stiffness degradations of less than 20% at 15 MPa of confinement. This difference stems from the compaction-induced reduction in rock porosity and consequently in the available reactive surface area. The stiffer the initial pore structure of the rock, as in the case of a micrite-rich limestone (El Husseiny and Vanorio, 2015), the lower the stress dependence of fluid-rock interactions.

2.4.2.2. Failure behavior

Dissolution of inter-granular cementing minerals and grain surfaces in the pore space deteriorates contact surfaces and individual grains, causing pore collapse and microcracking at lower stress levels (Alam et al., 2014; Le Guen et al., 2007; Perera et al., 2016; Zhu et al., 2010; Xie et al., 2011). Such microstructural degradation yields lower tensile and compressive strengths in most carbonates and sandstones exposed to dissolved CO_2 (Table A3, Appendix I). Expectedly, carbonates and primarily chalks with high porosity and surface area undergo the largest chemically-driven weakening of the load-bearing capacity (Alam et al., 2014; Rinehart et al., 2016; Grgic, 2011; Perera et al., 2016; Rathnaweera et al., 2017). Pore collapse is markedly susceptible to chemical degradation (Fig. 9), whereas chemical controls on the friction yield surface are still unresolved. The friction coefficient of altered rocks may diminish (Fig. 9b) (Alam et al., 2014; Espinoza et al., 2018; Foroutan et al., 2021a; Lamy-Chappuis et al., 2016) or remain almost unaffected by CO_2 injection (Fig. 9a) (Hangx et al., 2015; Alam et al., 2014; Xie et al., 2011). Depending on the prevalence of compactive pore collapse and dilatant microcracking mechanisms, the rock permeability will probably decrease or increase, respectively (Zhu and Wong, 1997; Dewers et al., 2014) [208,209], notably affecting reservoir injectivity.

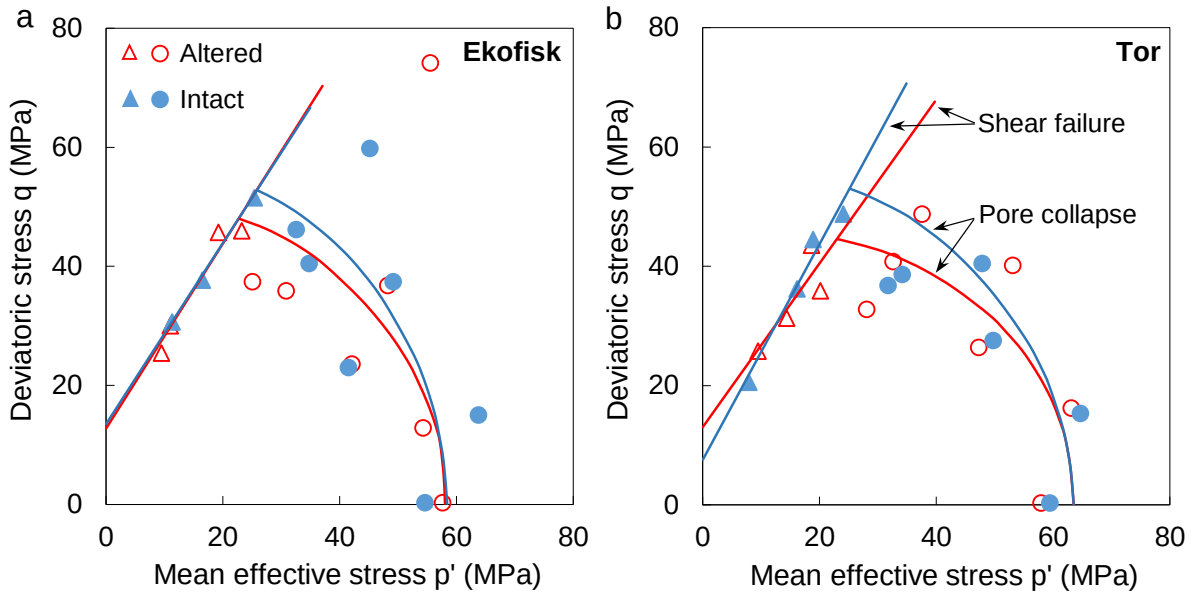

Figure 9. Deviatoric versus mean effective stress *q-p´* plots of failure properties of intact and CO_2-injected specimens from the (a) Ekofisk Chalk and (b) Tor Chalk. Circles, triangles, and solid lines indicate pore collapse onset (i.e., the point at which stress-strain curves deviate from linear elastic behavior), shear strength (i.e., the point where rock failure occurs under elevated deviatoric stresses), and failure envelopes (laboratory data fitting). Characteristics of intact and altered rocks are discriminated by blue and red colors, respectively (adapted from Alam et al., 2014).

Changes in the compressive strength of sandstone samples reacting with CO_2 over the exposure times in laboratory experiments span a broad range, from negligible to reduction by more than 50%, depending on their mineralogical content and the rock texture (Hangx et al., 2015; Rimmelé et al., 2010; Espinoza et al., 2018; Hangx et al., 2013). Dissolution of locally-concentrated reactive minerals acting as load-bearing cement or grains, even if the content is small, can give rise to significant strength degradation (Hangx et al., 2015; Foroutan and Ghazanfari, 2020). By contrast, the dissolution of dispersed pore-filling reactive cement may not affect the mechanical behavior, despite its potential effect on hydraulic conductivity enhancement (Hangx et al., 2013; 2015).

Naturally altered sandstones offer an opportunity to explore the strength degradation associated with long-term reaction mechanisms, e.g., those of quartz dissolution. The measured compressive strength of an outcrop Summerville specimen exposed to CO_2-charged brine leaking through an adjacent fault for over hundreds of thousand years was up to 90% lower than their apparently intact twin samples (Espinoza et al., 2018). The failure regime shifted from brittle strain-softening in intact specimens to ductile slightly strain-softening in altered ones, indicating a significant decrease in rock brittleness (Fig. 10d) (Kivi et al., 2018). Similar evolution trends, although less pronounced, were observed for the marginally more porous sample retrieved from the Entrada Sandstone at the same site (Fig. 10b). This discrepancy in the extent of alterations suggests that drastic strength deterioration of Summerville samples should not be viewed as purely long-term chemical effects. Indeed, altered Summerville samples could endure a variety of loading paths linked to their proximity to the fault core

(Laubach et al., 2019), leading to severe layering and partially mineralized fractures (Fig. 10c). Therefore, rock mechanical alterations are driven by the combination of geochemical interactions and the presence of heterogeneities, acting as planes of weakness.

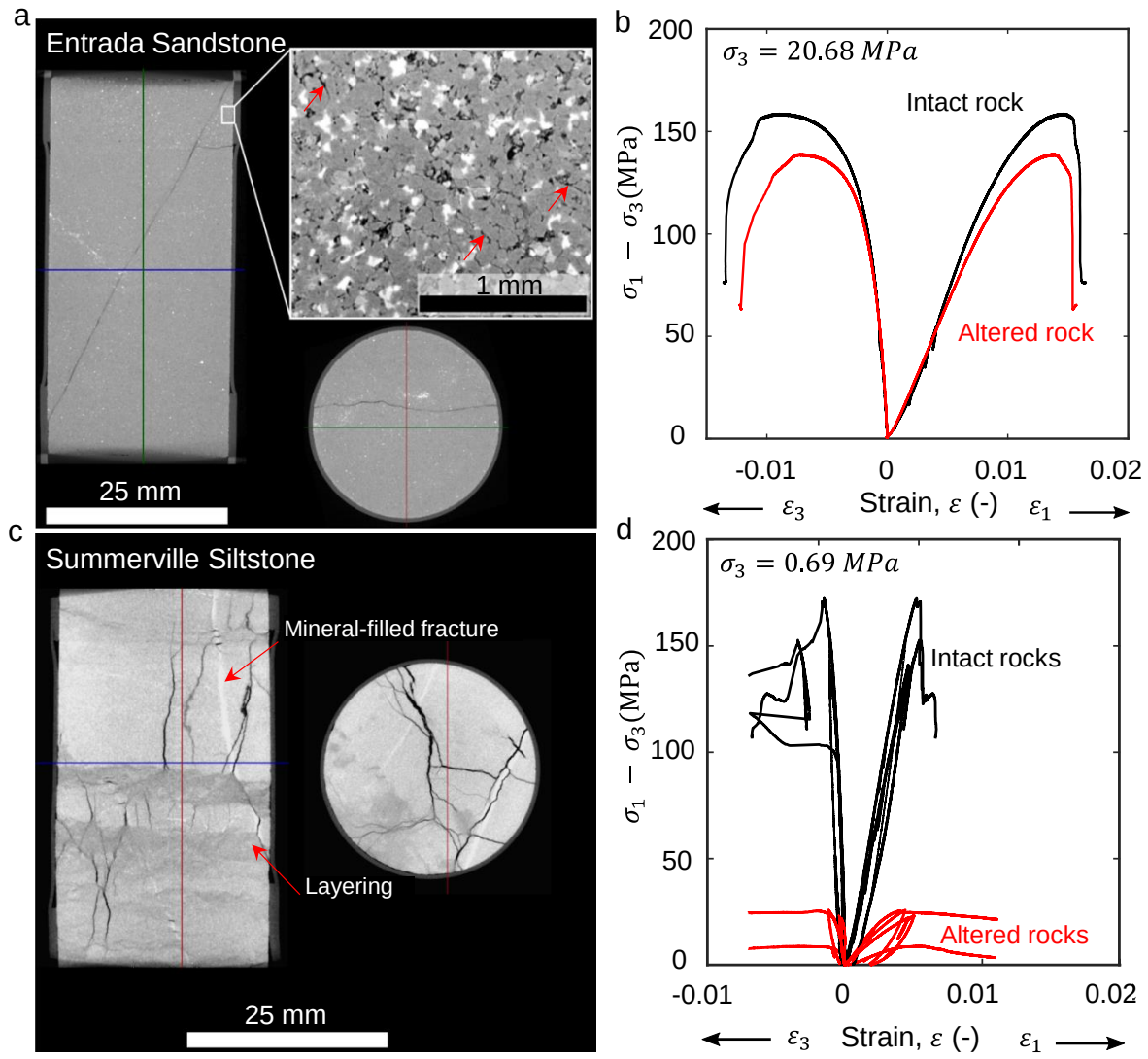

Figure 10. Deformation and failure characteristics of Entrada Sandstones (a and b) and Summerville Siltstone (c and d) (modified from Espinoza et al., 2018). (a) X-ray CT section of the altered specimen with an evident single plane shear failure. The magnified CT image shows enhanced porosity (black area) by cement dissolution (red arrows); (b) stress-strain curves show brittle failure for both intact and altered Entrada Sandstone; (c) X-ray CT image illustrating initial heterogeneities (red arrows) which likely affect strain localization and failure pattern in the altered sample; and (d) stress-strain curves depicting brittle failure for intact Summerville Siltstone and ductile slightly strain-softening for altered ones.

2.4.2.3. Time-dependent behavior

In addition to pure chemical effects of CO_2 in pores, i.e., dissolution and precipitation of minerals, a number of other fluid-controlled physicochemical processes may operate at grain-to-grain contacts. Intergranular pressure solution (Rutter, 1976; Spiers and Schutjens, 1990)

and subcritical cracking of grains (Atkinson, 1982; Heap et al., 2009) are commonly invoked to elucidate time-dependent rock deformation, i.e., rock deformation with time under elevated but constant external stress, referred to as compaction creep (Rohmer et al., 2016; Hangx et al., 2010).

Pressure solution is a deformation mechanism where the concentration of normal stress at grain contacts results in localized mineral dissolution, diffusive transport of reaction products through the grain boundary fluid film/coating, and potential precipitation of secondary minerals on the free-face grain surface in pores (Rutter, 1976). The interface reaction kinetics depends on the fluid chemistry, rock composition, porosity, grain size, temperature and stress state and is fast in granular chalk and limestone due to the high solubility and reaction rate of calcite (Grgic, 2011; Zhang and Spiers, 2005; Pietruszczak et al., 2006; Liteanu and Spiers, 2009; Zhang et al., 2010). CO_2 injection strongly accelerates pressure solution and, thus, compaction creep of porous granular carbonate rocks by up to two orders of magnitude (Liteanu et al., 2012; Le Guen et al., 2007; Grgic, 2011; Liteanu and Spiers, 2009; Renard et al., 2005). This creep-accelerating effect can be explained based on the notion that CO_2 injection increases the calcite dissolution rate (both in pores and grain contacts), which in turn increases the rock porosity, decreases the grain contact area and enhances stress-induced contact dissolution in parallel with grain sliding, rearrangement and crushing (Liteanu et al., 2012; Le Guen et al., 2007).

Subcritical crack growth is simply understood as quasi-static, stable crack (or fracture) propagation at stress levels well below the tensile failure strength, i.e., opening-mode fracture toughness according to linear elastic fracture mechanics (Atkinson, 1982). Adsorption of aqueous fluid species, i.e., H^+, OH^-, and H_2O, onto mineral surfaces and breakage of their bonds, e.g., Si-O bonds in quartz, by hydrolysis reduces the surface energy of the mineral, i.e., the energy required to create a new surface, and promotes the crack formation and subcritical growth, a process called stress-corrosion cracking (Xiao and Lasaga, 1994; Atkinson and Meredith, 1981). This chemically-activated cracking mechanism is primarily controlled by the solution pH (Dove, 1995). It is well established that the surface energy of quartz (and probably feldspar) increases with decreasing solution pH (Hangx et al., 2010; Li and De Bruyn, 1966). Accordingly, CO_2 injection into quartz- and feldspar-bearing sandstone, acidifying the pore fluid, progressively inhibits stress corrosion and, thus, creeping. In line with theory, experiments on samples from the Adamswiller Sandstone (Le Guen et al., 2007), Berea Sandstone (Oikawa et al., 2008) and Captain Sandstone (Hangx et al., 2010; Hangx et al., 2013) have revealed almost similar or even lower long-term compaction rates when converting the pore fluid from water to CO_2-rich water. Yet, siliciclastic rocks with even small contents of reactive cementing materials, i.e., carbonates and clays, could experience non-trivial time-dependent deformation, by up to a factor of 4 (Tarokh et al., 2020; Foroutan et al., 2021a).

These laboratory observations have implications for reservoir compaction and surface subsidence in the context of CO_2 storage, more importantly, in depleted reservoirs that already underwent significant time-dependent deformation in response to pore pressure decline (Liteanu et al., 2012; Hangx et al., 2013). CO_2 injection could exacerbate compaction creeping by promoting pressure solution in porous carbonate-rich formations while decelerating it in

quartz- and feldspar-bearing sandstones by attenuating grain-scale microcracking. Furthermore, CO_2 injection is likely to progressively hamper such time-dependent behaviors in the near-wellbore region by pervasively drying out the reservoir (Schimmel et al., 2022).

2.5. CHM effects of CO_2 on shales

Geochemical processes of CO_2 infiltration into water-saturated shales are fundamentally similar to those in sandstones and carbonates (Kampman et al., 2013; Rohmer et al., 2016; Minardi et al., 2021). However, as shales host ultrafine pores, chemical reactions between minerals and CO_2 are controlled by intrinsically slow diffusive transport (Kivi et al., 2022). Batch experiments of long durations are thus suitable to study these reactions and their subsequent hydromechanical effects (Table A2, Appendix I). However, as the rate of diffusive penetration of the dissolved CO_2 front (the reaction front) into a shale specimen is a few millimeters per month (Kivi et al., 2022) batch experiments are very time-consuming, costly and technically challenging, justifying their scarcity. It should also be pointed out that a significant body of literature explores the effect of CO_2 as a working fluid for hydraulic fracturing and enhanced gas recovery from shales (Zou et al., 2018; Lyu et al., 2016; 2018). As a result, the focus is primarily on shale failure behavior while ignoring possible changes in transport properties that are crucial for risk assessment of CO_2 leakage in geological storage. Moreover, candidate shales for fracturing are often calcite- and/or quartz-rich with low clay contents, which makes them relatively brittle and frackable (Vafaie et al., 2015; Kivi et al., 2018; Jin et al., 2015). Hence these shales may not be representative of ductile clay-rich caprocks suitable for geological CO_2 storage.

2.5.1. Changes in hydraulic properties: concerns about caprock sealing capacity

In long-duration batch experiments for shales, calcite dissolution is accompanied by dissolution of slowly-reacting minerals, including feldspar, chlorite, kaolinite, and even quartz, along with clay mineral transformations (more importantly, illitization of smectite and mixed layer illite-smectite) (Zou et al., 2018; Hadian and Rezaee, 2019; Dewhurst et al., 2018; Wigand et al., 2009). Mineral transformations may contribute to changing hydraulic properties of the rock if the density of the secondary minerals and, thus, the volume they occupy differ from the reactants (Busch et al., 2008). The extent of these reactions increases with the exposure time and temperature (Gaus, 2010; Kaszuba et al., 2003; 2005; Rezaee et al., 2017). Non-negligible dissolution of quartz can only be expected at notably high temperatures (>150 ºC) (Gaus, 2010). The consequent changes in shale microstructure contribute to noticeable porosity enhancement of up to 10% (Hadian and Rezaee, 2019; Rezaee et al., 2017; Dewhurst et al., 2018), which may even exceed those in reservoir rock samples (Hadian and Rezaee, 2019; Rezaee et al., 2017).

The risk of CO_2 leakage through altered shales may substantially increase with small perturbations in porosity because they lead to orders of magnitude enhancement in shale permeability (Zou et al., 2018). Indeed, the porosity-permeability relationships in low-permeability shales (in the nano-Darcy range) are found to follow power-laws with exponents

as high as 16 (i.e., $k = k_0(\phi/\phi_0)^{16}$, where k_0 and ϕ_0 are the initial permeability and porosity, respectively) (Kim and Makhnenko, 2020). Such a relationship implies that a small porosity increase of 1% will lead to a permeability enhancement by a factor of roughly 3. In addition, dissolution-induced enlargement of pore throats can reduce the capillary entry pressure of shales to a large extent (by a factor of up to 10 following 5% porosity increase (Hadian and Rezaee, 2019; Rezaee et al., 2017), suggesting degradation of the capillary sealing capacity (Busch et al., 2008; Makhnenko et al., 2017; Hildenbrand et al., 2002; Lyu et al., 2018). Nevertheless, batch experiments do not account for the potential coupling between multi-phase flow and chemical reactions. CO_2 bubbles flow preferentially through large pores due to their lower capillarity, which may direct supersaturated water into low-velocity tiny pores, enhancing mineral precipitation. Although dry CO_2 invasion into shales has been shown to cause mineral precipitation, resulting in slight permeability loss (Minardi et al., 2021; Choi et al., 2021), the governing mechanisms remain unresolved.

2.5.2. Geochemical effects on mechanical behavior: effect on caprock integrity

The mechanical response of shales to geochemical processes induced by CO_2 injection is critically important in terms of caprock integrity. The extent of reactions primarily depends on how CO_2 infiltrates the shale, whether by molecular diffusion dissolved in water (i.e., zone C_3 in Fig. 1) or by advection as a free phase (i.e., zone C_1 in Fig. 1). In the former case, mineral dissolution dominates the mechanical behavior of altered shales, resulting in less stiff, less brittle and weaker rock frameworks (Zou et al., 2018; Jayasekara and Ranjth, 2021; Choi et al., 2021; Lyu et al., 2016; 2018). The compressive and tensile strengths of shales exposed to dissolved CO_2 degraded by up to 66% (Huang et al., 2019) and 27% (Minardi et al., 2021), respectively. The shear failure of shaly caprocks is unlikely to significantly affect their sealing potential because of their ductile nature, hindering the formation of conductive flow paths upon rupture (Vilarrasa et al., 2019a). In contrast, tensile fracturing has the potential to dramatically enhance the shale permeability, jeopardizing the permanent containment of CO_2 underground (Guglielmi et al., 2021). Yet, stiffening and strengthening of shales due to the precipitation of secondary minerals, although underreported, can not be ruled out (Espinoza et al., 2018).

If the capillary entry pressure of the pore network, which commonly is in the order of a few megapascals, is exceeded, CO_2 would enter the caprock in free phase (Makhnenko et al., 2017; Hildenbrand et al., 2002). In such situation, a series of other physico-chemical processes may gain prominence. CO_2 intrusion volumetrically sweeps the pore fluid or evaporates the clay interlayer water at the CO_2/aqueous phase interface, leading to rock dehydration (Bhuiyan et al., 2020). Water progressively evaporates into the CO_2 phase as far as the solubility limits and the equilibrium state are not achieved (Spycher et al., 2003). Dehydration increases the salt concentration, leading to salt precipitation when the water becomes oversaturated, as in the case of sandstones near the injection well (see Section 2.4.1.1). The precipitated salt may clog the nanometer-sized shale pore throats, possibly decreasing its intrinsic permeability and strengthening the rock body, although these processes need to be experimentally verified.

Shales containing water-sensitive clay minerals, especially smectite, may shrink or swell in response to dehydration and hydration, respectively (Dewhurst et al., 2018; Horsrud, 2001).

Following hydration, the influx of water into the nanometer-spaced clay sheets causes the layered structure of the clay to expand and the shale to swell (Du et al., 2018). Likewise, physical or chemical adsorption of CO_2 on clay platelets may lead to expansion, the extent of which is correlated with the amount of adsorbed CO_2 – a function of temperature, pressure, interlayer water content and the surface area and charge of clay sheets (Giesting et al., 2012a; 2012b) – and the stiffness of the clay minerals, among others (Heller and Zoback, 2014). The stiffer the shale, the lower the volumetric deformation (Bhuiyan et al., 2020). Under no deformation constraints, montmorillonite (a subclass of the smectite clay group) has reportedly undergone expansion as high as 9% perpendicular to the layering direction (Giesting et al., 2012b). In the subsurface, where the rock deformation is restricted, swelling of clay minerals may yield swelling stresses, which deteriorate the shales's stiffness and strength if cementation bonds are overcome. While the mechanical weakening of water-sensitive shales resulting from hydration swelling has been broadly acknowledged (Oort et al., 1996; Kivi et al., 2016; Ewy, 2015), experimental evidence for similar weakening behaviors following CO_2 adsorption-induced swelling is rare (Feng et al., 2019). The synergy between directional swelling of clay-rich shales and deviatoric stresses originating from injection overpressure and cooling effects of the injected CO_2 may cause (micro)fracturing and damage the caprock.

Dehydration-induced shrinkage can also alter the microstructure of clay-rich shales. This mechanism has recently been shown to contribute to the stiffening and strengthening of saturated shales (up to 70% increase in tensile and compressive strengths and 44% increase in Young´s modulus (Dewhurst et al., 2020; Minaeian et al., 2017)). However, shrinkage remains a critical issue concerning crack development (Dewhurst et al., 2020). At the pore scale, given that clays are water-wet in the presence of CO_2 (Espinoza and Santamarina, 2012), capillary forces normal to the CO_2-water interface invading the pores or clay platelets push the surrounding particles away from the invasion area, resulting in crack formation and propagation, a process referred to as desiccation cracking (see Shin and Santamarina (2011) for a detailed explanation). The formed cracks degrade the rock strength and provide conductive pathways for CO_2 to migrate deeper into the caprock. Yet, desiccation cracking, a phenomenon observed in unconfined clays, is likely to be inhibited due to the high confining pressure at the depths of CO_2 storage.

Despite invaluable insights gained from laboratory observations into the mechanisms of dry CO_2 interactions with shales, it remains unknown under which conditions and to what extent these mechanisms control the mechanical response of the caprock to CO_2 intrusion. These mechanisms compete to potentially reinforce or compromise caprock integrity. Although the high capillarity of shales likely limits the pervasive invasion of CO_2 to the lowermost portion of the caprock (zone C_1, (Kivi et al., 2022)), shale (or clay) interactions with CO_2 may become significant under certain circumstances, e.g., (1) the presence of annulus between cement and the shaly caprock, (2) formation of (micro)fractures, and (3) dissolution-enhanced porosity and permeability, altogether extending the CO_2 rise and exposure to the caprock (Dewhurst et al., 2020; Busch et al., 2016), (4) CO_2 injection directly below an intraformational baffle (e.g., the Illinois Basin–Decatur project (Finley, 2014)) and (5) a reservoir containing non-negligible clay contents (Giesting et al., 2012a).

The described processes also have important implications for devising future laboratory plans to improve the understanding of CO_2-shale interactions. Particularly, they explicitly outline the challenging essence of evaluating the mechanical properties of shales and their subsequent effects of exposure to CO_2 under in-situ conditions. Even a small gain or loss in the water content or change in its activity can thoroughly change the shale behavior (Dewhurst et al., 2020; Busch et al., 2016; Sarout and Detournay, 2011). Consequently, the unsolicited wetting/drying effects have to be isolated from the physico-chemical process of CO_2 injection, although not addressed by the vast majority of existing studies. Outcrop samples, which have tolerated varying degrees of weathering, cannot represent deep, intact shale behaviors. Future laboratory experiments should be conducted on samples retrieved from the subsurface at relevant depths to CO_2 storage, well preserved and handled to retain their innate water and original structure. Furthermore, variations in temperature and applied stresses may cause microstructural damage in shales and alter their porosity, permeability, and swelling tendency (Sinha et al., 2013; Tang et al., 2008). Accordingly, initial equilibration of the shale specimen with the desired in-situ conditions and maintaining them throughout CO_2 injection has to be assured to avoid experimental artifacts.

2.6. Geochemical processes for CO_2 injection into fractured rocks

Fractures can create rapid flow pathways through the reservoir and seal rocks. Fracture permeability may be several orders of magnitude greater than that of the surrounding rock matrix, depending primarily on the roughness and degree of mismatch of fracture surfaces and the effective stress state (Neuzil, 2019; Houben et al., 2020; Phillips et al., 2020). A sufficiently high pressure gradient drives a long-lasting localized flow of fluids, likely out of chemical equilibrium with minerals on the fracture surfaces, rendering them prone to chemical reactions (Detwiler and Morris, 2018). Mineral precipitation and/or dissolution have been widely acknowledged from a diagenetic perspective, under prolonged deep burial and elevated temperature conditions, to extensively alter the fracture geometry and mineralogy and, thus, their hydraulic and mechanical properties (Laubach et al., 2019; Hajirezaie et al., 2022). Multiple lines of evidence from along-fault leakage of CO_2-charged fluid from natural accumulations over geological time scales at the Colorado Plateau region in Utah, US, including severe carbonate mineralization in the fracture network (Dockrill and Shipton, 2010; Frery et al., 2015), also reproduced by numerical simulations (Kampman et al., 2016), lend support to potential reactive CO_2 flow in fractures in the course of geologic storage. Despite observations of geochemically-modulated alterations of fracture mineralogy, geochemical controls of CO_2 injection on hydromechanical properties of fractures are still poorly constrained (Phillips et al., 2020).

2.6.1. Evolution of reaction and flow trajectories

Insights from recent experiments on fractured rock imply the primary control of the injection rate on geochemical reactions along the fracture (Elkhoury et al., 2013; Deng et al., 2015; Noiriel and Deng; 2018). Generally, at high injection rates, favoring short residence compared

to the reaction time (low *Da* number), minerals dissolve almost uniformly throughout the fracture (Elkhoury et al., 2013). In contrast, low injection rates, reproducing high *Da* numbers, result in channeled dissolution and fracture enlargement (Deng et al., 2015; Durham et al., 2001). Flow channeling establishes positive feedback between reaction progress and enlargement of fracture aperture, which may be accompanied by channel breakthrough along the rock and, thus, runaway permeability growth (Elkhoury et al., 2013; Spokas et al., 2018; Deng et al., 2015). Caution should be taken, however, when upscaling these reaction patterns to reservoir conditions where fracture length can vary across many orders of magnitude (Scholz, 2010). The residence time increases with the fracture length, causing reaction front instabilities and channel formation to occur at significantly higher injection rates than the ones registered in the laboratory (Szymczak and Ladd, 2011). In addition, precipitation may also take place if the fluid flowing through the fracture becomes supersaturated (Steefel and Lichtner, 1998). Mineral precipitation may take place in several conditions, e.g., (1) when CO_2-rich fluid rises along a fracture and CO_2 exsolution following pressure reduction results in pH increase and carbonate mineral precipitation (Hajirezaie et al., 2022), (2) locally at smaller aperture portions of a single fracture, where the water-to-mineral ratio is lowest (Jimenez-Martinez et al., 2020; Menefee et al., 2020) or (3) at fracture intersections where fluid mixing or splitting assist in attaining the supersaturation conditions (Steefel and Hu, 2022).

The evolution of flow and mechanical deformation that may change the dissolution patterns is profoundly affected by mineralogical heterogeneities, not only in abundance but also in spatial distribution (Garcia-Rios et al., 2017; Gouze et al., 2003; Andreani et al., 2009), and applied stresses (Spokas et al., 2018; Detwiler, 2008). In homogeneous mono-mineral fractured rocks, e.g., carbonate rocks, uniform mineral dissolution gives rise to stress concentration at contacting asperities of fracture walls, promoting pressure solution (Yasuhara et al., 2004) or brittle failure once the stress surpasses the compressive strength of asperities (Detwiler, 2008). The consequence is a competition between dissolution-enhanced flow and permeability loss caused by the well-documented mechanical compaction (Pyrak-Nolte and Morris, 2000; Min et al., 2004). In heterogeneous multi-mineral rocks, the different solubility and reaction kinetics of the minerals enable a number of other pore scale phenomena to occur concurrently or sequentially to control fracture evolution. Dissolution of the more reactive mineral leaves a trail of uncemented, less reactive minerals filling the fracture. The less reactive mineral particles may become contacting asperities (Elkhoury et al., 2015) and/or progressively reorganize as a diffusive barrier on the reactant grains (e.g., microporous clay coating on calcite grains in an argillaceous limestone), dramatically decreasing the fracture dissolution rate (Noiriel et al., 2007; Ellis et al., 2011). Therefore, the spatial pattern of minerals is the key determinant of flow trajectories. An extreme flow behavior happens as the less reacting minerals spread out over the fracture surface or form repetitive layering orthogonal to the flow direction, similar to shale beddings. In this scenario, normal fracture compaction hinders channeling and leaves only flow bottlenecks, drastically decreasing fracture permeability, reportedly by up to two orders of magnitude (Elkhoury et al., 2015). This self-sealing phenomenon is also plausible if the less-reactive minerals, particularly clays in shales, are removed from the fracture surface. The massive displacement of clay particles may clog the fracture (Noiriel et al., 2007). On the contrary, for a nodular distribution pattern of less reacting

minerals, warranting continuous bands of reactive minerals along the flow direction, channeling takes place around the nodular areas, acting as persistent asperities that sustain mechanical loads (Ellis et al., 2011). These laboratory observations can be numerically reproduced by coupling reactive transport and geomechanical processes (Spokas et al., 2018).

Basin-wide pressurization in gigatonne-scale injection may pose a risk to safe CO_2 storage by triggering perceivable seismicity, compromising the wellbore integrity, and creating leaking pathways through the caprock (Newell and Ilgen, 2019; Zoback and Gorelick, 2012; Vilarrasa et al., 2019a). Self-healing of fractures in the reservoir boosts overpressurization, whereas flow channeling leads to injectivity enhancement. Similarly, these mechanisms can be of utmost importance to the leakage risk through caprocks, as conductive fractures become primary threats to the caprock sealing capacity (Detwiler and Morris, 2018). Although the geochemical effects on the flow field are observed in the short laboratory experiments, their occurrence in the subsurface may be delayed or accelerated by variations in the fracture length, rock composition, pore pressure, and stress state (Spokas et al., 2018; Deng et al., 2015; Elkhoury et al., 2015). It is also questionable whether the spatial patterns of less-reactive minerals observed in the laboratory can be uniformly distributed across scales. In fact, vertically heterogeneous fractures/faults crossing multiple stratigraphic layers hinder upward CO_2 migration (Rinaldi et al., 2014). If the stratigraphic layers are of different chemical reactivity, the caprock sealing capacity would be even increased.

2.6.2. Localized deformation and fracture propagation

Reactive transport of CO_2 in fractures may alter their mechanical characteristics because the non-uniform erosion of the fracture surface increases the fracture roughness and local stress distribution is mainly transformed from intact asperities to new uncemented contacts. Numerical simulations show that the described geochemical processes divide the fracture surface into two regions: a flattened contact area, which rapidly stiffens even at low stress levels and does not contribute to further normal deformation afterward, and a rough surface that bounds the dissolution-induced channel and is susceptible to compaction at high stresses (Lang et al., 2016). Thus, the lower the contact surface area and poorly developed surface mating (higher roughness), the lower the fracture stiffness but the more sensitive the stiffness and flow to stress changes (Pyrak-Nolte and Morris, 2000). Laboratory experiments of CO_2 injection, albeit rare, give credence to insights obtained from simulations and conceptual models. Skurtveit et al. (2020) highlight markedly stress-sensitive flow in conductive fractures naturally exposed to dissolved CO_2, featuring normal stiffness values lower than half of those measured for low-permeability unaltered fractures. These observations point to the tightly coupled nature of fluid flow, deformation and geochemical reactions in fractures. Accordingly, Pyrak-Nolte and Nolte (2016) suggested considering geochemical alterations of fractures in a universal flow-stiffness scaling relationship. Furthermore, the localized time-dependent deformation of altered fractures may dominate the volumetric response of the reservoir and become relevant to risks associated with reservoir compaction or induced seismicity (Stefanou and Sulem, 2014).

Similar to fracture stiffness, experimental measurements to study the influence of CO_2 injection on fracture strength are scarce. Opening-mode fracture toughness as an indicator of the fracture resistance against propagation under tensile load has been found to systematically increase and decrease by up to two folds with carbonate cement precipitation and dissolution, respectively, in a suite of siliciclastic samples diagenetically altered by CO_2-rich water (Major et al., 2018). The resulting weakening effects may threaten caprock integrity far beyond the CO_2 injection and monitoring period. Coupled chemical-mechanical numerical models have been developed to address the weakening (strengthening) impacts of calcite dissolution (precipitation) on fracture initiation and/or tensile propagation in calcite-rich or -cemented rocks across spatial and temporal scales (Hu and Hueckel, 2013; Schuler et al., 2020).

Our understanding of the frictional behavior of fractured rocks is limited to a number of CO_2 injection experiments on fault gouge that better represent a mature, gouge-bearing fault. Friction coefficient values for treated fault gouges are systematically inconsistent, yielding negligible changes in some claystone and sandstone (Samuelson and Spiers, 2012) or reduction of up to 15% in an anhydrite sample (Pluymakers et al., 2014). At experimental slip and time scales, CO_2 injection does not impose any clear, strong influence on the slip velocity dependence. The slip behavior remains predominantly velocity-strengthening, meaning that the friction strength increases as the slip accelerates and seismic activities are unlikely (Dieterich, 1972). These observations imply that chemical weakening of the friction coefficient may drive slip on fractures that could otherwise remain stable, given the excess pore pressure and shear stress buildup or release by poroelastic and thermoelastic effects (Guglielmi et al., 2021). CO_2 injection does not change the propensity of reservoir and caprock faults to slip aseismically, not to negate induced seismicity risk in CCS projects. Yet, aseismic slip may enhance fracture permeability, reaping the benefits of enhanced injectivity in the reservoir (Vilarrasa et al., 2019a), but raising significant concerns around the loss of caprock integrity (Rutqvist, 2012).

2.7. Recent advances and the path forward

2.7.1 Fundamental understanding of the CHM processes of CO_2 injection

Laboratory experiments with reservoir and caprock specimens reacting at the *P*-*T* ranges relevant to geological CO_2 storage provide fundamental insights into the processes that control CO_2-water-rock interactions. The CO_2 fraction that dissolves in the pore fluid forms acidic CO_2-rich water (pH ≈ 3-5) that induce the dissolution of primary minerals and the precipitation of secondary minerals. These reactions lead to major changes in sedimentary rock properties, including mineralogy, pore structure, porosity, permeability, stiffness, strength and time-dependent deformation. The non-dissolved supercritical CO_2 (dry supercritical CO_2) barely reacts with primary minerals but dries out the formation fluids and causes salt precipitation, leading to alterations in hydromechanical properties. It is inferred that mineral reactions primarily depend on the content of highly soluble carbonate minerals. Moreover, the extent of reactions is a complex function of environmental variables (pressure, temperature, fluid chemistry, applied stresses), intrinsic rock properties (mineralogy, microstructure, porosity and permeability), and the hydrodynamics of CO_2 flow and transport in rock.

This review provides a perspective on the geochemical interactions of supercritical CO_2 with reservoir (carbonates, sandstones) and sealing rocks (shales) crucial to ensuring secure geological storage of CO_2. The identified gaps in the fundamental understanding of coupled CHM processes, their monitoring, prediction, and upscaling to industrial-scale CO_2 injection warrant further research. Figure 11 summarizes the insights gained from this review into the potential impacts of CO_2-water-rock interactions on hydromechanical rock properties and their implications for geological CO_2 storage, including the influences on reservoir injectivity and integrity, reservoir compaction and surface subsidence, wellbore integrity and caprock sealing capacity and integrity.

Carbonates: In laboratory experiments, flow conditions affect the geochemical processes. Exposure of carbonate rocks to CO_2-rich water under no-flow conditions results in minor changes in rock composition because the CO_2-rich solution rapidly reaches equilibrium with calcite, hindering further interactions (Sterpenich et al., 2014; Soong et al., 2016; Grgic, 2011; Khather et al., 2020). The most significant changes occur in cores flooded with CO_2-rich water under open-flow conditions with a continuous renewal of the acidic solution at the inlet, where minerals dissolve and porosity and permeability increase, resulting in mechanical weakening (Fig. 12).

The structure and heterogeneity of limestones affect the chemically-induced evolution of the hydromechanical properties. Given the high porosity, smaller grain-to-grain contacts and large reactive surface area, grain-supported carbonate rocks (chalks) commonly endure the most considerable CHM coupling effects both in the short and long terms. The rapid dissolution of carbonate minerals (e.g., calcite) when subjected to CO_2-rich water circulation depends on the inherent heterogeneity of the rock and leads to the formation of highly conductive flow channels, i.e., wormholes. Wormholes are susceptible to collapse under the elevated reservoir confinement pressure, potentially speeding up reservoir compaction and reducing reservoir injectivity.

At the moment, a better characterization of the processes leading to localized flow and deformation in wormholes is necessary (1) to evaluate the induced CHM effects as the continuity of the porous network is questioned and (2) to upscale the results from the laboratory to the field as the rock sample is no longer a representative elementary volume. Attempts to find appropriate injection rates to approach uniform dissolution patterns have been made by adjusting the *Pe* and *Da* numbers. Further research using real-time and high-resolution imaging of reacting rocks combined with reactive transport modeling would be highly instructive (Voltolini and Ajo-Franklin, 2019; Menke et al., 2017).

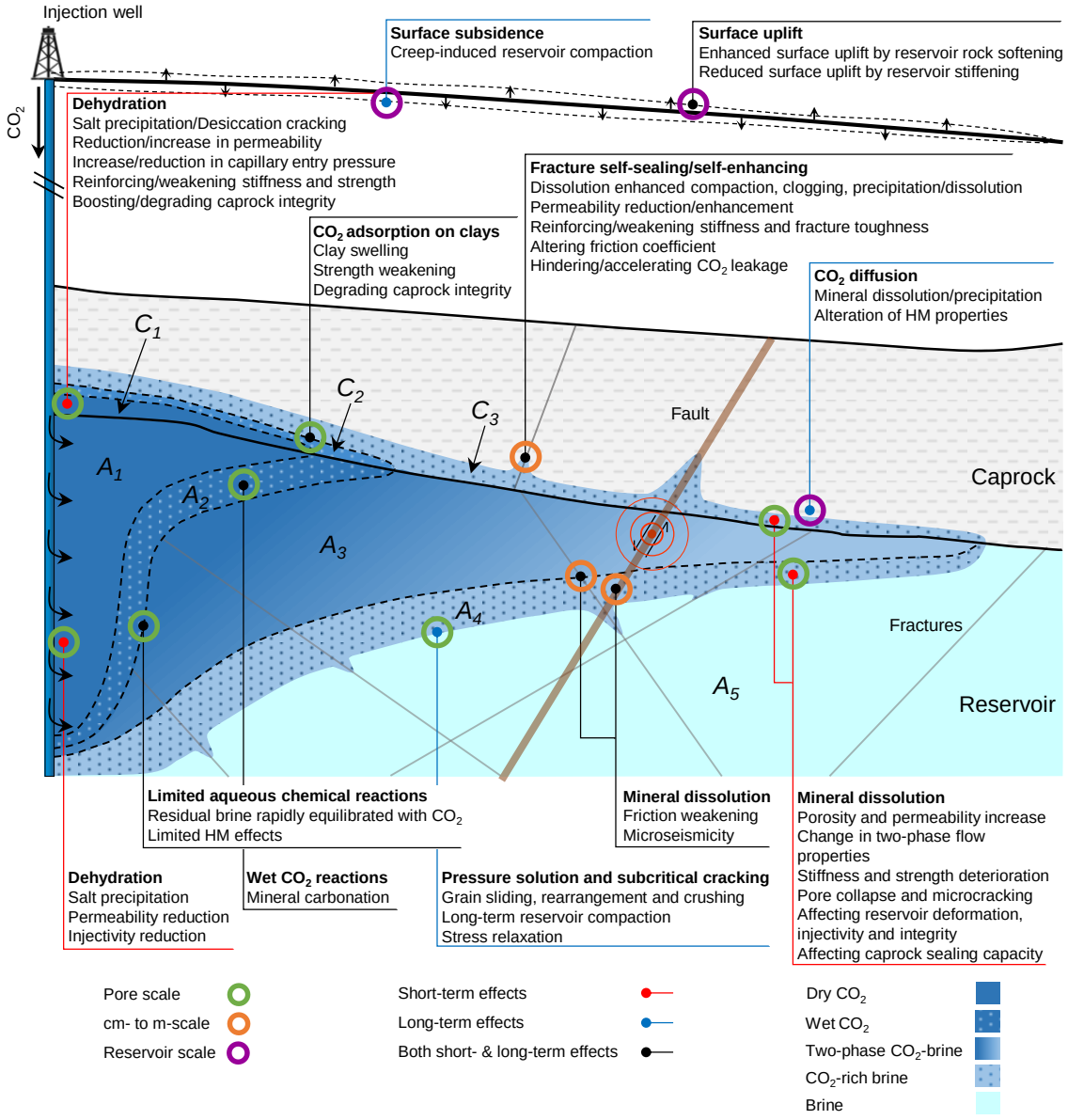

Figure 11. Overview of the geochemical effects of CO_2 injection on hydromechanical properties of the reservoir and sealing rocks and the associated key issues, including reservoir injectivity, deformation and integrity, caprock integrity and sealing capacity and induced seismicity. Note that zones A_1 to A_5 in the reservoir and C_1 to C_3 in the caprock are defined in the same way as in Fig. 1.

Sandstones: In sandstones, the content of carbonate minerals and their load-bearing role in the pore structure determine the fate of the mechanical properties. Quartz-rich sandstones undergo trivial interactions with CO_2 because of the slow dissolution kinetics of silicates, resulting in slight alterations in hydromechanical properties (Gaus, 2010). Measurable amounts of dissolved quartz over the time-scale of laboratory experiments are only expected under high-temperature conditions (e.g., $T > 150$ °C) can be anticipated (Rosenbauer et al., 2005; Akono et al., 2020; Li et al., 2020). In contrast, sandstones with intergranular carbonate cement have the most variable structures. Dissolution of a small amount of load-bearing carbonate cement can provoke drastic declines in stiffness and strength and cause time-dependent deformation

by promoting pressure solution at grain contacts. Clay and/or feldspar (alumino-silicate)-cemented sandstones with minor carbonate content can also undergo significant alterations through dissolution and transformation of the cement material. Therefore, the extent of alterations in hydromechanical properties depends on the mineralogical composition of sandstones. Considerable dissolution-enhanced porosity and permeability, and mechanical weakening greater than those of carbonates, can occur (Fig. 12). Although alterations in sandstone properties under no-flow and open-flow conditions are comparable (Fig. 12a,b), batch and flow-through experiments with the same sandstone samples and similar experimental conditions should be performed to more accurately isolate the effect of rock-to-CO_2 exposure hydrodynamics. In addition, given the scarcity of knowledge on relative permeability hysteresis (two-phase flow) in chemically-altered rocks (all rock types) (Juanes et al., 2006; Krevor et al., 2011), an improved understanding of this property is essential in order to better assess the efficiency of CO_2 residual trapping.

Shales: Technical challenges to characterize low-permeability shales have significantly limited the experimental assessment of CO_2 exposure effects on shaly caprocks. Usually, shales are treated under no-flow conditions to replicate diffusive CO_2 leakage through the caprock. Under these conditions, an increase in dissolution-driven mechanical weakening and an increase in permeability and attenuation of capillarity occur. These changes in shale properties can be even more striking than those of altered reservoir rocks (Fig. 12), with the potential to endanger the caprock sealing capacity.

If dry CO_2 reaches the caprock (note that the injected dry CO_2 takes water as it advances through the reservoir, i.e., zone C_2), the water within the pores or clay interlayers could be dehydrated, giving rise to self-sealing mechanisms and mechanical strengthening or self-enhancing and mechanical weakening, the influence of which is controversial (Bhuiyan et al., 2020; Dewhurst et al., 2020; Espinoza and Santamarina, 2012). Recent studies on the sealing capacity of caprock analogue specimens invaded by CO_2 also yield inconsistent observations. Nevertheless, free-phase CO_2 intrusion into shales is unlikely owing to their high capillarity. The knowledge of CHM coupling in shales remains undeveloped and should be subject to complementary experimental, observational and modeling research. Additional studies are warranted to elucidate the interplay between physical and chemical processes of CO_2 interactions with clay minerals.

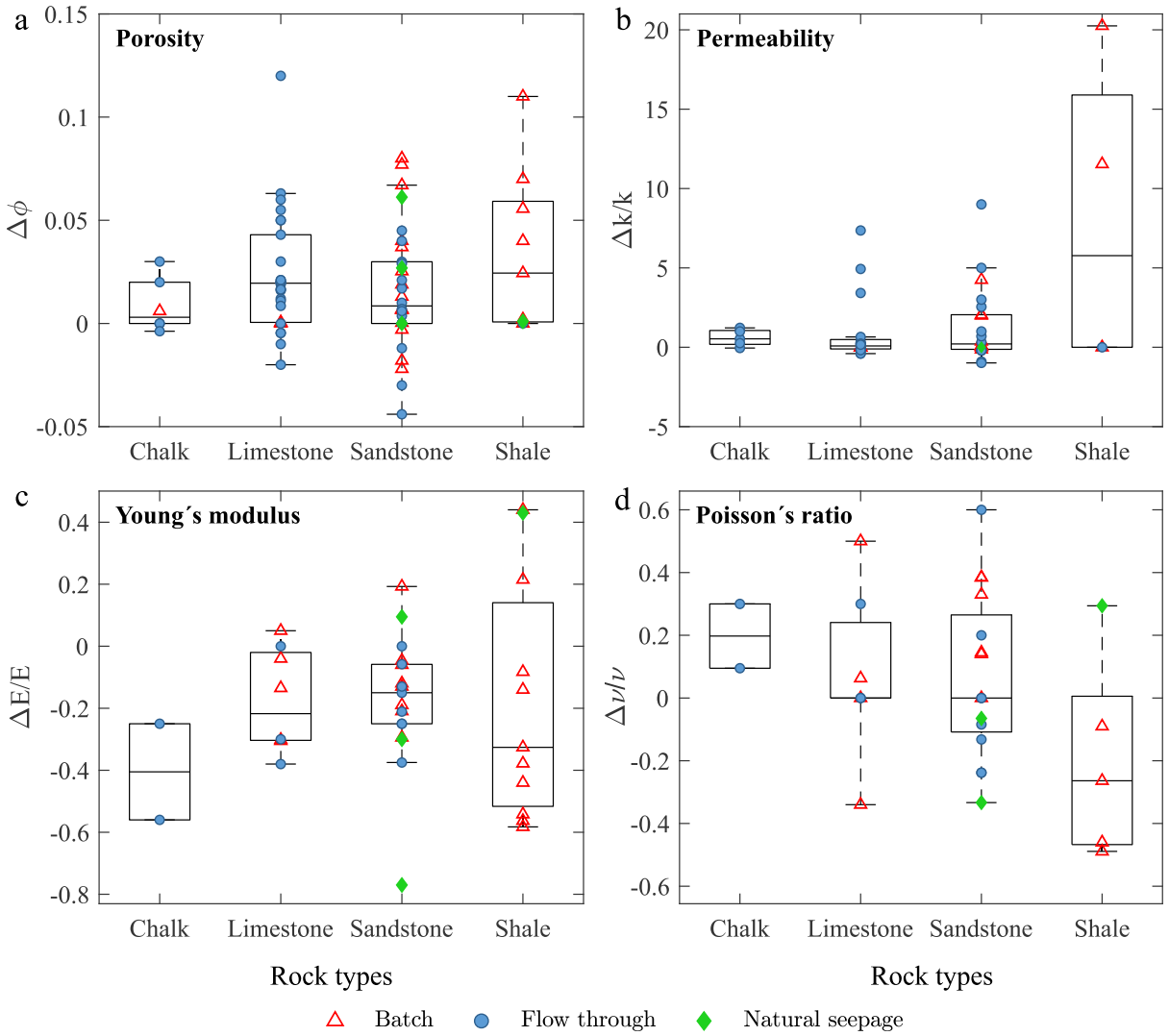

Figure 12. Box-and-whisker plots for changes in porosity (a), permeability (b), Young´s modulus (c), and Poisson´s ratio (d). The CO_2 exposure types, batch, flow-through, or natural, are highlighted in different colors. The dividing lines in the boxes indicate the median values, and the bottom and top edges illustrate the first and third quartiles, respectively. The whiskers extend to the most extreme data points not statistically considered outliers. The permeability enhancement of 125 folds measured by Noiriel et al. (200%) for Lérouville limestone is not illustrated in the figure for the sake of more clear observation of other experimental data. Data listed in Table A3 (Appendix I) used to plot this figure.

Fractured rocks: Chemical reactions of CO_2 with fractured caprocks or reservoir rocks and the ensuing changes in flow and mechanical behavior are tightly coupled and primarily controlled by the injection rate, length scale, fracture roughness, applied stresses and the content and spatial distribution of reactive minerals. Low injection rates (or at several tens to hundreds of meters from the injection well as the flux decreases with the logarithm of distance from the well) and mineral heterogeneity, featuring a continuous path of reactive minerals along the flow direction, favor fracture channeling. This dissolution regime results in runaway permeability growth, smaller stiffness, and heavily stress-dependent flow. In contrast, CO_2 injection at high rates into homogeneous fractures or certain distribution of less-reactive minerals on the fracture surface may impede channeled flow and reactions. The consequence

would be rapid compaction, stiffening, and self-sealing. The use of dimensionless Péclet and Damköhler numbers and the characterization of rock fabric evolutions across scales may be helpful to upscale these dissolution patterns to the field. Chemically-assisted flow channeling may increase reservoir injectivity, while it may jeopardize the caprock sealing capacity. Furthermore, geochemical processes may degrade both tensile and frictional strengths of fractures, raising concerns about loss of caprock integrity during and beyond the injection period.

I conclude that despite recent advances, chemo-mechanical coupling in fractured rocks, particularly in the context of CO_2 injection, is underappreciated. To move the field forward, I suggest focusing future research on the following directions:

- Experimental and modeling studies on reactive CO_2 transport in fractured rocks should accurately account for stress states representative of reservoir conditions. Neglecting the confining stress, using artificial fractures with unrealistic roughness and aperture, and holding the fracture open, e.g., by using proppant, may overlook geomechanical processes, leading to overestimation of the dissolution-induced permeability enhancement.

- At the field scale, fractures have presumably undergone prolonged shearing or may experience slip due to physical and chemical perturbations caused by CO_2 injection. Hence, fracture roughness is modulated, microfractures may branch, fine-grained gouge material forms and similar lithologies already juxtaposed may be offset along the flow direction (Crandall et al., 2017; Dang et al., 2019). Laboratory experiments on artificial shear-mode fractures offer an opportunity to study the evolution of flow and shear deformation in such morphologically heterogeneous fractures. Furthermore, CO_2 or CO_2-rich water can be used as the working fluid for fracture slip experiments to observe the combined effects of fracture reactivation and chemistry on flow and deformation.

- Laboratory experiments have mainly focused on single fractures, and a knowledge gap in the presence of fracture intersections is evident. Fluid mixing (where fractures of different origins converge) or splitting (where multiple fractures branch) may locally alter the fluid velocity field and chemistry (Steefel and Hu, 2022). Laboratory studies of fracture sets or networks can benefit from breakthroughs in 3D X-ray tomography at representative underground conditions (Wenning et al., 2019) and from a combination of etching, machining, and fast-evolving 3D printing techniques to produce fracture networks in a repeatable manner (Head and Vanorio, 2016; Ishibashi et al., 2020).

- Microfluidics and transparent analogue systems are promising techniques to visualize and elucidate coupled (multi-phase) flow, transport, deformation and geochemical processes in fractures under in-situ pressure, temperature and stress conditions. Three notable examples of using these techniques to study chemically-eroded fractures during CO_2 injection are Detwiler (2008), Fazeli et al. (2019) and Jimenez-Martinez et al. (2020).

- Multiple physical processes may simultaneously operate during CO_2 injection into fractured rocks. Physics-based models and numerical simulations are well-positioned to diagnose the relative importance and contribution of each process in the experiments. In addition, machine-learning approaches will improve the characterization and analysis of flow and fracture

evolution by extracting information from massive laboratory signals and images (Nolte and Pyrak-Nolte, 2022).

2.7.2. Upscaling in time and space

Laboratory experiments to understand CO_2-rich water-rock interactions have provided insights into short-term geochemical processes (up to 2-3 years). However, long-term reaction mechanisms, particularly those of quartz reaction, are less well understood and need further research (Gaus, 2010; Kampman et al., 2013). It has been demonstrated that evaluating naturally altered intact and fractured rocks exposed to CO_2 over geological time scales is essential to understand long-term CHM processes. Overall, the observed changes in hydraulic and mechanical properties of these samples are within the wide ranges recognized for laboratory-treated specimens (Fig. 12). However, samples taken from outcrops may differ from those retrieved from representative depths for CCS because they were commonly exposed to weathering and underwent smaller stresses. Thus, geological intuitions of CO_2-rock interactions sourced from outcrop observations should be treated with caution because reactive transport regimes that cause the hydraulic and mechanical properties of (fractured) rocks to evolve are strongly stress-sensitive. Moreover, outcrop samples probably endured various loading paths (see Laubach et al. (2019) for a review of relevant mechanisms), e.g., mechanical alterations due to their proximity to faults as the main conduits for CO_2 leakage (Miocic et al., 2016; Detwiler and Morris, 2018). Thus, differentiating between the coupled CHM effects of CO_2 and other processes operating over geological time scales is vital, although quite challenging (Espinoza et al., 2018). Integrating reactive transport modeling and thermo-hydromechanical simulators to reproduce these natural features may unlock new insights into their origin (Snippe et al., 2022). Numerical simulations help draw more accurate constraints on the kinetic rates of slow-reacting minerals (e.g., quartz) whose uncertainties in predicting the fate of CO_2 underground could grow nonlinearly over the geologic time of interest to CO_2 storage (Kampman et al., 2013; White et al., 2003).

Extending the research to field-scale injections, with all accompanying geologic complexities and heterogeneities, could see significant developments using purpose-designed, densely monitored experiments in highly characterized, in-situ, tens-of-meters-scale underground research laboratories (Bossart et al., 2017). These experiments are particularly valuable to advance our fundamental understanding of relevant physical processes gained from core-scale experiments and develop and test conceptual models, numerical approaches, and cutting-edge real-time monitoring technologies under more realistic conditions (Birkholzer et al., 2019). A pertinent example is the CO_2 Long-term Periodic Injection Experiment (CO2LPIE) at the Mont Terri rock laboratory, Switzerland, which aims at understanding coupled flow, geochemical and geomechanical processes for CO_2 injection into Opalynus Clay, a representative caprock (Sciandra et al., 2022).

The progress of CO_2-water-rock interactions in subsurface systems critically depends on the hydrodynamics of the CO_2 plume propagation in the reservoir and caprocks. Reproduction of these scenarios is complex and demands laboratory experiments with different CO_2 exposures and physical conditions. Coupled flow, reactive transport and geomechanical modeling is a

powerful tool for quantitatively linking laboratory-scale observations, intermediate-scale rock laboratory experiments and industrial-scale CO_2 injection (Dai et al., 2019; Vilarrasa and Rudqvist, 2017; Taron and Elsworth, 2009). At the moment, a fully coupled CHM modeling package is scarce owing to its complexities and multidisciplinary nature (see Ilgen et al. (2019) and Viswanathan et al. (2022) for a review of these models). Further efforts should be dedicated to developing CHM constitutive models that work for different rock types. By reproducing laboratory experiments, these numerical models would be validated to ensure upscaling of the key observed phenomena.

Chapter 3

Methodology

This chapter describes (1) information on the material under study (Pont du Gard Limestone), (2) experimental methodology including the percolation experiments and evaluation techniques used to characterize the rock properties before and after interactions with acid fluids, (3) digital rock physics approach to construct Darcy-scale porosity and permeability distribution maps, and (4) details on 3D reactive transport modelling of the experiments.

3.1. Experimental Methodology

3.1.1. Samples and experimental plan

The material under study is the heterogenous grain-supported Pont du Gard Limestone, which is composed of calcitic broken shell fragments. Five cylindrical samples (P_1 to P_5) were cored with a diameter of 25 mm and lengths of 44 to 78 mm (Table 2). Except for the 44-mm-long P_3 core, all cores have a length-to-diameter ratio ≥ 2 according to the International Society for Rock Mechanics (ISRM) recommendations (Culshaw, 2015) for uniaxial compression tests.

Percolation experiments were conducted on samples P_2 to P_5 using either CO_2-saturated water or HCl solution as injecting fluid. Sample P_1 was used in a uniaxial compression test to extract the stiffness and strength of the intact rock. Table 2 shows the experimental conditions and techniques employed to assess the alterations in the hydromechanical properties of the samples. The experiments are labeled according to the specimen's name (P_2-P_5), the injecting solution type (CO_2 or HCl), and the duration of the experiment (14 or 28 days). The *P_3-CO_2-28* experiment was stopped after 14 days to measure porosity, permeability, and ultrasonic wave velocities on the altered core. Thereafter, the injection was resumed for another 14 days, and the core was also characterized after 28 days.

The techniques used to evaluate the core alteration are as follows: effluent chemistry analysis, measurements of bulk porosity and permeability, Mercury Intrusion Capillary Pressure (MICP) tests, X-ray Micro Computed Tomography (XMCT), and ultrasonic wave propagation measurements before and after experiments. In addition, uniaxial compression tests were performed on flooded cores to measure their stiffness and strength properties as explained below.

Table 2. Experimental conditions and experimental techniques.

No.	diameter (mm)	length (mm)	experimental conditions		analyses and measurements
			label / injecting solution	duration (day)	
1	25	50	***P₁***	0	MICP, permeability, porosity, ultrasonic velocity, uniaxial compression
2	25	50	***P₂-CO₂-14*** / CO_2-saturated water	14	chemistry, permeability, porosity, ultrasonic velocity, uniaxial compression, XMCT
3	25	44	***P₃-CO₂-28*** / CO_2-saturated water	28	chemistry, permeability, porosity, ultrasonic velocity, XMCT
4	25	75	***P₄-HCl-14*** / HCl solution	14	chemistry, MICP, permeability, porosity, uniaxial compression, ultrasonic velocity, XMCT
5	25	78	***P₅-HCl-28*** / HCl solution	28	chemistry, MICP, permeability, porosity, ultrasonic velocity, uniaxial compression, XMCT

injection rate = 0.15 mL min^{-1} (all experiments)

3.1.2. Percolation experiments: apparatus and procedure

Two different flow-through setups were used. In the first one, CO_2-saturated water under supercritical CO_2 conditions (P_{CO2} = 100 bar and T = 60 °C) was injected into specimens P_2 and P_3. The system consisted of two water tanks of 1 L capacity, a compressor, a double-piston pump, a core holder, and a double-syringe sampling reactor (Fig. 13a, Fig. A1, Appendix II). The compressor supplied gaseous CO_2 with a constant pressure of 100 bar to the water tanks until gaseous and dissolved CO_2 reached equilibrium. Thereafter, the pump injected CO_2-equilibrated water into the limestone core at a constant flow rate (0.15 mL min^{-1}). A core with an inner Teflon and an outer shrink rubber wrapping was set into the core holder and kept isolated from confining water. A confining pressure of 1.5 times the injection pressure was applied to the core using a pressure multiplier. Output solutions were collected periodically (every 24 hours) in a pressurized double syringe system controlled by a back pressure regulator to maintain the pressure of 100 bar. Metal band heaters wrapping the water tanks and the core holder were used to keep the system at 60 ± 2 °C. Under these experimental conditions, a total CO_2 concentration of 1.03 mol L^{-1} in Milli-Q water yielded a pH of ~ 3.13. 9.90 mL of the output solutions were immediately acidified by adding 0.1 mL of 65% HNO_3 to prevent possible precipitation of calcite. Thereafter, the Ca concentration was measured using Inductively Coupled Plasma-Atomic Emission Spectrometry (ICP-AES) employing a Perkin Elmer Optima 8300 with a Ca detection limit of 6.3×10^{-6} M and 3% of analytical uncertainty.

The second series of experiments was conducted under atmospheric pressure (Fig. 13b, Fig. A2, Appendix II). In this flow-through system, an HCl solution tank of 5 L was connected to a peristaltic pump that injected the solution into the core at a constant flow rate of 0.15 mL min^{-1}. The output solutions were also collected periodically. The temperature of the system was kept at 60 ± 2 °C using heater bands that covered the tubing, the core, and the outflow collecting

tank. For the sake of comparison with the CO_2 supercritical experiments, the pH of the input solution (HCl) was adjusted to 3.13 by adding 3.79 mL of 1 M HCl to 5 L of Milli-Q water.

The pH of the input and output solutions was measured during the HCl experiments using a Thermo Scientific Orion Dual Star pH meter. pH was calibrated at 60 °C using standard pH 2, 7, and 9 buffer solutions with a pH uncertainty of 0.02 pH units. Thereafter, 9.90 mL of the output solutions were immediately acidified and the Ca concentration was measured using ICP-AES as explained above.

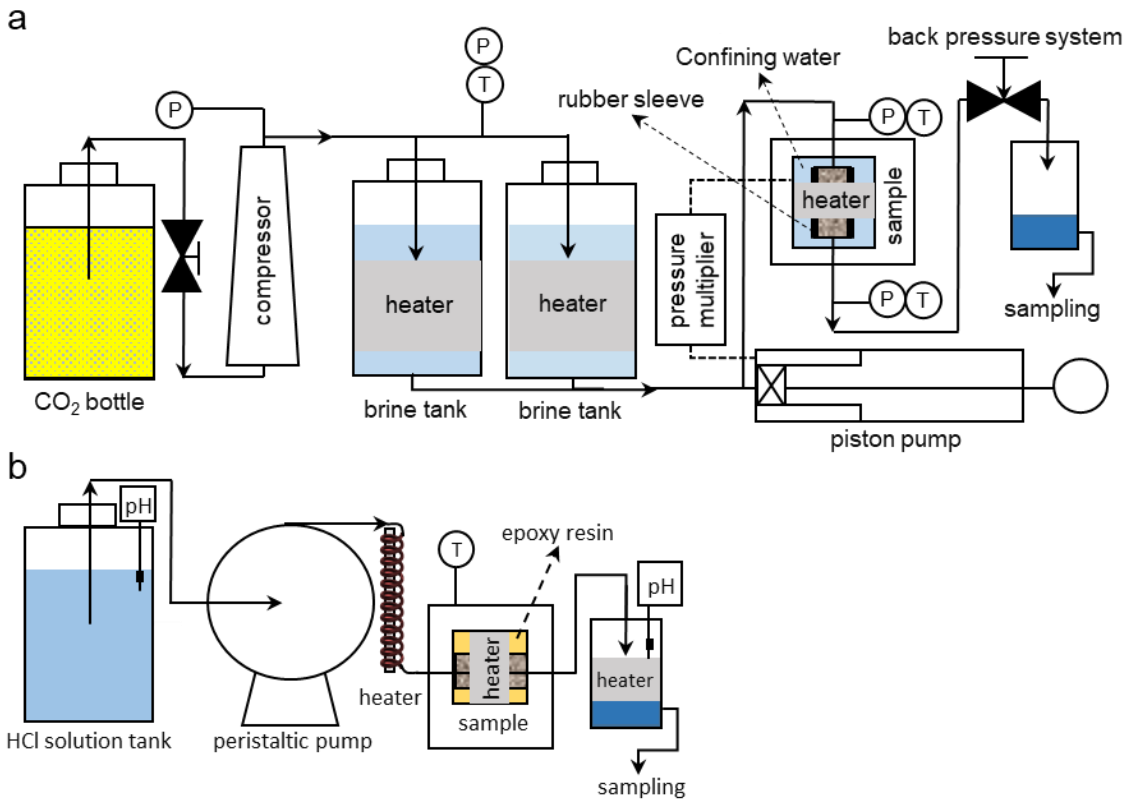

Figure 13. Schematics of the two setups used to run the (a) supercritical CO_2 and (b) atmospheric HCl percolation experiments.

3.1.3. Evaluation of microstructural and transport properties

3.1.3.1. Porosity and pore size distribution

Total porosity of the dry cores was determined by weight measurements based on the bulk volume of each specimen, bulk density (ρ_b) and the core mass. Considering an average grain density (ρ_{ca}) of 2.65 g cm^{-3} for calcite, total core porosity (ϕ) was calculated as $\phi = 1 - \rho_b/\rho_{ca}$. Core porosity was not calculated by subtracting dry from water-saturated weights (Bemer et al., 2016; Nguyen et al., 2016) as it resulted in big errors owing to abrupt water losses in examined highly permeable rock.

Mercury intrusion porosimetry (MICP) (Diamond, 2000) conducted on small fragments cut from the intact core and from the inlet of the HCl-treated limestone cores enabled us to

determine the connected porosity and pore throat size distributions before and after the experiments. MICP was not applied to the cores altered with CO_2-saturated water because their pore network was not representative of the localized dissolution structures that formed (see Section 3.2). With low- and high-pressure chambers, the device reached pressures up to 60000 psi (414 MPa) by which mercury penetrated the pore network, and the injected mercury volume was accurately measured. As pressure rose, the interconnected pores were intruded from larger to smaller sizes. Adopting the Young–Laplace equation (Washburn, 1921), the mercury pressure (p_{hg}) is expressed as a function of the pore throat diameter (d), the contact angle (θ), and the interfacial tension (γ) of the liquid mercury in contact with its vapor

$$p_{hg} = -4\gamma Cos\theta / d \quad (4)$$

Mercury has a contact angle of 140° and an interfacial surface tension of 480.0 mN/m at the experimental temperature (22 ± 2 °C). Pore size distribution and interconnected porosity were evaluated from the volume of the intruded mercury at each pressurization step. Partition of the inferred pore size distribution was made according to the IUPAC classification: (1) micropores with radii < 0.002 μm, (2) mesopores with radii between 0.002 and 0.05 μm and (3) macropores with radii > 0.05 μm.

3.1.3.2. Pore-scale imaging

X-ray Micro Computed Tomography (XMCT) was conducted on all cores except for P_1, before and after the experiments under dry conditions to determine the initial and evolving porosity and pore structures. 3D grayscale images with a resolution of 20-21 micrometers were obtained and exported as 8-bit 2D slice-based TIFF image stacks. After applying appropriate thresholding the images were binarized and used to determine the pore and solid phase fractions (image-based porosity and calcite content).

3.1.3.3. Permeability measurement

The initially high permeability of the cores gave rise to a very small pressure drop across the cores that could not be detected by the pressure transducers during the experiments. Thus, the classic column experiment setup was used (Fig. A3, Appendix II) to measure the initial and final permeabilities of the intact and altered cores following Darcy´s law (Darcy, 1856)

$$k = \mu LQ / S\rho gH \quad (5)$$

where k, S, and L are the intrinsic permeability, cross-section area, and length of the cores, respectively, g is gravity acceleration, μ is the dynamic fluid viscosity, ρ is the fluid density,

Q denotes the steady-state flow rate of fluid through the core, and *H* is the hydraulic head. An average permeability value was obtained by repeating the measurements three times.

3.1.3.4. Quantification of calcite dissolution

Given Pont du Gard Limestone is exclusively composed of calcite, the increase in total porosity ($\Delta\phi$) of the cores was calculated as

$$\Delta\phi = M_{ca} \cdot \bar{V}_{ca}/V_c \quad (6)$$

Where V_c and $\bar{V}_{ca}$ are the volume of the core and calcite molar volume, respectively, and M_{Ca} is the moles of calcite dissolved during injection which is written as follows

$$M_{ca} = \sum_{\Delta t} [Ca]_{out}.Q.\Delta t \quad (7)$$

where $[Ca]_{out}$ is the output Ca concentration, Q is the flow rate, and Δt is the sampling interval.

3.1.4. Evaluation of mechanical properties

The mechanical behavior of the intact and altered cores was assessed using two methods distinguished by the exerting strain rate on the specimen: (1) destructive uniaxial compression experiments (low strain rate) and (2) ultrasonic wave propagation experiments (high strain rate).

3.1.4.1. Uniaxial compression test

To obtain the full stress-strain curves, uniaxial compression tests (a.k.a static loading) with unloading and reloading cycles were conducted on all cores except for P_3 (Fig. A4, Appendix II). Results from the intact P_1 core are representative of the characteristic behavior of the Pont du Gard Limestone, whereas those from the P_2, P_4, and P_5 cores are characteristic of the acid-induced weakening in the rock load-bearing frameworks. Compression tests were all conducted under dry conditions and at room temperature. Specimens were loaded in axial displacement control mode at a constant low rate of 0.0002 mm s^{-1} (corresponding to a nominal axial strain rate of 4×10^{-6} s^{-1} for a 50-mm-long specimen), delineating a static loading situation. The applied load and axial and lateral deformations were continuously measured and recorded until the rock failure stress, i.e., the uniaxial compressive strength (UCS) and the post-failure behavior were determined.

Deformation measurements were made using two pairs of strain gauges glued to the mid-height of the specimens at diametrically-opposed positions. Two deformation coefficients were measured: (1) the ratio of axial stress changes to the axial rock deformation and (2) the ratio of lateral deformation to axial deformation at the linear (elastic) portions of the stress-strain curves

with the tangent approach applied on the first loading and on the unloading portion of the cycles. The defined elastic constants are equivalent to Young´s modulus and Poisson´s ratio of continuum porous rocks, respectively, that can be considered representative elementary volume (Hudson and Harrison, 2000). Although the heterogeneous dissolution patterns in the chemically-altered cores (see Section 3.2) question the continuity conditions, hereinafter the above-mentioned coefficients are referred to as Young's modulus (E_s) and Poisson's ratio (v_s) for the analogy to those measured dynamically.

3.1.4.2. Ultrasonic wave propagation

To determine the dynamic elastic moduli of the cores, compressional and shear wave velocities (V_P and V_s, respectively) at 2.25 MHz were measured before and after the percolation experiments using a pulse-transmission technique (Brich, 1960) with an EPOCH 650 OLYMPUS apparatus (Fig. A5, Appendix II). Measurements were taken at atmospheric pressure and room temperature on dry core specimens. The ultrasonic elastic wave was generated by the source transducer placed at the core inlet and received by the receiver transducer placed at the outlet. A high-viscosity bonding agent ensured an optimum coupling between the sample-end surfaces and the transducers, preventing a potential elastic wave attenuation in this gap. Compressional or shear wave velocities were computed by dividing the sample length by the measured wave arrival time. Dynamic values of Young's modulus (E_d) and Poisson's ratio (v_d) were determined using the bulk density and the measured velocities according to the following expressions (Jaeger et al. 2007)

$$E_d = \rho_b V_s^2 (3V_p^2 - 4V_s^2)/V_p^2 - V_s^2 \quad (8)$$

$$v_d = V_p^2 - 2V_s^2/2(V_p^2 - V_s^2) \quad (9)$$

Note that by measuring E_d and v_d, bulk (K) and shear (G) moduli can be calculated using the existing relationships among elastic moduli (Jaeger et al., 2007; Mavko et al., 2009).

3.2. Digital rock models

Digital rock physics, i.e., imaging and computing, emerged in the 1990s as a powerful tool to visualize the internal structure of rocks and inferring effective rock properties from 3D realizations of the rock microstructure (Fredrich et al., 1995; Spanne et al., 1994). Since then, this technology has been increasingly employed as a complementary instrument to conventional core experiments not only for the nondestructive characterization of geomaterials but also for developing a deep understanding of relevant physical processes, mainly including fluid flow and rock deformation (Andrä et al., 2013). The latter is achieved by numerically simulating physical processes in digital rocks, featuring representative distribution of relevant properties, and making quantitative comparisons with experimental measurements (Rabbani and Jamshidi, 2014; Jackson et al., 2018). The simulations are commonly carried out at the

continuum scale, where the numerical grid blocks are representative elementary volumes (REV) comprising a large enough assembly of pores and grains with equivalent properties (Hao et al., 2013; Jackson et al., 2020; Smith et al., 2017). The size of the grids is assigned primarily based on computational costs (in particular for 3D models where the computational time and memory may become exceedingly high for fine grid blocks) and constraints on the applicability of physical models. Accordingly, digital rock physics applies statistical or homogenization approaches to derive representative distribution maps of rock properties from microstructural data. These techniques have been successfully used to evaluate a variety of Elector-Thermo-Chemo-Hydro-Mechanical (ETCHM) properties of rocks (Durán et al., 2019; Ettemeyer et al., 2020; Hao et al., 2013; Smith et al., 2017; Vanorio and Mavko, 2011; Wu et al., 2020). Among these properties, porosity is a primary parameter that can be derived from XMCT data but is also a key input variable to predict other physical rock properties (Eberli et al., 2003).

As digital rock physics gains momentum in geosciences and engineering applications, the need for appropriate approaches to construct 3D image-based maps of rock properties becomes a priority. Such approaches are computationally demanding as they require analyzing large imaging datasets. Here a simple yet computationally efficient and accurate MATLAB-based method (Appendix III) is proposed to construct a 3D representation of porosity distribution in heterogeneous carbonate rocks. The proposed method includes 1) decomposition of the 3D volumetric image of the rock into equal-size sub-domains, 2) processing of individual, equidistributed 2D images and calculating porosity along each sub-domain, and 3) assembling slice-averaged porosity and mapping onto a continuum rock domain defined by arbitrary-sized grids. Decomposition of the rock domain and 2D slice-by-slice image processing minimizes the computational cost, in particular, in terms of the required memory to handle data.

3.2.1. Description of the approach

3.2.1.1. Image acquisition

The proposed method relies on discretizing the full core XMCT image into smaller sub-volumes along the axis of the rock sample (z-direction). The discretization enables the parallelization of subsequent data processing on sub-volumes, which significantly reduces the computational cost. To this end, the "vol. format" image dataset is opened using the open-access myVGL 2022.4 (viewer for data processed Volume Graphics Software) and the 3D volumetric image is discretized into an arbitrary number of rectangular cuboids along the core axis. Equal-size 2D grayscale cross-section images are then exported out for each cuboid using an equal lengthwise interval. To avoid errors in porosity calculations associated with small-scale heterogeneities along the core axis, the interval length (equivalently, the thickness of images) is kept at the minimum value equal to the voxel resolution. Excluding the non-rock portions at the bottom and top sides of the images, the remaining cross-section images are exported for each sub-volume.

Extracted images are first cropped to squares fitting the circular core cross-sections. The images are then segmented by applying a global threshold to differentiate the pore network from the solid matrix and obtain a stack of 2D binary images (Fig. 14). Accordingly, pixels on

the grayscale image with intensities smaller than the threshold value are generally characterized as pores and converted to black pixels on binary images, while those remaining above the threshold represent the solid rock matrix. The non-rock region surrounding the core is manually converted to solid material (white area) after segmentation and before exporting images as will be discussed in the following.

The choice of threshold values is however uncertain and thus intrinsically prone to user perception. Appropriate criteria should be applied to calibrate segmentation. On the one hand, a simple approach is to set the threshold value in a way that the measured total porosity equals independent, reference measurements (e.g., from helium or mercury porosimetry). Nevertheless, this method is well known to result in over-segmentation and unrealistic representation of the rock structure (Berg et al., 2018). On the other hand, the binarization scheme can be optimized through the comparison of a dry scan (air-saturated) image with that of water–saturated rock, as this technique eliminates the need for knowing the CT number of the solid matrix (Akin and Kovscek, 2003; Pini and Madonna, 2015).

Here a simplistic segmentation procedure is proposed since more accurate measurements on fluid–saturated samples are not available in this study. This approach includes the application of several, automatic algorithms that statistically find optimal threshold values from intensity histograms (indicating how many pixels of each image share the same gray level). The best thresholding method is selected by looking for visual similarities in sharp structural features between grayscale and binary images at several points along the core. The same algorithm is applied to all images for the sake of consistency. The sub-resolution pores may still result in a significant underestimation of the rock porosity, which is compensated by randomly distributing small pores on the rock matrix (explained in detail in the following sections). All image processing steps are done in an automated manner using the open-access java-based ImageJ software (Schneider et al., 2012) (Fig. 14). Note that image segmentation could have also been performed using MATLAB or other suitable programs (Abdulrahman and Varol, 2020; Rabbani and Ayatollahi, 2015). All binarized images from the core inlet to the core outlet are saved in 8-bit .tif format (Fig. 15), stored in a specified folder, and subsequently used as input files for the MATLAB code.

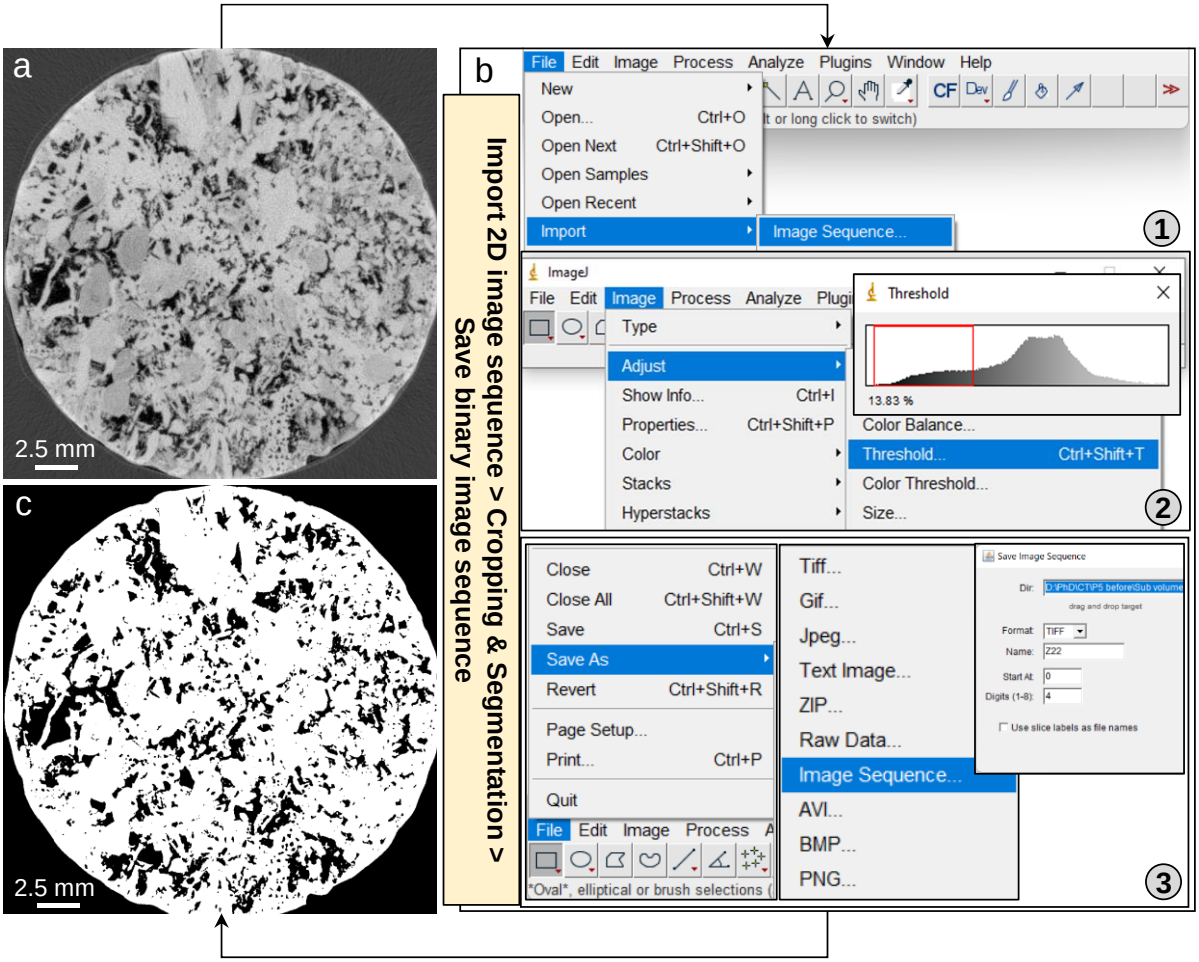

Figure 14. (a) A 2D grayscale cross-section image of the Pont Du Gard limestone, (b) flow diagram of adjusting segmentation threshold using the ImageJ software, and (c) extracted 2D binary images.

3.2.1.2. Domain discretization

To build a 3D porosity representation over the core domain using the obtained 2D binarized images, the domain is first discretized into grid blocks. The number of grids is selected based on the problem of interest. The larger the number (or the smaller the size) of grids, the closer the 3D representation to the actual rock microstructure, but the higher the computational cost. An arbitrary number of cells on the horizontal plane (Cell_X_No and Cell_Y_No) can be assigned but the number of cells along the core length (Cell_Z_No) equals that of horizontal segments for which binary images were acquired. This information together with binary 2D images is given as input to the code.

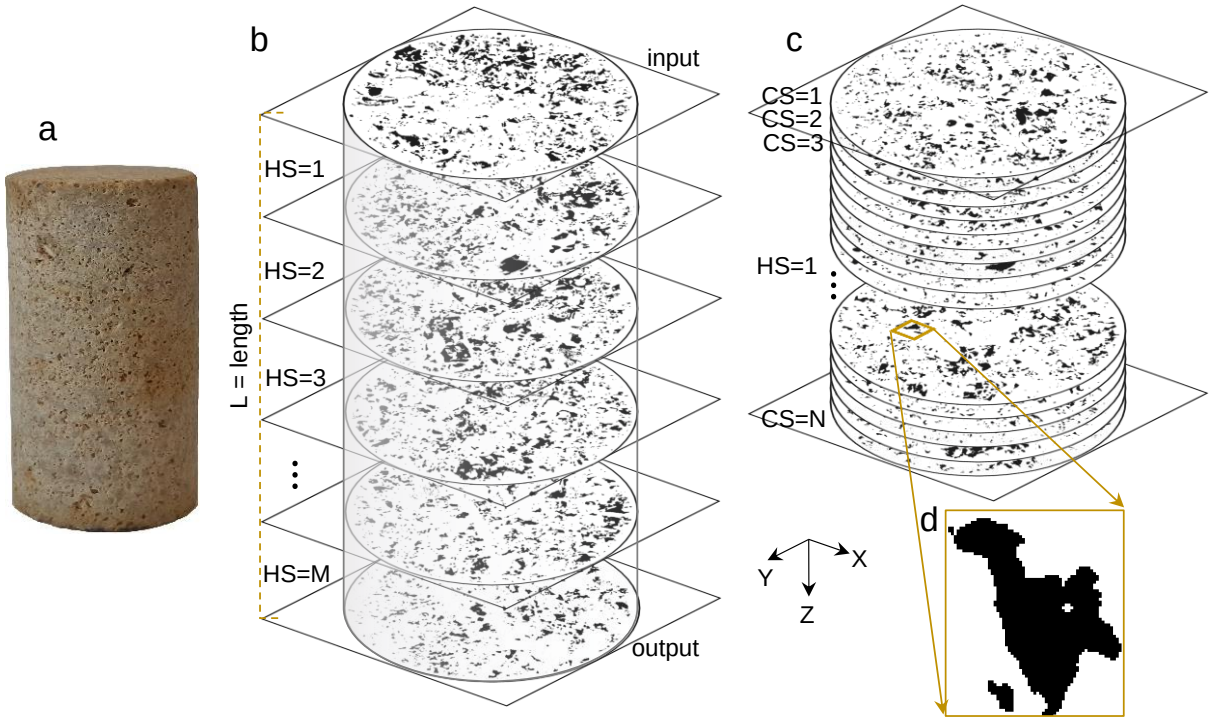

Figure 15. (a) Photograph of a sample of Pont Du Gard Limestone used in this study, (b) illustration of the horizontal segments (HS) along the core length, (c) 2D binary cross-section (CS) images in one segment, and (d) a magnified pixel-based illustration of a pore in a cross-section.

3.2.1.3. Porosity map reconstruction

The code first reads 2D binary images of the core from the inlet to the outlet but separately and consecutively for the sub-volumes along the core sample. These images are matrices (named IMG in the code) of the same size, in which the number of rows and columns are equal to the number of pixels in the Y and X directions (not necessarily the same), respectively. Each element within these matrices is either 0 or 1, referring respectively to black (pores) and white pixels (solid part) (Fig. 16). The obtained 3D array of binary images in this step is the basis of the 3D porosity reconstruction algorithm.

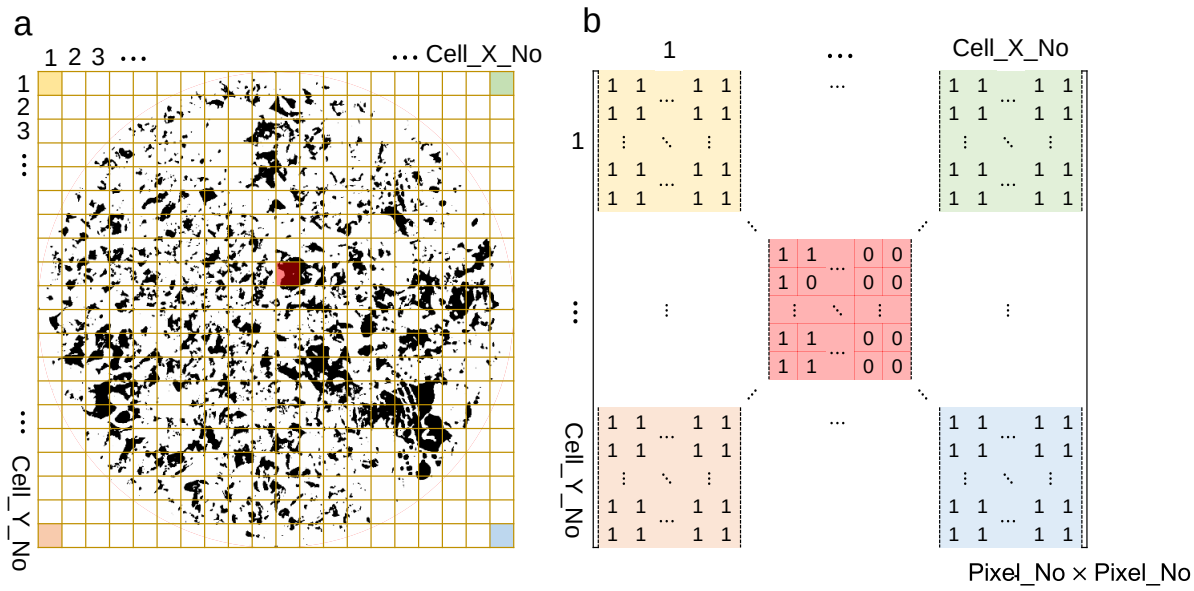

Figure 16. (a) Illustration of a discretized 2D binary image in X and Y directions and (b) the corresponding (0,1) matrix representation of the image with the size of Pixel_No × Pixel_No.

Figure 17 illustrates the entire workflow of the proposed algorithm, which includes six steps:

1. Locating the core cross-section in the image

Given that 2D binary images are square, a white marginal area surrounds the circular core cross-section of the core. Image processing starts with diagnosing the image pixels located on the core (named Section_Domain matrix in the code) from those pixels belonging to the marginal area. Assuming that the core cross-section is perfectly circular, the image pixels with a coordinate of (X,Y) belong to the rock only if $(X - X_0)^2 + (Y - Y_0)^2 \leq r^2$, where ($X_0$,$Y_0$) and r are the coordinate of the center and radius of the core, respectively. These pixels are set to 1 in the Section_Domain matrix while the pixels of the white marginal area are set to 0.

2. Calculating the average XMCT porosity of the core specimen

The porosity of 2D cross-section images (named Porosity_slice_total in the code) is calculated by dividing the number of pore elements by the total number of the core cross-section elements equal to 1 (Section_Domain elements). The numerator of this ratio is obtained by subtracting the sum of elements in the IMG matrix from the total number of pixels in each image. Subsequently, the average XMCT porosity of each sub-volume (Porosity_zgrid_total in the code) and the whole core (Porosity_total in the code) are derived by calculating the arithmetic mean of the porosity of all images in domains of interest. Note that the calculated porosity accounts for both connected and isolated pores.

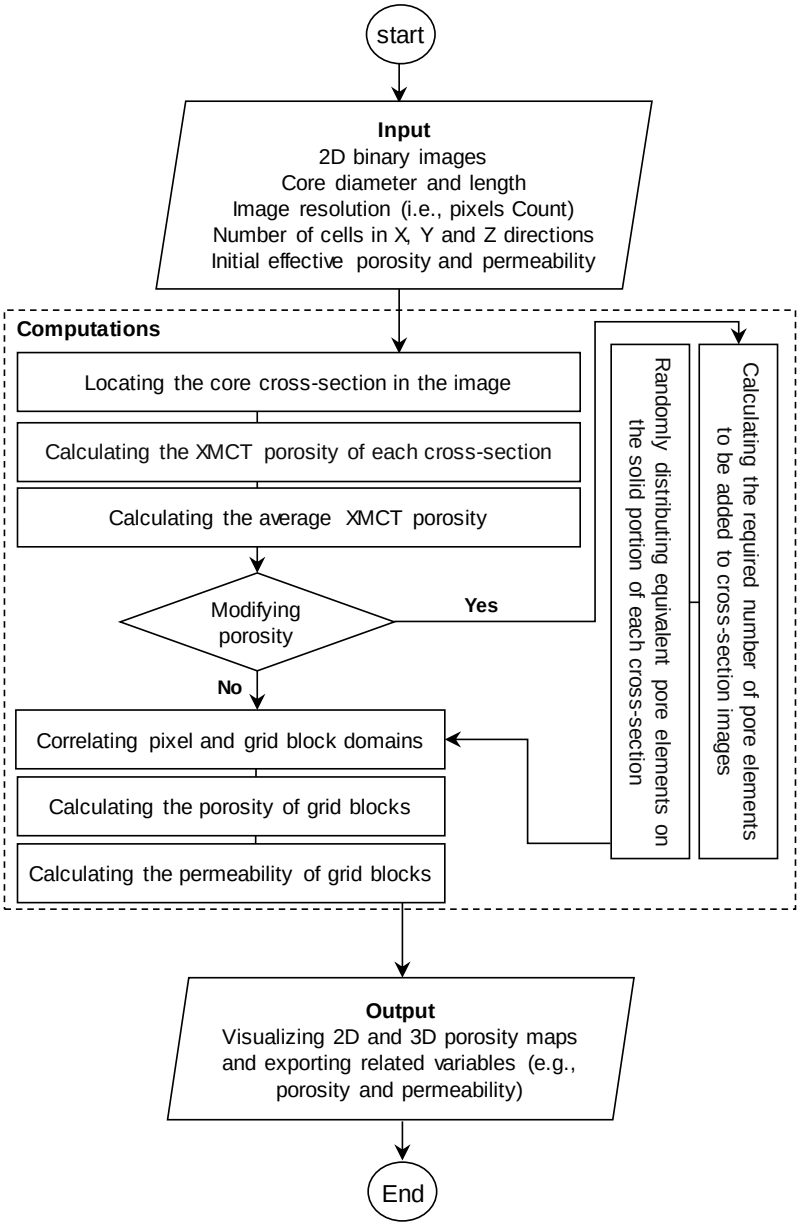

Figure 17. Workflow of the algorithm proposed to reconstruct 3D maps of porosity and associated parameters.

3. Modifying XMCT-based porosity (optional)

The average XMCT porosity previously may be considerably smaller than the core effective porosity (Por_Eff in the code). This difference is due to the XMCT resolution that limits the diagnosis of relatively small pores (Mayo et al., 2015; Ramandi et al., 2016). To use the 3D porosity maps in ETHMC numerical simulations, the effective porosity distribution should be first adopted. As explained above, this is done by adding the difference between the effective porosity and the average XMCT porosity, i.e., Porosity_Eff - Porosity_total, to the porosity of each cross-section image. Accordingly, the equivalent number of additional pore elements (Delta_Pixel in the code) is randomly distributed on the solid portion of the core cross-section in 2D binary images. The solid portion of the core cross-sections is identified by dot

multiplying (element by element multiplication) IMG and Section_Domain matrices, which returns a matrix of the same dimension with elements equal to 1 denoting the solid portion of the rock.

4. Correlating pixel and grid block domains

Whether or not the porosity modification step is implemented, the workflow is continued with correlating the pixel domain with the grid block (or cell) domain to reconstruct the grid-based porosity map across the core as these two domains have different dimensions. A matrix (Cell_Phi in the code) with the size of Cell_Y_No × Cell_X_No is created for each cross-section image (Fig. 16). Each cell in the Cell_Phi matrix is correlated with a number of pixels in the IMG matrix based on the relative size and coordinates of pixels in the cells.

5. Calculating the porosity of grid blocks

The porosity of each grid block is calculated using the same logic as step 2, i.e., by counting the number of the pore (0) elements and dividing it by the total number of elements occupying each cell. It is worth noting that the zero-porosity grid blocks, i.e., the white marginal area, surrounding the core form a non-reactive, impervious zone in reactive transport simulations and help impose appropriate boundary conditions. However, these elements are excluded for illustration purposes.

6. Visualizing and exporting the 3D porosity map

Following the calculation of porosity in grid blocks of each sub-volume, an output 2D array (Porosity_2D in the code) is defined to store (X,Y) coordinates of the cells' centers and their corresponding porosities. These matrices are then used to plot grid-based porosity distribution maps in each segment. The higher the Cell_Y_No and Cell_X_No, the more precise the porosity representation map. The compilation of porosity distribution matrices for 2D cross-sections (Porosity_2D in the code) is used to construct the 3D porosity map over the core. Several options are provided to create different 2D and 3D porosity maps. 3D arrays of all initial and adjusted binary images, porosity distribution on the grid domain, and grid information are exported for further analyses.

3.2.2. Application to Pont du Gard Limestone

3.2.2.1. Porosity distribution of the samples

The described image processing approach is implemented on a 3D XMCT data acquired from sample P_3 with a diameter of 25 mm and length of 44 mm. The grayscale image of the rock volume, already reconstructed from the X-ray CT radiographs, comprises 1400 × 1400 × 2300 voxels with a resolution of 20 μm represented by a dataset of 8-bit unsigned integers with an approximate size of 4.5 GB. The dataset is discretized into 20 sub-volumes along the core axis. 108 cross-section images at a minimum distance of 20 μm, i.e., the voxel resolution, are exported from each sub-volume. Cropping images to squares fitting the cylindrical core yields cross-sections containing 1250 × 1250 pixels, i.e, Pixel_No= 1250.

It is found that the Otsu thresholding technique (Otsu, 1979) returns more reliable realizations of the rock structure. This segmentation technique selects appropriate thresholds from gray-level histograms by minimizing the intra-class intensity variance or equivalently by maximizing the inter-class intensity variance

$$\sigma^2 = w_p \times w_s \times (\mu_p - \mu_s)^2 \tag{10}$$

where σ^2 is the inter-class variance and μ is the average values of intensities weighted by w as the number of pixels occupying the corresponding intensity range. Indices p and s point to pore (intensities smaller than the threshold) and solid (intensities larger than the threshold) classes, respectively.

As a representative example, a cross-section image of the core sample, the corresponding gray-level histogram and the evolving inter-class variance are illustrated in Figure 18. Two sharp peaks and a wide valley in between can be recognized in the histogram (Fig. 18c). One should notice that the first peak includes both the pore region and the non-rock region surrounding the core. If the marginal area was eliminated before segmentation, the CT porosity would be dramatically overestimated (portions of the solid background are wrongly counted as the pore). In particular, it is widely stated that the Otsu approach performs well when the histogram features a bimodal distribution with sharp peaks (Kittler and Illingworth, 1985). The inter-class variance peaks at 109, meaning that intensities larger than this threshold serve as the solid rock mineral whereas the smaller gray levels point to either pores or the surrounding non-rock region. Each binary image (Fig. 18b) of the studied sample has a size of 1.49 MB.

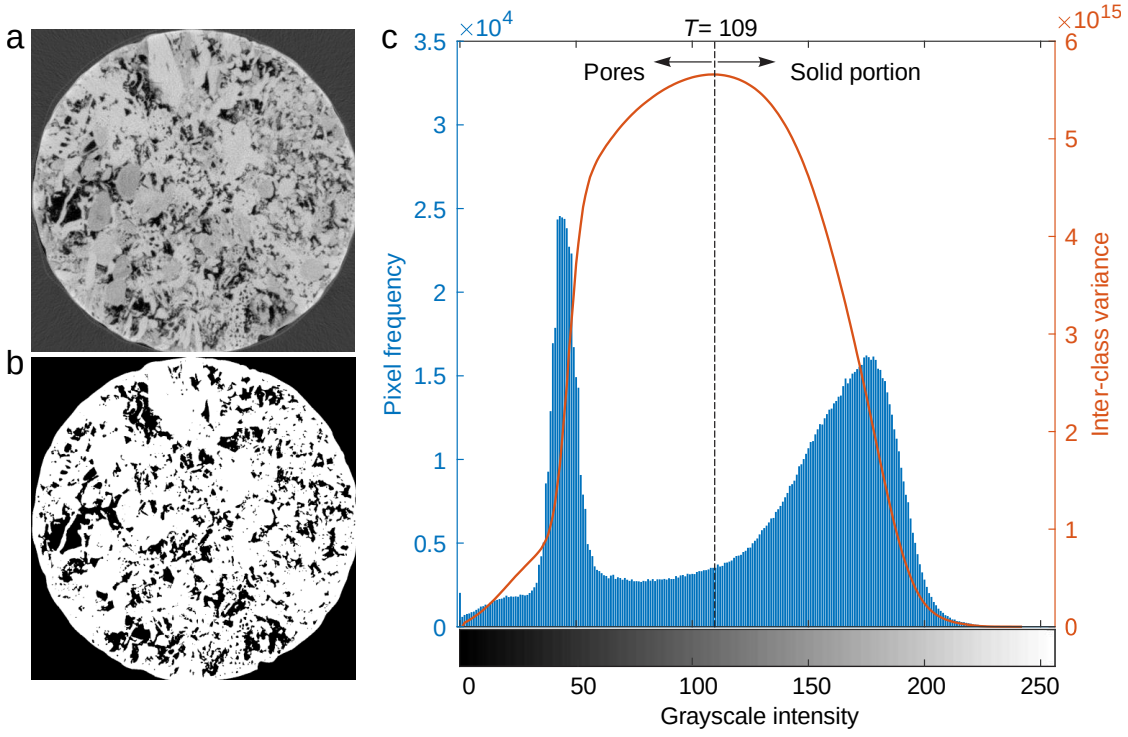

Figure 18. (a) An 8-bit gray-level image from the XMCT data of sample P_3 (Pont Du Gard Limestone), (b) the corresponding binary image, and (c) the segmentation procedure based on the Otsu method.

The core domain is uniformly discretized into 20 × 20 × 20 grid blocks, corresponding to a grid width of 1.25 mm in the X and Y directions and a length of nearly 2.2 mm in the Z direction. Each grid thus contains 62 × 62 × 108 voxels at the original CT resolution. Figure 19 shows the variation of computed XMCT porosity along the length of the limestone sample, highlighting the heterogeneous nature of the rock structure. The average porosity over the grid blocks satisfactorily captures the microstructural patterns rendered by the high-resolution cross-section images. The initial CT porosity (blue curves in Fig. 19) varies from 0.1 to 0.16 with an average of 0.13, meaning that the imaging approach underestimates by 0.11 the bulk rock porosity measured by bulk porosimetry. The observed porosity layering pattern is replicated by the adjusted porosity (brown curves in Fig. 19) owing to the adopted porosity updating strategy of adding uniformly the porosity difference of 0.11 to all cross-section images. It should be noticed that comparison with the effective rock porosity is subject to the assumption that the volume fraction of isolated pores in the Pont Du Gard Limestone is negligible.

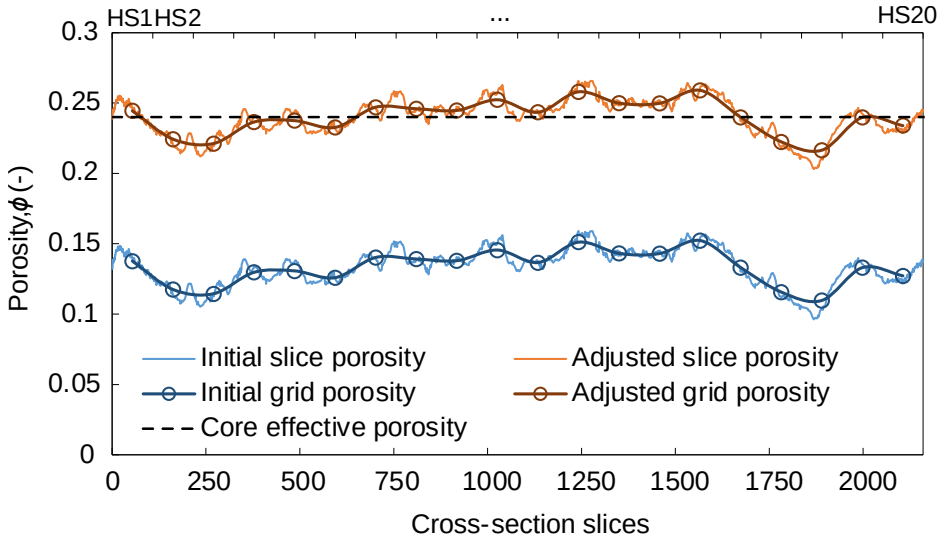

Figure 19. Distribution of initial and adjusted XMCT porosity along sample P_3 (Pont Du Gard Limestone).

Figure 20 illustrates the porosity adjustment procedure for a single image with general validity for the whole sample. Adding the pores randomly at the highest resolution of pixel size results in uniform porosity enhancement across the rock slice (compare the subplots in the two rows of Fig. 20). While image processing initially recognizes a solid crystalline texture in several grids (subplots on the top row), adjusted images point to a porous background accounting for sub-resolution porosity, i.e., pores < 20 μm (subplots on the bottom row). The grid-based porosity distribution maps with the reference size of 20 × 20 well reproduce structural features observed in binary images, importantly the distribution of large pores that could contribute to flow localization. Further refinement of the grid network (40 × 40) significantly increases the porosity distribution accuracy although at the expense of increasing the computational cost for numerical simulations built on the extracted porosity maps.

The heterogeneous distribution of porosity over the examined core can be also inferred from the 3D porosity map constructed by image processing and the corresponding frequency distribution (Fig. 21). The extracted porosity map yields a mean value of 0.217 with a standard deviation of 0.102. The mean porosity of the digital rock at a large grid size is reasonably smaller than the effective rock porosity as the grid domain has a square-edged shape that deviates from the cylindrical core shape and adds to the real bulk rock volume while the pore volume remains the same as the real core. Mean digital rock porosities of 0.227, 0.231, 0.233, and 0.235 were calculated for 40 × 40, 60 × 60, 80 × 80, and 100 × 100 grid schemes perpendicular to the core axis, respectively. The larger the number of grids, the closer the grid domain shape to a cylinder and thus, the more accurate the calculated mean grid porosity.

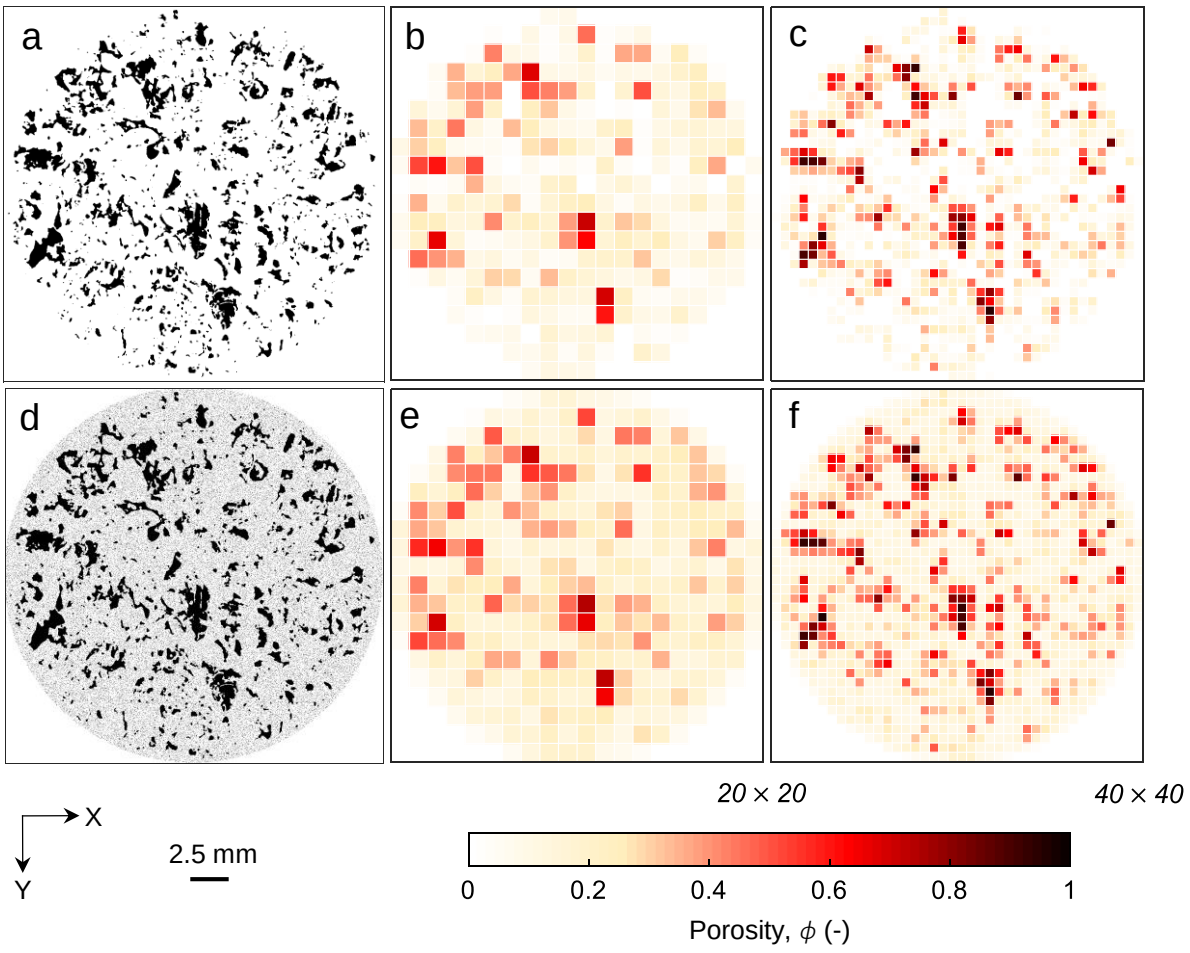

Figure 20. 2D illustrations of: (a) a raw binary cross-section image, (b) a reconstructed grid-based porosity map with a size of 20 × 20 and (c) a reconstructed grid-based porosity map with a size of 40 × 40. Similar plots (d, e, and f) provided for the cross-section after adjusting the XMCT porosity to effective porosity from mercury porosimetry.

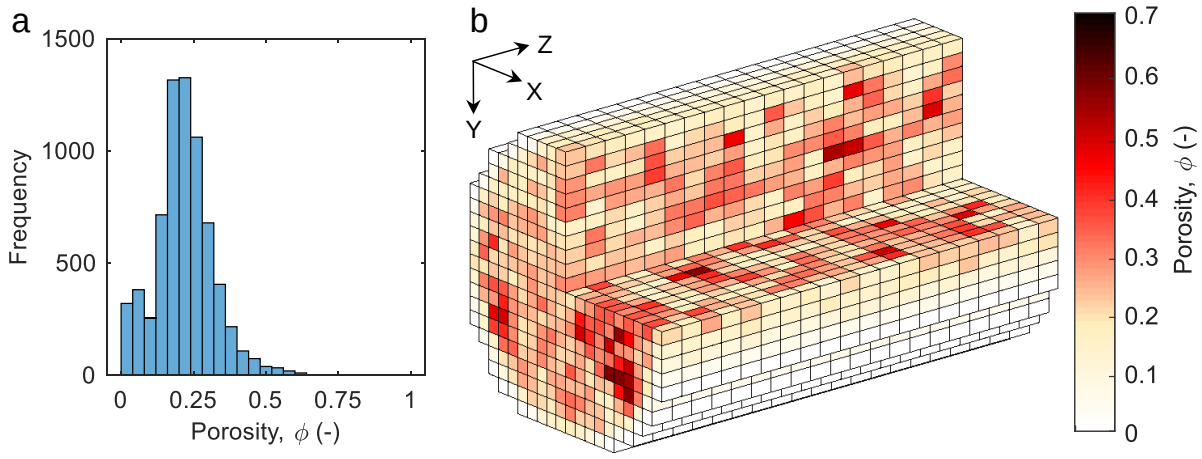

Figure 21. Heterogeneous distribution of porosity over the examined core: (a) histogram showing the grid-based distribution of total porosity obtained from image processing and (b) 3D porosity map reconstructed over sample P_3 (Pont Du Gard Limestone).

The same workflow was implemented on image data sets of the intact sample P_5 and also on the chemically-altered samples to interpret dissolution patterns and make comparisons with model predictions on the continuum domain (see Section 3.3 for model description).

3.2.2.2. Code Performance

The described image processing steps were implemented in MATLAB version 2010b on a quad-core Intel Core i7-4790 (up to 3.6 GHz) with a maximum of 8 GB RAM. The total runtime was 211 s, divided by 57.7 s for importing and calculating porosity for all images, 130.2 s for adjusting the calculated porosity to the effective porosity obtained from mercury porosimetry, 6.4 s for building porosity maps on the grid block domain of 20 × 20 size and 16.8 s for calculating permeability maps (as described in the Discussion Section) and exporting data for further analyses. MATLAB used a total memory of less than 750 MB to perform the whole calculations. The code can be further optimized to conserve more memory and make processing larger datasets affordable with low-power computational resources.

3.3. Reactive transport modeling

Numerical simulations of the percolation experiments were performed for a quantitative interpretation of the experimental results and a better understanding of the mechanisms governing the acidic fluid interactions. Two experiments with samples P_3 (CO_2-saturated water) and P_5 (HCl solution) run for 28 days were selected. Reproduction of the experimental observations (outflow calcium concentration, changes in porosity and permeability and formation of dissolution patterns) is used to calibrate and validate the numerical simulations. Figure 22 shows an overview of the used workflow that is explained in detail in the next sections.

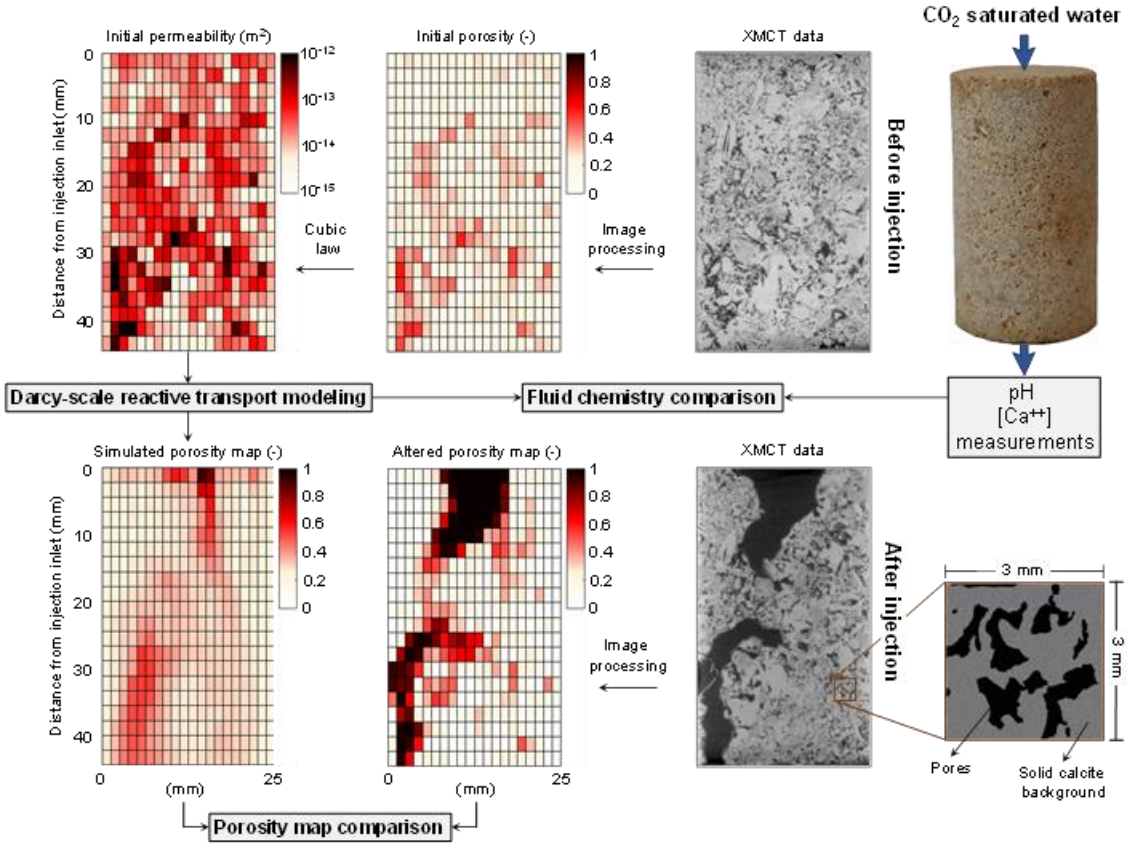

Figure 22. Overview of the workflow and data used. The grayscale images illustrate center vertical XMCT scans of a specimen before and after flooding with acidic solutions. To the left of the XMCT data before injection are the resulting initial porosity and permeability maps from image processing and a power-law porosity-permeability relationship, respectively. To the left of the XMCT data after injection are dissolution patterns inferred directly from image processing or indirectly from continuum-scale reactive transport modeling, respectively (illustrating an example for the specimen flooded with CO_2-rich water). Configuration of the best predictive model is achieved through comparison between model predictions and measurements of the effluent chemistry evolution.

3.3.1. Description of the reactive transport code

The flow-through experiments were simulated using the CrunchFlow code (Steefel and Molins, 2009), a software package for multicomponent multidimensional reactive transport in porous media. CrunchFlow numerically solves the advection-dispersion-diffusion equations using the finite difference method (Steefel et al., 2015). Mineral reactions are described using kinetic rate laws, initial mineral surface area, and several reaction rate parameters have to be fed into the code as inputs. For these simulations, the reaction rate laws used are in the form of

$$R_m = -A_m \sum_{terms} k_m \left(\prod_i a_i^{n_i}\right) f_m(\Delta G) \tag{11}$$

where R_m is the reaction rate ($R_m < 0$ dissolution, and $R_m > 0$ precipitation) for a given mineral, i.e., calcite here (mol m^{-3}_{rock} s^{-1}), A_m is the mineral surface area ($m^2_{mineral}$ m^{-3}_{rock}), and $a_i^{n_i}$ is the term describing the effect of species i (e.g., H^+ denoting the effect of pH) on the rate. The summation term specifies that several parallel rate laws may be used to describe the rate dependence on the pH or other species. k_m is the reaction rate constant (mol $m^{-2}_{mineral}$ s^{-1}) at the temperature of interest, i.e., T = 60 ºC (333.15 K), and is calculated from the measured rate constant value at standard temperature (k_{25}, see Table 4 for the utilized values) using the Arrhenius law

$$ln\left(\frac{k_m}{k_{25}}\right) = -\frac{E_a}{R}\left(\frac{1}{T} - \frac{1}{298.15}\right) \quad (12)$$

where E_a (kcal mol^{-1}) and R (kcal mol^{-1} K^{-1}) are the activation energy and ideal gas constant, respectively.

The $f_m(\Delta G)$ function in Eq. (11) is written as

$$f_m(\Delta G) = \left(1 - \left(IAP/K_{eq}\right)^{m_2}\right)^{m_1} \quad (13)$$

where ΔG is the Gibbs energy of reaction (J mol^{-1}), the term IAP stands for the solution ionic activity product, K_{eq} is the equilibrium constant for the dissolution/precipitation reaction, and m_1 and m_2 are empirical exponents. The equilibrium constant is temperature-and pressure-dependent (Brantly et al., 2008). Thus, values at representative experimental conditions are used (Table 4).

The code solves for the flow field, concentrations of aqueous species, and mineral volume fractions in all grid blocks of the numerical domain. The stoichiometric coefficients that were taken from EQ3/6 database (Wolery et al., 1990) were included in the CrunchFlow code. Activity coefficients were calculated using the extended Debye Hückel formulation (b-dot model) with parameters obtained from the EQ3/6 database included in CrunchFlow. The calculated changes in mineral volume fraction resulting from mineral dissolution/precipitation are used to update the porosity field at the end of each numerical time step. Appropriate relations are used to update the permeability and surface area maps following porosity changes (see Section 3.3.4 for further details), which in turn affect the flow and reactive transport processes.

3.3.2. Model setup

Each core of 25 mm in diameter and 44 or 78 mm in length is considered as a cylinder surrounded by a non-reactive substance, i.e., pure calcite with small porosity, ultralow permeability, and zero surface area, to facilitate simulations and their interpretation in a

rectangular cube domain. The rock domain was discretized into 20 × 20 × 20 grid blocks (each 1.25 × 1.25 × 2.2 mm^3) and 20 × 20 × 22 grid blocks (each 1.25 × 1.25 × 3.54 mm^3) for *P_3-CO_2-28* and *P_5-HCl-28* experiments, respectively (Fig. 22). To ensure uniform distribution of fluid flow at the inlet of the specimens, a fictitious inlet slice of 20 × 20 grid blocks was used with the same size as the nominal grid size in the rock domain. This slice is assumed to be composed of pure calcite with porosity equal to the average porosity of the sample, very large permeability (10^{-9} m^2), and zero surface area. As a result, continuum numerical models of the *P_3-CO_2-28* and *P_5-HCl-28* experiments consist of a total number of 8400 and 9200 elements, respectively. Details on the grid block size and numbers are given in Table 3.

The initial and boundary conditions used in the numerical model replicate those imposed experimentally with (1) no-flow lateral boundaries, (2) constant flow rate at the inlet, and (3) constant pressure at outlet boundaries (Fig. 23). The initial pressure in the whole domain was set to 100 and 1 bar for *P_3-CO_2-28* and *P_5-HCl-28* experiments, respectively. Transport of chemical species is controlled by advection and diffusion, with a uniform diffusion coefficient of 10^{-9} m^2 s^{-1} for all species. The longitudinal dispersivity was set to 2.5 × 10^{-3} m equal to 0.1 of core diameter, and the transversal dispersivity was set to one-tenth of the longitudinal dispersivity (Smith and Chapman, 1983; Park and Lee, 2021).

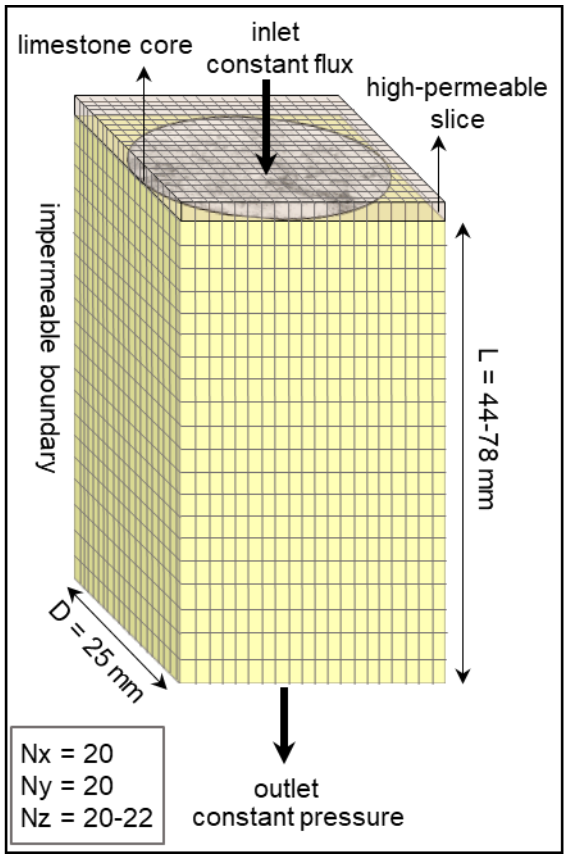

Figure 23. 3D conceptual model, numerical discretization and boundary conditions of flow domain used in the reactive transport simulations.

Table 3. Data of numerical discretization and flow properties of different zones used in 3D numerical simulations.

	P_3-CO_2-28	***P_5-HCl-28***
sample dimensions		
diameter (mm)	25	25
length (mm)	44	78
discretization		
total number of elements in X - element size (mm)	20 – 1.25	20 – 1.25
total number of elements in Y - element size (mm)	20 – 1.25	20 – 1.25
total number of elements in Z - element size (mm)	21 – 2.2	23 – 3.54
zones		
Pont du Gard core	limestone	limestone
initial average permeability (m^2)	2.54×10^{-14}	3.76×10^{-14}
initial average porosity (%)	23.8	28.5
non-reactive surrounding	calcite	calcite
initial permeability (m^2)	1.0×10^{-22}	1.0×10^{-22}
initial average porosity (%)	5.8	5.8
highly permeable inlet	calcite	calcite
initial permeability (m^2)	1.0×10^{-9}	1.0×10^{-9}
initial average porosity (%)	23.8	28.5

3.3.3. Rock and solution compositions

Table 4 lists the initial volume fraction of calcite as the only mineral constituting each core, i.e., $1 - \phi_b$, reaction rate parameters, and apparent activation energies taken from rate laws for calcite dissolution (Palandri and Kharaka, 2004; Xu et al. 2012). Equilibrium constants and stoichiometric coefficients for calcite dissolution reaction were taken from the PhreeqC code (v3.6.2). Initial compositions, i.e., aqueous species, and the pH of injecting solutions are listed in Table 4 as well. The initial pore fluids in both experiments were assumed to be at equilibrium with the calcite phase at experimental pressure and temperature conditions.

3.3.4. Constructing the initial permeability map

High-resolution XMCT images with a voxel resolution of 20 μm and 21 μm for dry *P_3* and *P_5* specimens, respectively, have been used to capture the effects of pore space heterogeneities in the continuum model. The initial permeability map of the specimens was constructed by applying an explicit power-law permeability-porosity relationship with an exponent of 3 (initial permeability in Fig. 24; see Section 3.3.5 for details). The generated permeability map for sample P_3 yields a mean value of 4.7×10^{-14} m^2 with a standard deviation of 1.27×10^{-13} m^2 (Fig. 24).

To assess the validity of the initial permeability maps, these maps were used to simulate a water percolation experiment conducted on sample *P_3* prior to CO_2-saturated water injection. In this case test, the water was injected into the core at a constant flow rate of 0.15 mL min^{-1} for 3 h (≈ 5 pore volumes). The differential pressure ΔP across the core after reaching steady state conditions was 0.1 bar equal to the resolution of the pressure transducers. By imposing the

constant flow rate at the inlet, the simulation returns a ΔP = 0.089 bar across the specimen that in general agrees with the measured ΔP. In addition, putting the flow rate and numerically measured ΔP into Darcy's law (Eq. 55) returns a bulk rock permeability of 2.55×10^{-14} m^2 that is well consistent with the experimentally measured value of 2.54×10^{-14} m^2 (Table 5). The small absolute relative error of 0.03% in predicting the bulk rock permeability indicates (1) the ability of the constructed permeability map to effectively reproduce the Darcy-scale single-phase flow behavior of the core under intact conditions and (2) the validity of the described approach to develop the digital rock model. Similar observations were made for the generated permeability map of sample P_5.

Table 4. Reaction parameters, calcite volume fraction in cores and chemical composition and pH of input solutions.

	P_3-CO_2-28	***P_5-HCl-28***
calcite volume fraction	0.762	0.715
input solution		
pH	3.13	3.13, 2.66
(primary) species concentrations (mol kg^{-1})		
[H^+]	10^{-pH}	10^{-pH}
[Cl^-]	0.0	7.58×10^{-4}, 2.1×10^{-3}
[CO_2(aq)]	1.03	equilibrium with atmospheric CO_2
reaction	$CaCO_3(s) + H^+ \Leftrightarrow Ca^{2+} + HCO_3^-$	
reaction parameters		
	p = 100 bar	p = 1 bar
log K_{eq} (60 °C)	-8.78	-8.88
	acidic conditions	neutral conditions
log k_{25} (25 °C) (mol m^{2}mineral s^{-1})	-0.3	-5.81
Ea (kcal mol^{-1})	3.44	5.62
$a_{H^+}^{n_{H^+}}$	1.0	-
m_1	3.0	3.0
m_2	1.0	1.0

*ideal gas constant (R =1.987 × 10^{-3} kcal mol^{-1} K^{-1})

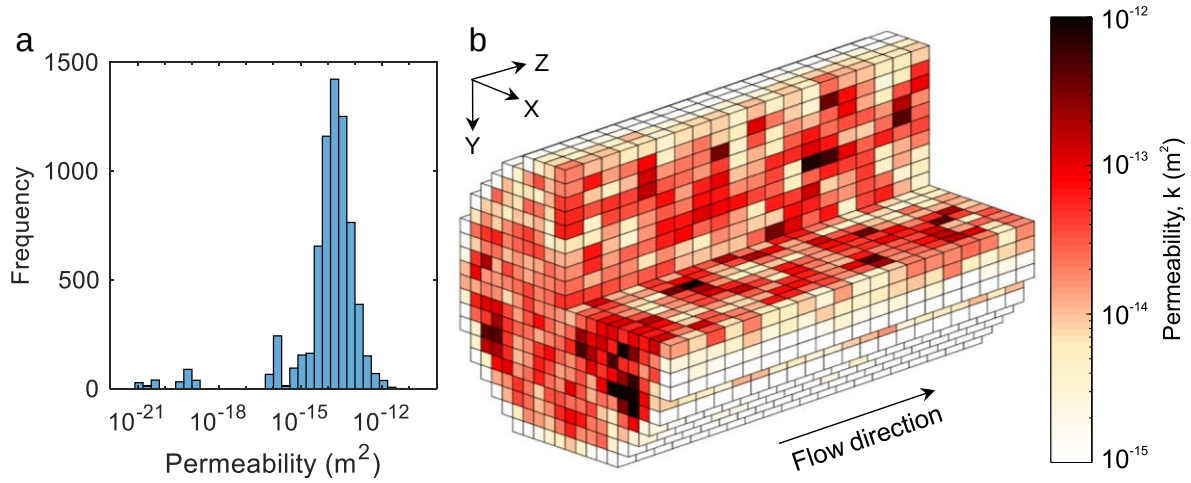

Figure 24. Permeability for sample P_3 (Pont Du Gard Limestone): (a) histogram and (b) 3D map of the grid-based distribution of permeability.

3.3.5. Porosity-permeability-surface area relationship

The porosity-permeability relationship that couples heterogeneities in pore size distribution and flow field, is a critical factor in the modeling of reactive flow at the continuum scale. In this study, a power-law relationship based on the original Kozeny-Carman equation (Hommel et al., 2018) is used to calculate the time-dependent variation of the permeability with porosity due to the mineral dissolution

$$k/k_0 = (\phi/\phi_0)^n \cdot ((1-\phi_0)/(1-\phi))^2 \quad (14)$$

where ϕ and k are porosity and permeability for each grid cell, respectively, and ϕ_0 and k_0 are reference porosity and permeability values. The exponent n is an empirical parameter. By setting n = 3, the equation reduces to the original form of the Kozeny-Carman equation, which was assumed to apply to intact samples and was used for building the initial permeability maps. During the initialization phase, ϕ_0 and k_0 respectively refer to the bulk porosity and permeability of the specimens measured experimentally. During the reactive flow phase, the exponent n may deviate from the initial value. Indeed, different n values were assigned to numerically reproduce the outflow chemistry variation (Fig. 22). In this phase, ϕ_0 is the bulk porosity of the specimen, and k_0 equals the initial values in each grid block of the reconstructed permeability map. Accordingly, the pore structure heterogeneity exclusively manifests in the permeability map. The full range of permeability in grid blocks and its evolution with porosity changes for sample P_3 are illustrated in Figure 24. The same trend exists for sample P_5.

Two distinct simple relations were used to calculate changes in mineral surface area A_m (m^{-1}), proportional to porosity evolution caused by mineral dissolution and precipitation

$$A_m = A_{m_0}(\phi/\phi_0)^{2/3}((1-\phi)/(1-\phi_0))^{2/3} \quad \text{mineral dissolution} \quad (15)$$

$$A_m = A_{m_0}(\phi/\phi_0)^{2/3} \quad \text{mineral precipitation} \quad (16)$$

where ϕ and A_m are the porosity and mineral surface area for each grid cell, respectively, and ϕ_0 and A_{m_0} are initial bulk porosity and surface area values. Several approaches can be employed to adjust A_{m_0} using data on either grains or pore geometry (Brosse et al., 2005; Lai et al., 2015; Al-Khulaifi et al., 2017; Garcia-Rios et al., 2017) or using phenomenological or empirical laws (Noiriel et al., 2009). In this study, however, the initial surface area was treated as a fitting parameter. A_{m_0} was changed with n = 3 to match the effluent Ca concentration of 1-2 days of injection. It is assumed that over this period, the dissolution front is not yet penetrated deep enough into the specimen and thus not affected by potential localization of flow and the choice of power n. As a result, A_{m_0} = 59 m^{-1} for the CO_2 experiment and A_{m_0} = 55 m^{-1} for the HCl experiment were obtained and used in the numerical simulations. Note that the reactive surface area of each grid block may decrease following mineral precipitation or initially increase, reach a peak and then decline following dissolution-induced porosity enhancement (see the example for sample P_3 in Fig. 25). As the surface area approaches zero for the two extreme scenarios of ϕ= 0 and ϕ= 1, Eq. (15) and (16) ensure that no further precipitation and dissolution take place, respectively.

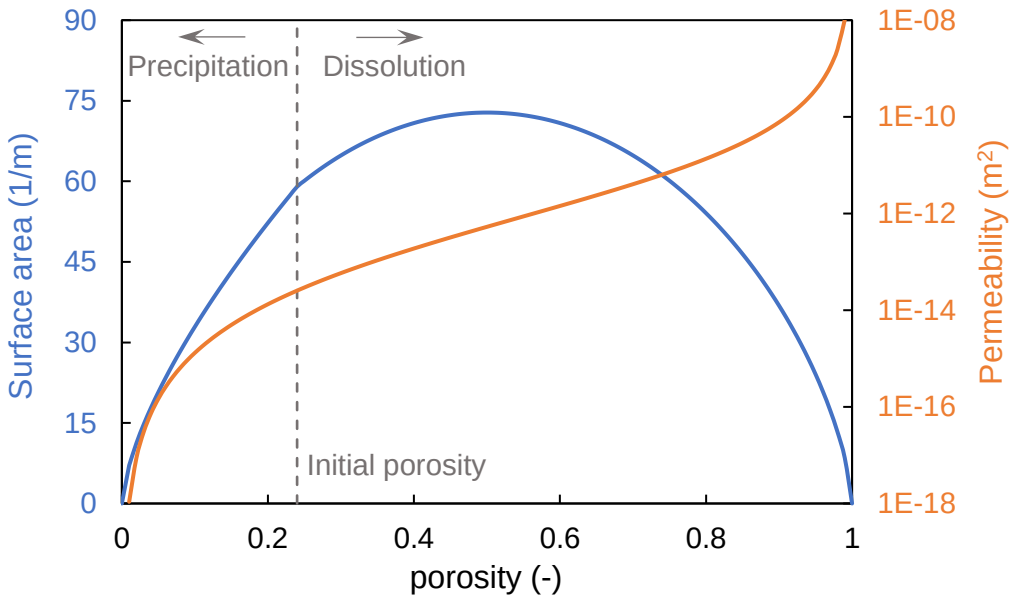

Figure 25. Possible range of changes in the reactive surface area and permeability of each numerical grid block as a result of chemically-induced changes in porosity.

Chapter 4

Results

This chapter brings together (1) experimental observations on the evolution of hydromechanical properties of samples from the Pont du Gard Limestone upon interactions with CO_2-saturated water and HCl solutions, and (2) results from the numerical simulation of the percolation experiments. Experimental observations include the evolution of outflow fluid chemistry, pore structure, porosity, pore size distribution, permeability, as well as ultrasonic velocity, and stiffness and strength properties of the rock. Numerical simulations describe quantitatively the dissolution processes take place during the experiments. Comparison between numerical simulation results with experimental observations is made to calibrate and validate numerical simulations.

4.1. Experimental results

4.1.1. Acid-induced dissolution

Figure 2 shows the variation in the output Ca concentration ($[Ca]_{output}$) over time in the experiments. In all experiments, $[Ca]_{output} > 0$, indicating a continuous calcite dissolution. The increase in $[Ca]_{output}$ is up to more than 20 times higher in the CO_2-saturated water experiments than in the HCl ones (Fig. 26a, b), even though the pH of the injected solution is about the same ($pH \approx 3.13$).

The variation in $[Ca]_{output}$ depends on the injected acidic solution. The injection of CO_2-saturated water results in three stages of calcite dissolution: (1) an initial peak of $[Ca]_{output}$ associated with the propagation of a calcite dissolution front along the cores; (2) a subsequent sharp decrease in $[Ca]_{output}$ owing to the formation of preferential flow paths, which reduce the accessible reactive surface area with time, and (3) a constant concentration that results from a complete localization of flow and dissolution and a constant reactive surface area. The initially homogenous dissolution in the pore network only lasts for a few hours. The small increase in $[Ca]_{output}$ between 2 and 4 days in the *P_3-CO_2-28* experiment arises from the first attempts to find an appropriate injection rate and not from an evolving dissolution pattern. The time required for the dissolution front to break through the cores varies between 4 days (*P_2-CO_2-14*) and nearly 16 days (*P_3-CO_2-28*). This difference could be attributed to the initial heterogeneity of the specimens that control the evolution of the dissolving pore network as discussed in Section 4.1.2. Similar trends for the variation in $[Ca]_{output}$ and reactive surface area due to

localized dissolution in carbonate-rich rocks percolated with CO_2-saturated solutions have been previously observed (Garcia-Rios et al., 2017; Leger et al., 2022; Luquot and Gouze, 2009).

In the HCl experiments (*P_4-HCl-14* and *P_5-HCl-28*), $[Ca]_{output}$ is fairly constant during the injection (Fig. 26b). This behavior is associated with a constant calcite dissolution rate characterized by an invariant surface area. It should be noted that in the last eleven days of the *P_5-HCl-28* experiment, a more acidic HCl solution (pH ≈ 2.66) was injected. The decrease in pH by 0.47 units sharply increased the calcite dissolution rate, resulting in a steady-state $[Ca]_{output}$ (0.021 M) that is a factor of ≈ 3 higher than the previous one (0.00075 M) (Fig. 26b), and consistent with the calcite dissolution rate law ($R = k \cdot a_{H+}$ (Atanassova et al., 2013)). Nevertheless, calcite dissolution caused by a more acidic HCl solution was still much slower than that achieved by CO_2-saturated solutions.

4.1.2. Transport properties and pore structure evolution

4.1.2.1. Change in porosity and dissolution patterns

Table 5 lists the porosities (ϕ) of all tested specimens (P_1-P_5) obtained from different techniques before and/or after the experiments. In all experiments, porosity increase is observed due to calcite dissolution and is higher in the CO_2-injected cores, where the greatest value ($\Delta\phi_{bulk}$ = 9.7%) is obtained in the longest run (P_3-CO_2-28). $\Delta\phi_{bulk}$ values agree well with those calculated using $[Ca]_{output}$ ($\Delta\phi_{[Ca]out}$). Porosities obtained by XMCT are comparatively smaller: ϕ_{XMCT} of the intact cores are between 2.5 and 5.4 times smaller than ϕ_{bulk}. There is, therefore, a considerable fraction of relatively small pores (< 30-40 μm) that lie below the XMCT resolution limit and cannot be accounted for. XMCT, however, does provide porosity evolution (ϕ_{XMCT}) along the cores (Fig. 27) and $\Delta\phi_{XMCT}$ values are comparable to those measured by weight-based measurement or solution chemistry. Likewise, MICP underestimates porosity (ϕ_{MICP} is between 1.2 and 1.7 times smaller than ϕ_{bulk}) since pores with radii > 88 μm (upper bound detection limit in the utilized porosimeter) make an important contribution to the total pore volume.

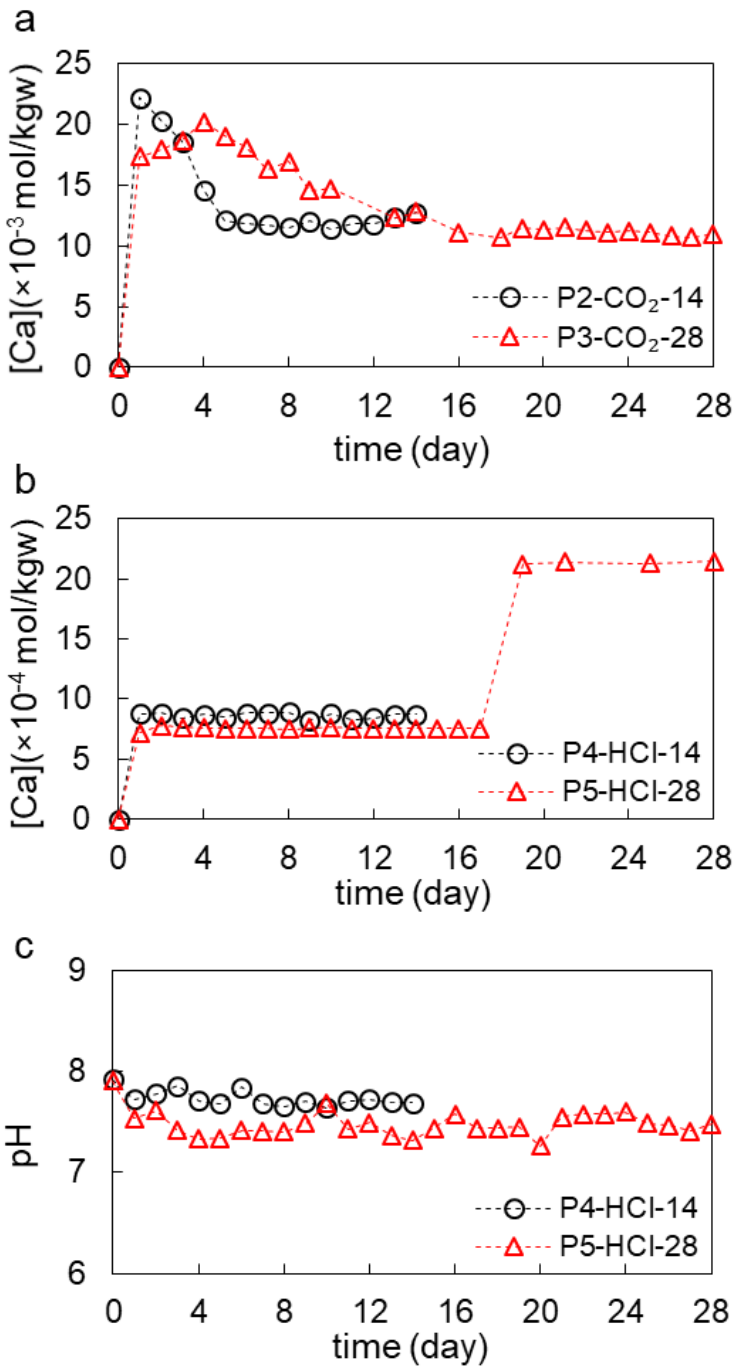

Figure 26. Variation in water chemistry as a function of time: $[Ca]_{output}$ for (a) CO_2-saturated water experiments and (b) HCl solution experiments and (c) output pH in the HCl experiments.

Figure 27 depicts ϕ_{XMCT} profiles along the flow direction in the cores. The initial average porosity of the cores varies between 4.8 and 9.5 (Table 5). Porosity values also change along the length of the cores implying the heterogeneous nature of the Pont du Gard Limestone. However, final porosity profiles represent more non-uniform distribution along the altered cores. Moreover, the type of acid largely affects the porosity evolutions. In the CO_2 injection experiments (*P_2-CO_2-14* and *P_3-CO_2-28*), there is a sharp increase in average porosity near the inlet (16.1% and 57.5% in the first 5 mm of P_2 and P_3, respectively) whereas a moderate

increase (4.1-5.2%) occurs in the remaining part of the cores (Fig. 27a, b). In contrast, in the HCl injection experiments (*P_4-HCl-14* and *P_5-HCl-28*), porosity only increases at the inlet as $\Delta\phi_{XMCT} < 0.5\%$ in the remaining part of the cores (Fig. 27b, d).

Table 5. Porosity and permeability calculated using the intact and altered cores. ϕ_{bulk}: porosity calculated by weight measurement.

sample	state	ϕ (%)			$\Delta\phi$			permeability [m^2]
	intact/altered	bulk	XMCT	MICP	bulk	ICP	XMCT	
P_1	intact	26.5	-	20.42	-	-	-	2.1×10^{-13}
P_2-CO_2-14	Intact	28.5	6.6	-	5.1	4.7	5.0	8.1×10^{-14}
	altered	33.6	-	-				8.3×10^{-11}
P_3-CO_2-28	Intact	23.8	9.5	-	5.9	5.5	4.0	2.5×10^{-14}
	altered*	29.7	-					3.6×10^{-11}
	altered	33.5	-	-	9.67	9.31	13.78	5.5×10^{-11}
P_4-HCl-14	intact	26.0	4.8	-	0.3	0.3	0.6	1.0×10^{-13}
	altered	26.3	-	16.11				3.2×10^{-13}
P_5-HCl-28	intact	28.5	8.0	-	0.9	0.8	1.7	3.8×10^{-14}
	altered	29.4	-	25.4				2.7×10^{-13}

*measured after 14 days of injection

The porosity profiles reveal the formation of distinct dissolution patterns caused by the different acid solutions. Two-dimensional porosity maps of the *P_3* and *P_5* cores before and after the experiments display the resulting porosity variation and dissolution patterns (Fig. 28). Interaction with HCl induces calcite dissolution only at the inlet (Fig. 28a, b), yielding a compact dissolution. This dissolution pattern is consistent with the variation in $[Ca]_{output}$ (*P_5-HCl-28* in Fig. 26b) as the HCl solution contacts a nearly constant reactive surface area throughout the experiment.

In the CO_2-water saturated experiment (*P_3-CO_2-28*), calcite dissolution led to wormhole formation (Fig. 28c,d). A three-dimensional (3D) XMCT reconstruction of porosity shows the wormhole morphology that consists of a long channel with fine ramifications (Fig. 28e). Wormhole formation is consistent with the decrease in $[Ca]_{output}$ before steady state (Fig. 26a). As calcite dissolves, wormhole propagation restricts the fluid-rock interaction to the channel, reducing the effective accessible reactive surface area. When the channel reaches the outlet, the interaction takes place only at the wall of the wormhole, yielding a steady-state Ca release. Similar but less pronounced patterns developed in the shorter *P_2* and *P_4* experiments. Moreover, it should be noted that initial heterogeneities are responsible for the different timing and shape of the dissolution channels in the *P_2* and *P_3* cores reacted with CO_2-saturated water. It appears that chemical reactions localized in a narrower channel in *P_2* lead to a dominant wormhole

(Fredd and Fogler, 1998) with a smaller volume and a faster wormhole breakthrough (Fig. 26a).

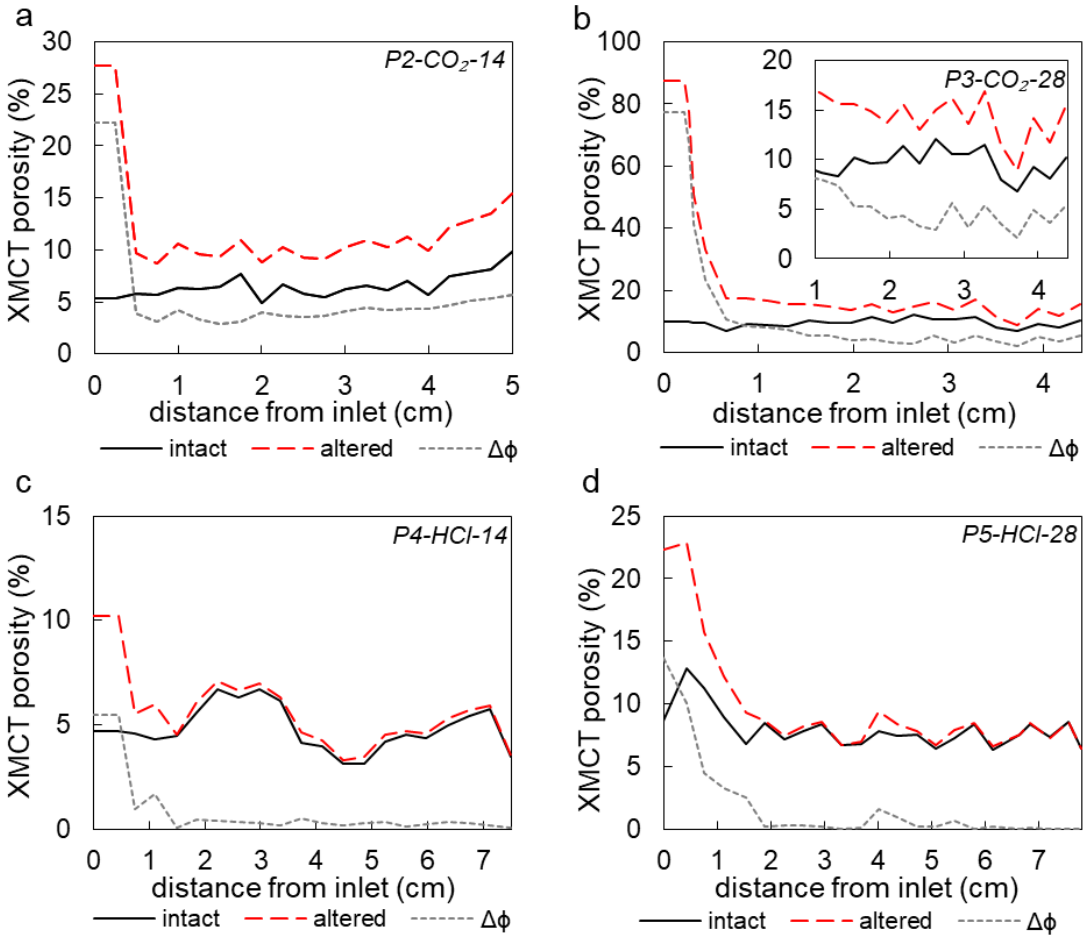

Figure 27. Average XMCT porosity profiles along the cores before and after the experiments: (a) and (b) = CO_2-saturated water; (c) and (d) = HCl solution. Increments in porosity ($\Delta\phi$) due to calcite dissolution are shown by gray dashed lines. In (b), the inset shows lower porosity values after the core inlet (between 1 cm and 4.5 cm).

4.1.2.2. Variation in permeability

In all experiments, the permeability of the cores increased because of calcite dissolution and porosity enhancement (Table 5). In the HCl experiments (*P_4-HCl-14* and *P_5-HCl-28*), permeability increased by a factor of 3-7 whereas, in the CO_2-saturated experiments (*P_2-CO_2-14* and *P_3-CO_2-28*), the increase was of 3 orders of magnitude caused by wormhole formation. However, permeability measurements in these samples are subject to the validity of the Darcy flow assumption in the wormholes. Note that the permeability values were obtained by using the initial core cross-section in Eq. (5) while the flow channeled through wormholes.

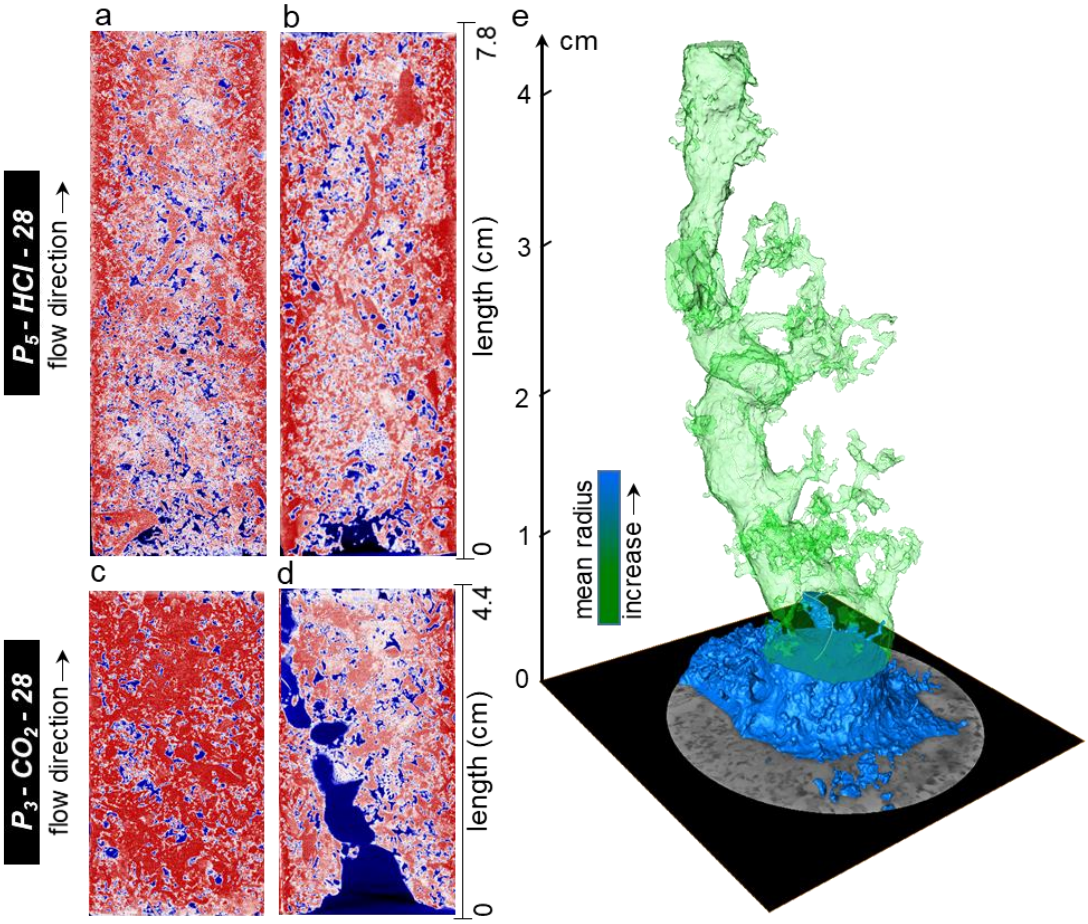

Figure 28. Porosity changes and dissolution patterns deduced from XMCT images. 2D porosity maps for a central slice along the P_5 and P_3 cores before (a and c) and after (b and d) injection of HCl and CO_2-saturated solutions. A two-color filter is used in images (a) to (d) to distinguish between calcite grains (red areas) and pore space (blue areas). 3D reconstruction of dissolution-induced porosity changes in P_3 (e), resolving the structure of the formed wormhole.

4.1.2.3. Variation in pore size distribution

MICP pore size distribution shows that pores in the intact and HCl-treated specimens are mostly macropores and mesopores. Macropores contribute significantly to total porosity as opposed to micropores that make a negligible contribution (Fig 29a). The pore size distribution curves indicate an increase in the mesopore fraction in HCl-treated samples because of dissolution denoting the formation of new pores and/or the enlargement of the existing ones (Fig. 29b). In the longer P_5 experiment (28 days), these pores get enlarged or connected and form macropores (throat radius of 1-80 µm). Although the fractions of larger pores (throat sizes > 3 µm) are smaller in HCl-altered cores than in the intact rock, their volume is not (Leger et al., 2022; Tutolo et al., 2020). Note also that MICP excludes pores with throat sizes > 88 µm and underestimates total porosity as explained in Section 4.1.2.1. Differences in the pore size distribution may also be caused by existing heterogeneities in the cores.

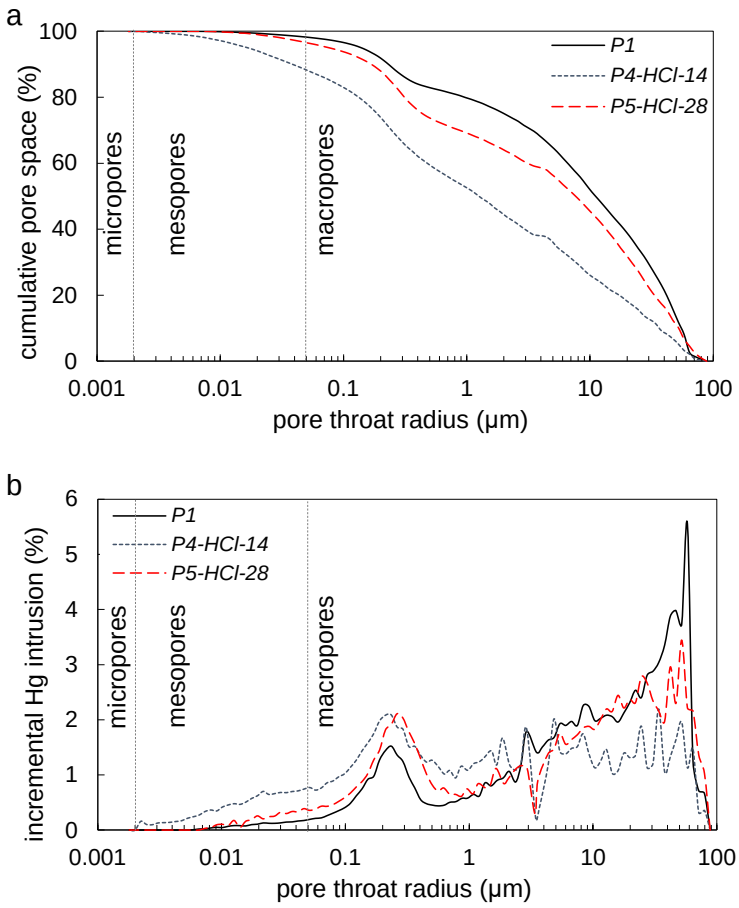

Figure 29. (a) Cumulative and (b) incremental distributions of the pore throat size in intact (P_1) and HCl-altered specimens (P_4 and P_5).

4.1.3. Stiffness and strength weakening

Compressional and shear wave velocities (V_P and V_s, respectively) diminish with an increase in the core porosity as calcite dissolves (Fig. 30). Although the heterogeneous dissolution patterns that form in the cores may raise concerns about the continuity of the porous medium, the fall in the acoustic velocities is in agreement with the velocity-porosity trend observed on intact carbonates (Assefa et al., 2003; Eberli et al., 2003; Fournier et al., 2011; Miller et al., 2019; Vanorio and Mavko, 2011). Diminishes in V_P and V_s are correlated with the reduction in the elastic constants of the rock frame after exposure to acid solutions (Table 6).

The velocity and rock stiffness attenuations are more pronounced in the CO_2 percolation experiments and escalate with the injection period (i.e., injected pore volume) linked with higher porosity increases (e.g., P_3 shows the highest drop in V_p and V_s: ≈ 19% and ≈ 15%, respectively). These velocity attenuations correspond to ≈ 39%, ≈ 47%, and ≈ 37% degradation in dynamic Young's (E_d), bulk (K_d), and shear moduli (G_d), respectively. Similar mechanical weakening effects have been observed in other CO_2-treated carbonates, such as Ekofisk and Tor chalks, and Estaillades, Indiana, and Apulian limestones (Alam et al., 2014; Al-Ameri et al., 2018; Kim et al., 2018; Pimienta et al., 2017; Vialle et al., 2014; Vialle and Vanorio, 2011).

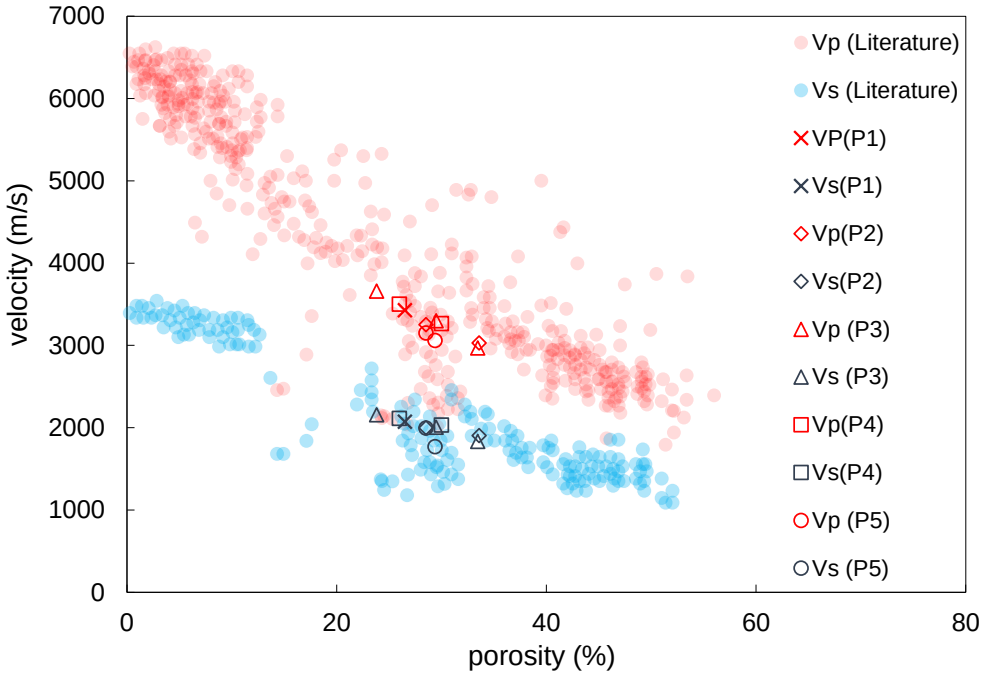

Figure 30. Variation in the sonic velocity as a function of porosity in the studied limestone under study (large symbols) upon exposure to acid solutions. Higher porosity-lower velocity data for each specimen consistently refer to the post-injection state. Colored symbols represent the velocity-porosity data for intact carbonate rocks reported in earlier experimental studies (El Husseiny and Vanorio, 2015; Eberli et al., 2003; Vanorio et al., 2008).

Tests for the stress-strain behavior of the specimens under uniaxial compression indicate a substantial decrease in the static Young's modulus of the acid-treated cores compared with the intact rock one (Fig. 31 and Table 6). For the sake of comparison between different experiments, I rely on the first-loading elastic moduli that are available for all specimens. These moduli are up to 10% smaller than those from the subsequent unloading-reloading cycle. This difference can be attributed to the inelastic deformation captured during the first loading stage, which does not relax, at least during the laboratory time scale (Sone and Zoback, 2013; Vafaie and Kivi, 2020). As expected, the reduction in E_s is higher in the CO_2 treatment (from 19.22 GPa to 11.99 GPa) than in the HCl one (from 19.22 GPa to 16.24 GPa) in agreement with the measured ultrasonic velocities.

With the exception of specimen P_5, the static Young's moduli are consistently lower than the dynamic ones following earlier observations in carbonate rocks (Eissa and Kazi, 1988; Fjær, 2019; Mavko et al., 2009; Sone and Zoback, 2013). The deviation from this general trend in sample P_5 is probably caused by the localization of deformation around the hole that formed at the core inlet (i.e., compact dissolution pattern) and was not accounted for by the strain gauges attached to the center of the specimen, potentially overestimating E_s. Although the measured Poisson´s ratio, whether dynamic or static, generally points to smaller values in altered specimens, a firm conclusion on chemical reactions' effect on the evolution of Poisson's ratio (v_s) cannot be made.

Uniaxial compressive strength (UCS) of the rock, i.e., the stress level at which the rock undergoes failure under unconfined loading conditions, decreases from 17.27 MPa for intact P_1 specimen to 6.10 MPa for CO_2-saturated water P_2 core and 7.34 MPa for HCl-solution P_5 core (Fig. 31). Although the CO_2 treatment causes more defects in the rock compared with the HCl one as a result of a large wormhole formation, the UCS values for both specimens are nearly within the same range, with an absolute difference of 1.24 MPa. This small difference may be attributed to rock deformation and failure under static loading that is highly sensitive to even small defects in the rock framework. Therefore, the compact dissolution pattern at the inlet of specimen P_5, despite its insignificant contribution to porosity enhancement, leads to stress localization and rock failure at significantly low stress levels.

To better understand the effect of stress and deformation localization around the dissolution features, the first 2.5 cm (inlet portion) of the specimen P_4 altered by HCl injection for 14 days was cut, and the remaining intact part (P_4^{**}; Table 3) was loaded. The values of elastic moduli (both static and dynamic) and UCS for this specimen are the highest, even exceeding those of the intact rock P_1 (Fig. 1, Table 6). The measured values agree with the lower porosity of P_4^{**} compared with the cut inlet portion and P_1 (by nearly 1.5% and 2%, respectively), originating from the intrinsic rock heterogeneity. This mechanical behavior is consistent with the XMCT images that show an affected inlet in HCl-treated cores, while the remaining part of the cores remained almost untouched.

Table 6. Static and dynamic elastic moduli values measured for intact and altered cores.

sample	state intact/altered	E_d (GPa)	v_d	K_d (GPa)	G_d (GPa)	E_s (GPa)	v_s	*UCS* (MPa)
P₁	intact	20.3	0.21	11.7	8.4	19.2	0.21	17.3
P₂-CO₂-14	intact	18.2	0.20	9.9	7.6	-	-	-
	altered	14.9	0.17	7.6	6.4	11.9	0.32	6.1
	intact	23.2	0.23	14.5	9.4	-	-	-
P₃-CO₂-28	altered*	18.1	0.21	10.3	7.5	-	-	-
	altered	14.1	0.19	7.6	5.9	-	-	-
P₄-HCl-14	intact	21.2	0.21	12.4	8.7	-	-	-
	altered	19.1	0.18	10.1	8.1			
P₄-HCl-14**	altered	25.5	0.22	15.2	10.5	23.6	0.19	20.9
P₅-HCl-28	intact	18.1	0.21	10.6	7.5	-	-	-
	altered	15.3	0.20	8.6	6.4	16.2	0.1	7.3

altered* = measurement on P_3 core after 14 days of injection; P_4^{**} = part of P_4 core that is unaffected by HCl injection

E_d = dynamic Young's modulus; E_s = static Young's modulus; v_d = dynamic Poisson´s ratio; v_s= static Poisson´s ratio

K_d = dynamic Bulk modulus: K_s = static Bulk modulus; *UCS = Uniaxial Compressive Strength*

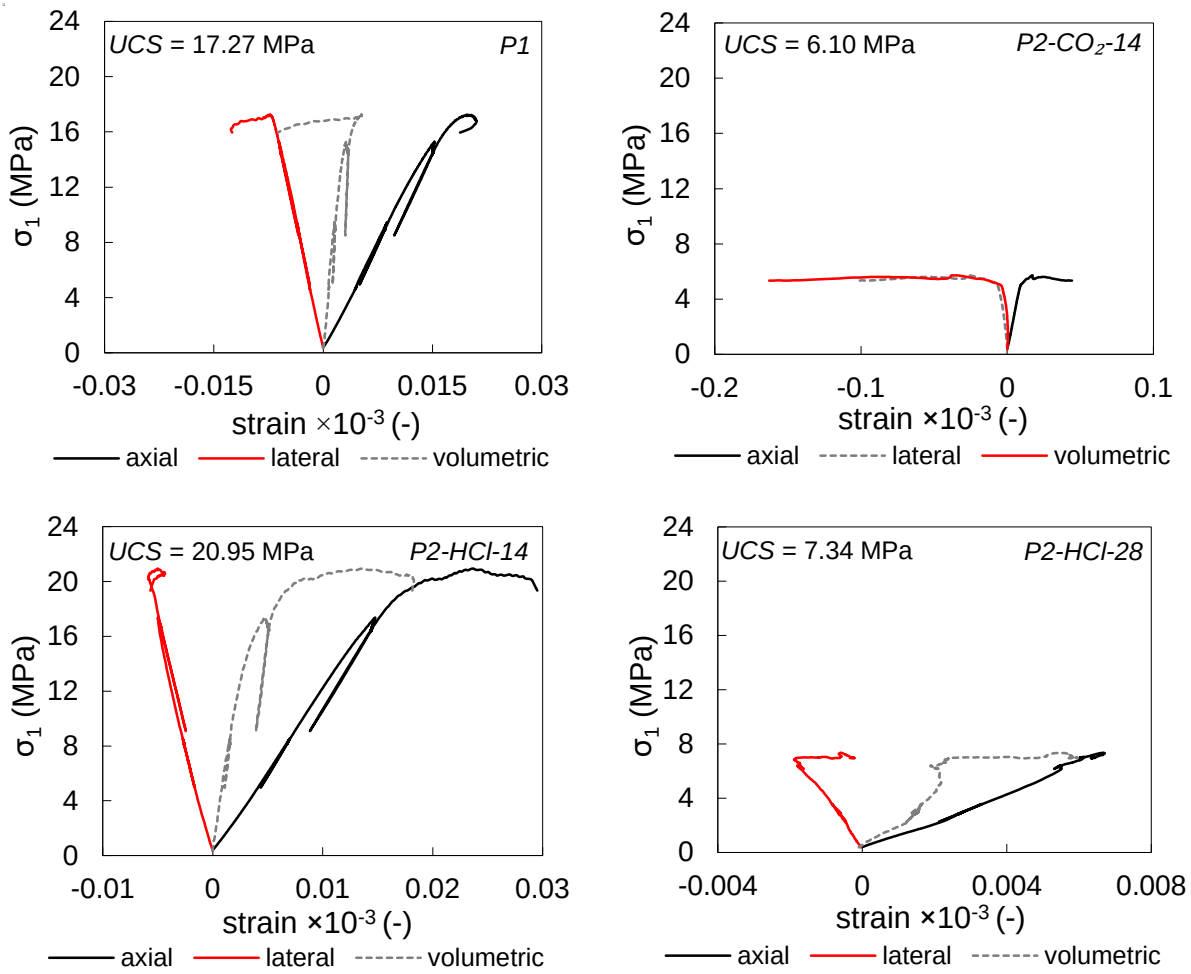

Figure 31. Stress-strain response of (a) intact P_1 and altered (b) P_2-*CO₂-14*, (c) P_4^{**}-*HCl-14*, and (d) P_5-*HCl-28* cores under uniaxial compression. Axial stress is shown as a function of axial (black solid line), lateral (red solid line), and volumetric (gray dashed line) strains.

4.2. Reactive transport simulation results

4.2.1. CO_2-saturated water injection: wormhole formation

Reactive transport modeling results of the CO_2 injection experiment on sample P_3 using different *n* values in Eq. 14 are presented here. Simulations show that the fluid flow and calcite dissolution begin to concentrate in areas of high porosity and high permeability from the onset of the experiment (Fig. 32). A comparison between the XMCT cross-section image of the core inlet before CO_2 injection (Fig. 33) and the respective simulation result (Fig. 32) shows that calcite dissolves at the same locations over short periods (≈ 96 h) irrespective of the *n* value used. This observation is consistent with simulation results for the output Ca concentration over time that illustrates nearly the same trend and value of $[Ca]_{out}$ for different *n* values over short time spans (Fig. 34a).

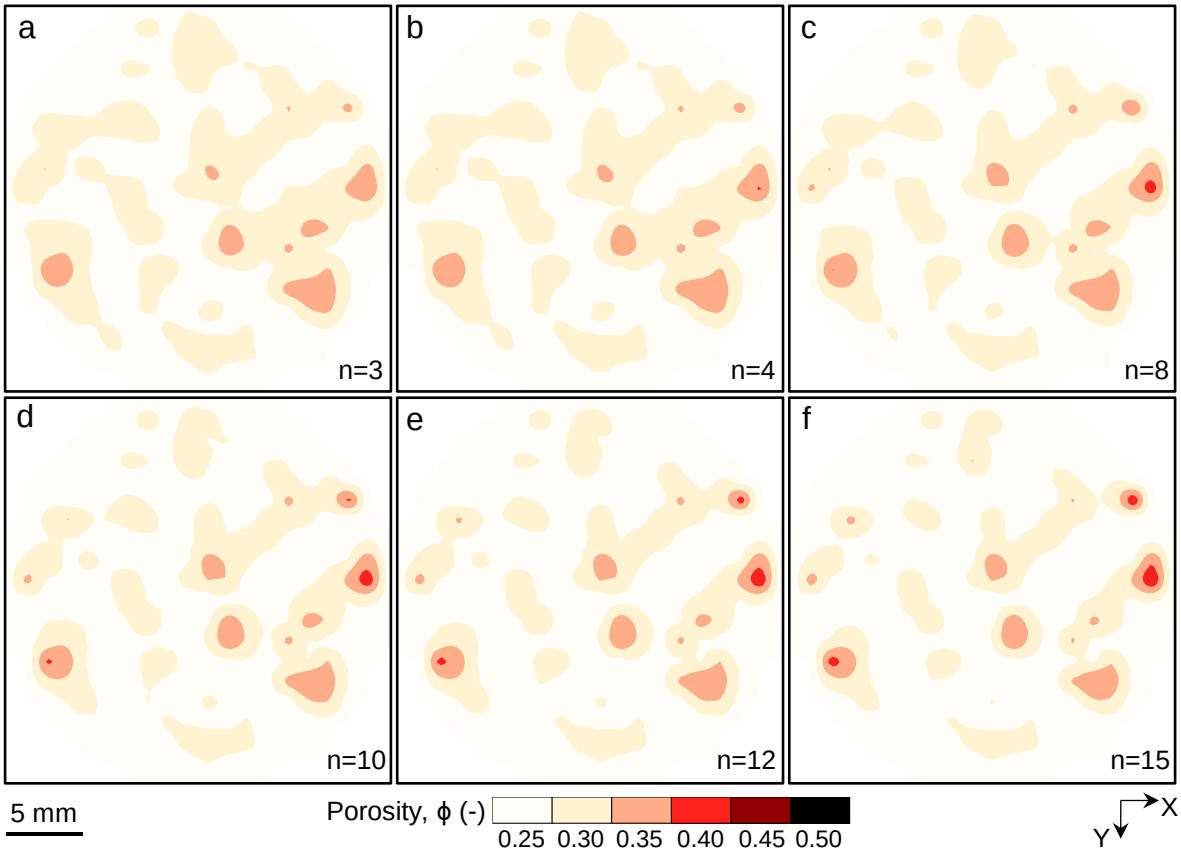

Figure 32. Simulated spatial development of porosity at the core inlet after CO_2-saturated water injection for 96 h using porosity-permeability relationship (Eq. 14) with n ranging between 3 and 15 (a-f).

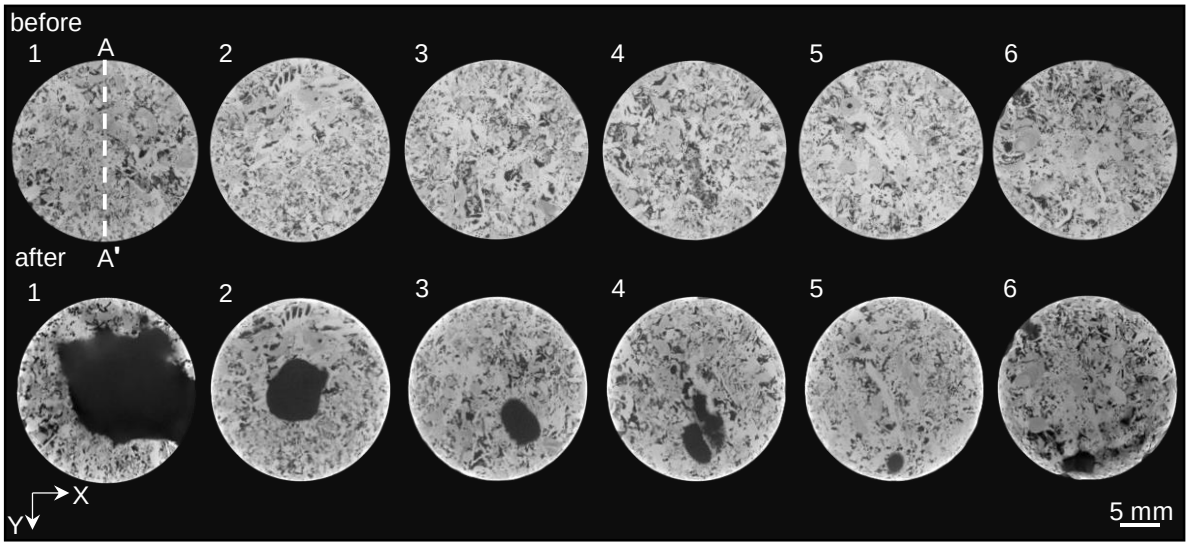

Figure 33. 2D XMCT cross-section images perpendicular to the flow direction (Z) along the P_3 core before (upper row) and after (lower row) 28 days of reaction with CO_2-saturated water. In the lower sequence, the dark area is new porosity caused by calcite dissolution. The numbers indicate the position of the images along the Z axis separated at a constant distance of 0.88 mm (1: inlet, 6: outlet). Section AA´ along the core was used to plot the simulations displayed in Fig. 35.

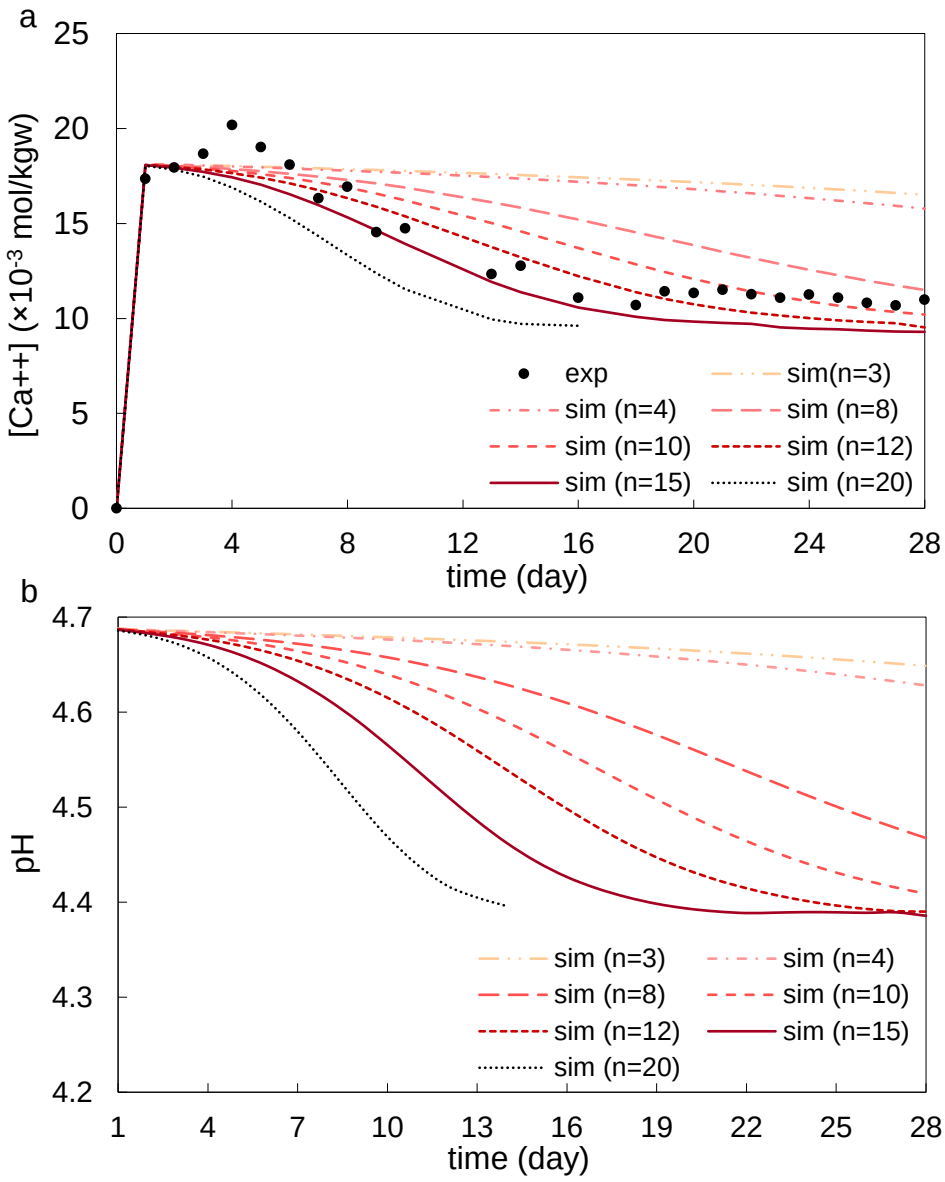

Figure 34. Experimental and simulated variation in the output fluid chemistry over time in the P_3 experiment with n = 3, 4, 8, 10, 15, and 20 (Eq. 14): (a) Ca concentration and (b) solution pH. Line colors are gradually lightened with the decrease in the n value.

As the dissolution front penetrates further into the core and is localized in the heterogeneous pore structure of the rock, the exponent n starts to play a critical role in the evolution of the fluid flow and chemistry. Variation in $[Ca]_{out}$ and XMCT porosity profiles are used as useful criteria to understand the effect of n on the temporal and spatial development of dissolution in the limestone core. Increasing the n lowers the $[Ca]_{out}$ due to a gradual localization of dissolution reaction in preferential flow pathways (Fig. 34a). While the estimated outflow concentration profiles drop steadily with n < 8, the change in the slope of the curves pointing to wormhole breakthrough across the core appears when larger n values are used. This change is slight and happens after ≈ 24 days for n = 10 but becomes sharper and happens earlier for n = 12 and 15. An optimal match with experimental observation is achieved with n = 15. A

further increase in *n* results in unrealistically fast localization of flow and underestimation of calcite dissolution.

Simulations show that calcite dissolution takes place mainly near the injection point with n = 3, yielding a compact dissolution pattern (Fig. 35d,j). By increasing n to 15, the developed dissolution pattern gradually evolves toward a major wormhole as observed in XMCT images (Fig. 35 c,o). For n = 15, the simulated shape and orientation of the dissolution front match well the dissolution patterns observed by XMCT (Fig. 35c). The wormhole deviates toward the right on the Y axis, i.e., through a region of high initial porosity. Moreover, simulation results show the formation of a localized dissolution zone simultaneously but in opposite direction to the main wormhole where a less pronounced contrast in the initial porosity exists. Nevertheless, the numerically predicted porosity in grid blocks does not perfectly conform to XMCT estimates, particularly in the wormhole area where major calcite dissolution shifts porosity to unity. Accordingly, the model predicts a total porosity enhancement of 6.2%, which is slightly smaller than direct measurements (Table 5).

Although outflow pH was not measured in the CO_2-saturated water experiments, simulation results provide insights into pH evolution at the core outlet (Fig. 34b). Output pH is 1.55 units higher than input solution pH (3.13) after one day of injection as a result of proton consumption during calcite dissolution. The increase in pH diminished during the experiment and also with the increase in n (Eq. 14) where the formation of a channel-like dissolution front forced most of the injected fluid to move through the highly permeable channel without encountering or reacting with the remaining part of the limestone, further maintaining the solution acidity. Consequently, although the fluid pH increases slightly while passing through the limestone core, it remains acidic and undersaturated with respect to calcite during the experiment.

Simulation data have been leveraged to estimate the evolution of the bulk rock permeability upon reaction with CO_2-rich water (Fig. 36) while direct experimental measurements were made only before and after 14 and 28 days of injection. To this end, numerical estimates of the pressure difference across the core sample at a constant flow rate (0.15 mL/min) were used in Eq. (5) to calculate the average core permeability. The calculated permeability after 28 days is of the same order as the experimentally measured value (see Table 5). However, the model underestimates the rock permeability after 14 days of injection by approximately one order of magnitude. This discrepancy may arise from the morphology of the dissolution pattern (a narrow wormhole forms along the core within 14 days yielding a highly permeable path). In contrast, simulations predict a relatively thicker wormhole structure with a locally smaller increase in porosity (Fig. 35i) that causes larger overpressures at the inlet and equivalently smaller permeabilities. The core-scale permeability-porosity relation is fitted with a power-law with an exponent of 27.6 (Eq. 14) which is 1.8 times larger than n = 15 used at the grid scale.

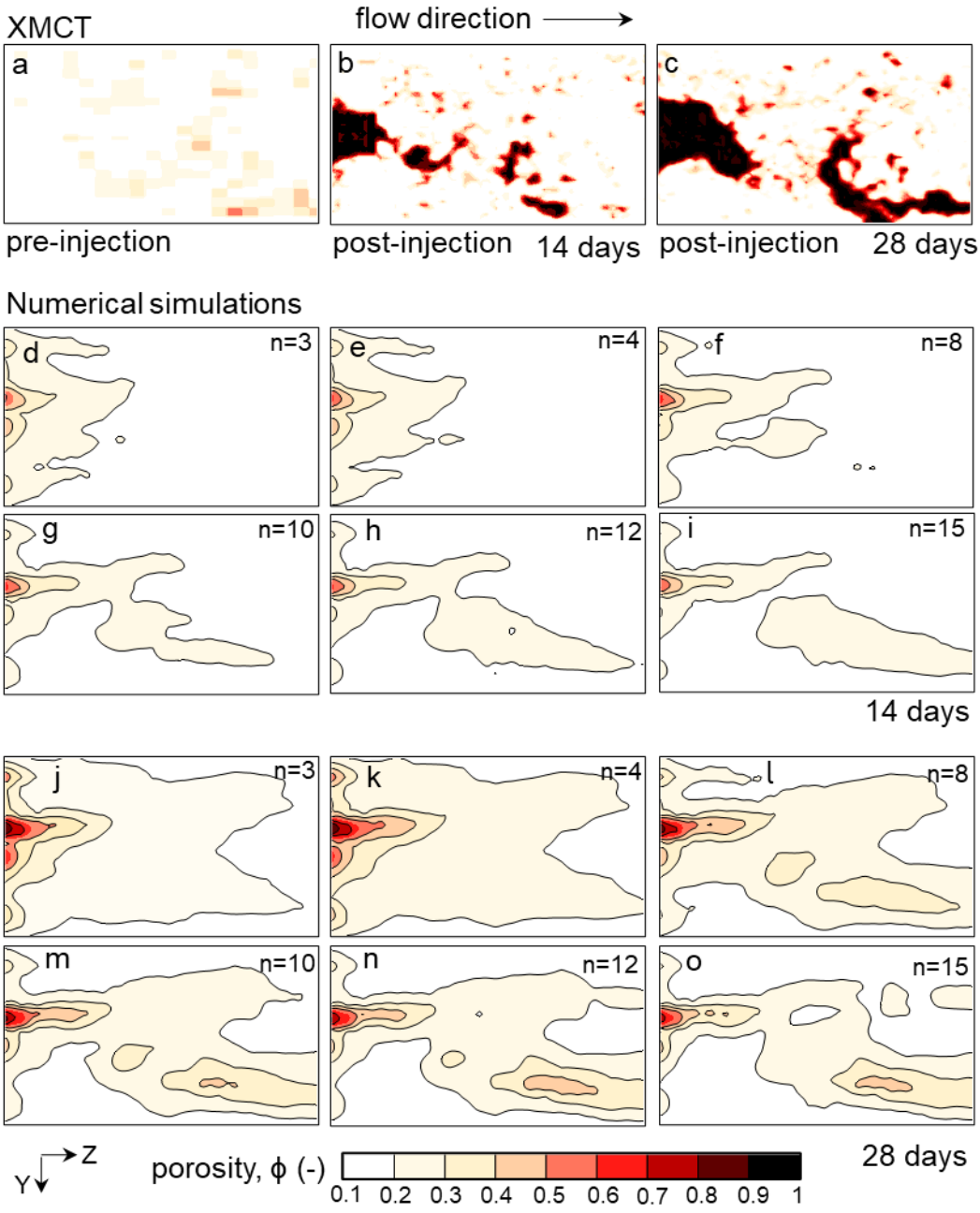

Figure 35. Experimental (a-c) and simulated (d-o) distribution of porosity in a vertical cross-section along the flow direction in sample P_3 (section AA' shown in Fig. 33): (a) before CO_2 injection and (b,c) after CO_2 injection for 14 days and 28 days inferred from XMCT images; (d-o) simulations after reaction with CO_2-saturated water for 14 days and 28 days using n = 3, 4, 8, 10, 12, and 15 (Eq. 14).

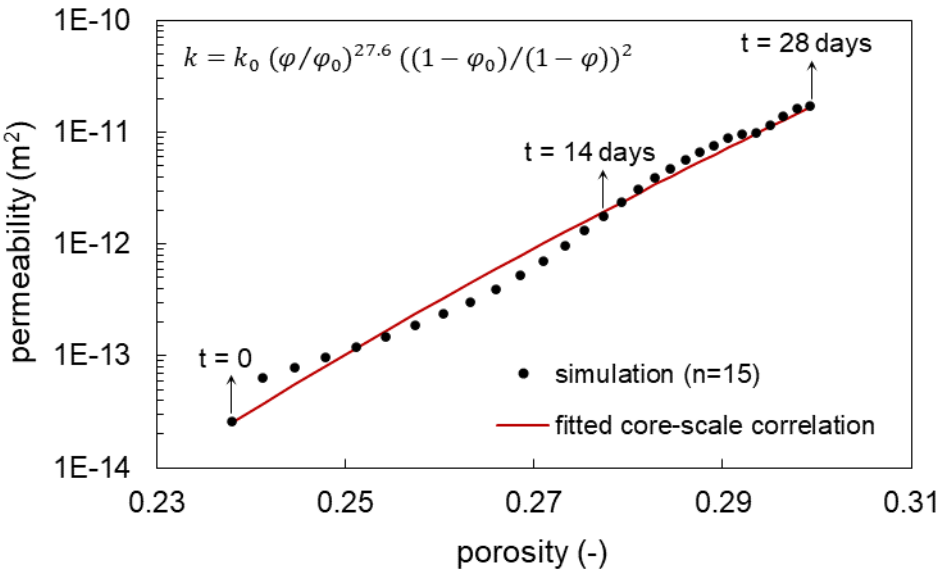

Figure 36. Change in bulk core permeability as a function of average porosity estimated from numerical simulations (black circles). The fitted core-scale power-law correlation (solid line) measures an exponent of 27.6.

4.2.2. HCl solution injection: compact dissolution

Figures 37 to 39 compare the measured and simulated output solution chemistry and dissolution front structure for the HCl-reacted sample P_5. The steady-state $[Ca]_{out}$ during both injection stages (HCl solutions of pH = 3.13 and pH = 2.66), the variation in effluent pH (Fig. 37) and the observed compact dissolution structure (Fig. 38) are satisfactorily reproduced using the conventional cubic porosity-permeability relationship, i.e., $n = 3$ (Eq. 14, Fig. 39). Both model and experimental results demonstrated constant outflow pH values larger than 7, indicating a drop in solution acidity through the core. Indeed, calcite dissolution neutralized the initial pH while reaching equilibrium with calcite. This high increase in pH contrasts with the slight one (ΔpH $\approx$1.55) obtained in the CO_2-saturated water experiments, outlining the effect of acid type on calcite dissolution.

n values higher than 3 (e.g., *n* = 4, 8, 12, and 15) were used to simulate the first stage (17 days of injection with pH = 3.13). Although an increase in *n* slightly change the dissolution front shape, the variation of dissolved calcite remained unaffected. An increase in the *n* value did not improve the match between the numerically predicted porosity distribution in the altered sample and the porosity profile acquired from XMCT imaging. Yet, all models predicted an increase in bulk porosity enhancements $\approx$ 0.7%, which agrees well with the experimental measurements.

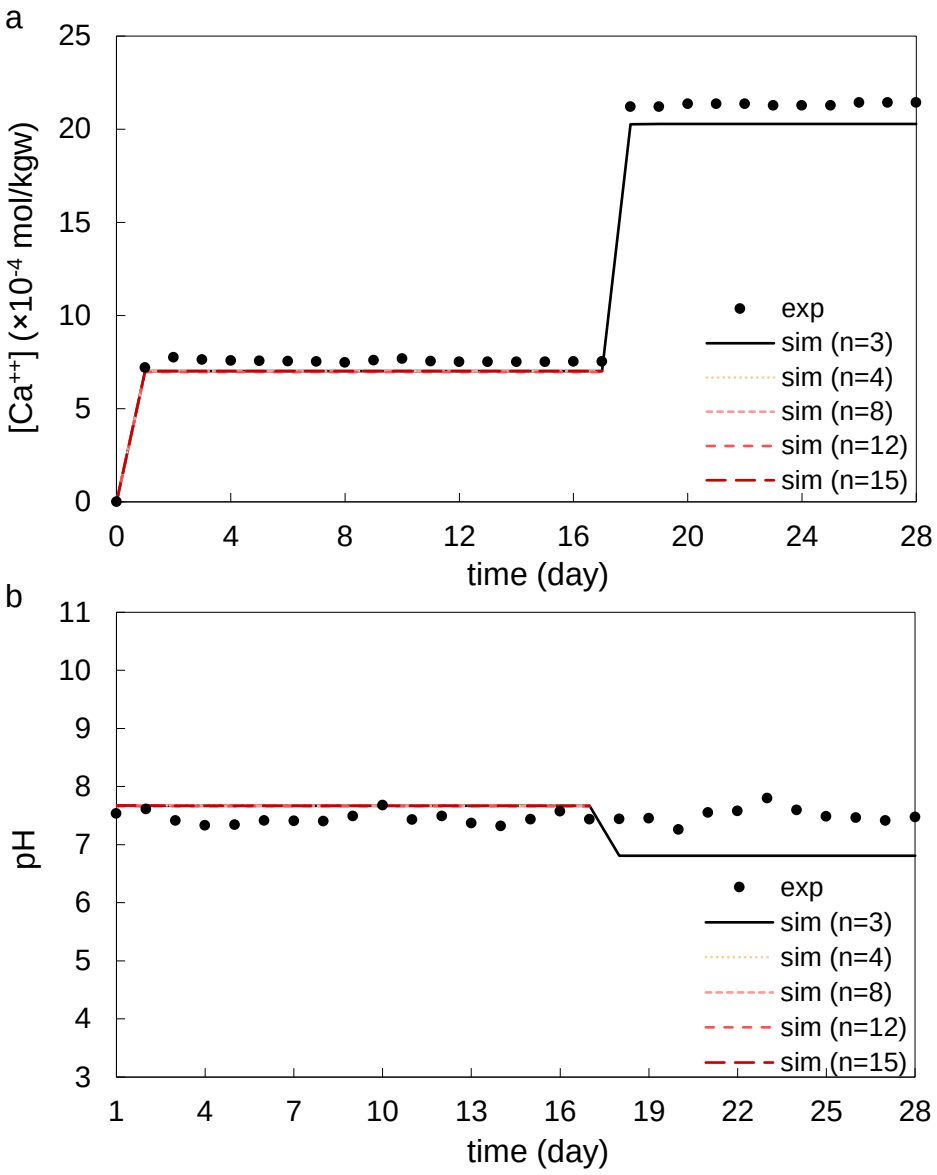

Figure 37. Experimental (solid symbols) and calculated with n = 3, 4, 8, 12, and 15 (lines) variation in the outflow chemistry in the P_5 experiment: (a) experimental output Ca concentration and (b) experimental output pH. Note that the scale of the Ca concentration is one order of magnitude smaller than that in Fig. 34 for CO_2-saturated water injection. All simulations coincide because changes were not observed in the effluent chemistry by varying the n exponent (Eq. 14).

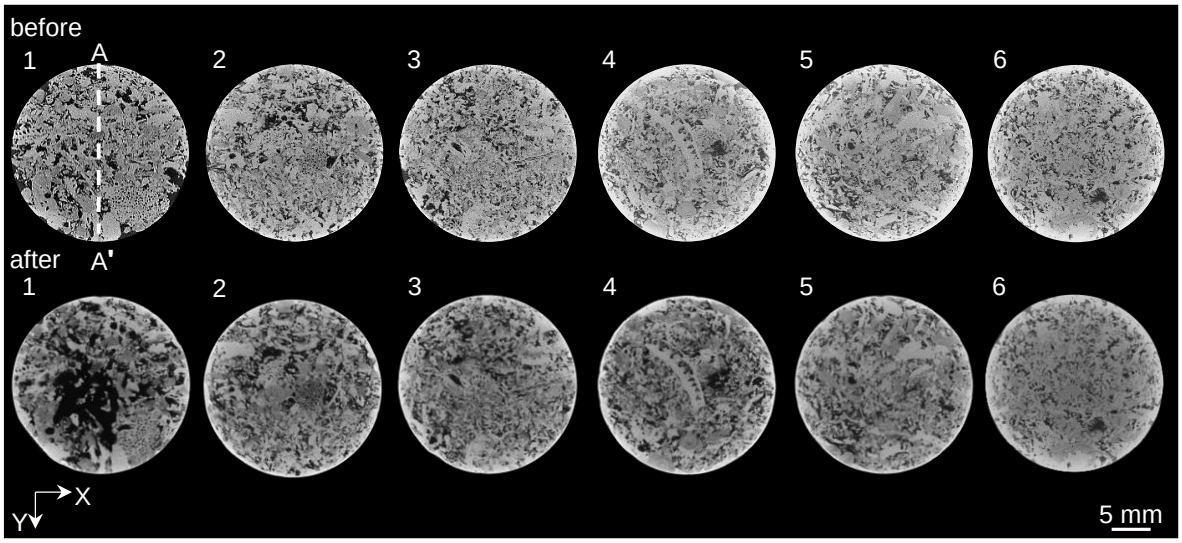

Figure 38. 2D XMCT images perpendicular to the flow direction (Z) along the P_5 core before (upper row) and after (lower row) reaction with HCl solution. The large dark area in the first slice shows dissolution-induced porosity enhancement concentrated at the inlet (compact dissolution). The numbers indicate the position of the images along the Z axis separated by a constant distance of 1.56 mm (1: inlet, 6: outlet). Section AA´ along the core was used to plot results in Fig. 39.

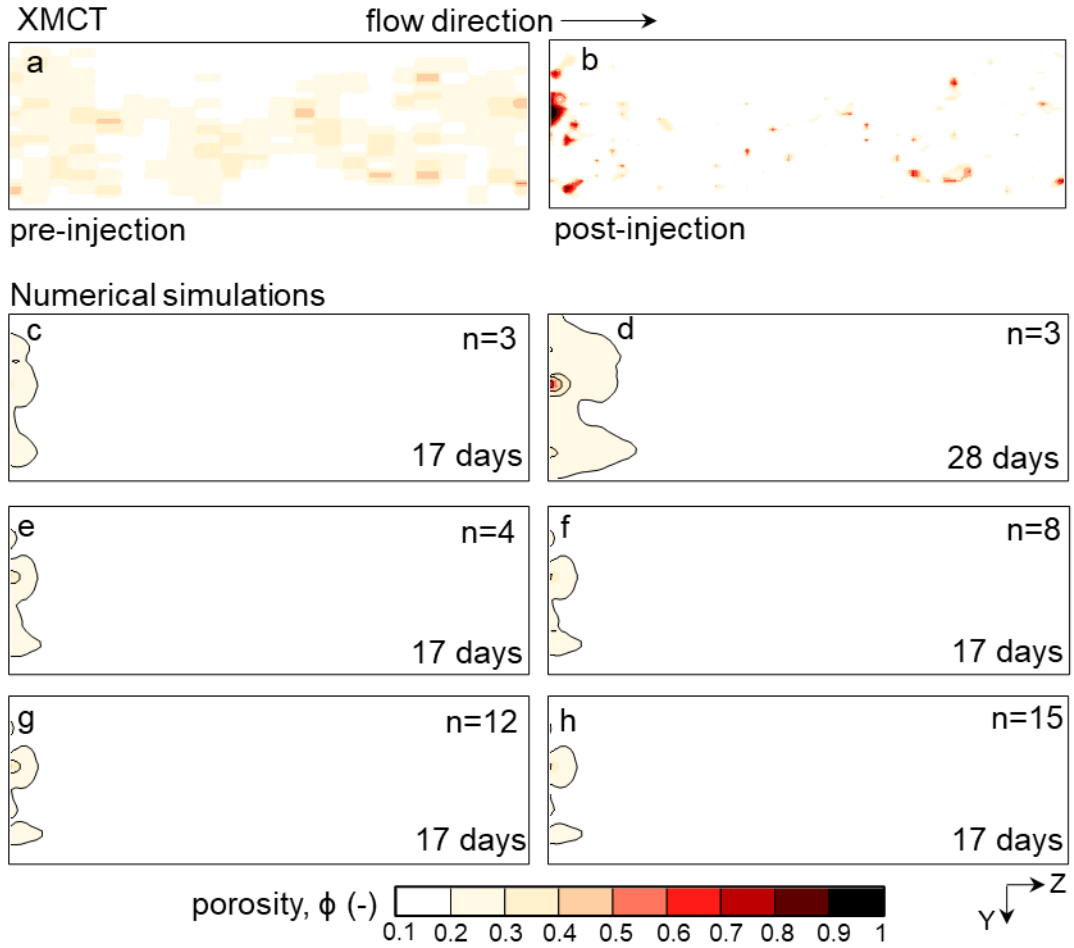

Figure 39. Distribution of measured (a,b) and simulated (c-h) porosity in a vertical cross-section along the P_5 core (section AA' shown in Fig. 38): (a) before and (b) after HCl injection inferred from XMCT images; (c,d) simulations of the core-HCl interaction after17 and 28 days using n = 3 and (e-h) simulations of core-HCl interaction after 17 days using n = 4, 8, 10, 12 and 15 (Eq. 14).

Chapter 5

Discussion

This chapter discusses the insights gained from the experimental results and numerical simulations of the chemically-induced alteration in the limestone cores. I discuss (1) the limitations of the employed Darcy-scale reactive transport model, (2) the most important factors ruling the dissolution processes in carbonate rocks, (3) the significance of adequate scaling of the porosity-permeability relationship to assess the evolution of flow in chemically-altered carbonate rocks, (4) the ability of the effective medium theories to reproduce the stiffness of acid-injected carbonate rocks, and (5) potential implications for field-scale operations.

5.1. Limitations of the Darcy-scale numerical model

In this study I have developed a 3D Darcy-scale reactive transport model for centimeter-scale limestone cores injected with acidic solutions. The model satisfactorily captures the general structure (i.e., shape and orientation) of dissolution patterns formed in the CO_2-saturated water and HCl experiments. The model is also capable of reproducing the bulk flow and chemical behavior of limestone specimens, changes in porosity, permeability, and dissolved calcite mass. It can also qualitatively reproduce the XCMT-acquired maps of porosity at the grid scale.

Deviations of the model predictions from laboratory observations stem primarily from the size of grid blocks in the continuum model selected to afford computational costs. Coarse meshing schemes unavoidably mask some details of the pore space heterogeneity and, thus, flow and reaction processes at the grid scale. Another factor could be the depiction of the pore structure heterogeneity only in the initial permeability distribution of the rock. Indeed, the initial mineral surface area of the rock is treated in the model as a fitting parameter with a uniform distribution over the core domain. The reactive surface area evolves with dissolution-induced porosity enhancement (Eq. 14) and gradually reaches a heterogeneous distribution as the reactive flow and thus, chemical reactions localize at regions of high local permeability. Still, neglecting initial heterogeneities in the reactive surface area may affect the spatial distribution of chemical reactions while returning reliable predictions on the bulk scale.

Another factor that brings in inconsistency between experimental and simulation results is the utilized surface area-porosity relationship (Eqs. 15 and 16). Since, this correlation is developed based on a simple representation of porous media (i.e., a package of spherical grains of the same size (Noiriel et al., 2009)), the effects of grain geometry and grain size distribution on the evolution of the mineral surface area are overlooked (Noiriel et al., 2009; Soulaine et al., 2018). Noiriel et al. (2009) showed that neglecting realistic grain shapes by Eqs. (15) and (16) could result in erroneous estimates of the reaction rate. Using more complex models for the alterations in the mineral surface area including adequate physics of the problem could improve the simulations.

5.2 Factors controlling limestone alteration and dissolution patterns

The continuous dissolution of calcite (Fig. 26) led to changes in the limestone microstructure (Fig. 28b). Given that the flow rate was constant, either a change in the mass transfer of reactive solutes or a change in calcite dissolution kinetics could have controlled the changes in the calcite dissolution rate. Mass transfer of reactive solutes is controlled by the contributions of advection and diffusion transport mechanisms (Vialle et al., 2014; Noiriel et al., 2009). To assess the theoretical contribution of advection and diffusion in the percolation experiments, the Péclet number (*Pe*) is calculated as (Oelkers, 2018)

$$Pe = U_{avg} L/D \tag{17}$$

where $Uavg = q/\phi_{XMCT}$ is the average fluid pore velocity (m s^{-1}), q is the darcy velocity, L is the characteristic length (average pore diameter i.e., 165-265 μm, from XMCT images), and D is the Ca^{2+} molecular diffusion coefficient at 60 °C (5.36×10^{-9} m^2 s^{-1}) (Luquot et al., 2016). The obtained average initial *Pe* value is ≈ 3 (i.e., *Pe* > 1), which suggests that solute transport is controlled by advection in all the experiments. At pH < 4, the calcite dissolution kinetics depends on the H^+ activity and the calcite reactive surface area (Cama et al., 2019; Compton et al., 1989; Menke et al., 2017; Peng et al., 2015). Since the pH of the injected solutions is the same, and alteration of the pore structure slightly affects the mass transfer regime, a variation in the accessible reactive surface area must be responsible for the $[Ca]_{out}$ variation. The pore structure heterogeneities detected by XMCT may cause small differences in the calcite content evolution, but not in the dissolution trends. The evolution of the accessible reactive surface is influenced by the nature of the injected solution (acid type), which should be considered when assessing acid-rock interactions.

The partial dissociation of H_2CO_3 (weak acid) and the buffering of pH resulting from calcite dissolution renders a low-pH solution along the cores (Garcia Rios, 2015) with consequent fast calcite dissolution and porosity increase, which leads to wormhole formation under these flow conditions (Figs. 28d and 33). Nevertheless, calcite dissolution is stronger at the inlet because the reacting solution evolves towards calcite equilibrium along the core (Garcia Rios et al., 2017; Seyyedi et al., 2020). By contrast, HCl (strong acid) completely dissociates into H^+ and

Cl^- and strongly dissolves the limestone at the very inlet (Bernadiner et al., 2002; Fredd and Fogler, 1988; Gray et al., 2018; Raj et al., 2014), causing a fast increase in pH (Fig. 26c), which prevents the advance of the dissolution front (Chang et al., 2022; Garcia Rios, 2015) and yields a compact dissolution pattern (Fig. 28 and Fig 37).

Transport and reaction processes compete to form dissolution patterns in the specimens (Golfier et al., 2002; Menke et al., 2015; Szymczak and Ladd, 2009). As shown above, the *Pe* number concerns the transport process, whereas the Damnköhler number (*Da)* compares the calcite dissolution rate with advective flux. *Da* is calculated as (Menke et al., 2017)

$$Da = r/U_{avg}\, n \tag{18}$$

where r is the calcite rate constant at pH of 3.13 (9.05×10^{-4} mol m^{-2} s^{-1} (Atanassova et al., 2013; Peng et al., 2015)) and n is the number of moles of calcite per unit volume of rock ($n = \rho_{cal}\,(1-\phi_{bulk})/M_{cal}$ (Menke et al., 2017)), where ρ_{ca} is the density of calcite grains (2.65×10^3 kg m^{-3}), M_{ca} is the calcite molecular mass (0.1 kg mol^{-1}), and ϕ_{bulk} is total porosity (Table 5). In the experiments, the initial *Da* values and the ratio of the reaction to diffusion rate (*Pe·Da*) vary between 4.34×10^{-4} and 7.05×10^{-4} and between 1.47×10^{-3} and 2.29×10^{-3}, respectively, indicating that the reaction rate is slower than both the advection and diffusion rates. Although a uniform dissolution pattern would in principle be expected under these conditions when making use of these dimensionless numbers (Golfier et al., 2002; Luquot and Gouze, 2009; Ott and Oedai, 2015), compact dissolution (HCl solution) and wormhole formation (H_2CO_3 solution) are observed in the experiments. This deviation is mainly caused by rock heterogeneity and acid type, which are not included in the *Pe* and *Da* numbers. Hence, the prediction of dissolution patterns in heterogeneous carbonates should not rely on *Pe* and *Da* values. These numbers, however, may help clarify the effect of other parameters (e.g. flow rate) on the formation and evolution of dissolution patterns in similar acid-rock systems (Gray et al., 2018; Leger et al., 2022; Smith et al., 2013).

5.3 Porosity-permeability relationship

Simulation results show that the classical power-law porosity-permeability relationship with *n* = 3 (Eq. 14) can only reproduce satisfactorily the compact dissolution in the HCl-limestone system. An *n* value of 3 limits the increase in permeability for a given porosity change and distributes the acidic solution more evenly across the core cross-sections. As a result, mineral dissolution intensifies near the core inlet, leading to a slower propagation of the dissolution front. In contrast, dissolution features in the CO_2-treated specimen can only be inferred using a high *n =15*. A higher *n* value indicates a greater sensitivity of permeability to porosity changes and assists in acidic fluid channeling into the cores given the strong feedback between dissolution and localized flow. Indeed, the variability in the exponent n reflects transitions between different dissolution regimes (Noiriel et al. 2004; Al-Khulaifi et al., 2017).

Permeability changes in chemically altered carbonate rocks could be much larger than what is predicted by the classical Kozeny-Carman equation ($n = 3$, Eq. 14). Consequently, permeability increase in such rocks is not exclusively correlated with porosity alteration and relies more on the dissolution patterns than on the change in bulk porosity (Fig. 36). The numerical analysis performed in this study highlights a marked change in the porosity-permeability relationship corresponding to an increase in the power-law exponent from 15 to 27.6 when moving from the mm-scale numerical grids to the cm-scale core specimen injected with CO_2-rich water. The measured exponent representing the bulk core flow evolution is consistent with fitted values for bulk porosity and permeability measurements derived in earlier experimental acid injections (Noiriel et al., 2005; Hao et al., 2013; Garing et al., 2015; Smith et al., 2017; Menke et al., 2016 and 2017; Voltolini and Ajo-franklin, 2019; Hao et al., 2019). These observations point to strong scale dependence of porosity-permeability relationships and uncertainties in estimating permeability changes in chemically-altering carbonate rocks as heterogeneities tend to grow across scales.

Analysis of field-scale reactive flow would not still be surmountable with calibrated models for cm-long core samples since corresponding REVs to in-situ injections are usually of several-meter size (Cavanagh and Ringrose, 2011). Developing a rigorous upscaling approach could benefit from intermediate-size experiments in underground rock laboratories (Sciandra et al., 2022). Reactive transport simulations of these experiments could employ calibrated core-length parameters to parameterize meter-to-decameter-long models following the approach used in this study. This way, multi-step implementation of Darcy-scale reactive transport modeling enables generating equivalent, large-scale flow and reaction functions. Incorporation of the effects of small-scale heterogeneities by implementing this upscaling framework would help constrain uncertainties in predicting field injection behaviors.

5.4 Pore structure controls on the mechanical behavior

The large differences in sonic velocities between different minerals that constitute the rocks and pore-filling fluids are the basis for determining rock porosity (Eberli et al., 2003; Wyllie et al., 1958) and subsurface fluid displacement using sonic data (Gassmann, 1951; Smith et al., 2003). Nevertheless, initial heterogeneities and complex fluid-rock interactions in carbonate rocks (e.g., this study) complicate interpretation of the velocity-porosity evolution and question the prediction capability of standard rock physics models (e.g., the Gassmann theory (Fournier and Borgomano, 2009; Vanorio and Mavko, 2011)). To account for these problems, a variety of homogenization schemes that consider key microstructural features of the rock have been developed to estimate the wave velocity and elastic properties of the rock (Agofack et al., 2020; Arson and Vanorio, 2015; Giraud et al., 2012).

In this study, a one-step Differential Effective Medium (DEM) model is used to reproduce the effective elastic constants of the Pont du Gard Limestone. The DEM homogenization scheme is widely used in composite materials and geophysics to estimate effective medium properties. This task is done by incrementally adding inclusions (e.g., pores) in the host phase until the desired proportion of the constituents is reached (Berryman et al., 2002; Mavko et al., 2009; Zimmerman, 1996). The effective properties calculated at each step constitute the host phase

in the subsequent step. This approach particularly suits a two-phase composite material such as the grain-supported Pont du Gard Limestone, which has a very low cement content (Fig. 40a) and a bimodal distribution of calcite grains and macropores (Figs. 29 and 40b). The calcite host medium is assumed to be non-porous, and macropore inclusions are supposed to be randomly oriented oblate-shape spheroids. The DEM model calculates the effective bulk (K*) and shear (G*) moduli of the limestone by solving two coupled ordinary differential equations (Berryman et al., 2002)

$$(1-y)\frac{d}{dy}K^*(y) = P(K_i - K^*)(y) \tag{19}$$

$$(1-y)\frac{d}{dy}G^*(y) = Q(G_i - G^*)(y) \tag{20}$$

where y is the concentration of the inclusions (i.e., macropores), and P and Q are geometric factors that depend on the aspect ratio of macropores (α; defined as the ratio of inclusion thickness to length) and the elastic moduli of the inclusions and host medium at each step. It is suggested, however, to treat α as a fitting parameter rather than the actual shape of the pores (Fournier et al., 2011; Miller et al., 2019). The values of the elastic moduli of the inclusions are $K_i = 10^{-4}$ GPa, and $G_i = 0$ GPa, and the initial elastic moduli of the host medium correspond to those of calcite ($K^*(t_0) = 71$ GPa, and $G^*(t_0) = 31$ GPa). The functional form of P and Q can are presented in Appendix IV (Mavko et al., 2009). The homogenization problem described in Eqs. (19) and (20) was iteratively solved using MATLAB.

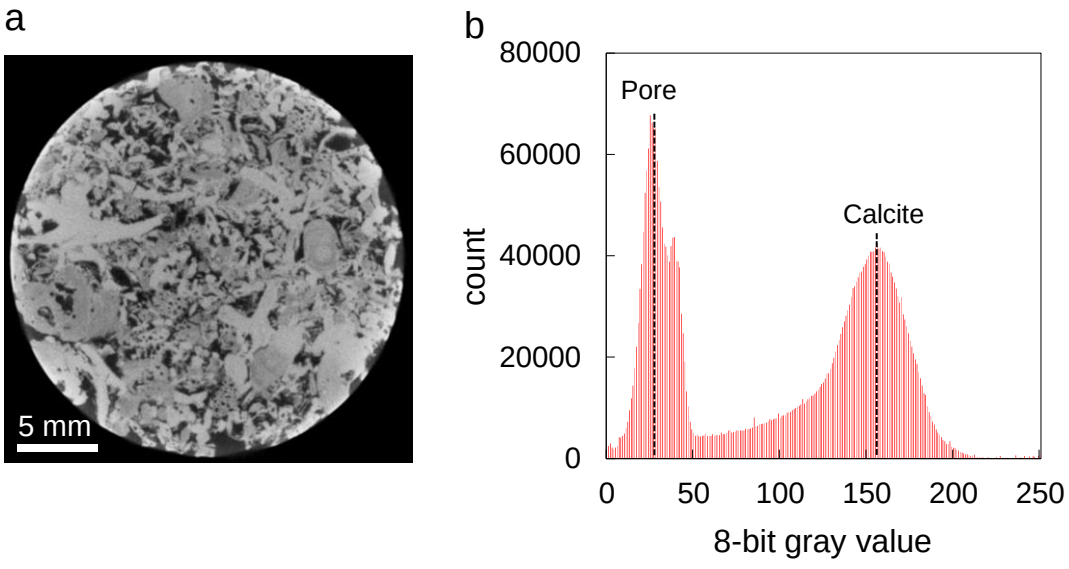

Figure 40. Grain-supported structure of the intact Pont du Gard Limestone: (a) a representative XMCT slice and (b) the histogram of grayscale values of the XMCT image. Vertical dashed lines indicate grayscale values of macropores and calcite grains.

Figure 41 shows that the evolution of elastic moduli with the variation in dissolution-induced porosity depends primarily on α. Calculated elastic moduli agree well with the experimental data when α varies between 0.1 and 0.125, which is in close agreement with those calculated for other limestones, i.e., $0.08 < \alpha < 0.2$ (Arson and Vanorio,2015; Fournier et al., 2011; Miller et al., 2019; Saneifar et al., 2015). The fit indicates that despite simplifications in the employed analysis (e.g., ignoring pore structure complexities and grain geometries and their time-evolving heterogeneous distribution), a unified aspect ratio may describe the elastic behavior of the altered limestone. Complementary studies on a wide range of carbonates with more complicated microstructures are necessary to figure out if a universal model able to predict effective elastic properties for chemically-altered carbonate rocks is within reach. Such a model would help accurately predict reservoir response to CO_2 injections and monitor the CO_2 plume migration in the subsurface.

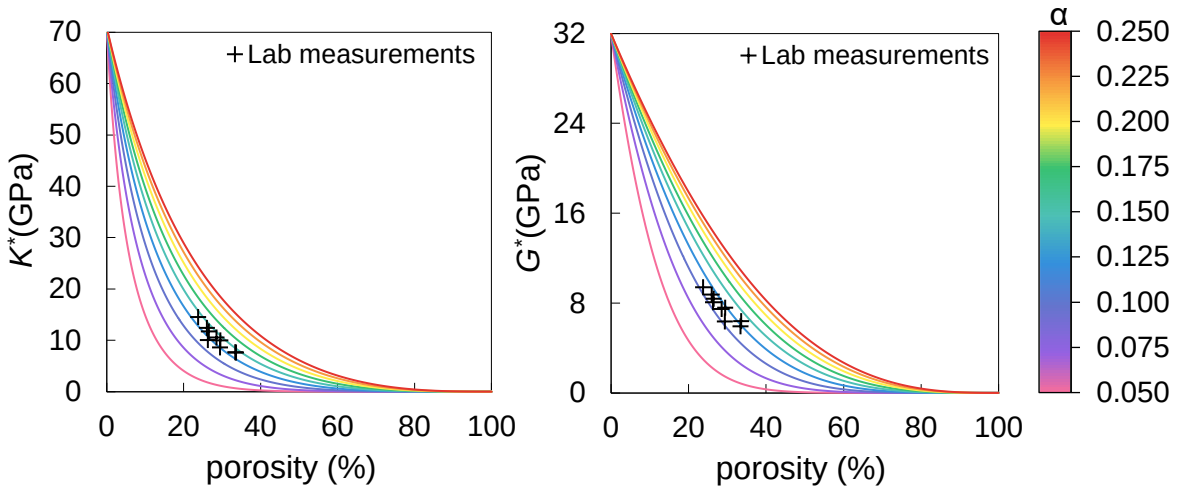

Figure 41. Evolution of (a) the effective bulk K* and (b) shear G* moduli measured in the laboratory for Pont du Gard specimen (cross symbols) and estimated using the DEM model (lines colored according to the aspect ratio of the inclusions).

5.5. Implications for field injections

The conducted percolation experiments in this study have direct implications for matrix-acidizing operations in the petroleum industry and underground CO_2 storage. Matrix-acidizing is used to form dominant wormholes with no ramifications, causing a high degree of pore connectivity and permeability increase. These wormholes are generally formed under intermediate flow rates (Economides and Nolte, 1989; Fredd and Fogler, 1998; Garing et al., 2015; Golfier et al., 2001) and are favored to increase hydrocarbon productivity as they minimize the acid volume required for a given penetration depth (Fredd and Fogler, 1999; Gouze and Luquot, 2011; Ott and Oedai, 2015). Nevertheless, the use of HCl (cost-effective fluid) in acidizing operations requires assisting agents (e.g., gas foams) to retard the rapid HCl-rock reaction and to shift compact dissolution to wormhole formation (Bernadiner et al., 1992; Chang et al., 2022; Raj et al., 2014; Selvaraj et al., 2020). Observations made in this study

suggest the use of dissolved CO_2 in carbonate reservoirs as an alternative to HCl to form wormholes and increase permeability.

Dissolved CO_2 injection (Pool et al., 2013; Pearce et al., 2022) or similar injection strategies relying on accelerating CO_2 dissolution in aquifers (e.g., alternating water and CO_2 injection (Leonenko and Keith, 2008; Imanovs et al., 2020), water injection on top of the injected CO_2 (Hassanzadeh et al., 2009) are technically-viable geological CO_2 storage concepts. These injection approaches reduce the leakage risk associated with the standard practice of supercritical CO_2 storage (Kivi et al., 2022; Pearce et al., 2022). CO_2 dissolution into the water can be achieved at the surface (Zendehboudi et al., 2011) or depth in the injection wellbore (Pool et al., 2013). However, continuous feeding of the reservoir rock with CO_2 solutions likely leads to severe wormholing in carbonate aquifers (Privalov et al., 2019). The possible formation of these highly conductive wormholes, even during conventional supercritical CO_2 injection, is not completely ruled out and wormholes may form (1) in the near-wellbore region before CO_2 dries out the resident brine (Kim and Santamarina, 2015; Ott et al., 2012; Vanorio et al., 2011) but are more likely occur (2) in the peripheral areas of the CO_2 plume in contact with the CO_2-rich brine (Gouze and Luquot, 2011; Rohmer et al., 2016).

In acidizing operations, wormholes are optimally engineered (Cohen et al., 2008; Fredd and Fogler, 1998). In the context of CO_2 storage, however, extensive spatiotemporal evolution of flow conditions and reservoir-scale heterogeneities introduce significant uncertainties in the density, shape, and interactions of the created wormholes (Daccord et al., 1989; Ennis-King and Paterson, 2007; Ott and Oedai, 2015). These uncertainties render wormhole formation and the ensuing effects on CO_2 flow and storage mechanisms difficult to predict. Given that wormholes make the altered rock much more permeable than the intact rock, they may increase reservoir injectivity if they occur in the near-wellbore region. However, flow localization reduces pore fluid sweeping efficiency and, probably, storage capacity (Selvadurai et al., 2017). Moreover, wormholes are susceptible to collapse under elevated overburden stress, potentially speeding up reservoir compaction (Lebedev et al., 2017; Rohmer et al., 2016; Snippe et al., 2017). This may result in weakening the caprock, compromising its sealing integrity (Hangx et al., 2013; Jeanne et al., 2020).

Chapter 6

Conclusions and recommendations

6.1. Conclusions

In this thesis, experiments and reactive transport modeling have been used to improve our understanding of CO_2 interactions with a highly-permeable limestone as a representative host rock for geologic CO_2 storage. Percolation experiments using CO_2-saturated water and HCl solutions have provided insights into the changes in microstructure and hydromechanical properties of the examined limestone. It is found that for a given constant flow rate and pH of the injected acidic solutions, acid type (weak or strong) controls the solute transport and chemical reactions (i.e., dissolution regime), yielding marked differences in the pore structure evolution. The complete dissociation of HCl gives rise to a compact dissolution pattern, whereas the partial dissociation of dissolved CO_2 results in wormhole formation. Under both conditions, dissolution patterns deviate from the theoretical uniform dissolution pattern suggested by the calculated *Pe* and *Da* numbers. HCl injection slightly increases the rock porosity (0.3%-0.7%), which correlates with a 3 to 7-fold increase in permeability and a reduction of less than 20% in elastic moduli. However, injecting CO_2-saturated water resulted in a significant enhancement in limestone porosity (by up to 9.67%) sharply attenuating the rock stiffness and strength (up to ≈ 50% and ≈ 65% reductions in elastic moduli and uniaxial compressive strength, respectively). Wormhole formation during CO_2 injection drastically increases limestone permeability by three orders of magnitude. The DEM homogenization approach captures the mechanical weakening as a function of rock porosity using a single geometrical factor that is consistent with earlier values for carbonates.

A MATLAB-based approach has been developed to quantify and visualize the porosity of limestones from X-ray CT images. The method has been applied to two specimens of the Pont Du Gard Limestone to construct 3D porosity distribution maps. The digital rock realizations unravel the extremely heterogeneous structure of the examined samples. Employing a power-law porosity-permeability relationship, I have generated heterogeneous permeability maps of the specimens that feed as inputs into 3D Darcy-scale reactive transport models of the experiments. This numerical model considering pore space heterogeneities solely on the permeability distribution map could satisfactorily reproduce the chemically-driven porosity evolutions and developed dissolution patterns in the cores, implying tightly coupled flow and reaction fields. However, a perfect quantitative match was missing likely due to coarse

numerical mesh utilized to afford the computational costs, simplifications in the initial distribution of reactive surface area, and the correlation used to address its evolution.

The simulations show that pore space heterogeneities impose a primary control on the formation of instabilities in the dissolution front. Yet, a proper porosity-permeability correlation is a key parameter to accurately capture the transition between different dissolution patterns. On the one hand, the slight modification in porosity in the form of compact dissolution in the HCl injection case could be simulated with the classical power-law correlation with $n = 3$. On the other hand, a large exponent n of ≈ 15 was required to capture the substantial porosity increase in the form of a wormhole during injection of CO_2-saturated water. Nevertheless, the correlations obtained from the laboratory experiments cannot be directly applied to field-scale simulations. This is because the extent of permeability evolution is highly scale-dependent with n growing to ≈ 27 for the bulk behavior of the core containing a wormhole. A multi-step implementation and calibration of the developed Darcy-scale reactive transport model from the scale of the percolation experiments to underground rock laboratories and to field-scale injections would contemplate the effects of small-scale heterogeneities on the interaction between the rock formation and the injected CO_2.

The findings of this study are of great importance to acid-rock interactions in particular in geological CO_2 storage and acid stimulation operations. The results outline wormhole formation as a phenomenon that may affect CO_2 storage security and efficiency in carbonate reservoirs and thus should be examined carefully. The combination of digital rock physics and reactive transport modeling enables capturing the dynamics of fluid-rock interactions that result in such complex dissolution regimes. The developed continuum-scale modeling framework provides a promising tool upon appropriate calibration to explore reactive transport across scales.

6.2. Recommendations

This study has provided insights into possible geochemical interactions of CO_2 with permeable limestone and their effects on hydraulic and mechanical properties of the rock. Nevertheless, some aspects remain unsolved and deserve investigation in future research:

1. In this study, the percolation experiments with CO_2-saturated water have been performed under open flow conditions. The continuous renewal of the acidic fluid at the core inlet results in a continuous dissolution of calcite and a significant increase in porosity and permeability and substantial mechanical weakening. Alterations of rock properties under such conditions represent an upper limit of the extent of interactions under underground conditions. CO_2 is injected in free phase but forms different regions around the wellbore depending on its saturation (volumetric proportion in the pore space) and the extent of dissolution in water. Therefore, the extent of reactions inferred from the conducted experiments should not come up with conclusive statements for the whole reservoir rock injected with CO_2. The gained knowledge should rather be used to calibrate numerical models for field-scale predictions.

2. This study has evaluated potential changes in single-phase flow properties of the reservoir rock as result of chemical reactions with CO_2. However, underground CO_2 injection involves two-phase flow of CO_2 and water. Assessing the impacts of chemical reactions on two-phase flow parameters (e.g., relative permeability of CO_2 and water and capillary entry pressure) deserves further investigation. This type of researchin carbonate rocks, however, is not straight forward because the mentioned parameters are continuum rock properties and need to be measured on continuum rock domains, a condition hardly met in limestones reacted with CO_2. Developing an appropriate approach to uniformly alter the porous structure of carbonate rocks remains a challenge.

3. This study has used a single step DEM approach to capture the attenuation in elastic constants of the rock as function of rock porosity using a single geometrical factor. This approach particularly suits two-phase composite material, well representing Pont Du Gard Limestone. If the rock contains non-negligible contents of cement/micrite-bearing carbonates, commonly containing micro- and nano-porosity, the effect of different porosity groups on the rock behavior should be considered separately. This can be achieved through performing multiple homogenization procedures in sequence. The application of multi-stage homogenization and alternative schemes to the utilized DEM method requires further verification.

4. Ex-situ XMCT imaging on the limestone samples before and after interactions with acidic solutions has been conducted to assess the initial and final status of the pore space and porosity distributions. Real-time imaging of percolation experiments using X-ray transparent cells would yield a better understanding of coupled fluid flow and reaction processes that control the dynamics of formation of different dissolution regimes .

5. 3D Darcy-scale simulations of percolation experiments using realistic permeability maps have enabled an efficient reproduction of the changes in effluent chemistry, porosity, and permeability, and the observed dissolution patterns in the examined limestone. However, a perfect quantitative match with image-based porosity of altered limestone cores at the grid level is missing. Improvements in the modelling can be made by considering heterogeneities on the distribution of mineral surface area as a key parameter that affects the extent of dissolution reactions at the grid scale. The use of imaging data combined with proper digital rock physic models helps evaluating the distribution of mineral surface area in the rock.

6. Explicit porosity- permeability relationships have been used to construct permeability maps of limestone specimens from the XMCT- based porosity distribution data to feed into3D Darcy-scale reactive transport models. This approach may bear some errors as the porosity estimated from CT images accounts also for isolated pores that not affect the flow field. More rigorous image processing techniques that deal with pore network connectivity in addition to porosity have been developed. Using such approaches to construct more accurate permeability maps wouldimprove the reproduction of the flow and reaction patterns.

7. Reactive transport modelling of CO_2 injection into cm-scale limestone samples helped calibrate reaction rates and porosity-permeability relationship during wormhole

formation. However, these parameters are dramatically scale-dependent and cannot be directly used for field-wide simulations. Conducting similar experiments on meter-size samples in the laboratory or at decametre-scale underground rock laboratories can be of great help to calibrate and validate numerical models for field-scale simulations.

References

Abdulrahman, A., Varol, S., 2020. A review of image segmentation using MATLAB environment. In 2020 8th International Symposium on Digital Forensics and Security (ISDFS) (pp. 1-5). IEEE.

Adam, L., MacFarlane, J., Wijk, K.V., Shragge, J., Higgs, K., 2015. Monitoring how carbonate cement dissolution affects rock frame properties due to CO_2 injection. In: 3rd International Conference on Rock Physics Perth Australia.

Aguilera, R., 1980. Naturally fractured reservoirs. United States: N. p.

Agofack, N., Ghabezloo, S., Sulem, J., 2020. Chemo-poro-elastoplastic modelling of an oilwell cement paste: macroscopic shrinkage and stress-strain behaviour. Cem. Concr. Res. 132, 106046.

Ahmadinejad, A., Kivi, I.R., 2021. An experimental investigation on the poroelastic response of a water-saturated limestone to hydrostatic compression. Bull. Eng. Geol. Environ. 80, 3817–3832.

Akin, S., Kovscek, A.R., 2003. Computed tomography in petroleum engineering research. Geol. Soc. Spec. Publ. 215(1), 23-38.

Akono, A.T., Davila, G., Druhan, J., Shi, Z., Jessen, K., Tsotsis, T., Fuchs, S., Crandall, D., Dalton, L., Tkach, M.K., Goodman, A.L., Frailey, S., Werth, C.J., 2019. A review of geochemical–mechanical impacts in geological carbon storage reservoirs. Greenhouse Gas Sci. Technol. 9, 474–504.

Akono, A.T., Davila, G., Druhan, G., Shi, Z., Jessen, K., Tsotsis, T., 2020. Influence of geochemical reactions on the creep behavior of Mt.Simon sandstone. Int. J. Greenhouse Gas Control 103, 103183.

Alam, M.M., Hjuler, M.L., Foged, H., Lykke, I., Christensen, H.F., Fabricius, I.L., 2014. Petrophysical and rock-mechanics effects of CO_2 injection for Enhanced oil recovery: experimental study on chalk from south Arne field, north sea. J. Pet. Sci. Eng. 122, 468–487.

Al-Ameri, W.A., Abdulraheem, A., Mahmoud, M., 2016. Long-term effects of CO_2 sequestration on rock mechanical properties. J. Energy Resour. Technol. 138, 012201-1.

Al-Khulaifi, Y., Lin, Q., Blunt, M.J., Bijeljic, B., 2018. Reservoir-condition pore-scale imaging of dolomite reaction with supercritical CO_2 acidified brine: Effect of pore-structure on reaction rate using velocity distribution analysis. Int. J. Greenhouse Gas Control 68, 99-111.

Aman, M., Espinoza, D.N., Ilgen, A.G., Major, J.R., Eichhubl, P., Dewers, T.A., 2018. CO_2-induced chemo-mechanical alteration in reservoir rocks assessed via batch reaction experiments and scratch testing. Greenhouse Gases Sci. Technol. 8(1), 133-49.

Andrä, H., Combaret, N., Dvorkin, J., Glatt, E., Han, J., Kabel, M., Keehm, Y., Krzikalla, F., Lee, M., Madonna, C., Marsh, M., 2013. Digital rock physics benchmarks—Part I: Imaging and segmentation. Comput. Geosci. 50, 25-32.

Andreani, M., Luquot, L., Gouze, P., Godard, M., Hoise, E., Gibert, B., 2009. Experimental study of carbon sequestration reactions controlled by the percolation of CO_2-rich brine through peridotites. Environ. Sci. Technol. 43(4), 1226-31.

Andre, L., Audigane, M., Azaroual, A.M., 2017. Numerical modeling of fluid-rock chemical interactions at the supercritical CO_2–liquid interface during CO_2 injection into a carbonate reservoir, the Dogger aquifer (Paris Basin, France). Energy Convers. Manage. 48, 1782-1797.

Arson, C., Vanorio, T., 2015. Chemomechanical evolution of pore space in carbonate microstructures upon dissolution: Linking pore geometry to bulk elasticity. J. Geophys. Res. Solid Earth 120(10), 6878-94.

Assayag, N., Matter, J., Ader, M., Goldberg, D., Agrinier, P., 2009. Water–rock interactions during a CO_2 injection field-test: implications on host rock dissolution and alteration effects. Chem. Geol. 265(1-2), 227–35.

Assefa, S., McCann, C., Sothcott, J., 2003. Velocities of compressional and shear waves in limestones. Geophys. Prospect. 51(1), 1-3.

Atanassova, R., Cama, J., Soler, J.M., Offeddu, F.G., Queralt, I., Casanova, I., 2013. Calcite interaction with acidic sulfate solutions: a vertical scanning interferometry and energy-dispersive XRF study. Eur. J. Mineral 25(3), 331-51.

Atkinson, B.K., Meredith, P.G., 1981. Stress corrosion cracking of quartz: a note on the influence of chemical environment. Tectonophysics 77(1-2), T1-11.

Atkinson, B.K., 1982. Subcritical crack propagation in rocks: theory, experimental results and applications. J. Struct. Geol. 4(1), 41-56.

Bachu, S., 2003. Screening and ranking of sedimentary basins for sequestration of CO_2 in geological media in response to climate change. Environ. Geol.44, 277-289.

Bachu, S., Adams, J.J., 2003. Sequestration of CO_2 in geological media in response to climate change: capacity of deep saline aquifers to sequester CO_2 in solution. Energy Convers. Manag. 44(20), 3151-3175.

Bemer, E., Lombard, J.M., 2010. From injectivity to integrity studies of CO_2 geological storage. Oil Gas Sci. Tech. 65, 445–459.

Bemer, E., Nguyen, M.T., Dautriat, J., Adelinet, M., Fleury, M., Youssef, S., 2016. Impact of chemical alteration on the poromechanical properties of carbonate rocks. Geophys. Prospect. 64(4), 810-827.

Benson, S., Pini, R., Reynolds, C., Krevor, S., 2013. Relative permeability analyses to describe multi-phase flow in CO_2 storage reservoirs. Glob Global CCS Institute Targeted Report.

Berg, S., Saxena, N., Shaik, M., Pradhan, C., 2018. Generation of ground truth images to validate micro-CT image-processing pipelines. Leading Edge 37(6), 412-420.

Bernadiner, M.G., Thompson, K.E., Fogler, H.S., 1992. Effect of foams used during carbonate acidizing. SPE Prod. Eng. 7(04), 350-6.

Berryman, J.G., Pride, S.R., Wang, H.F., 2002. A differential scheme for elastic properties of rocks with dry or saturated cracks. Geophys. J. Int. 151(2), 597-611.

Bertier, P., Swennen, R., Laenen, B., Lagrou, D., Dreesen, R., 2006. Experimental identification of CO_2–water-rock interactions caused by sequestration of CO_2 in Westphalian and Buntsandstein sandstones of the Campine Basin (NE-Belgium). J. Geochem. Explor. 89, 10–14.

Bhuiyan, M.H., Agofack, N., Gawel, K.M., Cerasi, P.R., 2020. Micro- and macroscale consequences of interactions between CO_2 and shale rocks. Energies 13, 1167.

Birkholzer, J.T., Zhou, Q., Tsang, C.F., 2009. Large-scale impact of CO_2 storage in deep saline aquifers: a sensitivity study on pressure response in stratified systems. Int. J. Greenhouse Gas Control 3, 181–194.

Birkholzer, J.T., Tsang, C.F., Bond, A.E., Hudson, J.A., Jing, L., Stephansson, O., 2019. 25 years of DECOVALEX-Scientific advances and lessons learned from an international research collaboration in coupled subsurface processes. Int. J. Rock Mech. Min. Sci. 122, 103995.

Bossart, P., Bernier, F,, Birkholzer, J., Bruggeman, C., Connolly, P., Dewonck, S., Fukaya, M., Herfort, M., Jensen, M., Matray, J.M., Mayor, J.C., Moeri, A., Oyama, T., Schuster, K., Shigeta, N., Vietor, T., Wieczorek, K., 2017. Mont Terri rock laboratory, 20 Years of Research: Introduction, Site Characteristics and Overview of Experiments. Swiss J. Geosci. 110(1), 3–22.

Brantley, S.L., Kubicki, J.D. and White, A.F. eds., 2008. Kinetics of water-rock interaction.

Brich, F., 1960. The Velocity of Compressional Waves in Rocks to 10 kbars. Part 1. J. Geophys. Res. 65, 1083-102.

Brosse, E., Magnier, C., Vincent, B., 2005. Modelling fluid-rock interaction induced by the percolation of CO_2-enriched solutions in core samples: the role of reactive surface area. Oil Gas Sci. Technol. IFP 60(2), 287-305.

Busch, A., Alles, S., Gensterblum, Y., Prinz, D., Dewhurst, D.N., Raven, M.D., Stanjek, H., Krooss, B.M., 2008. Carbon dioxide storage potential of shales. Int. J. Greenhouse Gas Control 2, 297–308.

Busch, A., Bertier, P., Gensterblum, Y., Rother, G., Spiers, C.J., Zhang, M., Wentinck, H.M., 2016. On sorption and swelling of CO_2 in clays. Geomech. Geophys. Geo-Energy Geo-Resour. (GGGG) 2, 111-130.

Bui, M., Adjiman, C.S., Bardow, A., Anthony, E.J., Boston, A., Brown, S., Fennell, P.S., Fuss, S., Galindo, A., Hackett, L.A., 2018. Carbon capture and storage (CCS): the way forward. Energy Environ. Sci. 11, 1062–1176.

Baumann, G., Henninges, J., De Lucia, M., 2014. Monitoring of saturation changes and salt precipitation during CO_2 injection using pulsed neutron-gamma logging at the Ketzin pilot site. Int. J. Greenhouse Gas Control 28, 134-146.

Cama, J., Soler, J.M., Ayora, C., 2019. Acid water–rock–cement interaction and multicomponent reactive transport modeling. Rev. Mineral Geochem. 85(1), 459-98.

Canal, J., Delgado, J., Falcon, I., Yang, Q., Juncosa, R., Barrientos, V., 2013. Injection of CO_2-saturated water through a siliceous sandstone plug from the Hontomin test site (Spain): experiment and modeling. Environ. Sci. Technol. 47, 159−167.

Carman, P.C., 1937. Fluid flow through granular beds. Trans. Inst. Chem. Eng. 15, 150-66.

Cavanagh, A. Ringrose, P., 2011. Simulation of CO_2 distribution at the In Salah storage site using high-resolution field-scale models. Energy Procedia, 4, 3730-3737.

Celia, M.A., 2017. Geological storage of captured carbon dioxide as a large-scale carbon mitigation option. Water Resour. Res. 53, 3527–3533.

Chang, F.F., Cairns, A.J., Sayed, M.A., 2022. Acid retardation for deeper stimulation—Revisiting the chemistry and evaluation methods. Can. J. Chem. Eng. 100(6), 1298-308.

Cheng, A.H.D., 2016. Poroelasticity. Theory and Applications of Transport in Porous Media 27.

Choi, C.S., Kim, J., Song, J.J., 2021. Analysis of shale property changes after geochemical interaction under CO_2 sequestration conditions. Energy 214, 118933.

Clark, A.C., Vanorio, T., 2016. The rock physics and geochemistry of carbonates exposed to reactive brines. J. Geophys. Res. Solid Earth 121, 1497–1513.

Cohen, C.E., Ding, D., Quintard, M., Bazin, B., 2008. From pore scale to wellbore scale: Impact of geometry on wormhole growth in carbonate acidization. Chem. Eng. Sci. 63, 3088-3099.

Compton, R.G., Pritchard, K.L., Unwin, P.R., 1989. The dissolution of calcite in acid waters: mass transport versus surface control. Freshwater Biol. 22(2), 285-8.

Crandall, D., Moore, J., Gill, M., Stadelman, M., 2017. CT scanning and flow measurements of shale fractures after multiple shearing events. Int. J. Rock Mech. Min. Sci. 100, 177–187.

Cui, G., Zhang, L., Ren, B., Enechukwu, E., Liu, Y., Ren, S., 2016. Geothermal exploitation from depleted high temperature gas reservoirs via recycling supercritical CO_2: Heat mining rate and salt precipitation effects. Appl. Energy 183, 837-852.

Cui, G., Ren, S., Dou, B., Ning, F., 2021. Geothermal energy exploitation from depleted high-temperature gas reservoirs by recycling CO_2: The superiority and existing problems. Geosci. Front. 12(6), 101078.

Culshaw, M.G., Ulusay, R., 2015. The ISRM suggested methods for rock characterization, testing, and monitoring.

Daccord, G., Touboul, E., Lenormand, R., 1989. Carbonate acidizing: toward a quantitative model of the wormholing phenomenon. SPE Prod. Eng. 4(01), 63-8.

Dai, J., Yang, S., Chen, H., Shen, X., 2005. Geochemistry and occurrence of inorganic gas accumulations in Chinese sedimentary basins. Org. Geochem. 36, 1664-1688.

Dai, Z., Viswanathan, H., Xiao, T., Hakala, A., Lopano, C., Guthrie, G., McPherson, B., 2019. Reactive transport modeling of geological carbon storage associated with CO_2 and brine leakage. Science of Carbon Storage in Deep Saline Formations, 67-88.

Dang, W., Wu, W., Konietzky, H., Qian, J., 2019. Effect of shear-induced aperture evolution on fluid flow in rock fractures. Comput. Geotech. 114:103152.

Darcy, H., 1856. Les fontaines publiques de la ville de Dijon: Exposition et application des principes à suivre et des formules à employer dans les questions de distribution d'eau: Ouvrage terminé par un appendice relatif aux fournitures d'eau de plusieurs villes, au filtrage des eaux et à la fabrication des tuyaux de fonte, de plomb, de tôle et de bitume.

Davila, M.G., Cama, J., Luquot, L., Soler, J.M., Ayora, C., 2017. Reactivity of a marl caprock in contact with acid solutions under different PCO_2 conditions (atmospheric, 10, and 37 bar). Procedia Earth Planet. Sci. 17, 528-531.

Davila, G., Dalton, L., Crandall, D.M., Garing, C., Werth, C.J., Druhan, J.L., 2020. Reactive alteration of an Mt. Simon Sandstone due to CO_2-rich brine displacement. Geochim. Cosmochim. Acta 271, 227–247.

Dawson, G.K., Pearce, J.K., Biddle, D., Golding, S.D., 2015. Experimental mineral dissolution in Berea Sandstone reacted with CO_2 or SO_2–CO_2 in NaCl brine under CO_2 sequestration conditions. Chem. Geol. 2(399), 87-97.

Deng, H., Fitts, J.P., Crandall, D., McIntyre, D., Peters, C.A., 2015. Alterations of fractures in carbonate rocks by CO_2-acidified brines. Environ. Sci. Technol. 49(16), 10226-10234.

Detwiler, R.L., 2008. Experimental observations of deformation caused by mineral dissolution in variable-aperture fractures. J. Geophys. Res. Solid Earth 113(B8).

Detwiler, R.L., Morris, J.P., 2018. Fracture initiation, propagation, and permeability evolution. Geological Carbon Storage: Subsurface Seals and Caprock Integrity. 119-35.

Dewers, T., Newell, P., Broome, S., Heath, J., Bauer, S., 2014. Geomechanical behavior of Cambrian Mount Simon Sandstone reservoir lithofacies, Iowa Shelf, USA. Int. J. Greenhouse Gas Control 21, 33–48.

Dewhurst, D.N., Delle Piane, C., Esteban, L., Sarout, J., Josh, M., Pervukhina, M., Clennell, M.B., 2018. Microstructural, geomechanical, and petrophysical characterization of shale caprocks. Geological Carbon Storage: Subsurface Seals and Caprock Integrity 1-30.

Dewhurst, D.N., Raven, M.D., Shah, S.S.B.M., Ali, S.S.B.M., Giwelli, M., Firns, S., Josh, M., White, C., 2020. Interaction of super-critical CO_2 with mudrocks: Impact on composition and mechanical properties. Int. J. Greenhouse Gas Control 102, 103163.

Diamond, S., 2000. Mercury porosimetry: An inappropriate method for the measurement of pore size distributions in cement-based materials. Cem. Concr. Res. 30(10), 1517-25.

Dieterich, J.H., 1972. Time-dependent friction in rocks. J. Geophys. Res. 77, 3690–3697.

Dockrill, B., Shipton, Z.K., 2010. Structural controls on leakage from a natural CO_2 geologic storage site: Central Utah, USA. J. Struct. Geol. 32(11), 1768-82.

Dove, P.M., 1995. Geochemical controls on the kinetics of quartz fracture at subcritical tensile stresses. J. Geophys. Res. Solid Earth 100(B11), 22349-22359.

Du, J., Hu, L., Meegoda, J.N., Zhang, G., 2018. Shale softening: Observations, phenomenological behavior, and mechanisms. Appl. Clay Sci. 161, 290-300.

Duan, Z., Sun, R., 2003. An improved model calculating CO_2 solubility in pure water and aqueous NaCl solutions from 273 to 533 K and from 0 to 2000 bar. Chem. Geol. 193(3–4), 257-271.

Durán, E.L., Adam, L., Wallis, I.C., Barnhoorn, A., 2019. Mineral alteration and fracture influence on the elastic properties of volcaniclastic rocks. J. Geophys. Res. Solid Earth 124(5), 4576-4600.

Durham, W.B., Bourcier, W.L., Burton, E.A., 2001. Direct observation of reactive flow in a single fracture. Water Resour. Res. 37(1), 1-12.

Eberli, G.P., Baechle, G.T., Anselmetti, F.S., Incze, M.L., 2003. Factors controlling elastic properties in carbonate sediments and rocks. The Leading Edge 22(7), 654-60.

Economides, M.J., Nolte, K.G., 1989. Reservoir stimulation. Englewood Cliffs, NJ: Prentice Hall.

Egermann, P., Bemer, E., Zinszner, B., 2006. An experimental investigation of the rock properties evolution associated to different levels of CO_2 injection like alteration processes. Int. Symp. Society Core Analysts. 1-15.

Eissa, E.A., Kazi, A., 1988. Relation between static and dynamic Young's moduli of rocks. Int. J. Rock Mech. Min. Sci. Geomech. Abstr. 25(6), 479-482.

El Husseiny, A., Vanorio, T., 2015. The effect of micrite content on the acoustic velocity of carbonate rocks. Geophysics 80, l45–l55.

Elkhoury, J.E., Ameli, P., Detwiler, R.L., 2013. Dissolution and deformation in fractured carbonates caused by flow of CO_2-rich brine under reservoir conditions. Int. J. Greenhouse Gas Control 16, S203-S215.

Elkhoury, J.E., Detwiler, R.L., Ameli, P., 2015. Can a fractured caprock self-heal? Earth Planet. Sci. Lett. 417, 99-106.

Ellis, B., Peters, C., Fitts, J., Bromhal, G., McIntyre, D., Warzinski, R., Rosenbaum, E., 2011. Deterioration of a fractured carbonate caprock exposed to CO_2-acidified brine flow. Greenhouse Gases Sci. Technol. 1(3), 248-260.

Ennis-King, J., Paterson, L., 2007. Coupling of geochemical reactions and convective mixing in the long-term geological storage of carbon dioxide. Int. J. Greenhouse Gas Control 1(1), 86-93.

Espinoza, D.N., Santamarina, J.C., 2010. Water-CO_2-mineral systems: Interfacial tension, contact angle, and diffusion—Implications to CO_2 geological storage. Water Resour. Res. 46.

Espinoza, D.N., Santamarina, J.C., 2012. Clay interaction with liquid and supercritical CO_2: the relevance of electrical and capillary forces. Int. J. Greenhouse Gas Control 10, 351–362.

Espinoza, D.N., Kim, S.H., Santamarina, J.C., 2011. CO_2 geological storage−geotechnical implications. KSCE J. Civil Eng.15, 707-719.

Espinoza, D.N., Jung, H., Major, J.R., Sun, Z., Ramos, M.R., Eichhubl, P., Balhoff, M.T., Choens, R.C., Dewers, T.A., 2018. CO_2 charged brines changed rock strength and stiffness at Crystal Geyser, Utah: Implications for leaking subsurface CO_2 storage reservoirs. Int. J. Greenhouse Gas Control 73, 16-28.

Ettemeyer, F., Lechner, P., Hofmann, T., Andrä, H., Schneider, M., Grund, D., Volk, W., Günther, D., 2020. Digital sand core physics: Predicting physical properties of sand cores by simulations on digital microstructures. Int. J. Solids Struct. 188, 155-168.

Ewy, R.T., 2015. Shale/claystone response to air and liquid exposure, and implications for handling, sampling and testing. Int. J. Rock Mech. Min. Sci. 80, 388-401.

Falcon-Suarez, I., North, L., Amalokwu, K., Best, A., 2016. Integrated geophysical and hydromechanical assessment for CO_2 storage: shallow low permeable reservoir sandstones. Geophysical Prospecting 64, 828–847.

Farquhar, S.M., Pearce, J.K., Dawson, G.K.W., Golab, A., Sommacal, S., Kirste, D., Biddle, D., Golding, S.D., 2015. A fresh approach to investigating CO_2 storage: Experimental CO_2–water-rock interactions in a low-salinity reservoir system. Chem. Geol. 399, 98–122.

Fazeli, H., Nooraiepour, M., Hellevang, H., 2019. Microfluidic study of fracture dissolution in carbonate-rich caprocks subjected to CO_2-charged brine. Ind. Eng. Chem. Res. 59(1):450-7.

Feng, G., Kang, Y., Sun, Z.D., Wang, X.C., Hu, Y.Q., 2019. Effects of supercritical CO_2 adsorption on the mechanical characteristics and failure mechanisms of shale. Energy 15(173), 870-882.

Finley, R.J., 2014. An overview of the Illinois Basin–Decatur project. Greenhouse Gases Sci. Technol. 4(5), 571-579.

Fischer, S., Liebscher, A., De Lucia, M., Hecht, L., 2013. Reactivity of sandstone and siltstone samples from the Ketzin pilot CO_2 storage site-Laboratory experiments and reactive geochemical modeling. Environ. Earth Sci. 70, 3687–3708.

Fjær, E., 2019. Relations between static and dynamic moduli of sedimentary rocks. Geophys. Prospect. 67(1), 128-39.

Foroutan, M., Ghazanfari, E., 2020. CO_2-enriched brine injection's impact on mechanical properties of a sandstone specimen. In: E3S Web of Conferences.

Foroutan, M., Ghazanfari, E., Amirlatifi, A., 2021a. Variation of failure properties creep response and ultrasonic velocities of sandstone upon injecting CO_2-enriched brine. Geomech. Geophys. Geo-energ. Geo-resour. 7, 27.

Foroutan, M., Ghazanfari, E., Amirlatifi, A., Moradian, O., 2021b. Evolution of fracture permeability and aperture during CO_2 storage in varyingly cemented sedimentary rocks. Geomech. Energy Environ. 27, 100289.

Fournier, F., Borgomano, J., 2009. Critical porosity and elastic properties of microporous mixed carbonate-siliciclastic rocks. Geophysics 74(2), E93-109.

Fournier, F., Leonide, P., Biscarrat, K., Gallois, A., Borgomano, J., Foubert, A., 2011. Elastic properties of microporous cemented grainstones. Geophysics 76(6), E211-26.

Fredd, C.N., Fogler, H.S., 1988. Alternative stimulation fluids and their impact on carbonate acidizing. SPE 3(01), 34-41.

Fredd, C.N., Fogler, H.S., 1998. Influence of transport and reaction on wormhole formation in porous media. Fluid Mech. Transp. Phenomena 4, 1933-1949.

Fredd, C.N., Fogler, H.S., 1999. Optimum conditions for wormhole formation in carbonate porous media: Influence of transport and reaction. SPE 4(03), 196-205.

Fredrich, J.T., Menéndez, B., Wong, T.F., 1995. Imaging the pore structure of geomaterials. Science 268(5208), 276-279.

Frery, E., Gratier, J.P., Ellouz-Zimmerman, N., Loiselet, C., Braun, J., Deschamps, P., Blamart, D., Hamelin, B., Swennen, R., 2015. Evolution of fault permeability during episodic fluid circulation: Evidence for the effects of fluid-rock interactions from travertine studies (Utah–USA). Tectonophysics 651, 121-37.

Fuchs, S.J., Espinoza, D.N., Lopano, C.L., Akono, A.T., Werth, C.J., 2019. Geochemical and geomechanical alteration of siliciclastic reservoir rock by supercritical CO_2-saturated brine formed during geological carbon sequestration. Int. J. Greenhouse Gas Control 88, 251-260.

Garcia Rios, M., 2015. Dissolved CO_2 effect on the reactivity of the Hontomin reservoir rocks (limestone and sandstone). Ph. D. thesis, Technical University of Catalonia, Barcelona.

Garcia-Rios, M., Cama, J., Luquot, L., Soler, J.M., 2015. Interaction between CO_2-rich sulfate solutions and carbonate reservoir rocks from atmospheric to supercritical CO_2 conditions: Experiments and modeling. Chem. Geol. 414, 95–108.

Garcia-Rios, M., Luquot, L., Soler, J.M., Cama, J., 2017. The role of mineral heterogeneity on the hydrogeochemical response of two fractured reservoir rocks in contact with dissolved CO_2. Appl. Geochem. 84, 202-217.

Garing, C., Gouze, P., Kassab, M., Riva, M.O.N.I.C.A., Guadagnini, A.L.B.E.R.T.O., 2015. Anti-correlated porosity–permeability changes during the dissolution of carbonate rocks: experimental evidences and modeling. Transp. Porous Media 107(2), pp.595-621.

Gassmann, F., 1951. Elastic waves through a packing of spheres. Geophysics 16, 673-685.

Gaus, I., Azaroual, M., Czernichowski-Lauriol, I., 2005. Reactive transport modelling of the impact of CO_2 injection on the clayey cap rock at Sleipner (North Sea). Chem. Geol. 3-4, 319-337.

Gaus, I., 2010. Role and impact of CO_2–rock interactions during CO_2 storage in sedimentary rocks. Int. J. Greenhouse Gas Control 4, 73–89.

Giesting, P., Guggenheim, S., Koster van Groos, A.F., Busch, A., 2012. X-ray Diffraction Study of K- and Ca-Exchanged Montmorillonites in CO_2 Atmospheres. Environ. Sci. Technol. 46(10), 5623–5630.

Giraud, A., Nguyen, N.B., Grgic, D., 2012. Effective poroelastic coefficients of isotropic oolitic rocks with micro and meso porosities. Int. J. Eng. Sci. 58, 57-77.

Gislason, S.R., Wolff-Boenisch, D., Stefansson, A., Oelkers, E.H., Gunnlaugsson, E., Sigurdardottir, H., Sigfusson, B., Broecker, W.S., Matter, J.M., Stute, M., Axelsson, G., Fridriksson, T., 2010. Mineral sequestration of carbon dioxide in basalt: A pre-injection overview of the CarbFix project. Int. J. Greenhouse Gas Control 4, 537-545.

Gherardi, F., Xu, T., Pruess, K., 2007. Numerical modeling of self-limiting and self-enhancing caprock alteration induced by CO_2 storage in a depleted gas reservoir. Chem. Geol. 244, 103–129.

Godsey, W.E. Fresh, brackish, or saline water for hydraulic fracs: What are the options? US Environmental Protection Agency. https://epa.gov

Golfier, F., Bazin, B., Zarcone, C., Lernormand, R., Lasseux, D., Quintard, M., 2001. Acidizing carbonate reservoirs: numerical modeling of wormhole propagation and comparison to experiments. SPE conference.

Golfier, F., Zarcone, C., Bazin, B., Lenormand, R., Lasseux, D., Quintard, M., 2002. On the ability of a darcy-scale model to capture wormhole formation during the dissolution of a porous medium. J. Fluid Mech. 457, 213-254.

Gouze, P., Noiriel, C., Bruderer, C., Loggia, D., Leprovost, R., 2003. X-ray tomography characterization of fracture surfaces during dissolution. Geophys. Res. Lett. 30(5), 1267.

Gouze, P., Luquot, L., 2011. X-ray microtomography characterization of porosity, permeability and reactive surface changes during dissolution. J. Contam. Hydrol. 120-121, 45-55.

Gray, K., 2015. Carbon Storage Atlas (No. DOE-SSEB-42590-120). Southern States Energy Board, Peachtree Corners, GA (United States).

Gray, F., Anabaraonye, B., Shah, S., Boek, E., Crawshaw, J., 2018. Chemical mechanisms of dissolution of calcite by HCl in porous media: Simulations and experiment. Adv. Water. Resour. 1, 121:369-87.

Greenwood, H.J., Barnes, H.L., 1966. Binary mixtures of volatile components. In Handbook of Physical Constants (ed. S. P. Clark). The Geological Society of America Memoir 97.

Grgic, D., 2011. Influence of CO_2 on the long-term chemomechanical behavior of an oolitic limestone. J. Geophys. Res. Solid Earth 116, 1–22.

Grombacher, D., Vanorio, T., Ebert, Y., 2015. Time-lapse acoustic, transport, and NMR measurements to characterize microstructural changes of carbonate rocks during injection of CO_2-rich water. Geophysics 77, WA169–WA179.

Guglielmi, Y., Nussbaum, C., Cappa, F., De Barros, L., Rutqvist, J., Birkholzer, J., 2021. Field-scale fault reactivation experiments by fluid injection highlight aseismic leakage in caprock analogues: Implications for CO_2 sequestration. Int. J. Greenhouse Gas Control 111, 103471.

Gunter, W.D., Wiwehar, B., Perkins, E.H., 1997. Aquifer disposal of CO_2-rich greenhouse gases: extension of the time scale of experiment for CO_2-sequestering reactions by geochemical modeling. Mineral Petrol. 59(1-2), 121.

Hadian, P., Rezaee, R., 2019. The effect of supercritical CO_2 on shaly caprocks. Energies 13, 149.

Hajirezaie, S., Peters, C.A., Cole, D.R., Sheets, J.M., Kim, J.J., Swift, A.M., Crandall, D., Cheshire, M.C., Stack, A.G., Anovitz, L.M., 2022. Sealing fractures to increase underground storage security: Lessons learned from a multiscale multimodal imaging study of a syntaxial vein in a mudrock. Chem. Geol. 614, 121164.

Hangx, S.J.T., Spiers, C.J., Peach, C.J., 2010. The effect of deformation on permeability development in anhydrite and implications for caprock integrity during geological storage of CO_2. Geofluids 10, 369–387.

Hangx, S., van der Linden, A., Marcelis, F., Bauer, A., 2013. The effect of CO_2 on the mechanical properties of the Captain sandstone: Geological storage of CO_2 at the Goldeneye field (UK). Int. J. Greenhouse Gas Control 19, 609–619.

Hangx, S., Bakker, E., Bertier, P., Nover, G., Busch, A., 2015. Chemical–mechanical coupling observed for depleted oil reservoirs subjected to long-term CO_2-exposure — a case study of the Werkendam natural CO_2 analogueue field. Earth Planet. Sci. Lett. 28, 230–242.

Han, D., Batzle, M.L., 2004. Gassmann's equation and fluid-saturation effects on seismic velocities. Geophysics 69(2), 398-405.

Hao, Y., Smith, M., Sholokhova, Y., Carroll, S., 2013. CO_2-induced dissolution of low permeability carbonates. Part II: Numerical modeling of experiments. Adv. Water Resour. 62, 388-408.

Hao, Y., Smith, M.M., Carroll, S.A., 2019. Multiscale modeling of CO_2-induced carbonate dissolution: From core to meter scale. Int. J. Greenhouse Gas Control 88, 272-289.

Harbert, W., Goodman, A., Spaulding, R., Haljasmaa, I., Crandall, D., Sanguinito, S., Kutchko, B., Tkach, M., Fuchs, S., Werth, C.J., Tsotsis, T., Dalton, L., Jessen, K., Shi, Z., Frailey, S., 2020. CO_2 induced changes in Mount Simon sandstone: Understanding links to post CO_2 injection monitoring, seismicity, and reservoir integrity. Int. J. Greenhouse Gas Control 100, 103109.

Hassanzadeh, H., Pooladi-Darvish, M., Keith, D.W., 2009. Accelerating CO_2 dissolution in saline aquifers for geological storage-Mechanistic and sensitivity studies. Energy Fuels 23(6), 3328-36.

Head, D., Vanorio, T., 2016. Effects of changes in rock microstructures on permeability: 3-D printing investigation. Geophys. Res. Lett. 43(14), 7494-7502.

Heap, M.J., Baud, P., Meredith, P.G., Bell, A.F., Main, I.G., 2009. Time-dependent brittle creep in Darley Dale sandstone. J. Geophys. Res. Solid Earth 114(B7).

Heller, R., Zoback, M., 2014. Adsorption of methane and carbon dioxide on gas shale and pure mineral samples. J. Unconv. Oil Gas Resour. 8, 14-24.

Hildenbrand, A., Schlomer, S., Krooss, B.M., 2002. Gas breakthrough experiments on fine-grained sedimentary rocks. Geofluids 2, 3-23.

Hommel, J., Coltman, E. Class, H., 2018. Porosity–permeability relations for evolving pore space: a review with a focus on (bio-) geochemically altered porous media. Transp. Porous Media 124(2), 589-629.

Horsrud, P., 2001. Estimating Mechanical Properties of Shale From Empirical Correlations. SPE Drill & Compl 16, 68–73.

Houben, M.E., van Eeden, J.C., Barnhoorn, A., Hangx, S.J., 2020. Fracture-induced permeability in Whitby mudstone. Environ. Sci. Technol. 54(15), 9564-72.

Hu, M.M., Hueckel, T., 2013. Environmentally enhanced crack propagation in a chemically degrading isotropic shale. Geotechnique 63(4), 313-321.

Hu, M., Rutqvist, J., 2022. Multi-scale coupled processes modeling of fractures as porous, interfacial and granular systems from rock images with the numerical manifold method. Rock Mech. Rock Eng. 55, 3041–3059.

Huang, Y.H., Yang, S.Q., Li, W.P., Hall, M.R., 2019. Influence of supercritical CO_2 on the strength and fracture behavior of brine-saturated sandstone specimens. Rock Mech. Rock Eng. 53, 653–670.

Hudson, J.A., Harrison, J.P., 2000. Engineering rock mechanics: an introduction to the principles. Elsevier.

Huq, F., Haderlein, S.B., Cirpka, O.A., Nowak, M., Blum, P., Grathwohl, P., 2015. Flowthrough experiments on water-rock interactions in a sandstone caused by CO_2 injection at pressures and temperatures mimicking reservoir conditions. Appl. Geochem. 58,136–146.

Ilgen, A.G., Aman, M., Espinoza, D.N., Rodriguez, M.A., Griego, J.M., Dewers, T.A., Feldman, J.D., Stewart, T.A., Choens, R.C., Wislon, J., 2018. Shale-brine-CO_2 interactions and the long-term stability of carbonate-rich shale caprock. Int. J. Greenhouse Gas Control 78, 244–253.

Ilgen, A.G., Newell, P., Hueckel, T., Espinoza, D.N., Hu, M., 2019. Coupled chemical-mechanical processes associated with the injection of CO_2 into subsurface. Science of Carbon Storage in Deep Saline Formations 337-359. Elsevier.

Imanovs, E., Krevor, S. Mojaddam Zadeh, A., 2020. CO_2-EOR and storage potentials in depleted reservoirs in the Norwegian continental shelf NCS. In SPE Europec. OnePetro.

Ishibashi, T., Fang, Y., Elsworth, D., Watanabe, N., Asanuma, H., 2020. Hydromechanical properties of 3D printed fractures with controlled surface roughness: Insights into shear-permeability coupling processes. Int. J. Rock Mech. Min. Sci. 128:104271.

Jackson, S.J., Agada, S., Reynolds, C.A., Krevor, S., 2018. Characterizing drainage multiphase flow in heterogeneous sandstones. Water Resour. Res. 54(4), 3139-3161.

Jackson, S.J., Lin, Q., Krevor, S., 2020. Representative elementary volumes, hysteresis, and heterogeneity in multiphase flow from the pore to continuum scale. Water Resour. Res. 56(6), e2019WR026396.

Jaeger, J.C., Cook, N.G.W., Zimmerman, R.W., 2007. Fundamentals of rock mechanics. Blackwell Publishing.

Jayasekara, D.W., Ranjth, P.G., 2021. Effect of geochemical characteristics on caprock performance in deep saline aquifers. Energy & Fuels 35 (3), 2443-2455.

Jeanne, P., Zhang, Y., Rutqvist, J., 2020. Influence of hysteretic stress path behavior on seal integrity during gas storage operation in a depleted reservoir. J. Rock. Mech. Geotech. Eng. 12(4), 886-99.

Jiang, F., Tsuji, T., 2014. Changes in pore geometry and relative permeability caused by carbonate precipitation in porous media. Phys. Rev. E. 90(5), 053306.

Jimenez-Martinez, J., Hyman, J.D., Chen, Y., Carey, J.W., Porter, M.L., Kang, Q., Guthrie, Jr. G., Viswanathan, H.S., 2020. Homogenization of dissolution and enhanced precipitation induced by bubbles in multiphase flow systems. Geophys. Res. Lett. 47(7), e2020GL087163.

Jin, X., Shah, S.N., Roegiers, J.C., Zhang, B., 2015. An integrated petrophysics and geomechanics approach for fracability evaluation in shale reservoirs. SPE J. 20, 518–526.

Johnson, J.W., Nitao, J.J., Knauss, K.G., 2001. Reactive transport modeling of CO_2 storage in saline aquifers to elucidate fundamental processes, trapping mechanisms, and sequestration partitioning. In: The first national conference on carbon sequestration Washington DC.

Johnson, J.W., Nitao, J.J., Morris, J.P., Blair, S.C., 2004. Reactive transport modeling of cap rock integrity during natural and engineered CO_2 storage. Lawrence Livermore National Laboratory Livermore CA.

Juanes, R., Spiteri, E.J., Orr, F.M.J., Blunt, M.J., 2006. Impact of relative permeability hysteresis on geological CO_2 storage. Water Resour. Res. 42.

Kampman, N., Bickle, M.J., Wigley, M., Dubacq, B., 2013. Fluid flow and CO_2-fluid-mineral interactions during CO_2 storage in sedimentary basins. Chem. Geol. 369, 22-50.

Kampman, N., Busch, A., Bertier, P., Snippe, J., Hangx, S., Pipich, V., Di, Z., Rother, G., Harrington, J.F., Evans, J.P., Maskell, A., 2016. Observational evidence confirms modeling of the long-term integrity of CO_2-reservoir caprocks. Nat. Commun. 7, 12268.

Kane, A.V., 1979. Performance review of a large-scale CO_2-WAG enhanced recovery project, SACROC Unit Kelly-Snyder Field. J. Pet. Technol. 31(02), 217-231.

Kaszuba, J.P., Janecky, D.R., Snow, M.G., 2003. Carbon dioxide reaction processes in a model brine aquifer at 200 C and 200 bars: implications for geologic sequestration of carbon. Appl. Geochem. 18(7), 1065-80.

Kaszuba, J.P., Janecky, D.R., Snow, M.G., 2005. Experimental evaluation of mixed fluid reactions between supercritical carbon dioxide and NaCl brine: Relevance to the integrity of a geologic carbon repository. Chem. Geol. 217, 277– 293.

Kaszuba, J., Yardley, B., Andreani, M., 2013. Experimental perspectives of mineral dissolution and precipitation due to carbon dioxide-water-rock interactions. Rev. Mineral Geochem. 77(1), 153-88.

Khather, M., Saeedi, A., Myers, M.B., Giwelli, A., 2020. Effects of CO_2-saturated brine on the injectivity and integrity of chalk reservoirs. Transp. Porous Media 135, 735–751.

Kim, S., Santamarina, J.C., 2014. CO_2 geological storage: hydro-chemo-mechanical analyses and implications. Greenhouse Gases Sci. Technol. 4, 528–543.

Kim, S., Santamarina, J.C., 2015. Reactive fluid flow in CO_2 storage reservoirs: A 2-D pore network model study. Greenhouse Gases Sci. Technol. 5(4), 462-73.

Kim, K., Vilarrasa, V., Makhnenko, R.Y., 2018. CO_2 injection effect on geomechanical and flow properties of calcite-rich reservoirs. Fluids 3, 66.

Kim, K., Makhnenko, R.Y., 2020. Coupling between poromechanical behavior and fluid flow in tight rock. Transp. Porous Media 135, 487-512.

Kim, K., Makhnenko, R.Y., 2021. Changes in rock matrix compressibility during deep CO_2 storage. Greenhouse Gases Sci. Technol. 11(5), 954-73.

Kittler, J., Illingworth, J., 1985. On threshold selection using clustering criteria. IEEE transactions on systems, man, and cybernetics, (5), 652-655.

Kivi, I.R., Ameri, M.J., Ghassemi, A., 2016. Experimental and numerical study of membrane properties and pore pressure transmission of Ghom shale. Measurement 91, 93-100.

Kivi, I.R., Ameri, M.J., Molladavoodi, H., 2018. Shale brittleness evaluation based on energy balance analysis of stress-strain curves. J. Pet. Sci. Eng. 167, 1-19.

Kivi, I.R., Makhnenko, R.Y., Vilarrasa, V., 2022. Two-phase flow mechanisms controlling CO_2 intrusion into shaly caprock. Transp. Porous Media 141, 771–798.

Kozeny, J., 1927. Uber kapillare leitung der wasser in boden. Royal Academy of Science, Vienna, Proc. Class I. 136, 271-306.

Krevor, S.C.M., Pini, R., Li, B., Benson, S.M., 2011. Capillary heterogeneity trapping of CO_2 in a sandstone rock at reservoir conditions. Geophys. Res. Lett. 38, L15401.

Kwak, J.H., Hu, J.Z., Turcu, R.V., Rosso, K.M., Ilton, E.S., Wang, C., Sears, J.A., Engelhard, M.H., Felmy, A.R., Hoyt, D.W., 2015. The role of H_2O in the carbonation of forsterite in supercritical CO_2. Int. J. Greenhouse Gas Control 5(4), 1081–92.

Lai, P., Moulton, K. and Krevor, S., 2015. Pore-scale heterogeneity in the mineral distribution and reactive surface area of porous rocks. Chem. Geol. 411, 260-273.

Lamy-Chappuis, B., Angus, D., Fisher, Q., Grattoni, C., Yardley, B.W., 2014. Rapid porosity and permeability changes of calcareous sandstone due to CO_2-enriched brine injection. Geophys. Res. Lett. 41(2), 399-406.

Lamy-Chappuis, B., Angus, D., Fisher, Q.J., Yardley, B.W.D., 2016. The effect of CO_2-enriched brine injection on the mechanical properties of calcite-bearing sandstone. Int. Greenhouse Gas Control 52, 84-95.

Lang, P.S., Paluszny, A., Zimmerman, R.W., 2016. Evolution of fracture normal stiffness due to pressure dissolution and precipitation. Int. J. Rock Mech. Min. Sci. 88, 12-22.

Laubach, S.E., Lander, R.H., Criscenti, L.J., Anovitz, L.M., Urai, J.L., Pollyea, R.M., Hooker, J.N., Narr, W., Evans, M.A., Kerisit, S.N., Olson, J.E., 2019. The role of chemistry in fracture pattern development and opportunities to advance interpretations of geological materials. Rev. Geophys. 57(3), 1065-111.

Lebedev, M., Zhang, Y., Sarmadivaleh, M., Barifcani, A., Al-Khdheeawi, E., Iglauer, S., 2017. Carbon geosequestration in limestone: Pore-scale dissolution and geomechanical weakening. Int. J. Greenhouse Gas Control 66, 106–119.

Leger, M., Roubinet, D., Jamet, M., Luquot, L., 2022. Impact of hydro-chemical conditions on structural and hydro-mechanical properties of chalk samples during dissolution experiments. Chem. Geol. 594, 120763.

Le Guen, Y., Renard, F., Hellmann, R., Brosse, E., Collombet, M., Tisserand, D., Gratier, J., 2007. Enhanced deformation of limestone and sandstone in the presence of high P CO_2. Fluids 112, 1–21.

Leonenko, Y., Keith, D.W., 2008. Reservoir engineering to accelerate the dissolution of CO_2 stored in aquifers. Environ. Sci. Technol. 42(8), 2742-7.

Li, H.C., De Bruyn, P.L., 1966. Electrokinetic and adsorption studies on quartz. Surf. Sci. 5, 203–220.

Li, S., Zhang, S., Zou, Y., Ma, X., Ding, Y., Li, N., Zhang, X., Kasperczyk, D., 2020. Pore structure alteration induced by CO_2–brine–rock interaction during CO_2 energetic fracturing in tight oil reservoirs. J. Pet. Sci. Eng. 191, 107147.

Liteanu, E., Spiers, C.J., 2009. Influence of pore fluid salt content on compaction creep of calcite aggregates in the presence of supercritical CO_2. Chem. Geol. 265(1-2), 134-47.

Liteanu, E., Niemeijer, A., Spiers, C.J., Peach, C.J., De Bresser, J.H.P., 2012. The effect of CO_2 on creep of wet calcite aggregates. J. Geophys. Res. 117, B03211.

Liteanu, E., Spiers, A., De Bresser, J.H.P., 2013. The influence of water and supercritical CO_2 on the failure behavior of chalk. Tectonophysics 599, 157–169.

Loring, J.S., Thompson, C.J., Wang, Z., Joly, A.G., Sklarew, D.S., Schaef, H.T., Ilton, E.S., Rosso, K.M., Felmy, A.R., 2011. In situ infrared spectroscopic study of forsterite carbonation in wet supercritical CO_2. Environ. Sci. Technol. 45(14), 6204–6210.

Luquot, L., Gouze, P., 2009. Experimental determination of porosity and permeability changes induced by injection of CO_2 into carbonate rocks. Chem. Geol. 265(1-2), 148-159.

Luquot, L., Gouze, P., Niemi, A., Bensabat, J., Carrera, J., 2016. CO_2-rich brine percolation experiments through Heletz reservoir rock samples (Israel): Role of the flow rate and brine composition. Int. J. Greenhouse Gas Control 48, 44–58.

Lyu, Q., Ranjith, P.G., Long, X., Ji, B., 2016. Experimental investigation of mechanical properties of black shales after CO_2-water-rock interaction. Materials 9, 663.

Lyu, Q., Long, X., Ranjith, P.G., Tan, J., Kang, Y., Wang, Z., 2018. Experimental investigation on the mechanical properties of a low-clay shale with different adsorption times in sub-/super-critical CO_2. Energy 147, 1288-1298.

Major, J.R., Eichhubl, P., Dewers ,T.A., Olson, J.E., 2018. Effect of CO_2–brine–rock interaction on fracture mechanical properties of CO_2 reservoirs and seals. Earth Planet. Sci. Lett. 499, 37-47.

Makhnenko, R.Y., Vilarrasa, V., Mylnikov, D., Laloui, L., 2017. Hydromechanical aspects of CO_2 breakthrough into clay-rich caprock. Energy Procedia 114, 3219–3228.

Marbler, H., Erickson, K.P., Schmidt, M., Lempp, C., Pöllmann, H., 2013. Geomechanical and geochemical effects on sandstones caused by the reaction with supercritical CO_2: an experimental approach to in situ conditions in deep geological reservoirs. Environ. Earth Sci. 69, 1981–1998.

Mavko, G., Mukerji, T., Dvorkin, J., 2009. The rock physics handbook. Cambridge Unversity Press.

Mayo, S., Josh, M., Nesterets, Y., Esteban, L., Pervukhina, M., Clennell, M.B., Maksimenko, A., Hall, C., 2015. Quantitative micro-porosity characterization using synchrotron micro-CT and xenon K-edge subtraction in sandstones, carbonates, shales and coal. Fuel 154, 167-173.

Menefee, A.H., Welch, N.J., Frgash, L.P., Hicks, W., Carey, J.W., Ellis, B.R., 2020. Rapid mineral precipitation during shear fracturing of carbonate-rich shales. J. Geophys. Res. Solid Earth 125(6), e2019JB018864.

Menke, H.P., Bijeljic, B., Andrew, M.G., Blunt, M.J., 2015. Dynamic three-dimensional pore-scale imaging of reaction in a carbonate at reservoir conditions. Environ. Sci. Technol. 49(7), 4407-14.

Menke, H., 2016. Reservoir condition pore-Scale imaging of reaction. Ph.D. thesis Department of Earth Science and Engineering Imperial College London.

Menke, H.P., Andrew, M.G., Blunt, M.J. and Bijeljic, B., 2016. Reservoir condition imaging of reactive transport in heterogeneous carbonates using fast synchrotron tomography—Effect of initial pore structure and flow conditions. Chem. Geol. 428, pp.15-26.

Menke, H.P., Bijeljic, B., Blunt, M.J., 2017. Dynamic reservoir-condition microtomography of reactive transport in complex carbonates: Effect of initial pore structure and initial brine pH. Geochim. Cosmochim. Acta 204, 267-285.

Metz, B., Davidson, O., De Coninck, H., Loos, M., Meyer, L., 2005. Carbon Dioxide Capture and Storage. Summary for Policymakers. IPCC.

Michael, K., Golab, A., Shulakova, V., Ennis-King, J., Allinson, G., Sharma, S., Aiken, T., 2010. Geological storage of CO_2 in saline aquifers—A review of the experience from existing storage operations. Int. J. Greenhouse Gas Control 4(4), 659-67.

Mikhaltsevitch, V., Lebedev, M., Gurevich, B., 2014. Measurements of the elastic and anelastic properties of sandstone flooded with supercritical CO_2. Geophys. Prospect. 62, 1266–1277.

Miller, Q.R.S., Thompson, C.J., Loring, J.S., Windisch, C.F., Bowden, M.E., Hoyt, D.W., Hu, J.Z., Arey, B.W., Rosso, K.M., Schaef, H.T., 2013. Insights into silicate carbonation processes in water-bearing supercritical CO_2 fluids. Int. J. Greenhouse Gas Control 15, 104–18.

Miller, K., Vanorio, T., Yang, S., Xiao, X., 2019. A scale-consistent method for imaging porosity and micrite in dual-porosity carbonate rocks. Geophysics 84, MR115-MR127.

Min, K.B., Rutqvist, J., Tsang, C.F., Jing, L., 2004. Stress-dependent permeability of fractured rock masses: a numerical study. Int. J. Rock Mech. Min. Sci. 41(7), 1191-1210.

Minaeian, V., Dewhurst, D.N., Rasouli, V., 2017. Deformational behavior of a clay-rich shale with variable water saturation under true triaxial stress conditions. Geomech. Energy Environ. 11, 1–13.

Minardi, A., Stavropoulou, E., Kim, T., Ferrari, A., Laloui, L., 2021. Experimental assessment of the hydro-mechanical behavior of a shale caprock during CO_2 injection. Int J Greenhouse Gas Control 106, 103225.

Miocic, J., Gilfillan, S.M.V., McDermott, C., Haszeldine, R.S., 2016. Controls on CO_2 storage security in natural reservoirs and implications for CO_2 storage site selection. Int. J. Greenhouse Gas Control 51, 118-125.

Miri, R., Hellevang, H., 2016. Salt precipitation during CO_2 storage-A review. Int. J. Greenhouse Gas Control 51, 136-147.

Myers, M., Roberts, J.J., White, C., Stalker, L., 2018. The impact of water on CO_2 leak rate measurements for CCS projects. 14th Greenhouse Gas Control Technologies Conference Melbourne.

Neuzil, C.E., 2019. Permeability of clays and shales. Annu. Rev. Earth Planet. Sci. 47, 247–273.

Newell, P., Ilgen, A.G., 2019. Overview of geological carbon storage (GCS). Science of Carbon Storage in Deep Saline Formations 1-13. Elsevier.

Nguyen, M.T., Bemer, E., Dormieux, L., 2011. Micromechanical modeling of carbonate geomechanical properties evolution during acid gas injection. ARMA, 11–207.

Nguyen, B.N., Hou, Z., Bacon, D.H., Murray, C.J., White, M.D., 2016. Three-dimensional modeling of the reactive transport of CO_2 and its impact on geomechanical properties of reservoir rocks and seals. Int. J. Greenhouse Gas Control 46, 100–115.

Niu, B., Krevor, S., 2020. The impact of mineral dissolution on drainage relative permeability and residual trapping in two carbonate rocks. Transp. Porous Media 131, 363–380.

Noiriel, C., Gouze, P. and Bernard, D., 2004. Investigation of porosity and permeability effects from microstructure changes during limestone dissolution. Geophys. Res. Lett. 31(24).

Noiriel, C., Bernard, D., Gouze, P., Thibault, X., 2005. Hydraulic properties and microgeometry evolution accompanying limestone dissolution by acidic water. Oil Gas Sci. Technol. Rev. IFP 60, 177-192.

Noiriel, C., Madé, B., Gouze, P., 2007. Impact of coating development on the hydraulic and transport properties in argillaceous limestone fracture. Water Resour. Res. 43.

Noiriel, C., Luquot, L., Madé, B., Raimbault, L., Gouze, P. van Der Lee, J., 2009. Changes in reactive surface area during limestone dissolution: An experimental and modeling study. Chem. Geol. 265(1-2), 160-170.

Noiriel, C., Deng, H., 2018. Evolution of planar fractures in limestone: The role of flow rate, mineral heterogeneity and local transport processes. Chem. Geol. 497, 100-14.

Nolte, D.D., Pyrak-Nolte, L.J., 2022. Monitoring fracture saturation with internal seismic sources and twin neural networks. J. Geophys. Res. Solid Earth 127(2), e2021JB023005.

Norouzi, A.M., Babaei, M., Han, W.S., Kim, K.y., Niasar, V., 2021. CO_2-plume geothermal processes: A parametric study of salt precipitation influenced by capillary-driven backflow. Chem. Eng. J. 425, 1385-8947.

Nover, G., Von Der Gonna, J., Heikamp, S., Köster, J., 2013. Changes of petrophysical properties of sandstones due to interaction with supercritical carbon dioxide; a laboratory study. Eur. J. Mineral. 70176.

Oelkers, E.H., Gislason, S.R., Matter, J., 2008. Mineral carbonation of CO_2. Elements 4, 333-337.

Oelkers, E.H., 2018. Physical and chemical properties of rocks and fluids for chemical mass transport calculations. Reactive transport in porous media 17, 131-192.

Oikawa, Y., Takehara, T., Tosha, T., 2008. Effect of CO_2 injection on mechanical properties of Berea Sandstone (ARMA 06-068). In: 42nd US Rock Mechanics Symposium/2nd US-Canada Rock Mechanics Symposium San Francisco CA.

Oort, E.V., Hale, A.H., Mody, F.K., Roy, S., 1996. Transport in shales and the design of improved water-based shale drilling fluids. SPE Drill Compl. 11(03), 137–146.

Otsu, N., 1979. A threshold selection method from gray-level histograms. IEEE transactions on systems, man, and cybernetics, 9(1), 62-66.

Ott, H., Kloe, K.D., Bakel, M.V., Vos, F., Pelt, A.V., Legerstee, P., Bauer, A., Eide, K., Linden, A.V.D., Berg, S., Makurat, A., 2012. Core-flood experiment for transport of reactive fluids in rocks. Rev. Sci. Instrum. 83, 084501.

Ott, H., Andrew, M., Snippe, J., Blunt, M.J., 2014. Microscale solute transport and precipitation in complex rock during drying. Geophys. Res. Lett. (23), 8369-8376.

Ott, H., Oedai, S., 2015. Wormhole formation and compact dissolution in single-and two-phase CO_2-brine injections. Geophys. Res. Lett. 42(7), 2270-6.

Palandri, J.L. Kharaka, Y.K., 2004. A compilation of rate parameters of water-mineral interaction kinetics for application to geochemical modeling. Science for a changing world. U.S. Geol. Surv. Open File Report 2004-1068.

Park, B.H., Lee, K.K., 2021. Evaluating anisotropy ratio of thermal dispersivity affecting geometry of plumes generated by aquifer thermal use. J. Hydrol. 602, 126740.

Pawar, R., Guthrie, G., 2019. Hydraulic-Chemical coupling associated with the injection and storage of CO_2 into the subsurface. Science of Carbon Storage in Deep Saline Formations, 291-309.

Pearce, J.K., Dawson, G.K., Law, A.C., Biddle, D., Golding, S.D., 2016. Reactivity of micas and cap-rock in wet supercritical CO_2 with SO_2 and O_2 at CO_2 storage conditions. Appl. Geochem. 72, 59–76.

Pearce, J.K., Dawson, G.K., Blach, T.P., Bahadur, J., Melnichenko, Y.B., 2018. Golding SD. Impure CO_2 reaction of feldspar, clay, and organic matter-rich cap rocks: Decreases in the fraction of accessible mesopores measured by SANS. Int. J. Coal Geol. 185, 79-90.

Pearce, J.K., Dawson, G.K., Golab, A., Knuefing, L., Sommacal, S., Rudolph, V., Golding, S.D., 2019. A combined geochemical and μCT study on the CO_2 reactivity of Surat Basin reservoir and cap-rock cores: porosity changes, mineral dissolution and fines migration. Int. J. Greenhouse Gas Control 80, 10-24.

Pearce, J.K., Khan, C., Golding, S.D., Rudolph, V. and Underschultz, J.R., 2022. Geological storage of CO_2 and acid gases dissolved at surface in production water. J. Pet. Sci. Eng. 210, 110052.

Peng, C., Crawshaw, J.P., Maitland, G.C., Trusler, J.M., 2015. Kinetics of calcite dissolution in CO_2-saturated water at temperatures between (323 and 373) K and pressures up to 13.8 MPa. Chem. Geol. 403, 74-85.

Perera, M.S.A., Rathnaweera, T.D., Ranjith, P.G., Wanniarachchi, W.A.M., Nasvi, M.C.A., Abdulagatov, L.M., Haque, A., 2016. Laboratory measurement of deformation-induced hydro-mechanical properties of reservoir rock in deep saline aquifers: An experimental study of Hawkesbury formation. Mar. Pet. Geol. 77, 640-652.

Phillips, T., Kampman, N., Bisdom, K., Inskip, N.D., den Hartog, S.A., Cnudde, V., Busch, A., 2020. Controls on the intrinsic flow properties of mudrock fractures: A review of their importance in subsurface storage. Earth Sci. Rev. 211, 103390.

Pietruszczak, S., Lydzba, D., Shao, J.F., 2006. Modelling of deformation response and chemo-mechanical coupling in chalk. Int. J. Numer. Anal. Methods Geomech. 30(10), 997-1018.

Pimienta, L., Esteban, L., Sarout, J., Liu, K., Dautriat, J., Delle Piane, C., Clennell, M.B., 2017. Supercritical CO_2 injection and residence time in fluid-saturated rocks: Evidence for calcite dissolution and effects on rock integrity. Int. J. Greenhouse Gas Control 67, 31-48.

Pini, R., Krevor, S., 2019. Laboratory studies to understand the controls on flow and transport for CO_2 storage. Science of Carbon Storage in Deep Saline Formations 109-137.

Pini, R., Madonna, C., 2016. Moving across scales: a quantitative assessment of X-ray CT to measure the porosity of rocks. J. Porous Mater. 23, 325-338.

Privalov, V., Randi, A., Sterpenich, J., Pironon, J., Morlot, C., 2019. Structural control of a dissolution network in a limestone reservoir forced by radial injection of CO_2 saturated solution: Experimental results coupled with X-Ray computed tomography. Geosciences 9(1), 33.

Pluymakers, A.M., Samuelson, J.E., Niemeijer, A.R., Spiers, C.J., 2014. Effects of temperature and CO_2 on the frictional behavior of simulated anhydrite fault rock. J. Geophys. Res. Solid Earth 119(12), 8728-8747.

Pokrovsky, O.S., Schott, J., 2003. Surface Chemistry and dissolution kinetics of divalent metal carbonates. Environ. Sci. Technol. 36(3), 426-432.

Pool, M., Carrera, J., Vilarrasa, V., Silva, O., Ayora, C., 2013. Dynamics and design of systems for geological storage of dissolved CO_2. Adv. Water Resour. 62, 533-42.

Pyrak-Nolte, L.J., Morris, J.P., 2000. Single fractures under normal stress: The relation between fracture specific stiffness and fluid flow. Int. J. Rock Mech. Min. Sci. 37(1-2), 245-62.

Pyrak-Nolte, L.J., Nolte, D.D., 2016. Approaching a universal scaling relationship between fracture stiffness and fluid flow. Nat. Commun. 7(1), 1-6.

Rabbani, A., Jamshidi, S., 2014. Specific surface and porosity relationship for sandstones for prediction of permeability. Int. J. Rock Mech. Min. Sci. 71, 25-32.

Rabbani, A., Ayatollahi, S., 2015. Comparing three image processing algorithms to estimate the grain-size distribution of porous rocks from binary 2D images and sensitivity analysis of the grain overlapping degree. Spec. Top. Rev. Porous Media: Int. J. 6(1), 71-89.

Radillal, G., Kacem, M., Lombard, J.M., Fourar, M., 2010. Transport properties of Lavoux limestone at various stages of CO_2-like acid-rock alteration. Oil Gas Sci. Technol. IFP 65(4), 557-563.

Raj, N., Pal, T.V., 2014. Enhancing efficiency of HCl-based stimulating fluids by creating in-situ carbonic acid using nickel nanoparticles. IPTC Conference.

Ramandi, H.L., Mostaghimi, P., Armstrong, R.T., Saadatfar, M., Pinczewski, W.V., 2016. Porosity and permeability characterization of coal: a micro-computed tomography study. Int. J. Coal Geol. 154, 57-68.

Rathnaweera, T.D., Ranjith, P.G., Perera, M.S.A., Haque, A., Lashin, A., Al Arifi, N., Chandrasekharam, D., Yang, S., Xu, T., Wang, S., Yasar, E., 2015. CO_2-induced mechanical behavior of Hawkesbury sandstone in the Gosford basin: An experimental study. Mater Sci. Eng. A 641, 123–137.

Rathnaweera, T.D., Ranjith, P.G., Perera, M.S.A., 2016. Experimental investigation of geochemical and mineralogical effects of CO_2 sequestration on flow characteristics of reservoir rock in deep saline aquifers. Sci. Rep. 6, 19362.

Rathnaweera, T.D., Ranjith, P.G., Perera, M.S.A., Ranathunga, A.S., Wanniarachchi, W.A.M., Yang, S.Q., Lashin, A., Al Arifi, N., 2017. An experimental investigation of coupled chemico-mineralogical and mechanical changes in varyingly-cemented sandstones upon CO_2 injection in deep saline aquifer environments. Energy 133, 404-414.

Raza, A., Gholami, R., Sarmadivaleh, M., Tarom, N., Rezaee, R., Bin, C.H., Nagarajan, R., Hamid, M.A., Elochukwu, H., 2016. Integrity analysis of CO_2 storage sites concerning geochemical-geomechanical interactions in saline aquifers. J. Nat. Gas Sci. Eng. 36PA, 224–240.

Raza, A,, Gholami, R., Sarmadivaleh, M., 2020. Feasibility of limestone reservoirs as a carbon dioxide storage site: An experimental study. AAPG Bulletin 104, 83–96.

Renard, F., Gundersen, E., Hellmann, R., Collombet, M., Le Guen, Y., 2005. Numerical modeling of carbon dioxide sequestration on the rate of pressure solution creep in limestone: Preliminary results. Oil Gas Sci. Technol. 60, 381–399.

Rezaee, R., Saeedi, A., Iglauer, S., Evans, B., 2017. Shale alteration after exposure to supercritical CO_2. Int. J. Greenhouse Gas Control 62, 91–99.

Rimmelé, G., Barlet-Gouédard, V., Renard, F., 2010. Evolution of the petrophysical and mineralogical properties of two reservoir rocks under thermodynamic conditions relevant for CO_2 geological storage at 3 km depth. Oil Gas Sci. Technol. 65, 565–580.

Rinaldi, A.P., Rutqvist, J., 2013. Modeling of deep fracture zone opening and transient ground surface uplift at KB-502 CO_2 injection well, In Salah, Algeria. Int. J. Greenhouse Gas Control 12, 155-67.

Rinaldi, A.P., Jeanne, P., Rutqvist, J., Cappa, F., Guglielmi, Y., 2014. Effects of fault-zone architecture on earthquake magnitude and gas leakage related to CO_2 injection in a multi-layered sedimentary system. Greenhouse Gases Sci. Technol. 4(1), 99-120.

Rinehart, A.J., Dewers, T.A., Broome, S.T., Eichhubl, P., 2016. Effects of CO_2 on mechanical variability and constitutive behavior of the Lower Tuscaloosa Formation, Cranfield injection site, USA. Int. J. Greenhouse Gas Control 53, 305–318.

Ringrose, P.S., Meckel, T.A., 2019. Maturing global CO_2 storage resources on offshore continental margins to achieve 2DS emissions reductions. Sci. Reports 9, 17944.

Rochelle, C.A., Czernichowski-Lauriol, I., Milodowski, A.E., 2004. The impact of chemical reactions on CO_2 storage in geological formations: a brief review. Geological Society London Special Publications 233, 87-106.

Rohmer, J., Pluymakers, A., Renard, F., 2016. Mechano-chemical interactions in sedimentary rocks in the context of CO_2 storage: Weak acid, weak effects? Earth Sci. Rev. 157, 86–110.

Rosenbauer, R.J., Koksalan, T., Palandri, J.L., 2005. Experimental investigation of CO_2–brine-–rock interactions at elevated temperature and pressure: Implications for CO_2 sequestration in deep saline aquifers. Fuel Process. Technol. 1581–1597.

Rosenbauer, R.J., Thomas, B., Bischoff, J.L., Palandri, J., 2012. Carbon sequestration via reaction with basaltic rocks: Geochemical modeling and experimental results. Geochim. Cosmochim. Acta 89, 116-33.

Rutqvist, J., 2012. The geomechanics of CO_2 storage in deep sedimentary formations. Geotech. Geol. Eng. 30,525–551.

Rutter, E.H., 1976. The kinetics of rock deformation by pressure solution. Philos. Trans. R. Soc. London Ser. A 283, 203–219.

Samper, J., Dai, Z., Molinero, J., Garcia-Gutierrez, M., Missana. T., Mingarro, M., 2006. Interpretation of solute transport experiments in compacted Ca-bentonites using inverse modeling. Phys. Chem. Earth 31, 640-648.

Samuelson, J., Spiers, C.J., 2012. Fault friction and slip stability not affected by CO_2 storage: Evidence from short-term laboratory experiments on North Sea reservoir sandstones and caprocks. Int. J. Greenhouse Gas Control 11, S78-90.

Saneifar, M., Conte, R., Chen Valdes, C., Heidari, Z., Pope, M.C., 2015. Integrated rock classification in carbonate formations based on elastic and petrophysical properties estimated from conventional well logs. AAPG Bull. 99(7), 1261-80.

Sarout, J., Detournay, E., 2011. Chemoporoelastic analysis and experimental validation of the pore pressure transmission test for reactive shales. Int. J. Rock Mech. Min. Sci. 48(5), 759-72.

Schaef, H.T., Windisch Jr, C.F., McGrail, B.P., Martin, P.F., Rosso, K.M., 2011. Brucite [Mg (OH_2)] carbonation in wet supercritical CO_2: An in situ high pressure X-ray diffraction study. Geochim. Cosmochim. Acta 75(23), 7458–7471.

Schimmel, M.T., Hangx, S.J., Spiers, C.J., 2022. Effect of pore fluid chemistry on uniaxial compaction creep of Bentheim sandstone and implications for reservoir injection operations. Geomech. Energy Environ. 29, 100272.

Schneider, C.A., Rasband, W.S., Eliceiri, K.W., 2012. NIH Image to ImageJ: 25 years of image analysis. Nat. methods, 9(7), 671-675

Scholz, C.H., 2010. A note on the scaling relations for opening mode fractures in rock. J. Struct. Geol. 32(10), 1485-7.

Schuler, L., Ilgen, A.G., Newell, P., 2020. Chemo-mechanical phase-field modeling of dissolution-assisted fracture. Comput. Methods Appl. Mech. Eng. 362, 112838.

Sciandra, D., Kivi, I.R., Vilarrasa, V., Makhnenko, R., Rebscher, D., 2022. Hydro-mechanical response of opalinus clay in the CO2 long-term periodic injection experiment (CO2LPIE) at the Mont Terri rock laboratory. Geomech. Geophys. Geo-Energy Geo-Resour. 10.1007/s40948-022-00442-x.

Selvadurai, A.P., Couture, C.B., Rezaei Niya, S.M., 2017. Permeability of wormholes created by CO_2-acidized water flow through stressed carbonate rocks. Phys. Fluids 29(9),096604.

Selvaraj, G., Maulianda, B., Wee, S.C., Akhir, N.A., Elraies, K.A., Malakooti, R., Prakasan, A., 2020. Experimental study of nanoparticles as catalyst in enhancing matrix acidizing for carbonate reservoir. J. Pet. Explor. Prod. Technol. 10(3), 1145-53.

Seyyedi, M., Mahmud, H.K.B., Verrall, M., Giwelli, A., Esteban, L., Ghasemiziarani, M., Clennell, B., 2020. Pore structure changes occur during CO_2 injection into carbonate reservoirs. Sci. Rep. 10, 3624.

Shi, Z., Sun, L., Haljasmaa, I., Harbert, W., Sanguinito, S., Tkach, M., Goodman, A., Tsotsis, T.T., Jessen, K., 2019. Impact of brine/CO2 exposure on the transport and mechanical properties of the Mt Simon sandstone. J. Pet. Sci. Eng. 177, 295–305.

Shin, H., Santamarina, J.C., 2011. Desiccation cracks in saturated fine-grained soils: particle-level phenomena and effective-stress analysis. Géotechnique 61(11), 961-972.

Shulakova, V., Sarout, J., Pimienta, L., Lebedev, M., Mayo, S., Clennell, M.B., Pervukhina, M., 2016. Effect of supercritical CO_2 on carbonates: Savonnieres sample, case study. Geophys Prospect 65, 1–15.

Sinha, S., Braun, E.M., Determan, M.D., Passey, Q.R., Leonardi, S.A., Boros, J.A., Wood, A.C., Zirkle, T., Kudva, R.A., 2013. Steady-state permeability measurements on intact shale samples at reservoir conditions – effect of stress, temperature, pressure, and type of gas. In: SPE Middle East Oil and Gas Show and Conference, Manama, Bahrain.

Skurtveit, E., Sundal, A., Bjørnarå, T.I., Soldal, M., Sauvin, G., Zuchuat, V., Midtkandal, I., Braathen, A., 2020. Experimental investigation of natural fracture stiffness and flow properties in a faulted CO_2 bypass system (Utah, USA). J. Geophys. Res. Solid Earth 125(7), e2019JB018917.

Smith, L., Chapman, D.S., 1983. On the thermal effects of groundwater flow: 1. Regional scale systems. J. Geophys. Res. Solid Earth 88(B1), 593-608.

Smith, T.M., Sondergeld, C.H., Rai, CH., 2003. Gassmann fluid substitutions: A tutorial. Geophysics 68(2), 430-440.

Smith, M.M., Sholokhova, Y., Hao, Y., Carroll, S.A., 2013. CO_2-induced dissolution of low permeability carbonates. Part I: Characterization and experiments. Adv. Water Resour. 62, 370-87.

Smith, M.M., Hao, Y., Carroll, S.A., 2017. Development and calibration of a reactive transport model for carbonate reservoir porosity and permeability changes based on CO_2 core-flood experiments. Int. J. Greenhouse Gas Control 57, 73–88.

Snippe, J., Gdanski, R., Ott, H., 2017. Multiphase modeling of wormhole formation in carbonates by the injection of CO_2. Energy Procedia 114, 2972-84.

Snippe, J., Kampman, N., Bisdom, K., Tambach, T., March, R., Maier, C., Phillips, T., Inskip, N.F., Doster, F., Busch, A., 2022. Modelling of long-term along-fault flow of CO_2 from a natural reservoir. Int. J. Greenhouse Gas Control 118:103666.

Sone, H., Zoback, M.D., 2013. Mechanical properties of shale-gas reservoir rocks—Part 1: Static and dynamic elastic properties and anisotropy. Geophysics 78(5), D381-92.

Soong, Y., Howard, B.H., Dilmore, R.M., Haljasmaa, I., Crandall, D.M., Zhang, L., Zhang, W., Lin, R., Irdi, G.A., Romanov, V.N., Mclendon, T.R., 2016. CO_2/brine/rock interactions in Lower Tuscaloosa formation. Greenhouse Gas Sci. Technol. 00, 1–14.

Soulaine, C., Roman, S., Kovscek, A. and Tchelepi, H.A., 2018. Pore-scale modeling of multiphase reactive flow: application to mineral dissolution with production of CO_2. J. Fluid Mech. 855, 616-645.

Spanne, P., Thovert, J.F., Jacquin, C.J., Lindquist, W.B., Jones, K.W., Adler, P.M., 1994. Synchrotron computed microtomography of porous media: topology and transports. Phys. Rev. Lett. 73(14), 2001.

Spiers, C.J-, Schutjens. P.. 1990. Densification of crystalline aggregates by fluid-phase diffusional creep. In: Deformation Processes in Minerals, Ceramics and Rocks Meredith 334–353.

Spokas, K., Peters, C.A., Pyrak-Nolte, L., 2018. Influence of rock mineralogy on reactive fracture evolution in carbonate-rich caprocks. Environ. Sci. Technol. 52(17), 10144-10152.

Spycher, N., Pruess, K., Ennis-king, J., 2003. CO_2–H_2O mixtures in the geological sequestration of CO_2. I. Assessment and calculation of mutual solubilities from 12 to 100 °C and up to 600 bar. Geochim. Cosmochim. Acta 67, 3015–3031.

Spycher, N., Pruess, K., 2010. A phase-partitioning model for CO_2–brine mixtures at elevated temperatures and pressures: application to CO_2-enhanced geothermal systems. Transp. in Porous Media 82(1), 173-96.

Steefel, C.I., Lichtner, P.C., 1998. Multicomponent reactive transport in discrete fractures: II: Infiltration of hyperalkaline groundwater at Maqarin, Jordan, a natural analogue site. J. Hydrol. 209(1-4), 200-224.

Steefel, C.I., Molins, S., 2009. CrunchFlow. Software for modeling multicomponent reactive flow and transport. User's manual. Lawrence Berkeley National Laboratory, Berkeley.

Steefel, C.I, Hu, M., 2022. Reactive transport modeling of mineral precipitation and carbon trapping in discrete fracture networks. Water Resour. Res. 58(9), e2022WR032321.

Steefel, C.I., Appelo, C.A.J., Arora, B., Jacques, D., Kalbacher, T., Kolditz, O., Lagneau, V., Lichtner, P.C., Mayer, K.U., Meeussen, J.C.L., Molins, S., 2015. Reactive transport codes for subsurface environmental simulation. Comput. Geosci. 19(3), 445-478.

Stefanou, I., Sulem, J., 2014. Chemically induced compaction bands: Triggering conditions and band thickness. J. Geophys. Res. Solid Earth 119(2), 880-899.

Sterpenich, J., Jobard, E., El Hajj, H., Pironon, J., Randi, A., Caumon, M.C., 2014. Experimental study of CO_2 injection in a simulated injection well: the MIRAGES experiment. Greenhouse Gas Sci. Technol. 4, 210–224.

Szymczak, P., Ladd, A.J.C., 2009. Wormhole formation in dissolving fractures. J. Geophys. Res. Solid Earth 114, B06203.

Szymczak, P., Ladd, A.J.C., 2011. The initial stages of cave formation: beyond the one-dimensional paradigm. Earth Planet. Sci. Lett. 301(3–4), 424–432.

Tang, A.M., Cui, Y.J., Barnel, N., 2008. Thermo-mechanical behaviour of a compacted swelling clay. Géotechnique 58(1), 45-54.

Tariq, Z., Abdulraheem, A., Elkatatny, S., Mahmud, M., Muqtadir, A., Murtaza, M., 2018. Geomechanical studies on CO_2 sequestrated rocks in an aqueous saline environment. In: SPE-122242-MS.

Tarokh, A., Makhnenko, R.Y., Kim, K., Zhu, X., Popovics, J.S., Segvic, B., Sweet, D.E., 2020. Influence of CO_2 injection on the poromechanical response of Berea sandstone. Int. J. Greenhouse Gas Control 95, 102959.

Taron, J., Elsworth, D. 2009. Thermal–hydrologic–mechanical–chemical processes in the evolution of engineered geothermal reservoirs. Int. J. Rock Mech. Min. Sci. 46(5), 855-864.

Thaysen, E.M., Soler, J.M., Boone, M., Cnudde, V., Cama, J., 2017. Effect of dissolved H_2SO_4 on the interaction between CO_2-rich brine solutions and limestone, sandstone, and marl. Chem. Geol. 450, 31-43.

Tsang, C.F., 1991. Coupled hydromechanical-thermochemical processes in rock fractures. Rev. Geophys. 4, 537-551.

Turner, L.G., Dawson, G.K., Golding, S.D., Pearce, J.K., 2022. CO_2 and NOx reactions with CO_2 storage reservoir core: NOx dissolution products and mineral reactions. Int. J. Greenhouse Gas Control 120, 103750.

Tutolo, B.M., Luhmann, A.J., Kong, X.Z., Bagley, B., Alba-Venero, D., Mitchell, N., Saar, M.O., Seyfried, W.E., 2020. Contributions of visible and invisible pores to reactive transport in dolomite. Geochem. Perspectives Lett. 14, 42-6.

Vafaie, A., Habibnia, B., Moallemi, S.A., 2015. Experimental investigation of the pore structure characteristics of the Garau gas shale formation in the Lurestan Basin, Iran. J. Nat. Gas Sci. Eng. 27, 432-442.

Vafaie, A., Kivi, I.R., 2020. An investigation on the effect of thermal maturity and rock composition on the mechanical behavior of carbonaceous shale formations. Mar. Pet. Geol. 116, 104315.

Vafaie, A., Kivi, I.R., Moallemi, S.A., Habibnia, B., 2021. Permeability prediction in tight gas reservoirs based on pore structure characteristics: A case study from South Western Iran. Unconv. Resour. 1, 9–17.

Vafaie, A., Cama, J., Soler, J.M., Kivi, I.R., Vilarrasa, V., 2023. Chemo-hydro-mechanical effects of CO_2 injection on reservoir and seal rocks: A review on laboratory experiments. Renewable Sustainable Energy Rev. 178, 113270.

Vanorio, T., Scotellaro, C., Mavko, G., 2008. The effect of chemical and physical processes on the acoustic properties of carbonate rocks. Leading Edge 27(8), 1040-8.

Vanorio, T., Nur, A., Ebert, Y., 2011. Rock physics analysis and time-lapse rock imaging of geochemical effects due to the injection of CO_2 into reservoir rocks. Geophysics 76, O23–O33.

Vanorio, T., Mavko, G., 2011. Laboratory measurements of the acoustic and transport properties of carbonate rocks and their link with the amount of microcrystalline matrix. Geophysics 76, E105–E115.

Vialle, S., Vanorio, T., 2011. Laboratory measurements of elastic properties of carbonate rocks during injection of reactive CO_2-saturated water. Geophys. Res. Lett. 38, 1–5.

Vialle, S., Contraires, S., Zinzsner, B., Clavaud, J.B., Mahiouz, K., Zuddas, P., Zamora, M., 2014. Percolation of CO_2-rich fluids in a limestone sample: Evolution of hydraulic, electrical, chemical, and structural properties. J. Geophys. Res. Solid Earth 119, 2828-2847.

Vialle, S., Druhan, J.L., Maher, K., 2016. Multi-phase flow simulation of CO_2 leakage through a fractured caprock in response to mitigation strategies. Int. J. Greenhouse Gas Control 44, 11–25.

Vilarrasa, V., Rudqvist, J., 2017. Thermal effects on geologic carbon storage. Earth Sci. Rev. 165, 245-256.

Vilarrasa, V., Makhnenko, R.Y., Rutqvist, J., 2019a. Field and laboratory studies of geomechanical response to the injection of CO_2. Science of Carbon Storage in Deep Saline Formations, 209-236.

Vilarrasa, V., Carrera, J., Olivella, S., Rutqvist, J., Laloui, L., 2019b. Induced seismicity in geologic carbon storage. Solid Earth 10(3), 871-892.

Viswanathan, H.S., Ajo-Franklin, J., Birkholzer, J.T., Carey, J.W., Guglielmi, Y., Hyman, J.D., Karra, S., Pyrak-Nolte, L.J., Rajaram, H., Srinivasan, G., Tartakovsky, D.M., 2022. From fluid flow to coupled processes in fractured rock: Recent advances and new frontiers. Rev. Geophys. 60(1), e2021RG000744.

Voltolini, M., Ajo-Franklin, J., 2019. The effect of CO_2-induced dissolution on flow properties in Indiana limestone: An in situ synchrotron X-ray micro-tomography study. Int. J. Greenhouse Gas Control 82, 38-47.

Wang, H., Alvarado, V., Bagdonas, D.A., McLaughlin, J.F., Kaszuba, J.P., Grana, D., Campbell, E., Ng, K., 2021. Effect of CO_2-brine-rock reactions on pore architecture and permeability in dolostone: Implications for CO_2 storage and EOR. Int. J. Greenhouse Gas Control 107, 103283.

Washburn, E.W., 1921. The dynamics of capillary flow. Phys. Rev. 17(3), 273.

Wenning, Q.C., Madonna, C., Kurotori, T., Pini, R., 2019. Spatial mapping of fracture aperture changes with shear displacement using X-ray computerized tomography. J. Geophys. Res. Solid Earth 124(7), 7320–7340.

White, A.F., Brantley, S.L., 2003. The effect of time on the weathering of silicate minerals: why do weathering rates differ in the laboratory and field? Chem. Geol. 202(3-4):479-506.

White, S.P., Allis, R.G., Moore, J., Chidsey, T., Morgan, C., Gwynn, W., 2005. Simulation of reactive transport of injected CO_2 on the Colorado Plateau. Chem. Geol. 217, 387-405.

Wigand, M., Kaszuba, J.P., Carey, J.W., Hollis, W.K., 2009. Geochemical effects of CO_2 sequestration on fractured wellbore cement at the cement/caprock interface. Chem. Geol. 265(1-2), 122-33.

Wolery, T.J., Jackson, K.J., Bourcier, W.L., Bruton, C.J., Viani, B.E., Knauss, K.G., Delany, J.M., 1990. Current Stetus of the EQ3/6 Software Package for Geochemical Modeling. In: Chemical Modeling of Aqueous Systems II, pp. 104–116.

Wollenweber, J., Alles, S., Busch, A., Krooss, B.M., Stanjek, H., Littke, R., 2010. Experimental investigation of the CO_2 sealing efficiency of caprocks. Int. J. Greenhouse Gas Control 4, 231-241.

Wu, Y., Lin, C., Yan, W., Liu, Q., Zhao, P., Ren, L., 2020. Pore-scale simulations of electrical and elastic properties of shale samples based on multicomponent and multiscale digital rocks. Mar. Petr. Geol. 117, 104369.

Wyllie, M.R., Gregory, A.R., Gardner, G.H., 1958. An experimental investigation of factors affecting elastic wave velocities in porous media. Geophysics 23(3), 459-93.

Xiao, Y., Lasaga, A.C., 1994. Ab initio mechanical studies of the kinetics and mechanisms of silicate dissolution: H+ (H3O+) catalysis. Geochim. Cosmochim. Acta 58, 5379–5400.

Xie, S.Y., Shao, J.F., Xu, W.Y., 2011. Influences of chemical degradation on mechanical behavior of a limestone. Int. J. Rock Mech. Min. Sci. 48, 741–747.

Xu, J., Fan, C. and Teng, H.H., 2012. Calcite dissolution kinetics in view of Gibbs free energy, dislocation density, and pCO_2. Chem. Geol. 322, 11-18.

Yasuhara, H., Elsworth, D., Polak, A., 2004. Evolution of permeability in a natural fracture: Significant role of pressure solution. J. Geophys. Res. Solid Earth 109(B3).

Yu, Z., Yang, S., Liu, K., Zhou, Q., Yang, L., 2019. An experimental and numerical study of CO2–brine-synthetic sandstone interactions under high-pressure temperature reservoir conditions. Appl. Sci. 9, 3354.

Zekri, A.Y., Shedid, A., Almehaideb, R.A., 2017. An experimental investigation of interactions between supercritical CO_2, aspheltenic crude oil, and reservoir brine in carbonate cores. In: SPE104750.

Zendehboudi, S., Khan, A., Carlisle, S., Leonenko, Y., 2011. Ex situ dissolution of CO_2: a new engineering methodology based on mass-transfer perspective for enhancement of CO_2 sequestration. Energy Fuels 25(7), 3323-33.

Zhang, X., Spiers, C.J., 2005. Compaction of granular calcite by pressure solution at room temperature and effects of pore fluid chemistry. Int. J. Rock Mech. Min. Sci. 42(7-8), 950-60.

Zhang, X., Spiers, C.J., Peach, C.J., 2010. Compaction creep of wet granular calcite by pressure solution at 28ºC to 150ºC. J Geophys. Res. Solid Earth 115(B9).

Zhang, R., Wu, Y.S., 2019. Hydrologic, mechanical, thermal, and chemical process coupling triggered by the injection of CO_2. Science of Carbon Storage in Deep Saline Formations, 291-309.

Zhang, Y., Zhang, Z., Arif, M., Lebedev, M., Busch, A., Sarmadivaleh, M., Iglauer, M., 2020. Carbonate rock mechanical response to CO_2 flooding evaluated by a combined X-ray computed tomography – DEM method. J. Nat. Gas Sci. Eng. 84, 103675A.

Zhou, C., Birkholzer, J.T., Mehnert, E., Lin, Y.F., Zhang, K., 2009. Modeling Basin- and Plume-Scale Processes of CO_2 Storage for Full-Scale Deployment. Ground Water 48,494-514.

Zhou, H., Hu, D., Zhang, F., Shao, J., Feng, X., 2016. Laboratory investigations of the hydro-mechanical–chemical coupling behavior of sandstone in CO_2 storage in aquifers. Rock Mech. Rock Eng. 49, 417–426.

Zhu, W., Wong, T.F., 1997. The transition from brittle faulting to cataclastic flow: Permeability evolution. J. Geophys. Res. Solid Earth 102, 3027-3041.

Zhu, W., Baud, P., Wong, T.F., 2010. Micromechanics of cataclastic pore collapse in limestone. J. Geophys. Res. Solid Earth 115, B04405.

Zimmerman, R.W., 1996. Effective conductivity of a two-dimensional medium containing elliptical inhomogeneities. Proc. R. Soc. London Ser. A 452(1950), 1713-27.

Zimmerman, R.W., Bodvarsson, G.S., 1996. Hydraulic conductivity of rock fractures. Transp. Porous Med. 23, 1–30.

Zoback, M.D., Gorelick, S.M., 2012. Earthquake triggering and large-scale geologic storage of carbon dioxide. PNAS 109, 164-168.

Zou, Y., Li, S., Ma, X., Zhang, S., Li, N., Chen, M., 2018. Effects of CO_2–brine–rock interaction on porosity/permeability and mechanical properties during supercritical-CO_2 fracturing in shale reservoirs. J. Nat. Gas Sci. Eng. 49, 157–168.

Appendix I

Complementary information on earlier experimental studies

Table A1. Summary of experimental conditions and measured parameters before and after exposure to CO_2. Reported studies are sorted chronologically for each rock type. Experimental studies that used more than one rock type are differentiated by adding a superscript labeled with "&" followed by LS, DO, SS, or SH standing, respectively, for limestone, dolostone, sandstone, and shale. Different types of water, i.e., deionized, fresh, brackish or saline water and brine, are differentiated based on total dissolved solids (TDS) (Godsey).

Reference	Fluid type	Experiment type (condition) Initial saturation state Flow rate (mL/s)	Measurements
Chalk			
Grombacher et al.$^{\&LS}$ (2015)	CO_2-saturated water	Flow-through (open flow) Dry sample $6.66 \cdot 10^{-2}$	Aqueous chemistry Elastic moduli Microstructure Mineralogy Permeability Porosity Pore size distribution Ultrasonic velocity
Liteanu et al. (2013)	Supercritical CO_2	Flow-through (no flow) Water-saturated sample	Young's modulus
Alam et al. (2014)	Supercritical CO_2	Flow-through (open flow) Brine-saturated sample $5.55 \cdot 10^{-4}$	Elastic moduli Electrical resistivity Microstructure Mineralogy Permeability Porosity Surface area Ultrasonic velocity
Soong et al.$^{\&SS}$ (2016)	Supercritical CO_2	Batch (immersion in brine) Brine-saturated sample	Aqueous chemistry Mineralogy Permeability Porosity
Khather et al. (2020) (composite core)	CO_2-saturated brine	Flow-through (open flow) Dry sample	Microstructure Mineralogy Permeability Porosity Pore size distribution
Limestone & Dolostone			
Noiriel et al. (2005)	CO_2-saturated deionized water (with/without 0.01 M NaCl)	Flow-through (no flow) Calcite equilibrated water-saturated sample $2.76 \cdot 10^{-2}$- $8.33 \cdot 10^{-2}$	Aqueous chemistry Microstructure Permeability Porosity
Rosenbauer et al.$^{\&SS}$ (2005)	Supercritical CO_2	Batch (immersion in brine) Brine-saturated sample	Aqueous chemistry Mineralogy Porosity
Le Guen et al.$^{\&SS}$ (2007)	Gaseous CO_2 Supercritical CO_2	Flow-through (open flow) Water-saturated sample $8.33 \cdot 10^{-5}$	Aqueous chemistry Microstructure Mineralogy Porosity
Bemer and Lombard (2010)	Retarded acid & brine (alternating)	Flow-through (open flow) brine-saturated sample	Elastic moduli Compressive strength Permeability Porosity

Table A1 (Continued)

Rimmele et al.[&SS] (2010)	Wet-supercritical CO_2 CO_2-saturated water	Batch (immersion/no immersion-water excluded) water-saturated sample	Elastic moduli Microstructure Mineralogy Permeability pH Porosity Compressive strength
Grgic (2011)	CO_2-saturated brine Supercritical CO_2 Gaseous CO_2	Flow-through (open flow & no flow) Brine-saturated sample 10^{-4}-10^{-2}	Aqueous chemistry Elastic moduli Microstructure pH
Vanario et al.[&SS] (2011)	Gaseous CO_2 CO_2-saturated brine	Flow-through (open flow) Brine-saturated/dry sample $6.66 \cdot 10^{-2}$- $1.33 \cdot 10^{-1}$	Aqueous chemistry Microstructure Permeability Porosity Ultrasonic velocity
Vialle and Vanario (2011)	CO_2-saturated water	Flow-through (open flow) Dry sample $1.33 \cdot 10^{-1}$	Aqueous chemistry Microstructure Permeability pH Porosity Ultrasonic velocity
Grombacher et al.[&CH] (2015)	CO_2-saturated water	Flow-through (open flow) Dry sample $6.66 \cdot 10^{-2}$	Aqueous chemistry Elastic moduli Microstructure Mineralogy Permeability Porosity Pore size distribution Ultrasonic velocity
Sterpenich et al.[&SH] (2014)	Supercritical CO_2	Batch (no immersion-water excluded) Water-saturated sample	Aqueous chemistry Microstructure Mineralogy
Smith et al. (2013)	CO_2-saturated brine	Flow-through (open flow) Brine-saturated sample $8.33 \cdot 10^{-4}$	Aqueous chemistry Microstructure Permeability Porosity Pore size distribution
Vialle et al. (2014)	CO_2-saturated Saline/fresh water	Flow-through (open flow) Saline water-saturated sample $8.33 \cdot 10^{-2}$	Aqueous chemistry Electrical Conductivity Formation factor Microstructure Mineralogy Permeability pH Porosity Ultrasonic velocity
El Husseiny and Vanario (2015)	CO_2-saturated water	Flow-through (open flow) Dry sample	Aqueous chemistry Microstructure Porosity Ultrasonic velocity
Al-Ameri et al.[&SH]) 2016(	Supercritical CO_2	Batch (no immersion-brine excluded) Brine-saturated sample	Elastic moduli Mineralogy Compressive strength Tensile strength
Clark and Vanario (2016)	CO_2-saturated Saline water	Flow-through (open flow) Dry sample $8.33 \cdot 10^{-3}$-$8.33 \cdot 10^{-2}$	Aqueous chemistry Microstructure Mineralogy Permeability Porosity Ultrasonic velocity

Table A1 (Continued)

Shulakova et al. (2016)	Supercritical CO_2	Flow-through (no flow) Dry sample	Microstructure Porosity
Lebedev et al. (2017)	CO_2-saturated brine	Flow-through (open flow) Brine-saturated sample $8.33 \cdot 10^{-3}$	Microstructure Nanoindentation modulus Porosity
Pimienta et al.[&SS] (2017)	Supercritical CO_2	Flow-through (no flow) Brackish water-saturated/dry sample $3.33 \cdot 10^{-2}$	Aqueous chemistry Electrical resistivity Microstructure Mineralogy Permeability Porosity P-wave velocity
Smith et al. (2017)	CO_2 & CO_2-brine mixture (sequential)	Flow-through (open flow) Brine-saturated sample $5.66 \cdot 10^{-4}$ - $5.66 \cdot 10^{-3}$	Aqueous chemistry Microstructure Mineralogy Permeability Porosity Surface area
Zekri and Shedid (2017)	CO_2	Flow-through (open flow) Brine/oil-saturated sample	Aqueous chemistry Mineralogical composition Permeability
Kim et al. (2018)	Liquid CO_2	Flow-through (no flow) Water-saturated sample $8.33 \cdot 10^{-2}$	Cohesion Elastic moduli Friction angle Permeability Porosity Relative permeability
Tariq et al.[&SS] (2018)	Supercritical CO_2	Batch (immersion in brine) Brine-saturated sample	Elastic moduli Porosity Permeability Ultrasonic velocity
Raza et al. (2020)	Supercritical CO_2	Flow-through (open flow) Brine-saturated sample $1.11 \cdot 10^{-4}$	Elastic moduli Microstructure Porosity Permeability
Niu and Krevor (2020)	T-controlled acid	Flow-through (no flow) Dry sample	Microstructure Permeability Porosity PSD Relative permeability
Seyyedi et al. (2020)	CO_2-saturated brine	Flow-through (open flow) Brine-saturated sample	Aqueous chemistry Microstructure Permeability Porosity
Zhang et al. (2019)	Supercritical CO_2 CO_2-saturated brine	Flow-through (open flow) Brine-saturated sample $8.33 \cdot 10^{-3}$-$2.5 \cdot 10^{-2}$	Porosity Compressive strength
Kim and Makhnenko.[&SS] (2021)	Liquid CO_2 Liquid CO_2	Flow-through (no flow) Water-saturated sample Batch (immersion in water) Water-saturated	Compressibility Elastic moduli Microstructure Porosity PSD Ultrasonic velocity
Wang et al. (2021)	CO_2-saturated brine	Batch (immersion in synthetic brine) Brine-saturated sample	Mineralogy Porosity Permeability Pore size distribution Diffusion Coefficient

Table A1 (Continued)

Sandstone			
Rosenbauer et al.[&LS] (2005)	Supercritical CO_2	Batch (immersion in brine) Brine-saturated sample	Aqueous chemistry Mineralogy Porosity
Bertier et al. (2006)	Supercritical CO_2	Batch (immersion in brine) Brine-saturated sample	Aqueous chemistry Permeability Porosity
Le Guen et al.[&LL] (2007)	Gaseous CO_2 Supercritical CO_2	Flow-through (open flow) Water-saturated sample $8.33 \cdot 10^{-5}$	Aqueous chemistryMicrostructure Mineralogy Porosity
Rimmele et al.[&LS] (2010)	Wet-supercritical CO_2 CO_2-saturated water	Batch (immersion/no immersion-water excluded) Water-saturated sample	Elastic moduli Microstructure Mineralogy Permeability pH Porosity Compressive strength
Vanario et al.[&LS] (2011)	Gaseous CO_2 CO_2-saturated brine	Flow-through (open flow) Brine-saturated/dry sample $6.66 \cdot 10^{-2}$- $1.33 \cdot 10^{-1}$	Aqueous chemistry Microstructure Permeability Porosity Ultrasonic velocity
Ott et al. (2012)	Supercritical CO_2	Flow-through (open flow) Brine-saturated sample	Microstructure
Canal et al. (2013)	Deionized water & CO_2-saturated deionized water (sequential)	Flow-through (open flow) Water-saturated sample $6.66 \cdot 10^{-4}$	Aqueous chemistry Microstructure Mineralogy Permeability pH Porosity Ultrasonic velocity
Lamy-Chappuis et al. (2014)	CO_2-saturated synthetic brine	Flow-through (open flow) Synthetic brine-saturated sample $1.66 \cdot 10^{-2}$-5.010^{-2}	Aqueous chemistry Microstructure Mineralogy Permeability pH Porosity
Fischer et al. (2013)	Gaseous CO_2	Batch (immersion in brine) Brine-saturated sample	Aqueous chemistry Microstructure Mineralogy
Hangx et al. (2013)	CO_2-saturated brine	Flow-through (open flow) Brine-saturated sample $4.16 \cdot 10^{-3}$-10^{-3}	Aqueous chemistry Elastic moduli Microstructure Mineralogy Ultrasonic velocity
Marbler et al. (2013)	Supercritical CO_2 Brine	Batch (no immersion-brine excluded) Brine-saturated/dry sample	Aqueous chemistry Failure strength Mineralogical composition pH
Nover et al. (2013)	Wet supercritical CO_2	Batch (no immersion-brine excluded) Brine-saturated sample	Aqueous chemistry Electrical conductivity Microstructure Mineralogy Permeability Porosity Compressive strength
Mikhlatsevitch et al.)2014(	Supercritical CO_2	Flow-through (no flow) Water-saturated sample	Elastic moduli Ultrasonic velocity

Table A1 (Continued)

Adam et al. (2015)	Gaseous CO_2	Batch (immersion in brine) Water-saturated sample	Ultrasonic velocity
Farquhar et al. (2015)	Supercritical CO_2	Batch (immersion in fresh/brackish water) Fresh/brackish water-saturated sample	Aqueous chemistry Microstructure Mineralogy pH Porosity
Hangx et al. (2015)	Natural analog samples	Natural exposure to CO_2	Elastic moduli Microstructure Mineralogy Permeability Porosity Ultrasonic velocity
Huq et al. (2015)	CO_2-saturated water CO_2-saturated brine	Flow-through (open flow) Brine-saturated sample $5 \cdot 10^{-4}$	Aqueous chemistry Permeability
Rathnaweera et al. (2015)	Supercritical CO_2	Batch (no immersion-water/brine excluded) Dry/water/ brine-saturated sample	Acoustic emission Elastic moduli Compressive strength Microstructure Mineralogy pH
Lammy-Chappuis et al. (2016)	CO_2-saturated brine	Flow-through (open flow) Dry sample	Cohesion Elastic moduli Friction angle Porosity
Falcon Suarez et al. (2016)	Brine & CO_2-saturated brine & supercritical CO_2 (sequential)	Flow-through (open flow) Brine-saturated sample $4.16 \cdot 10^{-3}$	Elastic moduli Electrical resistivity Permeability Relative permeability Ultrasonic velocity
Luquot et al. (2016)	CO_2-rich brine	Flow-through (no flow) Brine-saturated sample $8.33 \cdot 10^{-4}$-$5 \cdot 10^{-3}$	Aqueous chemistry Mineralogy Permeability
Perera et al. (2016)	Supercritical CO_2	Batch (no immersion-brine excluded) Brine-saturated sample	Acoustic Emission Elastic moduli Compressive strength Microstructure Mineralogy Permeability Porosity Toughness index
Rathnaweera et al. (2016)	Supercritical CO_2	Batch (immersion in brine) Brine-saturated sample	Aqueous chemistry Microstructure Mineralogy Permeability pH
Raza et al. (2016)	Supercritical CO_2	Flow-through (open flow) Brine-saturated sample	Microstructure Mineralogy Permeability Porosity Pore size distribution Ultrasonic velocity
Rinehart et al. (2016)	CO_2-saturated brine	Flow-through (open flow) Brine-saturated sample	Acoustic Emission Elastic moduli Compressive strength
Soong et al.[&CH] (2016)	Supercritical CO_2	Batch (immersion in brine) Brine-saturated sample	Aqueous chemistry Mineralogy Permeability Porosity
Zhou et al. (2016)	Gaseous CO_2 CO_2-brine mixture	Flow-through (open flow) Brine-saturated sample	Elastic moduli Permeability pH

Table A1 (Continued)

Pimienta et al.[&LS] (2017)	Supercritical CO_2	Flow-through (no flow) Brackish-saturated/dry sample $3.33 \cdot 10^{-2}$	Aqueous chemistry Electrical resistivity Microstructure Mineralogy Permeability Porosity P-wave velocity
Rathnaweera et al. (2017)	Gaseous CO_2 Supercritical CO_2	Batch (no immersion-brine excluded) Brine-saturated sample	Aqueous chemistry Elastic moduli Microstructure Mineralogy pH Compressive strength
Espinoza et al.[&SH] (2018)	Natural analog samples	Natural exposure to CO_2-charged brine.	Brittleness Microstructure Porosity Compressive strength
Tariq et al.[&LS] (2018)	Supercritical CO_2	Batch (immersion in brine) Brine-saturated sample	Elastic moduli Porosity Permeability Ultrasonic velocity
Fuchs et al. (2019)	Supercritical CO_2	Batch (immersion in brine) Brine-saturated sample	Aqueous chemistry Microstructure Mineralogy Porosity
Huang et al. (2019)	Supercritical CO_2	Flow-through (open flow) Brine-saturated sample	Fracture toughness Tensile strength Compressive strength
Pearce et al.[&SH] (2019)	Supercritical CO_2	Batch (immersion in fresh/brackish water) Fresh/brackish water-saturated sample	Aqueous chemistry Microstructure Mineralogy Porosity
Shi et al. (2019)	Supercritical CO_2 CO_2 and brine	Batch (immersion in brine) Brine-saturated sample Flow-through (open flow) Brine-saturated sample	Aqueous chemistry Elastic moduli Microstructure Mineralogy Permeability Porosity Pore size distribution Surface area Ultrasonic velocity
Yu et al. (2017)	CO_2-saturated brine	Flow-through (open flow) Dry sample	Aqueous chemistry Microstructure Mineralogy pH Porosity
Akono et al. (2020)	CO_2-saturated brine	Flow-through (open flow) Brine-saturated sample	Creep modulus Microstructure Porosity
Davila et al. (2017)	CO_2-saturated synthetic brine & supercritical CO_2 (alternating)	Flow-through (open flow) Dry sample 10^{-3}-$8.33 \cdot 10^{-2}$	Aqueous chemistry Microstructure Mineralogy Permeability
Foroutan and Ghazanfari (2017)	CO_2-saturated brine	Flow-through (open flow) Brine-saturated sample $8.8 \cdot 10^{-3}$	Aqueous chemistry Mineralogy Elastic moduli

Table A1 (Continued)

Harbert et al. (2020)	Supercritical CO_2	Batch (immersion in brine) Brine-saturated sample	Aqueous chemistry Brittleness Elastic moduli Compressive strength Microstructure Mineralogy Permeability Porosity Ultrasonic velocity
Li et al. (2020)	CO_2-saturated brine CO_2-subsaturated brine	Batch (immersion in brine) Brine-saturated sample	Microstructure Mineralogy Permeability Porosity Pore size distribution
Tarokh et al. (2020)	Liquid CO_2	Flow-through (open flow) Water-saturated sample (thermally damaged)	Acoustic Emission Elastic moduli Microstructure Mineralogy Permeability Porosity Skempton's coefficient Compressive strength Ultrasonic velocity
Foroutan et al. (2021a, 2021b)	CO_2-saturated brine	Flow-through (open flow) Brine-saturated sample $8.8 \cdot 10^{-3}$	Aqueous chemistry Cohesion Elastic moduli Friction angle Microstructure Mineralogy Porosity Ultrasonic velocity
Kim and Makhnenko[&LS] (2021)	Liquid CO_2 Liquid CO_2	Flow-through (no flow) Water-saturated sample Batch (immersion in water) Water-saturated	Compressibility Elastic moduli Microstructure Porosity PSD Ultrasonic velocity
Shales			
Kaszuba et al. (2003, 2005)	Supercritical CO_2	Batch (immersion in brine) Brine-saturated sample	Aqueous chemistry Microstructure Mineralogy pH
Busch et al. (2008)	Gaseous CO_2 Supercritical CO_2	Flow-through (open flow) Water-saturated sample	Diffusion coefficient Mineralogy
Sterpenich et al.[&LS] (2014)	Supercritical CO_2	Batch (no immersion-water excluded) Water-saturated sample	Aqueous chemistry Microstructure Mineralogy
Al-Ameri et al.[&LS] (2016)	Supercritical CO_2	Batch (no immersion-brine excluded) brine-saturated sample	Elastic moduli Mineralogy Compressive strength Tensile strength
Lyu et al. (2016, 2018)	Gaseous CO_2 Supercritical CO_2	Batch (immersion in water) Water-saturated sample	Acoustic Emission Elastic moduli Microstructure Mineralogy Compressive strength
Rezaee et al. (2017)	Wet-supercritical CO_2 CO_2-saturated synthetic brine	Batch (immersion/no immersion-brine excluded) Brine-saturated sample	Elastic moduli Microstructure Mineralogy Permeability pH Porosity Compressive strength

Table A1 (Continued)

Espinoza et al.[&SS] (2018)	Natural analog samples	Natural exposure to CO_2-charged brine.	Brittleness Microstructure Porosity Compressive strength
Ilgen et al. (2018)	Gaseous CO_2 Supercritical CO_2	Batch (immersion in brine) Brine-saturated	Aqueous chemistry Microstructure Mineralogy Porosity Scratch toughness Scratch hardness
Zou et al. (2018)	Supercritical CO_2	Batch (immersion in brine) Brine-saturated sample	Aqueous chemistry Friction coefficient Microstructure Mineralogy Permeability Porosity Tensile strength
Pearce et al.[&SS] (2019)	Supercritical CO_2	Batch (immersion in fresh/brackish water) Fresh/brackish water-saturated sample	Aqueous chemistry Microstructure Mineralogy Porosity
Dewhurst et al. (2020)	Supercritical CO_2	Batch (no immersion-Water excluded) Water-saturated sample	Cohesive strength Elastic moduli Compressive strength
Hadian and Rezaee (2019)	Wet supercritical CO_2	Batch (no immersion-brine excluded) Brine-saturated sample	Surface area Mineralogy Porosity Pore size distribution Threshold pressure
Choi et al. (2021)	Supercritical CO_2 Brine	Batch (immersion/no immersion in brine) Brine-saturated/dry sample	Aqueous chemistry Compressive strength Mineralogy pH Shore hardness Tensile strength Ultrasonic velocity
Jayasekara and Ranjith (2021)	Supercritical CO_2	Batch (no immersion-brine excluded) Brine-saturated sample	Aqueous chemistry Elastic moduli Compressive strength Microstructure Mineralogy Ultrasonic velocity
Minardi et al. (2021)	Gaseous Liquid CO_2	Flow-through (no flow) Brine-saturated/dry sample	Porosity Permeability Pore size distribution
Wigand et a. (2009)	Supercritical CO_2	Flow-through (no flow) Brine-saturated sample	Aqueous chemistry Microstructure Mineralogy

Table A2. List of laboratory studies conducted on different reservoir and seal rocks with varying carbonate content and initial hydraulic properties under different flow (i.e., Batch (B), or Flowthrough (F-T)) and experimental conditions (i.e., pressure, temperature, and duration) together with resultant hydraulic properties of altered rocks. Studies are sorted according to carbonate content and chronologically for those comprising the same carbonate content. Experimental studies that used more than one rock type are differentiated by adding a superscript labeled with "&" followed by LS, DO, SS, or SH standing, respectively, for limestone, dolostone, sandstone, and shale.

Reference	**Formation name** (country)	**Experiment type** (duration; h)	***P-T* conditions** (MPa & °C)	**Carbonate content** (%)	**ϕ[1] initial**	**ϕ final**	***k*[2] initial** (m^2)	***k* final** (m^2)
Chalks								
Grombacher et al.[&LS] (2015)	Mt. Acuto (Italy)	F-T (6 h)	12-20 & 25	100	0.30	0.30	1.08E-13	1.36E-13
Liteanu et al. (2013)	Sibbergroeve (Netherlands)	F-T (4 h)	10 & 80	100	0.42	-	3.50E-15	-
Khather et al. (2020)	Middle East	F-T (20 h)	7 & 65	100	0.29	0.29	3.36E-15	6.72E-15
Soong et al. [&SS] (2016)	Selma (USA)	B (4320 h)	23.8 & 85	90	0.12	0,13	2.17E-15	-
Alam et al. (2014)	Ekofisk (Denmark)	F-T (192 h)	12 & 115	76-100	0.25	0.27	2.25E-16	5.00E-16
Alam et al. (2014)	Tor (Denmark)	F-T (192 h)	12 & 115	78-100	0.33	0.36	1.70E-15	2.60E-15
Limestones & Dolostones								
Noiriel et al. (2005)	Lérouville (France)	F-T (23 h)	3 & -	100	0.11	0.17	3.94E-14	4.93E-12
Bemer and Lombard (2010)	Lavoux (France)	F-T (24-120 h)	- & 60	100	0.17	0.18	1.89E-13	1.68E-13
Bemer and Lombard (2010)	Lavoux (France)	F-T (24-120 h)	- & 60	100	0.20	0.22	2.51E-13	3.04E-13
Rimmele et al.[&SS] (2010)	Lavoux (France)	F-T (720 h)	28 & 90	100	0.23	0.26	3.97E-15	9.00E-15
Grgic (2011)	Lavoux (France)	F-T (1896 h)	4-30 & 70	100	0.26		1.00E-13	
Vanario et al.[&SS] (2011)	Micritic (-)	F-T (9.5 h)	15 & 25	100	0.20	0.25	4.93E-15	
Vialle and Vanario (2011)	Carbonate rocks (-)	F-T (8 h)	-	100	0.23	0.28	7.50E-14	4.45E-13
Grombacher et al.[&CH] (2015)	DK (Italy)	F-T (5 h)	12-20 & 25	100	0.25	0.25	1.67E-13	1.59E-13
Grombacher et al.[&CH] (2015)	Peschici (Italy)	F-T (2 h)	12-20 & 25	100	0.11	0.11	6.02E-14	2.66E-13
Vialle et al. (2014)	Estailldes (France)	F-T (2688 h)	- & 25	100	0.29	0.31	1.18E-13	9.86E-13
El Husseiny and Vanario(2015)	Synthetic (100 % micrite)	F-T (<1 h)	5 & 25	100	0.21		6.00E-17	
El Husseiny and Vanario(2015)	Synthetic (0 % micrite)	F-T (<1 h)	5 & 25	100	0.24		1.10E-13	
Al-Ameri et al.[&SH] (2016)	Indiana (USA)	B (336-2160 h)	13.7 &100	100				
Al-Ameri et al. [&SH] (2016)	Pink Dessert (USA)	B (336-2160 h)	13.7 &100	100				
Al-Ameri et al. [&SH] (2016)	Khuf (Middle East)	B (336-2160 h)	13.7 & 100	100				
Clark and Vanario (2016)	Grainstone (Brazil)	F-T (1 h)	15 & 25	100	0.19	0.18	1.80E-12	1.50E-12
Clark and Vanario (2016)	Boundstone (Brazil)	F-T (1 h)	15 & 25	100	0.19	0.18	3.70E-14	4.90E-14
Shulakova et al. (2016)	Savonniere (France)	F-T (4 h)	12.5 & -	100	0.26	0.30	5.49E-14	
Pimienta et al.[&SS] (2017)	Savonniere (France)	F-T (1.33 h)	12.5 & 50	100	0.26	0.27	6.90E-15	6.21E-15

[1] Porosity
[2] Permeability

Table A2 (continued)

Smith et al. (2017)	Arbuckle dolostone (USA)	F-T (70-1700 h)	3 & 60	100	0.03		8.38E-14	
Smith et al. (2017)	Arbuckle dolostone (USA)	F-T (70-1700 h)	3 & 60	100	0.03		1.18E-18	
Tariq et al.[&SS] (2018)	Khuff (Middle East)	B (240-2880 h)	8.27 & 120	100	0.07	0.07	4.38E-15	4.40E-15
Niu and Krevor (2020)	Estailldes (France)	F-T (80 h)	10 & 65	100	0.22	0.24	1.87E-13	2.17E-13
Niu and Krevor (2020)	Ketton (England)	F-T (80 h)	10 & 65	100	0.28	0.30	2.17E-12	
Seyyedi et al. (2020)	Savonnieres (France)	F-T (6.2 h)	4.8 & 50	100	0.27	0.29	3.73E-14	4.59E-14
Sterpenich et al.[&SH] (2014)	Lavoux (France)	B (780 h)	9.8-10.8 & 80	98	0.25	0.25	1.00E-13	1.00E-13
Kim et al. (2018)	Apulian (Italy)	F-T (72 h)	7 & 22	98	0.35	0.34	9.00E-15	5.5 E-15
Lebedev et al. (2017)	Savonniere (France)	F-T (0.6 h)	5 & 50	97	0.25	0.30	2.86E-14	
Raza et al. (2020)	Savonnieres (France)	F-T (18.75 h)	10 & 50	97	0.25	0.23	2.46E-14	
Zhang et al. (2019)	Savonniere (France)	F-T (2 h)	10 & 50	97	0.08	0.14		
Zhang et al. (2019)	Savonniere (France)	F-T (2 h)	10 & 50	97	0.08	0.20		
Kim and Makhnenko[&SS](2021)	Indiana (USA)	F-T (504 h)	7 & 22	97	0.13	0.14	1.00E-14	
Kim and Makhnenko[&SS](2021)	Apulian (Italy)	F-T (72 h)	7 & 22	95	0.37	0.39	1.00E-15	
Bemer and Lombard (2010)	Comblanchian (France)	F-T (24 h)	- & 60	90	0.15	0.17	1.38E-15	1.67E-15
Bemer and Lombard (2010)	Comblanchian (France)	F-T (24 h)	- & 60	90	0.15	0.17	1.72E-14	1.66E-14
Smith et al. (2013)	Weyburn limestone (Canada)	F-T (24-72h)	12.4 & 60	78-85	0.15	0.24	2.10E-17	
Smith et al. (2013)	Midale dolostone (Canada)	F-T (24-72h)	12.4 & 60	61-85	0.33		1.40E-15	
Le Guen et al.[&SS] (2007)	Estaillades (France)	F-T (4320 h)	0.1-40 & 80	55	0.31	0.33	2.66E-13	
Le Guen et al.[&SS] (2007)	Lavoux (France)	F-T (4320 h)	0.1-40 & 80	55	0.23	0.24	1.13E-14	
Rosenbauer et al. (2005)	Leadville (USA)	B (1440 h)	10-60 - 25-120	38				
Pimienta et al.[&SS] (2017)	Tuffeau (France)	F-T (1.33 h)	12.5 & 50	30	0.29		6.90E-15	4.14E-15
Zekri and Shedid (2017)	Abudabhi (UAE)	F-T (-)	27.5 & 93.33	-	0.21	0.23	3.80E-14	3.12E-14
Tariq et al.[&SS] (2018)	Ordinary (Middle East)	B (240-2880 h)	8.27 & 120	-	0.11	0.11	2.31E-14	2.31E-14
Wang et al. (2021)	Madison dolostone (USA)	B (400h)	34.5 & 93	100	0.18	0.195	6.50E-14	7.40E-14
Wang et al. (2021)	Madison dolostone (USA)	B (400h)	34.5 & 93	100	0.19	0.2	1.40E-14	1.50E-14
Sandstones								
Espinoza et al. (2018)	Summerville (USA)	Natural Seepage	-	23-38	0.04	0.10		
Hangx et al. (2015)	Rot Fringe (Netherlands)	Natural Seepage	-	1-45	0.07	0.07	2.76E-16	2.76E-16
Adam et al. (2015)	Taranki (New Zealand)	B (24 h)	1.37 & -	0-32	0.08			
Rathnaweera et al. (2017)	Hawkesbury (Australia)	B (8640 h)	4-10 & 35	30	0.28		9.30E-14	
Rathnaweera et al. (2016)	Hawkesbury (Australia)	B (12960 h)	10 & 40	27	0.29		9.30E-14	1.02E-13
Marbler et al. (2013)	Rotliegend (Germany)	B (336-672 h)	10 & 100	25	0.27		4.00E-13	
Li et al. (2020)	Chang-7 (China)	B (168 h)	20 & 80	19	0.12	0.13	2.91E-14	3.97E-14
Li et al. (2020)	Chang-7 (China)	B (168 h)	30 & 80	19	0.11	0.14	3.46E-14	1.82E-13
Yu et al. (2019)	Synthetic	F-T (96-384 h)	48.45 & 150	17	0.13	0.13		
Espinoza et al. (2018)	Entrada (USA)	Natural Seepage	-	14	0.08	0.11		
Luquot et al. (2016)	Heletz (Israel)	F-T (29-90 h)	15 & 60	9	0.23		1.00E-12	6.00E-12

Table A2 (continued)

Rathnaweera et al. (2017)	Silica-cemented Hawkesbury (Australia)	B (8640 h)	4-10 - 35	7	0.29		1.00E-14	
Foroutan & Ghazanfari (2020)	Pecos (USA)	F-T (72 h)	7.5-23.5 - 25	7				
Foroutan et al.(2021a,2021b)	Pecos (USA)	F-T (63 h)	7.5 -21.5 - 25	7	0.04	0.07		
Bertier et al. (2006)	Westphalian C (Belgium)	B (5760 h)	- & 80	6	0.10		5.92E-16	
Bertier et al. (2006)	Westphalian D (Belgium)	B (5760 h)	- & 80	6	0.17		1.38E-13	
Rathnaweera et al. (2015)	Hawkesbury (Australia)	B (2880 h)	8 & 32	6	0.37			
Perera et al. (2016)	Hawkesbury (Australia)	B (17280 h)	10 & 35	6	0.27	0.29	9.00E-14	9.81E-14
Lamy-Chappuis et al. (2016)	Cayton bay (England)	F-T (-)	3.4-27.5 & 50	6	0.34	0.39		
Huq et al. (2015)	Rotliegend (Germany)	F-T (144 h)	7.5 & 115	3-6	0.15	0.15	1.17E-14	1.98E-14
Marbler et al. (2013)	Silica-cemented Bunter (Germany)	B (336-672 h)	10 & 100	5	0.18		3.50E-17	
Zhou et al. (2016)	China	F-T (6000 h)	3-8 & 40	5	0.16	0.17	3.10E-15	3.01E-16
Lamy-Chappuis et al. (2014)	Gritstone (UK)	F-T (24-48h)	1 & -	5	0.33	0.38	9.90E-15	1.70E-14
Pimienta et al.[&LS] (2017)	Synthetic	F-T (1.33 h)	12.5 & 50	4	0.40		3.94E-12	3.15E-12
Le Guen et al.[&LS] (2007)	Arkosic (France)	F-T (4320 h)	0.1-40 & 80	3	0.16	0.18	4.54E-13	
Mikhlatsevitch et al.)2014(	Donnybrook (Australia)	F-T (48 h)	10 & 42	2	0.12		2.76E-16	
Raza et al. (2016)	Berea (USA)	F-T (24 h)	14 & 35	2	0.19		4.14E-13	
Shi et al.)2019(	Mt. Simon (USA)	B/F-T (168-336 h)	14-17 & 45-50	2	0.21	0.23	9.67E-15	3.43E-14
Harbert et al.)2020(	Mt. Simon (USA)	B (720 h)	13 & 53	2	0.17	0.18	2.56E-15	7.81E-15
Harbert et al. (2020)	Mt. Simon (USA)	B (720 h)	13 & 53	2	0.24	0.21	3.75E-13	4.01E-13
Soong et al.[&CH] (2016)	Tuscaloosa (USA)	B (4320 h)	23.8 & 85	1	0.27	0.25	2.22E-12	1.93E-12
Hangx et al. (2013)	Captain (England)	F-T (1-2 h)	14 & 20-60	0.3	0.26		6.50E-13	
Hangx et al. (2013)	Captain (England)	F-T (1-2 h)	14 & 20-60	0.3	0.29		2.10E-12	
Davila et al. (2017)	Mt. Simon (USA)	F-T (14.7 h)	10 & 53	0.3	0.18	0.17	9.17E-17	7.40E-17
Bertier et al. (2006)	Bunt (Belgium)	B (5760 h)	- & 80	0	0.13		3.84E-14	
Rimmele et al.[&LS] (2010)	Adamswiller (France)	F-T (720 h)	28 & 90	0	0.23	0.26	1.08E-14	1.08E-13
Vanario et al.[&LS] (2011)	Fontainebleau (France)	F-T (11 h)	15 & 25	0	0.15	0.12	1.72E-12	1.38E-12
Ott et al. (2012)	Berea (USA)	F-T (8 h)	10 & 45	0	0.22	0.18	1.30E-13	1.80E-15
Canal et al. (2013)	Arcera (Spain)	F-T (1176 h)	10 & -	0	0.07	0.08	1.00E-16	4.00E-16
Fischer et al. (2013)	Stuttgart (Germany)	B (2880 h)	5.5 & 40	0	0.21	0.28		
Marbler et al. (2013)	Silicate-cemented Bunter (Germany)	B (12960 h)	10 & 40	0	0.26		3.50E-14	
Nover et al. (2013)	Bernburg,Volperiehauser, Neidenbach (Germany)	B (240-4320 h)	10-20 & 100-200	0	0.15	0.16	1.10E-15	3.30E-15
Farquhar et al. (2015)	Precipice (Australia)	B (384 h)	12 & 60	0	0.15	0.15	3.20E-13	
Farquhar et al. (2015)	Evergreen (Australia)	B (384 h)	12 & 60	0	0.07	0.08	8.58E-14	
Farquhar et al. (2015)	Hutton (Australia)	B (384 h)	12 & 60	0	0.08	0.12	4.20E-13	
Falcon Suarez et al. (2016)	Synthetic	F-T (172 h)	8.2 & 35	0	0.26		1.00E-15	1.32E-15
Rinehart et al. (2016)	Tuscaloosa (USA)	F-T (<1 h)	13 & 100	0	0.19	0.19		
Tariq et al.[&LS] (2018)	Berea (USA)	B (240-2880 h)	8.27 & 120	0	0.17	0.17	1.99E-13	1.99E-13

Table A2 (continued)

Fuchs et al. (2019)	Mt. Simon (USA)	B (672-1344 h)	22.1 & 50	0	0.08	0.16		
Huang et al. (2019)	Zunyi (China)	F-T (28 h)	10 & 32	0	0.18		9.00E-13	
Pearce et al. (2019)	Precipice (Australia)	B (72)	12 & 60		0.21	0.28		
Pearce et al. (2019)	Hutton (Australia)	B (72)	12 & 60		0.06	0.12		
Akono et al. (2020)	Mt. Simon (USA)	B/F-T (120-168 h)	8-17 & 50-115	0	0.23	0.32		
Tarokh et al. (2020)	Berea (USA)	F-T (528 h)	6.9 & 22	0	0.20	0.22	1.48E-13	2.96E-13
Kim and Makhnenko[&LS](2021)	Berea (USA)	F-T (504 h)	7 & 22	0	0.22	0.22	1.00E-13	
Shales								
Minardi et al. (2021)	Opalinus (Switzerland)	F-T (240-2520 h)	1.5-16 &21-24	20-50	0.08	0.08	1.00E-20	1.00E-20
Sterpenich et al.[&LS] (2014)	Callovo (France)	B (780 h)	9.8-10.8 & 80	25	0.13	0.13	7.00E-13	7.00E-13
Zou et al. (2018)	Lujiaping (China)	B (0.5-168 h)	10-30 & 0-120	25	0.02	0.04	6.10E-20	7.65E-19
Espinoza et al. (2018)	Mancos (USA)	Natural Seepage	-	20	0.06	0.06		
Ilgen et al. (2018)	Mancos (USA)	B (1344 h)	0.7-17 & 90	18	0.22	0.23		
Zou et al. (2018)	Longmaxi (China)	B (0.5-168 h)	10-30 & 40-120	15	0.04	0.10	2.32E-20	4.93E-19
Dewhurst et al. (2020)	Shale	B (4320 h)	29 & 150	10	0.13			
Wigand et al. (2009)	Wolfcamp (USA)	B(2712h)	20 & 54	6.2				
Lyu et al. Gas (2016)	Longmaxi (China)	B (240-720 h)	7-9 & 40	4				
Lyu et al. SC (2016)	Longmaxi (China)	B (240-720 h)	7-9 & 40	4				
Lyu et al. Gas (2018)	Longmaxi (China)	B (240-720 h)	7-9 & 40	4				
Lyu et al. Sc (2018)	Longmaxi (China)	B (240-720 h)	7-9 & 40	4				
Busch et al. (2008)	Muderong (Australia)	B (-)	6.7 & 50	2	0.20		1.00E-21	
Rezaee et al. (2017)	Latrobe Group (Australia)	B (2160 h)	15.17 & 66	2	0.13	0.20		
Kaszuba et al. (2003, 2005)	Maple Wood (USA)	B (1080 h)	20 & 200	1				
Pearce et al. (2019)	Evergreen (Australia)	B(72)	12 & 60	> 0	0.045			
Hadian and Rezaee (2019)	Yalgroup Member & Eneabba (Australia)	B (2880-6480 h)	13.7 & 60	0	0.07	0.18	2.90E-19	
Hadian and Rezaee (2019)	Yalgroup Member & Eneabba (Australia)	B (2880-6480 h)	13.7 & 60	0	0.06	0.10	2.90E-19	
Choi et al. (2021)	Chungcheongnam-nonwet (South Korea)	B (1512 h)	10 & 50	0	0.04			
Choi et al. (2021)	Chungcheongnam-wet (South Korea)	B (1512 h)	10 & 50	0	0.04			
Jayasekara and Ranjith (2021)	Eidsvold (Australia)	B (2160 h)	10 & 60	0				
Al-Ameri et al.[&LS] (2016)	Shale (Middle East)	B (720 h)	13.7 & 100	-				

Table A3. List of laboratory studies on different reservoir or seal rocks and their acoustic and mechanical properties before and after exposure to CO_2. One should notice that by knowing two of four elastic moduli (i.e., *E*, *K*, *G*, and *v*), the other two can be calculated using the relationship among these elastic constants (Jaeger and Cook, 2007; Mavko et al., 2009). However, here I only include moduli reported in the studied papers. Studies are sorted according to carbonate content and chronologically for those comprising the same carbonate content (See Table A1). Experimental studies that used more than one rock type are differentiated by adding a superscript labeled with "&" followed by LS, DO, SS, or SH standing, respectively, for limestone, dolostone, sandstone, and shale.

Reference	***E*[3] initial**	***E* final**	***K*[4] initial**	***K* final**	***G*[5] initial**	***G* final**	***v*[6] initial**	***v* final**	**UCS[7] initial**	**UCS final**	***Ø*[8] initial**	***Ø* final**	**c[9] initial**	**c final**	***V_p* - *V_s*[10] initial**	***V_p* -*V_s* final**
	(GPa)	(GPa)	(GPa)	(GPa)	(GPa)	(GPa)	(-)	(-)	(MPa)	(MPa)	(º)	(º)	(MPa)	(MPa)	(km/s)	(km/s)
Chalks																
Grombacher et al.[&LS] (2015)															3.4 - 2.1	3.0 - 2.0
Alam et al. (2014)	15.5	11.6	5.5	4.0			0.23	0.30							2.3 - 2.1	3.7 - 2.2
Alam et al. (2014)	7.1	3.1	9.0	7.9			0.21	0.23							4.1 - 2.4	3.6 - 2.2
Limestones & Dolostone																
Bemer and Lombard (2010)			20.0	15.0	13.0	11.1										
Bemer and Lombard (2010)			20.0	15.0	13.0	11.1										
Rimmele et al.[&SS] (2010)			8.0	8.0			0.17	0.17	16	16						
Grgic (2011)			47.0	38.5	12.0	12.0										
Vialle and Vanario (2011)															3.5 - 2	2.5 - 1.5
Grombacher et al.[&CH] (2015)															3.8 - 2.2	3.5 - 2.1
Grombacher et al.[&CH] (2015)															5.2 -2.9	4.9 - 2.7
Vialle et al. (2014)															3.1-3.6 - 1.6-2	3-3.2 -
El Husseiny and Vanario(2015)															3.35 - 1.0	2.5 - 0.8
El Husseiny and Vanario(2015)															2.5 - 1.7	1.8 - 1.3
Al-Ameri et al.[&SH]) 2016(	23.4	16.8					0.32	0.34	36.0	33.0						
Al-Ameri et al.[&SH] (2016)	16.2	14.0					0.35	0.23	17.0	12.4						
Al-Ameri et al.[&SH] (2016)	32.7	22.8							33.0	29.0						

[3] Young's modulus
[4] Bulk modulus
[5] Shear modulus
[6] Poisson's ratio
[7] Uniaxial Compressive Strength
[8] Friction angle
[9] Cohesion
[10] Compressional (V_p) and Shear (V_s) wave velocities

Table A3 (continued)

Clark and Vanario)2016(															4.0 - 2.5	3.8 -
Clark and Vanario (2016)															4.3 - 2.3	4.0 -
Tariq et al.[&SS] (2018)	66.9	64.2					0.30	0.30								
Sterpenich et al. (2014)																
Kim et al. (2018)	7.1	4.4					0.25	0.25			21	14	5.6	3.0		
Raza et al. (2020)	22.7	15.9	18.9	9.0	8.7	6.5	0.21	0.30								
Zhang et al. (2019)									17.2	14.8						
Zhang et al. (2019)									17.2	7.9						
Kim and Makhnenko[&SS](2021)			65.9	55.0												
Kim and Makhnenko[&SS](2021)			42.7	34.0												
Bemer and Lombard (2010)			20.0	10.0	14.0	10.0										
Bemer and Lombard (2010)			20.0	10.0	14.0	10.0										
Tariq et al.[&SS] (2018)	31.6	33.1					0.20	0.10								
Sandstones																
Espinoza et al. (2018)	32.8	7.6					0.22	0.15	159.0	20.4						
Hangx et al. (2015)	19.0	21.0	20.1	22.7					117.0		45.0					
Adam et al. (2015)															2-37 -	1.6-3 -
Rathnaweera et al. (2017)									20.0	13.0						
Marbler et al. (2013)	16.7	14.7							61.7		57.0		9.2			
Espinoza et al. (2018)	20.0	14.0					0.32	0.30	66.1	57.0						
Rathnaweera et al. (2017)									22.0	24.0						
Foroutan & Ghazanfari (2020)	27.0	23.0	6.5	5.00	25.0	20.0	0.19	0.30								
Foroutan et al. (2021a,2021b)	27.5	21.7	26.2	16.6					175.0	100.0	34	27.5	110.0	48.7	3.8-4 - 1.8	2.9-3.3 - 1.5
Rathnaweera et al.(2015)	5.4	4.2					0.28	0.32	25.3	13.5						
Perera et al. (2016)	9.6	8.3					0.26	0.36	25.9	20.1						
Lamy-Chappuis et al. (2016)									80.0	42.0	16.0	8.3	14.5	10.5		
Marbler et al. (2013)	13.7	11.1							34.1		43.0		7.5			
Zhou et al. (2016)	7.9	4.9	6.9				0.21	0.21								
Mikhlatsevitch et al. (2014)			16.3	12.9	14.0	14.0									3.5-4 - 2-2.5	
Raza et al. (2016)	25.3				10.2		0.25	0.25	53.0						3.3-3.5 - 1.9-2.1	
Shi et al.)2019(	14.0	13.2	5.2	4.9												
Harbert et al. (2020)	17.1	12.0	7.2	5.3	7.7	5.4	0.11	0.13							2.8 - 1.9	2.4 - 1.5
Harbert et al.)2020(	16.2	19.4	7.5	10.1	7.5	8.6	0.13	0.17							2.7 - 1.8	2.9 - 1.9
Hangx et al. (2013)	21.7	16.3	13.6	8.8			0.24	0.18	80.2	74.1	34.0		3.0		3.5 - 1.8	3.5 - 1.8
Hangx et al. (2013)	21.7	16.3	13.6	8.8			0.24	0.18	80.2	74.1	34.0		3.0		3.5 -	3.5 -
Rimmele et al.[&LS] (2010)			6.0	6.0			0.25	0.25	25.0	25.0						
Vanario et al.[&LS] (2011)															3.7-5 - 2.5-3.2	3.8-5.3 - 2.6-3.6
Marbler et al.(2013)	10.8	10.3							36.1	0.0	40.0	55.8	8.40	0.0		
Nover et al. (2013)							0.26	0.36								

Table A3 (continued)

Falcon Suarez et al. (2016)													3.9 - 2.3	3.5 - 2.2
Rinehart et al. (2016)							65.0	35.0						
Tariq et al.[&LS] (2018)	32.08	30.16			0.10	0.10								
Huang et al. (2019)							40.0	30.0						
Tarokh et al. (2020)													2.3 - 1.5	2.2 - 1.4
Kim and Makhnenko[&LS](2021)			30.0	30.0										
Shales														
Zou et al. (2018)							15.0	13.1	31.0	31.0				
Espinoza et al. (2018)	6.0	8.6			0.17	0.22								
Zou et al. (2018)							8.9	6.5	34.0	32.6				
Dewhurst et al. (2020)	6.1	8.8			0.28	0.15	32.0	52.0	14.6	17.7	5.1	6.1		
Lyu et al. Gas (2016)	5.2	2.4					58.8	25.6						
Lyu et al. SC (2016)	5.2	2.3					58.8	20.0						
Lyu et al. Gas (2018)	6.0	4.3					56.1	43.2						
Lyu et al. Sc (2018)	6.0	3.7					56.1	41.2						
Rezaee et al. (2017)	5.2	2.9					58.8	31.9						
Choi et al. (2021)	24.2	29.4			0.14	0.13	171.0	190.3					3.8 - 2.2	3.9 - 2.2
Choi et al. (2021)	24.2	10.1			0.14	0.11	171.0	115.2					3.3 - 1.9	2.7 - 1.5
Jayasekara and Ranjith (2021)	12.0	10.3			0.47	0.24	52.2	42.7					3.3 - 2	-
Al-Ameri et al.[&LS] (2016)							58.0	53.2						

Appendix II

Experimental setups

High-pressure flow-through setup

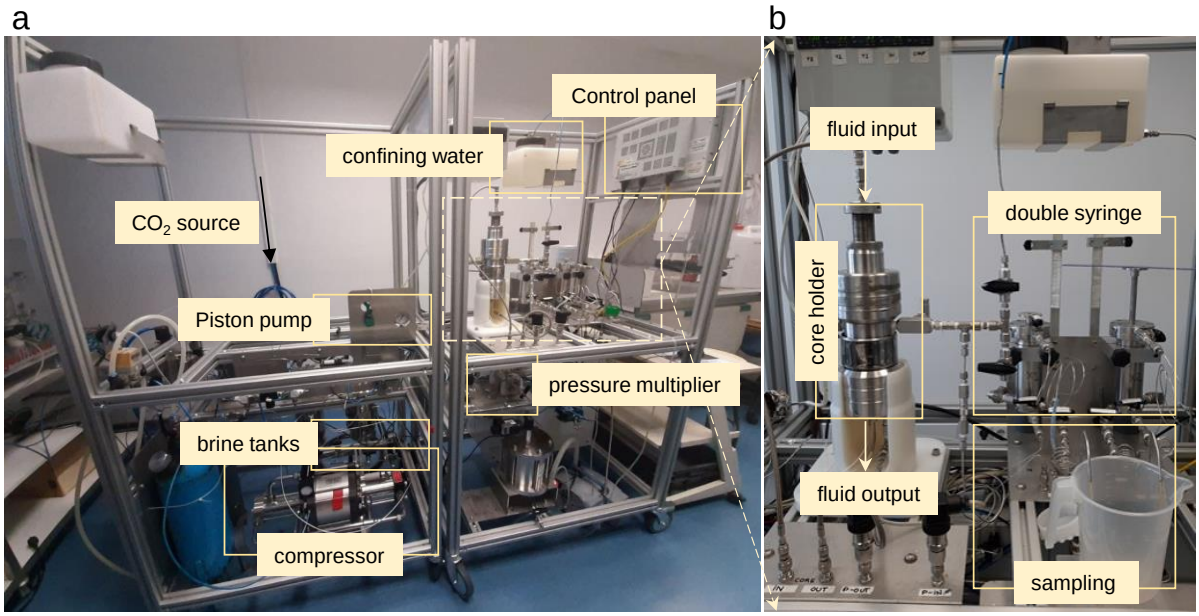

Figure A1. Photograph of the high-pressure flow-through setup used to inject CO_2-saturated water in the limestone cores under supercritical CO_2 conditions.

Atmospheric-pressure flow-through setup

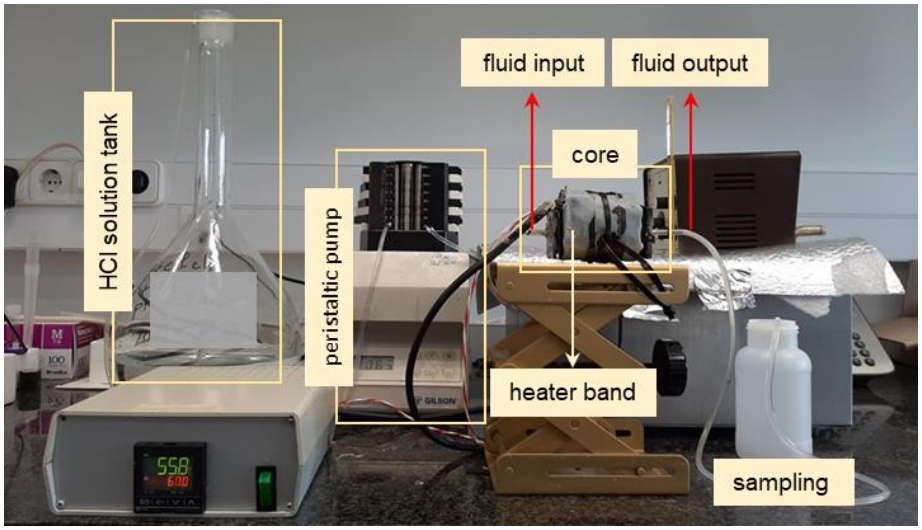

Figure A2. Photograph of the atmospheric flow-through setup used to inject HCl solution in the limestone cores under atmospheric pressure.

Classical permeability measurement setup

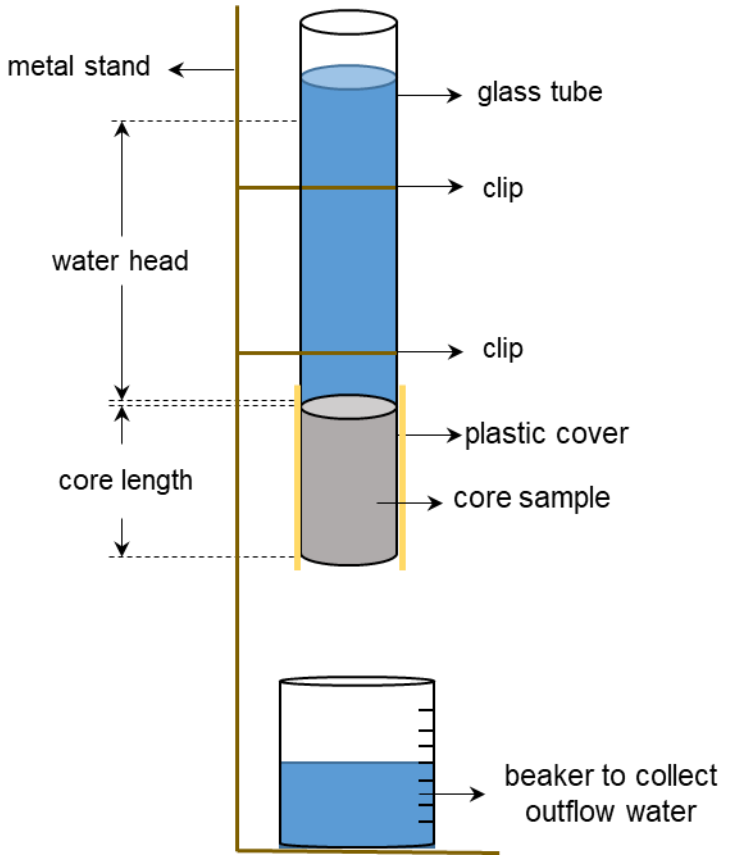

Figure A3. Schematic of the permeability measurement setup.

Uniaxial loading setup

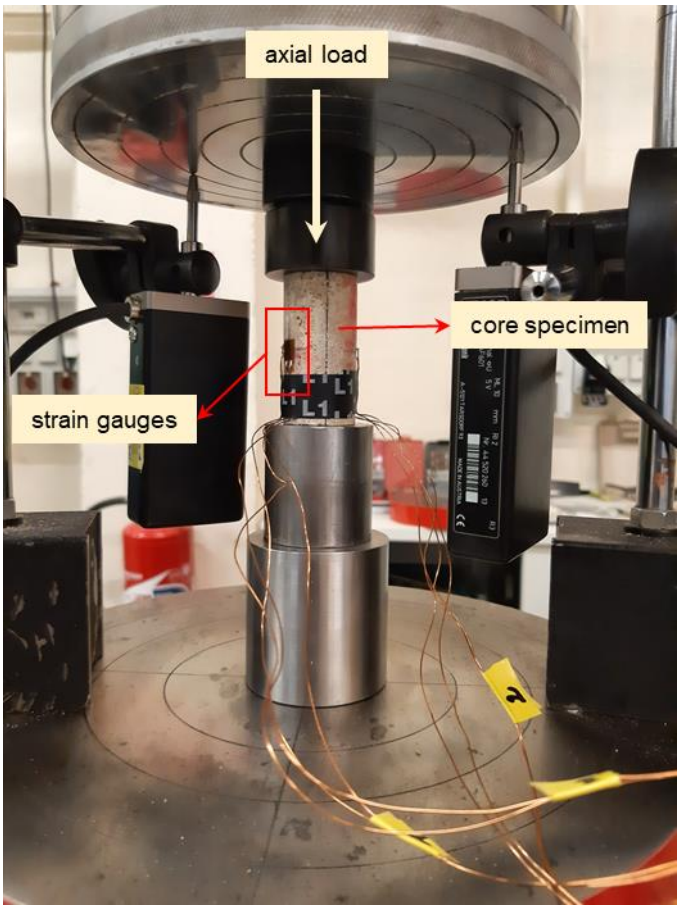

Figure A4. Photograph of the uniaxial loading setup.

Ultrasonic velocity measurement setup

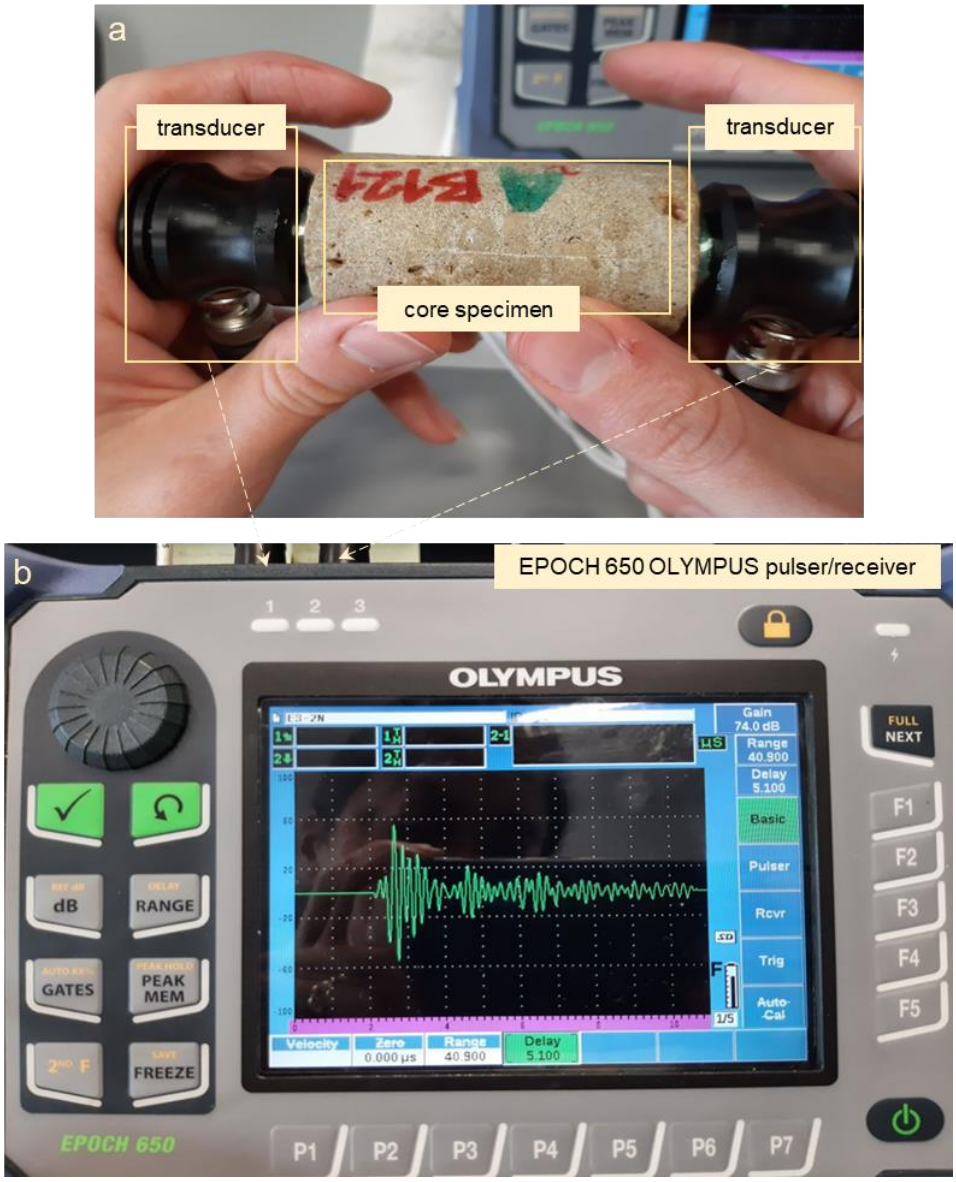

Figure A5. Photographs of: (a) a centimeter-scale core with attached pulser and receiver and (b) the EPOCH650 apparatus used to measure compressional and shear wave velocities.

Appendix III

A MATLAB code for digital reconstruction of rock porosity and permeability

Porosity and permeability calculation

```
clc;  clearvars;  close all

tic

currentfolder = pwd;
addpath(currentfolder)

image_folder = [currentfolder,'\Stack\Binary\'];
save_image_folder = [currentfolder,'\Stack\'];

% Increasing CT porosity to the effective porosity value
Porosity_Adjus='N';  % Y: yes % N: no

%% Initial rock properties

Por_Eff=0.24; %initial average porosity (from Helium porosimeter)

% input for CRUNCHFLOW CODE

Perm_Eff=2.54e-14; %initial average permeability of the rock

Perm_Pump=1.0e-9; %pump zone permeability

Por_Min=0.001; %minimum porosity

Por_Max=1; %maximum porosity

Perm_Inert=1.0e-22; %permeability of inert zone

Perm_Ghost=1.0e-22; %permeability of the ghost zones

% Power of porosity in porosity-permeability relationship to calculate

permeability_power=3; % permeability of each cell

%% Griding information

Cell_X_No=20; %number of grids in the X direction

Cell_Y_No=20; % number of grids in the Y direction

Cell_Z_No=20; % number of grids in the Z direction

%% Core length and diameter (width of CT cross-section in mm)

Core_Diameter=25.3;
Core_length=43.8;

Cell_width=Core_Diameter/Cell_X_No; % Width of each cell in millimeter (x and y direction)

Cell_length=Core_length/Cell_Z_No; % Length of each cell in millimeter (z direction)

%% Loading images and calculate initial CT porosity

for z=1:Cell_Z_No
   % Loading image names for each grid set in the Z direction
   image_information=dir([image_folder,'Z',num2str(z),'\','*.tif']);

   numslice=numel(image_information);

   for i=1:numslice
      % Reading binary images associated to each Z
      t=imread([image_folder,'Z',num2str(z),'\', image_information(i).name]);
```

```
        % Convert the image to 0,1
        t=(t~=0);

        % 3D stack of brightness matrices
        % Can be viewed in 3D using volume Viewer(IMG)
        % 1: solid, 0: pore
        IMG(:,:,i)=t;
    end;

    % Equal in both directions here
    Pixel_No = length(IMG);

    % Pixel width in millimeter
    Pixel_Width=Core_Diameter/Pixel_No;

    % Defining the core cross section on the loaded images we put the origin at the left-uppermost point

    Section_Domain=zeros(Pixel_No,Pixel_No);
    for m=1:Pixel_No
        for n=1:Pixel_No
            X_Pixel=(n-1/2)*Pixel_Width;
            Y_Pixel=(m-1/2)*Pixel_Width;

            if (X_Pixel-Core_Diameter/2)^2+(Y_Pixel-Core_Diameter/2)^2<=(Core_Diameter/2)^2
                % 1 for the part of images containing the rock
                Section_Domain(m,n)=1;
            end
        end;
    end;

    % Initial porosity of all slices along each Z grid
    % A matrix of (number_of_zgrid * number_of_slice)
    for s=1:numslice
        Porosity_slice_total(s,z)=(Pixel_No*Pixel_No-sum(sum(IMG(:,:,s))))/sum(sum(Section_Domain(:,:)));
    end;

    % Save intensity matrices for the whole sample (separated by zgrid)
    if exist([save_image_folder,'Intensity_matrices\'])==7
        save( [save_image_folder,'Intensity_matrices\','Intensity_','Z',num2str(z)],'IMG');
    else
        mkdir(save_image_folder,'Intensity_matrices');
        save( [save_image_folder,'Intensity_matrices\','Intensity_','Z',num2str(z)],'IMG');
    end;
end;

Porosity_zgrid_total=mean(Porosity_slice_total); % Average CT porosity of each Z grid

Porosity_total=mean(mean(Porosity_zgrid_total)); % Total sample porosity from CT

% Save porosity for all slices, Sectiodomain,
% Porosity_zgrid_total and total porosity
if exist([currentfolder,'\Results'])==7
    save( [currentfolder,'\Results','\Initial_CT_porosity'],'Porosity_slice_total','Section_Domain','Porosity_zgrid_total','Porosity_total');
else
    mkdir(currentfolder,'Results');
    save( [currentfolder,'\Results','\Initial_CT_porosity'],'Porosity_slice_total','Section_Domain','Porosity_zgrid_total','Porosity_total');
end;

toc

%% Porosity adjustment from CT to effective
if Porosity_Adjus=='Y';
tic
    if exist([currentfolder,'\Results','\Initial_CT_porosity.mat'])==2
        load([currentfolder,'\Results','\Initial_CT_porosity.mat'])
    else
        disp('Porosity calculations have to be performed first')
    end;

    for z=1:Cell_Z_No
        if exist([save_image_folder,'Intensity_matrices\','Intensity_','Z',num2str(z),'.mat'])==2
            load([save_image_folder,'Intensity_matrices\','Intensity_','Z',num2str(z),'.mat'])
        else
            disp('Porosity calculations have to be performed first')
        end;
```

```
        [Pixel_No Pixel_No numslice]=size(IMG);

        % Number of pixels that has to be added to each CT cross section to reproduce
        % Effective porosity of the rock
        Delta_Pixel=fix((Por_Eff-Porosity_total)*sum(sum(Section_Domain(:,:))));

        % We add "Delta_pixel" pixels to all CT slices of all Zgrids
        for s=1:numslice
            % Matrix containing pixel positions for the solid part of the rock
            % 1 for the matrix part
            Solid_Pixels=IMG(:,:,s).*Section_Domain;

            % Returns rows and columns that have value 1 (Solid) in Solid_pixels
            [R_mat,C_mat] = find(Solid_Pixels==1);

            % Select randomly "Delta_pixel" pixels
            idx = randsample(length(C_mat),Delta_Pixel);

            % In the brightness matrix IMG, replace matrix points with 0 (add porosity)
            for I=1:length(idx)
                IMG(R_mat(idx(I)),C_mat(idx(I)),s)=0;
            end;
            % Final porosity of each section after adding random pores
            Porosity_slice_total_updated(s,z)=(Pixel_No*Pixel_No-sum(sum(IMG(:,:,s))))/sum(sum(Section_Domain(:,:)));
        end;

        % Save updated intensity matrices for the whole sample
        if exist([save_image_folder,'Intensity_matrices_updated'])==7
            save( [save_image_folder,'Intensity_matrices_updated\','Intensity_','Z',num2str(z),'_updated'],'IMG');
        else
            mkdir(save_image_folder,'Intensity_matrices_updated');
            save( [save_image_folder,'Intensity_matrices_updated\','Intensity_','Z',num2str(z),'_updated'],'IMG');
        end;
    end;

    % Average CT porosity of each Z grid (updated)
    Porosity_zgrid_total_updated=mean(Porosity_slice_total_updated);

    % Total sample porosity from CT (updated)
    Porosity_total_updated=mean(mean(Porosity_zgrid_total_updated));

    % Save updated porosity for all slices and total porosity
    save(
[currentfolder,'\Results','\Updated_CT_porosity'],'Porosity_slice_total_updated','Porosity_zgrid_total_updated','Porosity_total_updated');

    toc
end;

%% Building permeability files in each direction (CrunchFlow code)
tic
% Cell_X_no+2 number of cells + 2 ghost cells in X direction
% 4: We need a matrix of (cell_X_no+2)*(cell_Y_no)*(Cell_Z_No) rows and 4 columns
Single_Column_Perm_X=zeros((Cell_X_No+2)*(Cell_Y_No)*(Cell_Z_No+1),4)+Perm_Ghost;

for Z=1:Cell_Z_No+1
    for Y=1:Cell_Y_No
        for X=1:Cell_X_No+2
            Single_Column_Perm_X(((Cell_X_No+2)*(Cell_Y_No))*(Z-1)+((Y-1)*(Cell_X_No+2))+X,1)=X-1;
            Single_Column_Perm_X(((Cell_X_No+2)*(Cell_Y_No))*(Z-1)+((Y-1)*(Cell_X_No+2))+X,2)=Y;
            Single_Column_Perm_X(((Cell_X_No+2)*(Cell_Y_No))*(Z-1)+((Y-1)*(Cell_X_No+2))+X,3)=Z;
        end
    end
end

% Cell_Y_no+2 number of cells + 2 ghost cells in Y direction
% 4: We need a matrix of (cell_X_no)*(cell_Y_no+2)*(numimage) rows and 4 columns
Single_Column_Perm_Y=zeros((Cell_X_No)*(Cell_Y_No+2)*(Cell_Z_No+1),4)+Perm_Ghost;

for Z=1:Cell_Z_No+1
    for Y=1:Cell_Y_No+2
        for X=1:Cell_X_No
            Single_Column_Perm_Y(((Cell_X_No)*(Cell_Y_No+2))*(Z-1)+((Y-1)*(Cell_X_No))+X,1)=X;
            Single_Column_Perm_Y(((Cell_X_No)*(Cell_Y_No+2))*(Z-1)+((Y-1)*(Cell_X_No))+X,2)=Y-1;
            Single_Column_Perm_Y(((Cell_X_No)*(Cell_Y_No+2))*(Z-1)+((Y-1)*(Cell_X_No))+X,3)=Z;
        end
```

```
    end
end

% numimage+2 number of cells plus 2 ghost cells in Z dircetion
% 4: We need a matrix of (cell_X_no+2)*(cell_Y_no)*(numimage+2) rows and 4 columns
Single_Column_Perm_Z=zeros((Cell_X_No)*(Cell_Y_No)*(Cell_Z_No+3),4)+Perm_Ghost;

for Z=1:Cell_Z_No+3
    for Y=1:Cell_Y_No
        for X=1:Cell_X_No
            Single_Column_Perm_Z(((Cell_X_No)*(Cell_Y_No))*(Z-1)+((Y-1)*(Cell_X_No))+X,1)=X;
            Single_Column_Perm_Z(((Cell_X_No)*(Cell_Y_No))*(Z-1)+((Y-1)*(Cell_X_No))+X,2)=Y;
            Single_Column_Perm_Z(((Cell_X_No)*(Cell_Y_No))*(Z-1)+((Y-1)*(Cell_X_No))+X,3)=Z-1;
        end
    end
end

toc

%% Calculating porosity values in all grid cells

tic
Porosity_vector=zeros(Cell_Y_No*Cell_X_No,Cell_Z_No); % 2D matrix file of porosity for permeability calculations
Porosity_2D=zeros(Cell_Y_No,Cell_X_No,Cell_Z_No);  % 3D array for plotting digitized porosity cross sections
Porosity_3D=zeros(Cell_Y_No,Cell_X_No,Cell_Z_No); % 3D array for plotting digitized porosity in 3D
Grid_coordinates=zeros(Cell_Y_No,Cell_X_No);  % 2D matrix of grid coordinates (X, Y)

for z=1:Cell_Z_No
    % Read binary images from image folders
    if Porosity_Adjus=='Y';
        if exist([save_image_folder,'Intensity_matrices_updated'])==7
            load([save_image_folder,'Intensity_matrices_updated\','Intensity_','Z',num2str(z),'_updated','.mat'])
        else
            disp('Porosity updating has to be performed first')
        end;
    else
        if exist([save_image_folder,'Intensity_matrices'])==7
            load([save_image_folder,'Intensity_matrices\','Intensity_','Z',num2str(z),'.mat'])
        else
            disp('Porosity calculations have to be performed first')
        end;
    end;

    [Pixel_No Pixel_No numslice]=size(IMG);

    % I increasing from left to right and from bottom to top
    for I=1:Cell_X_No*Cell_Y_No
        Cell_M=ceil(I/Cell_X_No);  % Row number of cell I

        Cell_N=rem(I,Cell_X_No);   % Column number of cell I

        if Cell_N==0
            Cell_N=Cell_X_No;
        end;

        % Number of the pixel located on the top row of the cells
        Pixel_Row_Up=Pixel_No-ceil(Cell_M*Cell_width/Pixel_Width);

        if Pixel_Row_Up<=0
            Pixel_Row_Up=1;
        end;

        % Number of the pixel located on the bottom row of the cells
        Pixel_Row_Down=Pixel_No-ceil((Cell_M-1)*Cell_width/Pixel_Width);

        % Number of the pixel located on the left column of the cells
        if Cell_N==1
            Pixel_Column_Left=1;
        else
            Pixel_Column_Left=ceil((Cell_N-1)*Cell_width/Pixel_Width);
        end;

        % Number of the pixel located on the right column of the cells
        Pixel_Column_Right=ceil(Cell_N*Cell_width/Pixel_Width);
```

```
        if Pixel_Column_Right>=Pixel_No
            Pixel_Column_Right=Pixel_No;
        end;

        % Exporting grid coordinates for plotting (X,Y)
        % We assume that the coordinates are the same along all z grids
        % X=0 on the left and Y=0 at the bottom
        if z==1
            Grid_coordinates(Cell_M,Cell_N,1)=(Cell_N-1)*Cell_width+Cell_width/2;
            Grid_coordinates(Cell_M,Cell_N,2)=(Cell_M-1)*Cell_width+Cell_width/2;

            % See if the grid is on rock or the surrounding media
            % 0 means surrounding media
            Section_domain_status(Cell_M,Cell_N)=sum(sum(Section_Domain(Pixel_Row_Up:Pixel_Row_Down,Pixel_Column_Left:
Pixel_Column_Right)));
        end;

        % Porosity of cell I
        for s=1:numslice
            Cell_Phi_slice(s)=(((Pixel_Row_Down-Pixel_Row_Up+1)*(Pixel_Column_Right-Pixel_Column_Left+1))-
sum(sum(IMG(Pixel_Row_Up:Pixel_Row_Down,Pixel_Column_Left: Pixel_Column_Right,s))))/((Pixel_Row_Down-
Pixel_Row_Up+1)*(Pixel_Column_Right-Pixel_Column_Left+1));
        end;

        Cell_Phi(I)=mean(Cell_Phi_slice);
        clear('Cell_Phi_slice');

        % Porosity file for permeability measurements
        % Columns: Z grid
        % Rows: porosity of grids (Cell_X_No*Cell_Y_No)
        Porosity_vector(I,z)=Cell_Phi(I);

        % Convert porosity to brightness for plotting purposes
        % Note that the order of cell rows are inverted for 2D plotting
        Porosity_2D(Cell_Y_No-Cell_M+1,Cell_N,z)=Cell_Phi(I);

        % Cell_Y_No*Cell_X_No matrix of porosity (for 3D porosity plot)
        Porosity_3D(Cell_M,Cell_N,z)=Cell_Phi(I);

        % The area or volume surrounding the rock is eliminated from plots
        if Section_domain_status(Cell_M,Cell_N)==0
            Porosity_2D(Cell_Y_No-Cell_M+1,Cell_N,z)=NaN;
            Porosity_3D(Cell_M,Cell_N,z)=NaN;
        end

    end
 end;

% Save 2D and 3D grid porosity
if Porosity_Adjus=='Y'
    Porosity_2D_adjusted=Porosity_2D;
    Porosity_3D_adjusted=Porosity_3D;

    save( [currentfolder,'\Results','\2D_grid_porosity_adjusted'],'Porosity_2D_adjusted','Cell_X_No','Cell_Y_No','Cell_Z_No');
    save(
[currentfolder,'\Results','\3D_grid_porosity_adjusted'],'Porosity_3D_adjusted','Cell_X_No','Cell_Y_No','Cell_Z_No','Cell_width','Cell_lengt
h');

else
    Porosity_2D_raw=Porosity_2D;
    Porosity_3D_raw=Porosity_3D;

    save( [currentfolder,'\Results','\2D_grid_porosity_raw'],'Porosity_2D_raw','Cell_X_No','Cell_Y_No','Cell_Z_No');
    save(
[currentfolder,'\Results','\3D_grid_porosity_raw'],'Porosity_3D_raw','Cell_X_No','Cell_Y_No','Cell_Z_No','Cell_width','Cell_length');
end;

toc

%% Permeability calculations from the porosity map
tic
% Output according to the CRUNCHFLOW code format
for z=1:Cell_Z_No
    for I=1:Cell_X_No*Cell_Y_No
```

```
    % Assigning a lower porosity threshold for numerical simulations of flow
    if Porosity_vector(I,z)<Por_Min
       Porosity_vector(I,z)=Por_Min;
    end;

    R=rem(I,Cell_X_No); % Determines in which column we are

    Q=(I-R)/Cell_X_No; % How many rows are filled

    % Permeability in each direction by considering ghost cells
    if R==0
      Q=Q-1;
      R=Cell_X_No;
    end;

    % Calculating permeability using a powerlaw equation (pump zone)
    if z==1
       if Porosity_vector(I,z)==Por_Min
          Single_Column_Perm_X((z-1)*((Cell_X_No+2)*Cell_Y_No)+Q*(Cell_X_No+2)+R+1,4)=Perm_Inert;
       else
          Single_Column_Perm_X((z-1)*((Cell_X_No+2)*Cell_Y_No)+Q*(Cell_X_No+2)+R+1,4)=Perm_Pump;
       end;

       if Porosity_vector(I,z)==Por_Min
          Single_Column_Perm_Y((z-1)*(Cell_X_No*(Cell_Y_No+2))+(Q+1)*(Cell_X_No)+R,4)=Perm_Inert;
        else
          Single_Column_Perm_Y((z-1)*(Cell_X_No*(Cell_Y_No+2))+(Q+1)*(Cell_X_No)+R,4)=Perm_Pump;
       end;

       if Porosity_vector(I,z)==Por_Min
          Single_Column_Perm_Z((z)*(Cell_X_No*(Cell_Y_No))+I,4)=Perm_Inert;
       else
          Single_Column_Perm_Z((z)*(Cell_X_No*(Cell_Y_No))+I,4)=Perm_Pump;
       end;
    end;

    % Calculating permeability using a powerlaw equation (other cells)
    if Porosity_vector(I,z)==Por_Min
      Single_Column_Perm_X((z)*((Cell_X_No+2)*Cell_Y_No)+Q*(Cell_X_No+2)+R+1,4)=Perm_Inert;
    else

Single_Column_Perm_X((z)*((Cell_X_No+2)*Cell_Y_No)+Q*(Cell_X_No+2)+R+1,4)=Perm_Eff*((Porosity_vector(I,z)/Por_Eff)^perme
ability_power)*((1-Por_Eff)^2/(1-Porosity_vector(I,z))^2);
    end;

    if Porosity_vector(I,z)==Por_Min
       Single_Column_Perm_Y((z)*(Cell_X_No*(Cell_Y_No+2))+(Q+1)*(Cell_X_No)+R,4)=Perm_Inert;
     else

Single_Column_Perm_Y((z)*(Cell_X_No*(Cell_Y_No+2))+(Q+1)*(Cell_X_No)+R,4)=Perm_Eff*((Porosity_vector(I,z)/Por_Eff)^permea
bility_power)*((1-Por_Eff)^2/(1-Porosity_vector(I,z))^2);
    end;

    if Porosity_vector(I,z)==Por_Min
      Single_Column_Perm_Z((z+1)*(Cell_X_No*(Cell_Y_No))+I,4)=Perm_Inert;
    else

Single_Column_Perm_Z((z+1)*(Cell_X_No*(Cell_Y_No))+I,4)=Perm_Eff*((Porosity_vector(I,z)/Por_Eff)^permeability_power)*((1-
Por_Eff)^2/(1-Porosity_vector(I,z))^2);
    end;

Single_Column_Perm_Z(((Cell_Z_No+2)*Cell_X_No*Cell_Y_No+1):(Cell_Z_No+3)*Cell_X_No*Cell_Y_No,4)=Single_Column_Perm_
Z(((Cell_Z_No+1)*Cell_X_No*Cell_Y_No+1):(Cell_Z_No+2)*Cell_X_No*Cell_Y_No,4);
  end;
end

% Save 3D grid permeability (only for plotting)
Permeability_3D=Perm_Eff*((Porosity_3D/Por_Eff).^permeability_power).*((1-Por_Eff)^2./(1-Porosity_3D).^2);

if Porosity_Adjus=='Y'
  Permeability_3D_adjusted=Permeability_3D;
  save( [currentfolder,'\Results','\3D_grid_permeability_adjusted'],'Permeability_3D_adjusted');
else
  Permeability_3D_raw=Permeability_3D;
  save( [currentfolder,'\Results','\3D_grid_permeability_raw'],'Permeability_3D_raw');
```

```
end;

% Single column porosity ofr plotting in surfer
for i=1:Cell_Z_No
    Porosity_3D_surfer(:,:,i)=transpose(Porosity_3D(:,:,i));
end;

% Only the rock section
Single_Column_Porosity=reshape(Porosity_3D_surfer,[Cell_X_No*Cell_Y_No*Cell_Z_No,1,1]);
Single_Column_Porosity(isnan(Single_Column_Porosity))=Por_Min;

% Save single column porosity
save([currentfolder,'\Results','\single_column_porosity'],'Single_Column_Porosity');

%% Exporting permeability data into Excel files
% Permeability files in each direction
if Porosity_Adjus=='Y'
    xlswrite( [currentfolder,'\Results','\PermX_adjusted'],Single_Column_Perm_X);
    xlswrite( [currentfolder,'\Results','\PermY_adjusted'],Single_Column_Perm_Y);
    xlswrite( [currentfolder,'\Results','\PermZ_adjusted'],Single_Column_Perm_Z);
else
    xlswrite( [currentfolder,'\Results','\PermX_raw'],Single_Column_Perm_X);
    xlswrite( [currentfolder,'\Results','\PermY_raw'],Single_Column_Perm_Y);
    xlswrite( [currentfolder,'\Results','\PermZ_raw'],Single_Column_Perm_Z);
end;

toc
memory

Mem_data=whos;
for z=1:length(Mem_data)
    Mem_size(z,1)=Mem_data(z).bytes;
end;

sum(Mem_size)
```

Plotting 2D images

```
clc
clear
close all

currentfolder = pwd;
addpath(currentfolder)

image_folder = [currentfolder,'\Stack\'];
Grid_data_folder = [currentfolder,'\Results\'];

load([Grid_data_folder,'2D_grid_porosity_adjusted.mat']);
load([Grid_data_folder,'Initial_CT_porosity.mat']);
load([Grid_data_folder,'Updated_CT_porosity.mat']);

image_position=[12 5 16.5 10];
background_color=[1 1 1];
image_title_fontsize=12;
subplot_title_fontsize=11;
colorbar_fontsize=10;
colorbar_title_fontsize=12;

% Design the plot structure
if Cell_Z_No<=10
    row=2;
    column=ceil(Cell_Z_No/row);
elseif Cell_Z_No<20
    row=3;
    column=ceil(Cell_Z_No/row);
elseif Cell_Z_No<30
    row=4;
    column=ceil(Cell_Z_No/row);
end

load('mycmap2');
```

```
%% 2D plots of raw grayscale images
plot for one slide (the first one in the stack) as an example
Raw_grayscale_images=figure('Color',[1 1 1]);;
Raw_grayscale_images.Units = 'centimeters';
Raw_grayscale_images.Position = image_position;

clf;

for z=1:Cell_Z_No
    image_information=dir([image_folder,'Grayscale\','Z',num2str(z),'\','*.tif']);

    Original_image=imread([image_folder,'Grayscale\','Z',num2str(z),'\', image_information(1).name]);

    subplot(row,column,z);
    imagesc(Original_image); axis equal tight;
    title(['Grid ',num2str(z)],'FontName', 'Helvetica', ...
        'FontSize',subplot_title_fontsize, 'interpreter', 'latex');
    colormap(gray)
    drawnow;

    set(gca,'DataAspectRatio',[1 1 1],...
    'XTick',zeros(1,0),'YTick',zeros(1,0));

end;

annotation('textbox',...
    [0.36 0.9 0.1 0.1],...
    'String',{'Original CT images'},...
    'FontName', 'Helvetica', ...
    'interpreter', 'latex',...
    'fontsize',image_title_fontsize,...
    'EdgeColor','none');

%% 2D plots of raw binary CT images
% Plot for one slide (the first one in the stack) as an example
Binary_images_raw=figure('Color',[1 1 1]);;
Binary_images_raw.Units = 'centimeters';
Binary_images_raw.Position = image_position;

clf;

for z=1:Cell_Z_No
    load([image_folder,'Intensity_matrices\','Intensity_Z',num2str(z),'.mat']);
    subplot(row,column,z);
    imagesc(IMG(:,:,1)); axis equal tight;
    title(['Grid ',num2str(z),' ($\phi$ = ',num2str(Porosity_zgrid_total(z),'%5.3f'),')'],...
        'FontName', 'Helvetica', ...
        'FontSize',subplot_title_fontsize, 'interpreter', 'latex');
    colormap(gray)
    drawnow;

    set(gca,'DataAspectRatio',[1 1 1],...
        'XTick',zeros(1,0),'YTick',zeros(1,0));

end;

% Annotation(Binary_images_raw,'textbox',...
annotation('textbox',...
    [0.36 0.9 0.1 0.1],...
    'String',{'Raw binary images'},...
    'FontName', 'Helvetica', ...
    'interpreter', 'latex',...
    'fontsize',image_title_fontsize,...
    'EdgeColor','none');


%% 2D plots of updated binary CT images
% Plot for one slide (the first one in the stack) as an example
Binary_images_updated=figure('Color',[1 1 1]);;
Binary_images_updated.Units = 'centimeters';
Binary_images_updated.Position = image_position;

clf;
```

```
for z=1:Cell_Z_No
    load([image_folder,'Intensity_matrices_updated\','Intensity_Z',num2str(z),'_updated.mat']);
    subplot(row,column,z);
    imagesc(IMG(:,:,1)); axis equal tight;
    title(['Grid ',num2str(z),' ($\phi$ = ',num2str(Porosity_zgrid_total_updated(z),'%5.3f'),')'],...
        'FontName', 'Helvetica', ...
        'FontSize',subplot_title_fontsize, 'interpreter', 'latex');
    colormap(gray)
    drawnow;

    set(gca,'DataAspectRatio',[1 1 1],...
        'XTick',zeros(1,0),'YTick',zeros(1,0));

end;

%Annotation(Binary_images_updated,'textbox',...
annotation('textbox',...
    [0.34 0.9 0.1 0.1],...
    'String',{'Updated binary images'},...
    'FontName', 'Helvetica', ...
    'interpreter', 'latex',...
    'fontsize',image_title_fontsize,...
    'EdgeColor','none');


%% Plot 2D digitized porosity maps
    Digitized_porosity=figure('Color',[1 1 1]);;
    Digitized_porosity.Units = 'centimeters';
    Digitized_porosity.Position = image_position;

    clf;

for z=1:Cell_Z_No
    imAlpha=ones(Cell_X_No);
    imAlpha(isnan(Porosity_2D_adjusted(:,:,z)))=0;

    subplot(row,column,z);

    imagesc(Porosity_2D_adjusted(:,:,z),'AlphaData',imAlpha);  axis equal tight;

    title(['Grid ',num2str(z)],'FontName', 'Helvetica', ...
        'FontSize',subplot_title_fontsize, 'interpreter', 'latex');

    map=mycmap_dark;     % Map=flip(hot);
    colormap(map)      % Parula  imcomplement(gray)  hot
    drawnow;

    set(gca,'DataAspectRatio',[1 1 1],...
        'XTick',zeros(1,0),'YTick',zeros(1,0));

end;

% Annotation(Digitized_porosity,'textbox',...
annotation('textbox',...
    [0.34 0.9 0.1 0.1],...
    'String',{'Digitized CT map'},...
    'FontName', 'Helvetica', ...
    'interpreter', 'latex',...
    'fontsize',image_title_fontsize,...
    'EdgeColor','none');

cbar = colorbar('Location','Eastoutside',...
    'FontName', 'Helvetica', ...
    'FontSize',colorbar_fontsize);
set(get(cbar,'ylabel'),'string','Porosity, \phi [-]',...
    'FontName', 'Helvetica', ...
    'fontsize',colorbar_title_fontsize);
```

Plotting 3D images

```
clc
clear
close all
```

```
phi_full='Y';
phi_3quarter='Y';
phi_cross='N';
phi_slice='N';
porosity_histogram='N';

permeability_full='N';
perm_3quarter='N';
permeability_slice='N';

permeability_histogram='N';

currentfolder = pwd;
addpath(currentfolder)

image_folder = [currentfolder,'\Stack\'];
Grid_data_folder = [currentfolder,'\Results\'];

load([Grid_data_folder,'3D_grid_porosity_adjusted.mat']);
load([Grid_data_folder,'3D_grid_permeability_adjusted.mat']);

load('mycmap2');

%% Full 3D plot of the porosity map
if phi_full=='Y'
    Fig_3D_phi_full=figure('Color',[1 1 1]);
    Fig_3D_phi_full.Units = 'centimeters';
    Fig_3D_phi_full.Position = [12 5 20 10];


    for k = 1:Cell_Z_No
        for j = 1:Cell_X_No
            for i = 1:Cell_Y_No
                Point_x=-[0 1 1 0 0 0;1 1 0 0 1 1;1 1 0 0 1 1;0 1 1 0 0 0] * Cell_width + j*Cell_width;
                Point_y=-[0 0 1 1 0 0;0 1 1 0 0 0;0 1 1 0 1 1;0 0 1 1 1 1] * Cell_width + i*Cell_width;
                Point_z=-[0 0 0 0 0 1;0 0 0 0 0 1;1 1 1 1 0 1;1 1 1 1 0 1] * Cell_length + k*Cell_length;

                color = ones(4,6)*Porosity_3D_adjusted(i,j,k);

                if (isnan(Porosity_3D_adjusted(i,j,k))==0)
                    for l=1:6
                        patch(Point_x(:,l),Point_z(:,l),Point_y(:,l),color(:,l));
                    end
                end
            end
        end
    end

    view(45, 20);
    hold off
    axis equal
    axis off



    cbar = colorbar('Location','Eastoutside',...
        'FontName', 'Helvetica', ...
        'FontSize',14);
    set(get(cbar,'ylabel'),'string','Porosity, $\phi$ [-]',...
        'Rotation',90,...
        'FontName', 'Helvetica', ...
        'interpreter', 'latex',...
        'fontsize',16);

    caxis([0 0.7])

    map=mycmap_dark;     % Map=flip(hot);
    colormap(map)      % Parula  imcomplement(gray)  hot
end;

%% 3 Quarter 3D plot of the porosity map
if phi_3quarter=='Y'
    Fig_3D_phi_3quarter=figure('Color',[1 1 1]);
    Fig_3D_phi_3quarter.Units = 'centimeters';
    Fig_3D_phi_3quarter.Position = [12 5 20 10];
```

```
    for k = 1:Cell_Z_No
        for j = 1:Cell_X_No
            for i = 1:ceil(Cell_Y_No/2)
                Point_x=-[0 1 1 0 0 0;1 1 0 0 1 1;1 1 0 0 1 1;0 1 1 0 0 0] * Cell_width + j*Cell_width;
                Point_y=-[0 0 1 1 0 0;0 1 1 0 0 0;0 1 1 0 1 1;0 0 1 1 1 1] * Cell_width + i*Cell_width;
                Point_z=-[0 0 0 0 0 1;0 0 0 0 0 1;1 1 1 1 0 1;1 1 1 1 0 1] * Cell_length + k*Cell_length;

                color = ones(4,6)*Porosity_3D_adjusted(i,j,k);

                if (isnan(Porosity_3D_adjusted(i,j,k))==0)
                    for l=1:6
                        patch(Point_x(:,l),Point_z(:,l),Point_y(:,l),color(:,l));
                    end
                end
            end
        end
    end

    for k = 1:Cell_Z_No
        for j = 1:ceil(Cell_X_No/2)
            for i = (ceil(Cell_Y_No/2)+1):Cell_Y_No
                Point_x=-[0 1 1 0 0 0;1 1 0 0 1 1;1 1 0 0 1 1;0 1 1 0 0 0] * Cell_width + j*Cell_width;
                Point_y=-[0 0 1 1 0 0;0 1 1 0 0 0;0 1 1 0 1 1;0 0 1 1 1 1] * Cell_width + i*Cell_width;
                Point_z=-[0 0 0 0 0 1;0 0 0 0 0 1;1 1 1 1 0 1;1 1 1 1 0 1] * Cell_length + k*Cell_length;

                color = ones(4,6)*Porosity_3D_adjusted(i,j,k);

                if (isnan(Porosity_3D_adjusted(i,j,k))==0)
                    for l=1:6
                        patch(Point_x(:,l),Point_z(:,l),Point_y(:,l),color(:,l));
                    end
                end
            end
        end
    end

    view(50, 20);
    hold off
    axis equal
    axis off

    cbar = colorbar('Location','Eastoutside',...
        'FontName', 'Arial', ...
        'FontSize',10);
    set(get(cbar,'ylabel'),'string','Porosity, \phi [-]',...
        'Rotation',90,...
        'FontName', 'Arial', ...
        'interpreter', 'tex',...
        'fontsize',10);
    caxis([0 0.7])

    map=mycmap_dark;     % Map=flip(hot);
    colormap(map)      % Parula  imcomplement(gray)  hot
end;

%% 3D cross plot of the porosity map
if phi_cross=='Y'
    Fig_3D_phi_cross=figure('Color',[1 1 1]);
    Fig_3D_phi_cross.Units = 'centimeters';
    Fig_3D_phi_cross.Position = [12 5 20 10];

    for k = 1:Cell_Z_No
        for j = ceil(Cell_X_No/2)
            for i = 1:Cell_Y_No
                Point_x=-[0 1 1 0 0 0;1 1 0 0 1 1;1 1 0 0 1 1;0 1 1 0 0 0] * Cell_width + j*Cell_width;
                Point_y=-[0 0 1 1 0 0;0 1 1 0 0 0;0 1 1 0 1 1;0 0 1 1 1 1] * Cell_width + i*Cell_width;
                Point_z=-[0 0 0 0 0 1;0 0 0 0 0 1;1 1 1 1 0 1;1 1 1 1 0 1] * Cell_length + k*Cell_length;

                color = ones(4,6)*Porosity_3D_adjusted(i,j,k);

                if (isnan(Porosity_3D_adjusted(i,j,k))==0)
                    for l=1:6
                        patch(Point_x(:,l),Point_z(:,l),Point_y(:,l),color(:,l));
                    end
```

```
            end
        end
    end
end

for k = 1:Cell_Z_No
    for j = 1:Cell_X_No
        for i = ceil(Cell_Y_No/2)
            Point_x=-[0 1 1 0 0 0;1 1 0 0 1 1;1 1 0 0 1 1;0 1 1 0 0 0] * Cell_width + j*Cell_width;
            Point_y=-[0 0 1 1 0 0;0 1 1 0 0 0;0 1 1 0 1 1;0 0 1 1 1 1] * Cell_width + i*Cell_width;
            Point_z=-[0 0 0 0 0 1;0 0 0 0 0 1;1 1 1 1 0 1;1 1 1 1 0 1] * Cell_length + k*Cell_length;

            color = ones(4,6)*Porosity_3D_adjusted(i,j,k);

            if (isnan(Porosity_3D_adjusted(i,j,k))==0)
                for l=1:6
                    patch(Point_x(:,l),Point_z(:,l),Point_y(:,l),color(:,l));
                end
            end
        end
    end
end

view(45, 15);
hold off
axis equal
axis off

cbar = colorbar('Location','Eastoutside',...
    'FontName', 'Helvetica', ...
    'FontSize',14);
set(get(cbar,'ylabel'),'string','Porosity, $\phi$ [-]',...
    'Rotation',90,...
    'FontName', 'Helvetica', ...
    'interpreter', 'latex',...
    'fontsize',16);

caxis([0 0.7])

map=mycmap_dark;     % Map=flip(hot);
colormap(map)      % Parula  imcomplement(gray)  hot
end;

%% Slice plot of the porosity map
if phi_slice=='Y'
    Fig_3D_phi_cross=figure('Color',[1 1 1]);
    Fig_3D_phi_cross.Units = 'centimeters';
    Fig_3D_phi_cross.Position = [12 5 20 10];


    for k = 1:Cell_Z_No
        for j = ceil(Cell_X_No/2-1)
            for i = 1:Cell_Y_No
                Point_x=-[0 1 1 0 0 0;1 1 0 0 1 1;1 1 0 0 1 1;0 1 1 0 0 0] * Cell_width + j*Cell_width;
                Point_y=-[0 0 1 1 0 0;0 1 1 0 0 0;0 1 1 0 1 1;0 0 1 1 1 1] * Cell_width + i*Cell_width;
                Point_z=-[0 0 0 0 0 1;0 0 0 0 0 1;1 1 1 1 0 1;1 1 1 1 0 1] * Cell_length + k*Cell_length;

                color = ones(4,6)*Porosity_3D_adjusted(i,j,k);

                if (isnan(Porosity_3D_adjusted(i,j,k))==0)
                    for l=1:6
                        patch(Point_x(:,l),Point_y(:,l),-Point_z(:,l),color(:,l),...
                            'LineWidth',0.1);
                    end
                end
            end
        end
    end

    view(45, 15);
    hold off
    axis equal
    axis off
```

```
    % Colorbar for the methodological overview figure
    cbar = colorbar('Position',...
   [[0.643200320225391 0.543516666666667 0.0244085427689588 0.383116666666667]],...
      'FontName', 'Arial', ...
      'FontSize',10);

   caxis([0 1])

   map=mycmap_dark;     % map=flip(hot);
   colormap(map)      % parula  imcomplement(gray)  hot
end;



%% Plot porosity histogram
if porosity_histogram=='Y'
   porosity_vector=reshape(Porosity_3D_adjusted,Cell_X_No*Cell_Y_No*Cell_Z_No,1,1);

   porosity_hist=figure('Color',[1 1 1]);
   porosity_hist.Units = 'centimeters';
   porosity_hist.Position = [12 2 6.7 6.3];

   bins = (0:0.04:1);
   hist(porosity_vector, bins);

   set(gca,'FontName','Arial','FontSize',10);

   ylabel('Frequency','FontSize',10,'FontName','Arial');
   xlabel('Porosity, \phi (-)','FontSize',10,'FontName','Arial');

   % Calculate standard deviation
   count=0;
   for i=1:length(porosity_vector)
      if (isnan(porosity_vector(i))==0)
         count=count+1;
         porosity_vector_value(count)=porosity_vector(i);
      end;
   end;

   std(porosity_vector_value)
   mean(porosity_vector_value)
end


%% Full 3D plot of the permeability map
if permeability_full=='Y'
   Fig_3D_perm_full=figure('Color',[1 1 1]);
   Fig_3D_perm_full.Units = 'centimeters';
   Fig_3D_perm_full.Position = [12 5 20 10];


   for k = 1:Cell_Z_No
      for j = 1:Cell_X_No
         for i = 1:Cell_Y_No
            Point_x=-[0 1 1 0 0 0;1 1 0 0 1 1;1 1 0 0 1 1;0 1 1 0 0 0] * Cell_width + j*Cell_width;
            Point_y=-[0 0 1 1 0 0;0 1 1 0 0 0;0 1 1 0 1 1;0 0 1 1 1 1] * Cell_width + i*Cell_width;
            Point_z=-[0 0 0 0 0 1;0 0 0 0 0 1;1 1 1 1 0 1;1 1 1 1 0 1] * Cell_length + k*Cell_length;

            color = ones(4,6)*Permeability_3D_adjusted(i,j,k);

            if (isnan(Permeability_3D_adjusted(i,j,k))==0)
               for l=1:6
                  patch(Point_x(:,l),Point_z(:,l),Point_y(:,l),color(:,l));
               end
            end
         end
      end
   end

   view(45, 20);
   hold off
   axis equal
   axis off
```

```
    cbar = colorbar('Location','Eastoutside',...
        'FontName', 'Helvetica', ...
        'YScale','log',...
        'FontSize',14);
    set(get(cbar,'ylabel'),'string','Permeability, $k$ [$m^2$]',...
        'Rotation',90,...
        'FontName', 'Helvetica', ...
        'interpreter', 'latex',...
        'fontsize',16);

    caxis([1e-16 1e-12])

    map=mycmap_dark;     % Map=flip(hot);
    colormap(map)      % Parula  imcomplement(gray)  hot
end



%% 3 Quarter 3D plot of the permeability map
if perm_3quarter=='Y'
    Fig_3D_perm_3quarter=figure('Color',[1 1 1]);
    Fig_3D_perm_3quarter.Units = 'centimeters';
    Fig_3D_perm_3quarter.Position = [12 5 20 10];

    for k = 1:Cell_Z_No
        for j = 1:Cell_X_No
            for i = 1:1:ceil(Cell_Y_No/2)
                Point_x=-[0 1 1 0 0 0;1 1 0 0 1 1;1 1 0 0 1 1;0 1 1 0 0 0] * Cell_width + j*Cell_width;
                Point_y=-[0 0 1 1 0 0;0 1 1 0 0 0;0 1 1 0 1 1;0 0 1 1 1 1] * Cell_width + i*Cell_width;
                Point_z=-[0 0 0 0 0 1;0 0 0 0 0 1;1 1 1 1 0 1;1 1 1 1 0 1] * Cell_length + k*Cell_length;

                color = ones(4,6)*Permeability_3D_adjusted(i,j,k);

                if Permeability_3D_adjusted(i,j,k)>1e-19
                    for l=1:6
                        patch(Point_x(:,l),Point_z(:,l),Point_y(:,l),color(:,l),'LineWidth',0.3);
                    end
                end
            end
        end
    end

    for k = 1:Cell_Z_No
        for j = 1:ceil(Cell_X_No/2)
            for i = (ceil(Cell_Y_No/2)+1):Cell_Y_No
                Point_x=-[0 1 1 0 0 0;1 1 0 0 1 1;1 1 0 0 1 1;0 1 1 0 0 0] * Cell_width + j*Cell_width;
                Point_y=-[0 0 1 1 0 0;0 1 1 0 0 0;0 1 1 0 1 1;0 0 1 1 1 1] * Cell_width + i*Cell_width;
                Point_z=-[0 0 0 0 0 1;0 0 0 0 0 1;1 1 1 1 0 1;1 1 1 1 0 1] * Cell_length + k*Cell_length;

                color = ones(4,6)*Permeability_3D_adjusted(i,j,k);

                if Permeability_3D_adjusted(i,j,k)>1e-19
                    for l=1:6
                        patch(Point_x(:,l),Point_z(:,l),Point_y(:,l),color(:,l),'LineWidth',0.3);
                    end
                end
            end
        end
    end

    view(45, 20);
    hold off
    axis equal
    axis off

    cbar = colorbar('Location','Eastoutside',...
        'FontName', 'Arial', ...
        'YScale','log',...
        'FontSize',10);
    set(get(cbar,'ylabel'),'string','Permeability, k (m^2)',...
        'Rotation',90,...
        'FontName', 'Arial', ...
        'interpreter', 'tex',...
        'fontsize',10);
```

```
    caxis([1e-15 1e-12])

    map=mycmap_dark;     % Map=flip(hot);
    colormap(map)      % Parula  imcomplement(gray)  hot
end;


%% Slice plot of the permeability map
if permeability_slice=='Y'
    Fig_3D_perm_full=figure('Color',[1 1 1]);
    Fig_3D_perm_full.Units = 'centimeters';
    Fig_3D_perm_full.Position = [12 5 20 10];

    for k = 1:Cell_Z_No
        for j = ceil(Cell_X_No/2)
            for i = 1:(Cell_Y_No)
                Point_x=-[0 1 1 0 0 0;1 1 0 0 1 1;1 1 0 0 1 1;0 1 1 0 0 0] * Cell_width + j*Cell_width;
                Point_y=-[0 0 1 1 0 0;0 1 1 0 0 0;0 1 1 0 1 1;0 0 1 1 1 1] * Cell_width + i*Cell_width;
                Point_z=-[0 0 0 0 0 1;0 0 0 0 0 1;1 1 1 1 0 1;1 1 1 1 0 1] * Cell_length + k*Cell_length;

                color = ones(4,6)*Permeability_3D_adjusted(i,j,k);

                if (isnan(Permeability_3D_adjusted(i,j,k))==0)
                    for l=1:6
                        % To draw a vertical cross section
                        patch(Point_x(:,l),Point_y(:,l),-Point_z(:,l),color(:,l),...
                            'LineWidth',0.1);
                    end
                end
            end
        end
    end

    view(45, 20);
    hold off
    axis equal
    axis off

     % Colorbar for the methodological overview figure
     cbar = colorbar('Position',...
    [[0.643200320225391 0.543516666666667 0.0244085427689588 0.383116666666667]],...
        'FontName', 'Arial', ...
        'YScale','log',...
        'FontSize',10);

    caxis([1e-15 1e-12])

    map=mycmap_dark;     % Map=flip(hot);
    colormap(map)      % Parula  imcomplement(gray)  hot
end;


%% Plot permeability histogram

if permeability_histogram=='Y'
    permeability_vector=reshape(Permeability_3D_adjusted,Cell_X_No*Cell_Y_No*Cell_Z_No,1,1);

    permeability_hist=figure('Color',[1 1 1]);
    permeability_hist.Units = 'centimeters';
    permeability_hist.Position = [12 2 6.7 6.3];

    bins = 10.^(-22:0.3:-11);
    hist(permeability_vector, bins);

    set(gca,'FontName','Arial','FontSize',10,'XMinorTick','on','XScale','log');

    ylabel('Frequency','FontSize',10,'FontName','Arial');
    xlabel('Permeability (m^2)','FontName','Arial');

    % Calculate standard deviation
    count=0;
    for i=1:length(permeability_vector)
        if (isnan(permeability_vector(i))==0)
            count=count+1;
```

```
            permeability_vector_value(count)=permeability_vector(i);
        end;
    end;

    std(permeability_vector_value)
    mean(permeability_vector_value)
end
```

Appendix IV

Functional form of geometric factors P and Q

The coefficients P and Q for ellipsoidal inclusions of arbitrary aspect ratio are given by

$$P = \frac{1}{3}T_{iijj} \tag{A1}$$

$$Q = \frac{1}{5}(T_{ijij} - \frac{1}{3}T_{iijj}) \tag{A2}$$

The tensor T_{ijkl} relates the unfirm far-field strain field to the strain within the ellipsoidal inclusion (Wu, 1966). Berryman gives the pertinent scalers required for comparing P and Q as

$$T_{iijj} = 3\frac{F_1}{F_2} \tag{A3}$$

$$T_{ijij} - \frac{1}{3}T_{iijj} = \frac{2}{F_3} + \frac{1}{F_4} + \frac{F_4F_5+F_6F_7-F_8F_9}{F_2F_4} \tag{A4}$$

where

$$F_1 = 1 + A\left[\frac{3}{2}(f+\theta) - R(\frac{3}{2}f + \frac{5}{2}\theta - \frac{4}{3})\right] \tag{A5}$$

$$F_2 = 1 + A\left[1 + \frac{3}{2}(f+\theta) - \left(\frac{R}{2}\right)(3f+5\theta)\right] + B(3-4R) + (\frac{A}{2})(A+3B)(3-4R)[f+\theta-R(f-\theta+2\theta^2)] \tag{A6}$$

$$F_3 = 1 + A\left[1 - \left(f + \frac{3}{2}\theta\right) + R(f+\theta)\right] \tag{A7}$$

$$F_4 = 1 + (\frac{A}{4})[f + 3\theta - R(f-\theta)] \tag{A8}$$

$$F_5 = A\left[-f + R(f+\theta-\frac{4}{3})\right] + B\theta(3-4R) \tag{A9}$$

$$F_6 = 1 + A[1 + f - R(f+\theta)] + B(1-\theta)(3-4R) \tag{A10}$$

$$F_7 = 2 + \left(\frac{A}{4}\right)[3f + 9\theta - R(3f+5\theta)] + B\theta(3-4R) \tag{A11}$$

$$F_8 = A\left[1 - 2R + \left(\frac{f}{2}\right)(R-1) + (\frac{\theta}{2})(5R-3)\right] + B(1-\theta)(3-4R) \tag{A12}$$

$$F_9 = A[(R-1)f - R\theta] + B\theta(3-4R) \tag{A13}$$

with A, B, and R is given

$$A = \frac{\mu_i}{\mu_m} - 1 \tag{A14}$$

$$B = \frac{1}{3}\left(\frac{Ki}{Km} - \frac{\mu_i}{\mu_m}\right) \tag{A15}$$

$$R = \left[\frac{(1-2\vartheta_m)}{2(1-\vartheta_m)}\right] \tag{A16}$$

The functions θ and *f* are given

$$\theta = \begin{cases} \frac{\alpha}{(\alpha^2-1)^{\frac{3}{2}}}\left[\alpha(\alpha^2-1)^{\frac{1}{2}} - \cosh^{-1}\alpha\right] \\ \frac{\alpha}{(1-\alpha^2)^{\frac{3}{2}}}\left[\cos^{-1}\alpha - \alpha(1-\alpha^2)^{\frac{1}{2}}\right] \end{cases} \tag{A17}$$

For prolate and oblate spheroids, respectively, and

$$f = \frac{\alpha^2}{1-\alpha^2}(3\theta - 2) \tag{A18}$$

Note that α<1 for oblate shapes, and α>1 for prolate spheroids.